Capacitor Probe Calibration and Optimization for NDE

Application to Portland Cement Concrete

Aref Alderbas Alzaabi

Dissertation submitted to the Faculty of the
Virginia Polytechnic Institute and State University
In partial fulfillment of the requirements for the degree of

Doctor of Philosophy
in
Civil and Environmental Engineering

Imad L. Al-Qadi, Chairman
Professor of Civil and Environmental Engineering

Sedki M. Riad, Co-Chairman
Professor of Electrical and Computer Engineering

Richard M. Barker
Professor of Civil and Environmental Engineering

Ioannis M. Besieris
Professor of Electrical and Computer Engineering

Siegfried M. Holzer
Alumni Distinguished Professor of
Civil and Environmental Engineering

August 28, 2000
Blacksburg, Virginia

Keywords: Portland Cement Concrete, Deterioration, Nondestructive Evaluation, Dielectric Constant, Capacitor Probe

Capacitor Probe Calibration and Optimization for NDE Application to Portland Cement Concrete

Aref Alderbas Alzaabi

(**ABSTRACT**)

Three main objectives have been set for this research. The first is to develop an accurate method for measuring the dielectric constant of PCC using a capacitor probe (C-Probe) that has been recently developed at Virginia Tech and validate it for field application to detect internal PCC flaws such as delamination. The C-Probe consists of two flexible conducting plates, connected to a Network Analyzer, with a specific separation between them. The second is to optimize the C-Probe design configuration for different PCC slab thicknesses. The third objective is to develop a predictive model that correlates the bulk dielectric constant of PCC with its critical parameters (cement, aggregate, and air content). Five calibration methods have been developed and evaluated for the C-Probe to measure the dielectric properties of PCC. This evaluation has demonstrated that open, short, Teflon material (OSM) calibration method is the most appropriate one for the C-Probe. The selected calibration method was used to validate the C-Probe fixture for field application by measuring 1.5 x 1.5 m PCC slabs prepared with different mix properties, thicknesses, and induced deterioration. The C-Probe has been proved to detect induced voids in the PCC slabs. In addition, the effect of steel reinforcement on measurements can be mastered by controlling the penetration of electromagnetic (EM) field in the PCC slabs. The effective penetration depth of the EM field for different C-Probe design configuration was optimized by computer simulation. The results have been used to develop a predictive model that correlates the effective penetration depth with the plates' size, separation between them, and the dielectric constant of the PCC under test. Thus, an optimum design for different desired penetration depth was achieved. Two experimental designs were developed to identify the critical parameters that affect the bulk dielectric constant of PCC. A computer simulation was used to identify the significance of each parameter. A predictive model has been developed to correlate the PCC bulk dielectric constant to the critical parameters. The estimated dielectric constant of PCC using the predictive model was correlated to that obtained by other theoretical mixture models; the predictive model has found to correlate well with Looyenga theoretical mixture model.

Acknowledgements

I wish to express my great thanks to Dr. Imad Al-Qadi, my advisor, and committee chairman, and Dr. Sedki Riad, my committee co-chairman, for their continuous support and sincere advisory. Without their patience and cooperation throughout this research, it would not have been possible to finish this project.

I would like also to express my sincere thanks to Dr. Richard Barker for his sincere assistance through my Ph.D. study at Virginia Tech, for serving in my committee, and for his inputs to my education. I also owe Dr. Siegfried Holzer and Ioannis Besieris special thanks for serving on my committee, and for their encouragement.

I dedicated this work to my parents, my brother Engineer Jamal Alderbas Alzaabi, whom I owe the credit for instilling in me the value of education, my wife Dr. Intesar Al-Loughani, and my children Yousef, Sheikha, Abdullah, and Maryam. I am in debt to them for their love, unlimited support, sacrifices, and patience throughout the course of this work.

Finally, I thank all my friends in Blacksburg and back home who supported me with their love, care, and prayers. This work was supported in part by the Kuwait University.

Table of Content

List of Figures

List of Tables

1 CHAPTER 1: INTRODUCTION

This chapter introduces the research of C-Probe calibration, optimization, and validation for nondestructive evaluation (NDE) of Portland cement concrete (PCC) and consists of five sections. Section 1.1 identifies the work conducted in this research; Section 1.2 presents the research background; Section 1.3 states the problem; and Section 1.4 presents the objectives of the research. In addition, Section 1.5 describes the scope and the limitations of the research and outlines the rest of the document.

1.1 Identification of the Research

This research deals with the dielectric properties of PCC and includes both experimental and computational work. The experimental work focused on developing an appropriate calibration technique for measuring the dielectric properties of PCC using the recently developed capacitor probe (C-Probe). The new calibration method has been used to validate the C-Probe for field application by measuring PCC slabs of different mix structure properties. The computational work consisted of developing a simulation technique to optimize the C-Probe design and study the mixture theory of the PCC. In the C-Probe optimization phase, the effect of changing the plates' size as well as the separation between them, on the penetration depth of the electric field in the PCC specimen under test has been studied. In the mixture theory phase, the correlation between the bulk dielectric constant and the physical property of PCC components (cement, aggregate, and air content) has also been investigated.

1.2 Background

Portland cement concrete (PCC), the most used construction material in the world, has several characteristics that maks it such a popular material. It resists water-related deterioration better than other construction materials such as wood and steel. Unlike many other construction materials, it can be formed into unlimited shapes and sizes due to its plastic consistency, which allows it to flow into any formwork during its early curing phase. It is also relatively cheap because its mix components (cement, aggregate, and water) are readily available at low cost throughout the world. Finally, PCC production requires less production energy than other construction material (Mehta and Monteiro, 1993).

In spite of the simplicity of its mix components, concrete is a complex material, and, therefore, its behavior is still not well understood. The internal mix structures control both its physical and chemical properties. Portland cement concrete's structure, which is heterogeneous and highly complex, consists of three phases: hydrated cement paste, aggregate, and the transition zone between the hydrated cement paste and the aggregate. The hydrated cement paste, developed from the reaction of Portland cement with water, is responsible for the strength of PCC. The aggregate, which forms the skeleton of the mix, plays an important role in shaping PCC's structure and providing its durability, despite the fact that it is only filler in normal strength PCC. The transition zone, located around the surface of the aggregate, is the weakest area of the PCC.

The composition of PCC plays a significant role in the stability and life of PCC infrastructures, i.e. the physical facilities that provide essential public services, such as highways, utilities, buildings, and the like (Hudson *et al*., 1997). In the United States, the infrastructure system, including all categories, represents about $20 trillion (NSF, 1995), a sizeable investment of assets. Over time, PCC infrastructures deteriorate because of loading and environmental conditions and need maintenance or rehabilitation. For example, approximately 32 percent of the United States' 581,000 bridges are classified as functionally deficient or obsolete because of excessive deterioration (ASCE, 1998). Portland cement concrete deterioration may result from poor materials, improper mix design, consolidation, and/or curing process. In addition, inadequate coverage of steel reinforcement, chloride intrusion, freeze/thaw cycles, and chemical attacks may lead to permanent deterioration of the PCC infrastructures. As a result, preventative measure and major repairs to the total infrastructure cost more than $80 billion annually (Hudson *et al.*, 1997)

Since most of the deterioration of the PCC infrastructure takes place underneath the surface, it is difficult to be detected by visual inspection in its early stages. When deterioration reaches the surface and becomes visible, the rehabilitation or the maintenance of the PCC infrastructure becomes costly and complicated. Therefore, detecting its deterioration at early stages will significantly reduce the cost of rehabilitation and maintenance, as well as the disruption of the facility's use.

Destructive techniques, such as taking core samples, for evaluating PCC structures are costly and may cause disruptions that inconvenience facility users. However, nondestructive evaluation (NDE) methods are usually inexpensive and noninvasive in nature, and have the advantage of providing measurement results more rapidly than the destructive test methods do.

Nondestructive evaluation methods have, therefore, become more attractive to civil engineers for evaluating facilities constructed of PCC. Among the NDE methods, the electromagnetic (EM) techniques have received considerable attention in recent years for evaluating the structure of PCC. Electromagnetic methods have been used to evaluate deterioration in PCC structure, such as the corrosion potential of reinforcing steel and detecting defects using magnatic flux leakage (Lauer, 1991).

Portland cement concrete is considered a dielectric material that stores energy when exposed to an electric field. Therefore, the PCC can be characterized by its dielectric properties using EM methods. In addition, the study of the dielectric properties of any material including PCC is important, because EM energy transformation, whether it occurs reversibly or irreversibly, is always a result of the interaction of EM waves with the actual material (Tinga in Priou, 1992). Furthermore, the complex dielectric constant is one of the most important properties that allows the detection of PCC deterioration, because the real part shows the ability of PCC to store energy as an electric charge, while the imaginary part shows the loss of energy due to molecular friction and conduction (Al-Qadi and Riad, 1996). Therefore, changes in chemical and physical properties of PCC due to deterioration can be detected by monitoring both the dielectric constant of PCC and the EM excitation propagation in PCC.

Al-Qadi and Riad (1996) have investigated the dielectric properties of PCC over a wide band of frequencies (0.1 MHz to 10 GHz) using three newly developed fixtures, the parallel-plate capacitor, coaxial transmission line, and TEM horn antenna. The parallel-plate capacitor setup, which uses low frequencies ranging from 0.1 MHz to 40.1 MHz, showed feasible results for detecting different types of deterioration in PCC, such as chloride contamination. However, although this fixture proved to be beneficial in characterizing concrete dielectric properties in the laboratory, it is not suitable for use in the field.

For in-situ measurements of the dielectric properties of PCC, Al-Qadi *et al*. (1998) have developed a capacitor probe that allows engineers to measure the dielectric constant of concrete structures with access from one surface only, regardless of the concrete structure's shape. Although preliminary testing results have shown the feasibility of this technique to detect concrete deterioration such as internal flaws, the C-Probe needs an appropriate calibration technique and further testing before it can be validated and used in the field. In addition, further research is needed to optimize the design of the capacitor probe configuration with respect to the sizes of the plates and the distance between them.

1.3 Problem Statement

The developed C-Probe still lacks the following:

1) Acceptable dielectric constant measurements.

2) A simulation technique to optimize its design, which includes plates' size and the separation between them.

3) Simulation techniques to correlate the measured bulk dielectric constant of PCC with its components and its relation to a PCC mixture behavior.

1.4 Objectives

To address the aforementioned needs, this research has three main objectives:

1) To develop an appropriate calibration method for the C-Probe.

2) To evaluate different designs of the C-Probe configuration with regard to its plates' size and the separation between them.

3) To develop a predictive model that correlates the bulk dielectric constant of PCC with the dielectric constants of its constituents.

1.5 Scope of the Research

To achieve the above objectives, this research project has been divided into four main tasks: C-Probe calibration, C-Probe design optimization, C-Probe field validation, and mixture theory evaluation.

1.5.1 C-Probe Calibration

For the C-Probe calibration, five different schemes were developed using both scattering-parameter and bilinear transformation methods. For the scattering-parameter methods, three standards (open, short, and load) were used in the calibration scheme of the C-Probe. For the bilinear transformation methods, two standard materials with known dielectric constants (such as Teflon and Nylon) were used with the open and the short standards to calibrate the C-Probe measurements, which were obtained over a frequency range of 0.1 kHz to 40.1 MHz.

To verify the calibration procedure, a reference-measuring device, such as capacitor meter (C-Meter), has been used. Both the standard materials and the C-Probe PCC specimen (450 x 300 x 100 mm) were measured using the C-Meter. To verify the C-Meter measurements of the dielectric constant of PCC, PCC specimen (75 x 75 x 100 mm) has been measured using both the PCC fixture and the C-Meter. In addition, the resulting measurements were used to compare the PCC specimen to the C-Probe specimen that has the same mix design.

1.5.2 C-Probe Design Optimization

A computer simulation has been used to optimize the C- Probe design configuration (plates' size and separation between them) to obtain the maximum effective penetration depth of the EM field in the PCC slab under test. Different relative dielectric constants of PCC (10, 30, 50) were also considered in the optimization study. A predictive model has been developed to correlate the C-Probe design configuration, as well as the relative dielectric constant of PCC, with the effective penetration depth of the EM fields in the PCC slab under test. The developed model has been used to obtain an optimum design configuration for different PCC slab thicknesses ranging from 63 to 127 mm.

1.5.3 C-Probe Field Validation

To validate the use of the C-Probe for detecting different PCC properties and internal flaws, the dielectric constants of PCC specimens (450 x 300 x 100 mm) were measured using the C-Probe fixture. These specimens, prepared and used by Diefenderfer *et al.* (1998), were cast using Type I Portland cement and limestone aggregate with a water to cement ratio of 0.45. They were made with two different air contents (2 and 6 percent) to study the effect of different PCC components on the measured dielectric constant of PCC using the C-Probe. In addition, to validate the use of the C-Probe in detecting deterioration, these PCC specimens were cast with simulated void thicknesses using Styrofoam of 7.5 mm and 15 mm thick. These specimens were measured from both surfaces to study the effect of the void depth on the measured dielectric constant of PCC using the C-Probe.

The C-Probe has been also validated for field application by measuring concrete slabs (1.5 x 1.5 m) prepared by Loulizi (1999). These slabs were prepared using Type I Portland cement and different types of aggregate with a water to cement ratio of 0.45. They were cast with three

thicknesses; 102 mm, 127 mm, and 152 mm, with air-void-induced thicknesses of 6.4 mm and 12.7 mm at 51 mm below the surface. In addition, these slabs were made with different mixes and included both one-way and two-way reinforcement.

1.5.4 Mixture Theory Evaluation

In this task, the mixture behavior of PCC has been investigated using computer simulation with parallel plate capacitor setup. A statistical factorial design has been developed to correlate the bulk dielectric constant of PCC with its critical mix parameters such as aggregates, cement, and air content that affect the dielectric constant. Besides, factors such as aggregate shape and gradation were also investigated in this study. The computer simulation has been used to obtain the required data for the experimental designs. The effective parameters were identified using ANOVA and a predictive model has been developed, using regression analysis technique, to correlate the bulk dielectric constant of PCC with those critical parameters. To determine the best mixture theory for PCC, the results obtained from the developed model were compared with results computed from major theoretical mixture formulas developed in the past, such as the Maxwell mixture formula.

This document consists of five chapters. Chapter 2 provides thorough information about the background needed for conducting this research and consists of five sections. While Section 2.1 presents information about the PCC mix structure and components, cement, aggregates, and water, Section 2.2 gives summary about major PCC deterioration that occurs in United States. In addition, Section 2.3 briefs the reader about the concept of the dielectric material and Section 2.4 provides a literature review about the use of NDE techniques used for detecting PCC deterioration. Systems used in the study were presented in Section 2.5.

Chapter 3 explains the research program used and consists of four sections. Section 3.1 discusses the methodology used to calibrate the C-Probe measurements; Section 3.2 explains the methodology used in optimizing the C-Probe design configuration (the size of the plates and the separation between them); Section 3.3 illustrates the method used in validating the use of the C-Probe for field application; and Section 3.4 reports the methodology of developing a predictive model that correlates the bulk dielectric constant of PCC with its critical mix parameters (cement, aggregates, and air content) and using this model in evaluating the theoretical mixture formulas.

Chapter 4, which consists of four sections related to those of chapter 3, discusses the results of the research and analyzes the data. Section 4.1 discusses the results of the C-Probe calibration task; Section 4.2 gives the results of the optimization work; Section 4.3 reports the results of the C-probe field application using the best calibration method from Section 4.1; and Section 4.4 discusses the mixture theory results.

Chapter 5 highlights the major conclusions obtained from the data analyses and gives recommendations for future work in the area of this research.

Four appendices are provided with this document. Appendix A presents the data obtained in the C-Probe calibration task. Appendix B gives the output data of the C-Probe optimization task. Appendix C contains the mix design, quality control data, and the dielectric constant measurements for all PCC specimens and slabs used in this research for validating the C-Probe fixture, and Appendix D presents all output data of the mixture theory task as well as the results of the statistical analyses.

2 CHAPTER 2: PRESENT STATE OF KNOWLEDGE

This chapter provides thorough background information related to the subject of the research and consists of five sections. Section 2.1 discusses the physical properties and the chemical composition of PCC mix structures, while Section 2.2 gives the associated deterioration of these mix structures. Section 2.3 provides the necessary background about dielectric materials, such as PCC, and discusses the polarization concept. Since the research subject is considered one of the NDE methods, Section 2.4 provides a literature survey about the use of electromagnetic waves techniques for PCC characterization and detecting PCC deterioration. Finally, Section 2.5 describes the systems used in this research: the capacitor probe fixture, parallel-plate capacitor fixture, capacitor meter, and HP Network Analyzer.

2.1 Portland Cement Concrete Mix Structure

Material characterization is the heart of the Civil Engineering research on Portland cement concrete, which recognizes that material properties are originated (or controlled) by internal mix structure of PCC. Portland cement concrete mix structure is heterogeneous and highly complex. Therefore, it is difficult to draw a model that relates PCC behavior to its complex mix structure. However, knowledge of PCC mix structure components and their relationship to each other is very helpful in understanding and controlling the PCC properties. Portland cement concrete mix structure consists of three major phases namely: the hydrated cement paste, the aggregate, and the transition zone between the cement paste and the aggregate. The dynamic nature of the PCC mix structure components increases the difficulty of deriving structure-property model (Mehta and Monteiro, 1993).

Portland cement concrete mix structure has some unique features. One is the transition zone that forms the weakest phase of this structure and influences the mechanical behavior of PCC. Another is the multiphase nature of each component of the PCC mix structure: aggregate contains minerals, voids, and cracks; the hydrated cement paste contains solids, micro-cracks, and voids; and the transition zone contains solids, micro-cracks, and voids. In addition, properties of two components of the PCC mix structure; the hydrated cement paste and the transition zone, change with time and environmental load (Mehta and Monteiro, 1993).

2.1.1 Portland Cement

The term cement paste used in this dissertation refers to paste made from Portland cement. Cement paste is much weaker than aggregate and consequently is responsible for most of the physical and mechanical properties of the mix. Since the cement paste is the more important phase in PCC, it is essential to understand its structures and its chemical compositions as well as their relation with properties of PCC.

Portland cement is manufactured out of lime, silica, alumina, and iron oxide. These raw materials when they interact in the kiln form several complex chemical compounds, which are then interground with approximately 5% gypsum. The four main compounds are Tricalcium silicate C_3S (55% of wt.), Dicalcium silicate C_2S (20% of wt.), Tricalcium aluminate C_3A (10% of wt.), and Tetracalcium aluminoferrite C_4AF (8% of wt.). C_3S and C_2S are responsible for the strength of the cement paste. Alumina and iron, which produce C_3A and C_4AF, are used to reduce the required temperature for producing C_3S. In addition, several minor compounds, such as magnesium oxide, titanium oxide, manganese oxide, sodium oxide, and potassium oxide, are present in smaller percentages of weight. Two of these minor, compounds, however, play an important role in PCC disintegration when they interact chemically with aggregate such as sodium oxide (Na_2O) and potassium oxide (K_2O), creating a reaction called alkalis silica reaction (ASR) at the presence of water and under suitable temperature (Mamlouk and Zaniewski, 1999; Young and *et al.,* 1998).

2.1.2 Hydration of Portland Cement

Cement paste results from the hydration process, is a complex chemical reaction between Portland cement and water. The main compounds listed above react with water concurrently and produce hydration products. Calcium silicates (both tricalcium and dicalcium) react with water forming calcium silicate hydrate (C-S-H) and calcium hydroxide (C-H). When hydrated completely, dicalcium silicate produces a higher percentage of C-S-H and a lower percentage of C-H than what tricalcium silicate does. The C-S-H is the strength-producing hydration product of the cement paste and the C-H is susceptible to acidic water and sulfate attack. Therefore, increasing the content of the dicalcium silicate relative to the amount of tricalcium silicate will enhance the ultimate strength of PCC and improves its durability too. Tricalcium aluminate compound reacts with water in the presence of gypsum to produce ettringite.

Without gypsum, the tricalcium aluminate would react with water vigorously and produce in a short time a large amount of hydration products, which can cause PCC to set within few minutes, flash setting. Gypsum is used to prevent flash setting from occurring in the cement paste because it slows down the hydration process of the aluminate, which it is much faster than the hydration process of the silicate. The presence of gypsum is also beneficial in that it may cause sulfate ions in the solution to accelerate the hydration process of tricalcium silicate to produce the calcium silicate hydrate (C-S-H) that contributes to the final set time and early strength gain of the cement paste. As the gypsum is consumed in the hydration process, the ettringite reacts further with the tricalcium aluminate and water to produce monosulfoaluminate. Tetracalcium aluminoferrite (C_4AF) would react with water and C-H to produce tetracalcium aluminate hydrate and ferric-aluminum hydroxide. Young *et al.* (1998) simplified the reactions of the hydration process by the following equations:

$$2C_3S + 7H \rightarrow C_3S_2H_8 + 3CH$$

$$2C_2S + 5H \rightarrow C_3S_2H_8 + CH$$

Calcium Silicate + Water $\rightarrow$ Calcium Silicate Hydrate + Calcium Hydroxide

$$C_3A + 3C\underline{S}H_2 + 26H \rightarrow C_6A\underline{S}_3H_{32}$$

Tricalcium aluminate + gypsum + water $\rightarrow$ ettringite

$$C_6A\underline{S}_3H_{32} + 2C_3A + 4H \rightarrow 3C_4A\underline{S}H_{12}$$

Ettringite + Tricalcium aluminate + water $\rightarrow$ Calcium monosulfoaluminate hydrate

$$C_4AF + 14H + 2CH \rightarrow C_4(A,F)H_{13} + (A,F)H_3$$

Tetracalcium aluminoferrite + water + calcium hydroxide $\rightarrow$ tetracalcium aluminate hydrate + ferric-aluminum hydroxide.

The aforementioned chemical reactions occur at different rates and the strength generated by the hydration products is different. The strength of cement paste is mostly due to the hydration products of calcium silicates (Mamlouk and Zaniewski, 1999; Young and *et al.,* 1998).

Although the solid phase, which the aforementioned chemical reactions have produced, significantly affects the properties of the cement paste, voids have important influences on the cement paste too. Three types of voids can be identified in cement paste. Interlayer voids, which consist of 28 percent of the porosity in the solid C-S-H, are too small to have a negative effect on the strength and the permeability of hydrated cement paste. However, hydrogen bonding can hold water in these voids and its removal from these voids may lead to drying shrinkage and creep. Capillary voids represent the space not filled by the solid components of the hydrated cement paste and their shapes are characterized by irregularities. Porosity is the volume of the capillary voids. Macropores (> 50 nm) are assumed to be detrimental to strength and impermeability, whereas micropores (< 50 nm) are more important to drying shrinkage and creep. Air voids, which are much larger in size than capillary voids and spherical in shapes, adversely affect PCC strength and permeability.

The existence of water in cement paste also affects the paste significantly. Its presence there has been grouped into four categories. One, the interlayered water, is associated with C-S-H. The C-S-H structure shrinks considerably when the interlayer water is lost, but this loss occurs only in strong drying, as when the relative humidity (RH) is 11 percent. Another category, capillary water, is the water that is free from the attractive forces of the solid surfaces. It is divided into two sub-categories: larger than 50 nm, that is called free water and whose removal does not cause any volume change, and smaller than 50 nm that is held by capillary tension, and whose removal may cause shrinkage of the system. The third category, adsorbed water, is close to solid surfaces where water molecules are physically adsorbed by the surface of the solids in the hydrated cement paste. The loss of the adsorbed water is mainly responsible for the shrinkage of the hydrated cement paste in drying. Drying the hydrated cement paste to 30 percent relative humidity (RH) will lead to a loss of a major portion of the adsorbed water. The chemically combined water is an integral part of the structure of various cement-hydrated products and it is not lost in drying (Mehta and Monteiro, 1993).

Portland cement concrete properties consisting of strength, dimensional stability, and durability are influenced by the proportion and the properties of the hydrated cement paste, which, in turn, depends on the microstructure features of the hydrated cement paste: the types and amount of the hydrated cement paste and the distribution of solids and voids. Strength

results from the existence of the van der Waals forces of attraction. These are physical forces that exist between two solid adhesive surfaces. Saturated hydrated cement paste is not dimensionally stable. When the relative humidity starts to drop down to less than 100%, shrinkage will start to occur due to the removal of water. Water removal can also be due to external sustained loads, a phenomeneon called creep. Durability relates to the material service life under given environmental loads. Since the hydrated cement paste is alkaline, acidic water is detrimental to the material. Consequently, impermeability, also called watertightness, is a primary factor in determining durability of the material or the hydrated cement paste. Permeability is the ease with which a fluid can flow through a solid. The size and the continuity of the pores in the structure of the solid determine its permeability. An increasing degree of hydration greatly reduces the permeability (Mehta and Monteiro, 1993).

2.1.3 Aggregate

Aggregate forms 60 to 75 percent of PCC volume and 79 to 85 percent of its weight and are considered as filler to reduce the amount of cement paste needed in the mix. Since aggregate has greater volume stability than the hydrated cement paste, its amount is maximized to a certain extent to enhance the quality and economy of the mix (Mamlouk and Zaniewski, 1999).

The aggregate phase is responsible for the unit weight, elastic modulus, and dimensional stability of PCC. Porosity, shape, and texture are the aggregate structures that influence PCC properties. The aggregate has no direct influence on the strength of the PCC elements, except in the case of some highly porous and weak aggregates. However, larger sizes and a higher proportion of elongated and flat particles leads to the formation of a thicker water film next to the aggregate surface that weakens the transition zone. This phenomenon is known as internal bleeding (Mehta and Monteiro, 1993).

2.1.4 Transition Zone

The transition zone is responsible for several phenomena in PCC behaviors, such as brittle failure in tension, and inelastic behavior in uniaxial compression. It makes PCC tensile strength lower by an order of magnitude than its compressive strength. Furthermore, the permeability of PCC mix is higher by an order of magnitude than that of hydrated cement paste due to the formation of the transition zone in the mix (Mehta and Monteiro, 1993).

The transition zone is composed of the same elements of the hydrated cement paste, however, its structure and properties are different from the bulk hydrated cement paste. Its formation starts when water films form around large aggregate particles and lead to higher water cement ratio (w/c) around the aggregate than away from it. Then, as in the bulk hydrated cement paste, calcium, sulfate, hydroxide, and aluminate ions combine to form calcium sulfoaluminates (ettringite) and C-H. Due to the high w/c ratio near large aggregate, these crystalline products consist of relatively large crystals. Therefore, they form a more porous framework than that in the bulk cement paste or mortar. As the hydration process continues to progress, poor crystalline C-S-H, a second generation of smaller crystals of calcium sulfoaluminates (ettringite), and C-H start filling the empty space between the framework created by the large ettringite and the large C-H crystals. Thus, this step improves the density and hence the strength of the transition zones (Maso, 1980).

As in the case of the hydrated cement paste, the strength of the transition zone is due to van der Waals force of attraction between the hydration products and the aggregate particles. Therefore, the strength of the transition zone depends on the volume and the size of the voids present. In the early stages of the hydration process, the volume and size of the voids in the transition zone will be larger than in the bulk hydrated cement paste. Consequently, the transition zone is weaker in strength than the bulk hydrated cement paste. However, with increasing age of hydration, the transition zone becomes equal or even stronger than the bulk hydrated cement paste. The increase in the strength occurs because of both the formation of the second generation of chemical products that fill the voids and the new products that resulted from the slow chemical reaction between the cement paste constituents and the aggregate. Microcracks in the transition zone are considered one of the major factors that contribute to its weakness. The number of microcracks depends on several parameters, such as aggregate size and gradation, cement content, w/c ratio, degree of consolidation of fresh PCC, curing conditions, environmental humidity, and thermal history of PCC (Mehta and Monteiro, 1993). These microcracks will make the strength of the transition zone to be much lower than that of the hydrated cement paste bulk.

2.1.5 Durability

Because most of the properly designed, mixed, and placed PCC exhibits premature deterioration that shortens its service life, attention is now being paid to the durability issues of

PCC. Durability means the ability of a material to resist certain environmental conditions and retain its original quality and serviceability. Durability is the key to reducing the cost of rehabilitation and increasing the service life of PCC structures. This attention to the durability of PCC structures comes in part as a response to the socioeconomic factors of developing countries.

Water is the center of the most durability problems of PCC because it controls both the physical and chemical processes of degradation. The type of concentration of ions in water as well as the chemical composition of the solid affects the rate of deterioration of PCC structures. Because PCC is a basic medium due to the existence of the alkaline calcium, acidic waters can be very harmful to PCC. Water molecules are small enough to penetrate into small pores or cavities. It contains many ions and gases that increase its ability to dissolve more substances than any other liquid. Water requires the highest heat energy to evaporate among the common liquids and tends to remain in a material in a liquid state instead of leaving material dry at an ordinary temperature. Internal movements and changes of the structure of water in porous solids cause disruptive volume changes.

The permeability of PCC controls the physical and chemical phenomena associated with water movements. In cement paste, the size and the continuity of the pores control the coefficient permeability of the hydrated cement paste. The capillary porosity of typical cement paste in hardened PCC is about 40 percent. The discontinuity of the pores is reached at 30 percent of the capillary porosity, after which the coefficient of the permeability drops substantially. The volume of pores in most natural aggregate is usually under 3 percent and rarely exceeds 10 percent, the coefficient of permeability of the aggregate is expected to be much lower than that of the cement paste. However, some types of aggregate have permeability higher than that of cement paste. The size of capillary voids in some types of aggregate is much larger than that in cement paste. The permeability of mortar or PCC is higher than that of cement paste and aggregate because of the existence of the transition zone. The high percentage of microcracks and the continuity between them that exist in the transition zone contribute significantly to the increase of the coefficient of permeability of the system. The volume of the large capillary voids in the paste matrix is proportional to the permeability coefficient. Reducing the volume of the capillary void by using a lower water/cement ratio, adequate cement content, and proper compaction and curing conditions could lower the permeability of the PCC.

Since the transition zone plays a major role in the magnitude of the permeability coefficient of the PCC system, special attention needs to be paid to it in order to reduce the microcracks in it. Selecting proper aggregate size and grading and avoiding premature or excessive loading are some of the necessary precautions that need to be taken to reduce the microcracks in the transition zone (Mehta and Monteiro, 1993).

2.2 Concrete Infrastructure Deterioration

The construction of the PCC infrastructure boomed between the 1950's, and 1970's in the United States and other parts of the world. The civil infrastructure assets in United States alone are estimated at $20 trillion (NSF, 1995). However, the planning and cost of the developed infrastructures did not include future preventive maintenance. Consequently, the infrastructure started to deteriorate long before the end of its expected life cycle. As a result, millions of dollars are spent annually in United States on preservation and major repair of the infrastructure. The deterioration of the nation's highway infrastructure has proceeded at an alarming rate (Cady and Weyers, 1992). The Federal Highway Administration's report classified 23 percent of the bridges in United States as structurally deficient (Hudson *et al.*, 1997). Approximately 32% of the more than 581,000 bridges in the United States are classified as functionally or structurally deficient or obsolete due to their excessive deterioration (ASCE 1998). A large percentage of the PCC infrastructure deterioration is due to chloride-induced corrosion, alkali silica reaction, and freezing and thawing expansion. The following sections present a brief description of the causes of this deterioration.

2.2.1 Chloride Induced Corrosion

Chloride-induced corrosion of the reinforcement steel in concrete is the primary cause of the deterioration of reinforced concrete bridge components (Heralds *et al.,* 1992; Prowell *et al.,* 1993). Many concrete bridges in the United States deteriorate before they reach the end of their planned life span due to premature corrosion of the reinforcing steel (Virmani and Clemena, 1998). Currently, there is a serious problem in the United States and elsewhere with the deterioration of PCC bridges due to corrosion induced by chloride intrusion into the concrete (Thompson *et al.,* 1992). Mehta and Monteiro (1993) have reported that the US Interstate Highway System's bridge required $6 billion for repairs necessitated by deterioration due to steel reinforcement corrosion.

It is believed that when embedded steel reinforcement is adequately covered by thick and low-permeable PCC, the chance of corrosion to begining is very small. However, low-permeable PCC is not fully met in practice letting corrosion become one of the major deterioration factors in PCC infrastructure.

The corrosion of PCC steel reinforcement is an electrochemical process. Differences in concentration of dissolved ions near steel, such as alkalies, chlorides, and oxygen, may cause the corrosion cells to be formed by electrochemical potential. Consequently, some parts of the steel become anodic while others become cathodic. In the anode, the iron metallic atoms are oxidized to Fe^{+2} ions, which dissolve into the surrounding solution. In the cathode, the cathodic reaction consumes electrons and leads to the formation of OH^- ions. Moisture and oxygen presence at the cathodic area is necessary for the cathodic reaction to occur. Electrons, flowing in the steel bar from the anode to the cathode, form an electrical current loop, while the ions move into the PCC pore systems between the anode and the cathode areas. The Fe^{+2} and OH^- ions interact chemically close to the anode to form iron oxide, which is known as rust. Therefore, the corrosion itself is in the anode area. The corrosion process reduces the cross section area of the reinforcing bar, which in turn reduces its load-bearing capacity. In addition, the corrosion product (rust) can lead to an increase as large as 600 percent in the volume of the original metal. This volume increase exerts internal stresses that cause PCC expansion, thus cracking, delamination and then spalling (Young *et al.,* 1998).

Portland cement concrete mix is characterized by high pH, which leads to spontaneous formation of a protective iron oxide film, called a passivation film, around the reinforcement. The steel bar is immune as long as this passivation film is stable. The stability of this film will be altered when the content of chloride ions adjacent to the steel reaches a value in the range of 0.7 kg/m^3 of PCC. In addition, carbonation of PCC lowers the pH value, thereby causing the passivation film to be unstable. Chloride-induced corrosion is one of the major causes for concrete deterioration in United States, while carbonation is of primary concern in other parts of the world.

Portland cement concrete deterioration due to corrosion can be controlled by protecting the passivation film or by slowing the rate of the corrosion process if the stability of the film has been altered. The stability of the passivation film can be maintained if the presence of the chloride and the carbonation is kept minimized. This can be achieved by providing good-quality PCC with a sufficient depth of cover and designing the structure so that the width of loading and drying cracks will be limited. The diffusion of oxygen can also be minimized by these means,

which leads to slowing down the rate of corrosion. Higher electrical resistivity can also reduce the rate of corrosion by slowing down the flow of ions in the pores system of the PCC between the anode and the cathode. Dense PCC is characterized by high electrical resistivity (Young *et al.,* 1998).

2.2.2 Alkali Silica Reaction (ASR)

Alkali-silica reaction can compromise the long-term durability of some PCC structures (Kurtis *et al.,* 1998). This reaction can lead to severe damage that may ultimately endanger the performance and safety of PCC structures (Abou-Zeid *et al.,* 1996). It has been identified as a major cause of PCC deterioration in many places such as the Maritime Provinces of Canada (Gillott, 1993). A study done by Swamy and Asali (1988) showed that loss in engineering properties due to ASR do not occur at the same rate or in proportion to the expansion-undergone PCC. It showed also that the two major properties affected by ASR were flexural strength and dynamic modulus of elasticity. A better understanding of ASR and expansion mechanisms is necessary to control the deterioration processes and to help predict future structural behavior.

Alkali-silica reaction is a chemical reaction between alkalis in the cement and silica in the aggregate. Certain types of aggregate contain reactive forms of silica that react with alkalis that enter the pore systems from the cement paste hydration or from deicing chemicals.

Alkali ions, which are released from the cement during the hydration process, increase the concentration of hydroxide ions in the pore solution. Then aggregate integrity will be destroyed due to the initial hydrolysis of the siliceous fraction of the aggregate in the highly alkaline pore solution. Amorphous alkali silicate gel will be formed. As water enters into the mix, the alkali silicate gel starts to swell thereby causing localized swelling, internal pressure, and cracking. At this critical stage, the gel goes from an amorphous solid to semisolid phase. As water continue to be presented in the structure, the gel will go to a liquid phase that results in expulsion of liquid gel through the cracks. If PCC could be kept dry, ASR would not cause any damage to the mix. Avoiding reactive aggregate or keeping the alkali content of the cement low will help in controlling the ASR (Young *et al.,* 1998).

2.2.3 Freezing and Thawing

When subjected to freezing and thawing, a porous brittle material such as PCC deteriorates. The cause of the deterioration is the fracture of micro-pores due to water freezing and moving in them (Hori and Morihiro, 1998). In cold regions, constructed PCC pavements are subjected to a harsh environment, characterized by cycles of freezing and thawing. These environmental conditions lead to PCC deterioration, a material-related distress that can result in untimely failure of the pavement (Van and Aldrich, 1998). Therefore, the resistance of PCC to freeze-thaw cycles is an important concern in many countries (Aavik, 1995). It has noticed that the most important aspect of concrete durability in Canada and much of the northern United States is resistance to freezing and thawing deterioration (Johnston, 1994).

Power (1958) described the mechanism of freezing and thawing in the cement paste and it is applicable to aggregate too. As water freezes in the capillary voids, its volume increases. This increase of volume in the capillary voids will result in the development of disruptive pressures in the saturated cement unless every capillary is not farther than 0.15 or 0.2 mm from the nearest escape boundary. Air entraining agents are used to provide closely spaced boundaries. Power also proposes that osmotic pressure due to the partial freezing of solutions in water causes damage to the mix. Water in the capillaries contains soluble substances such as chlorides, alkalies, and calcium hydroxide. Aggregate plays a major role in the freezing and thawing damage as well. It follows the same mechanism as the cement paste (Mehta and Monteiro, 1993).

D-cracking, a form of deterioration in PCC pavement, is brought on by freezing and thawing cycles. It has become a serious and widespread problem in United States and in Canada. D-cracking primarily results from the use of certain type of aggregate in the PCC that disintegrate when they become saturated and are subjected to repeated cycles of freezing and thawing (Schwartz, 1987). Air entrainment has been used to reduce freezing and thawing damages.

2.3 Dielectric Materials and Polarization Concepts

This section presents brief background information about the electrical characteristic of dielectric material and the polarization concept.

2.3.1 Dielectric Materials

Dry PCC is typically viewed as a dielectric material. Dielectric materials are considered as insulators (non-conductors). They have bound negative and positive charges in their atoms and molecules. These charges are held in their places by atomic and molecular forces and are not free to travel. Ideal dielectric materials are neutrally charged, and unlike conductors, do not contain any free charges, as shown in Figure 2.1.

However, when dielectric materials are exposed to an external electrical field, the bound positive and the negative charges start to move slightly from their position opposing the atomic forces, while in conductor materials, the charges are free to move but are bound by the conductor boundaries (surfaces). This illustrates the fundamental difference between the bound charges in dielectric materials and the free charges in conductor materials (Balanis, 1989), as shown in Figure 2.1.

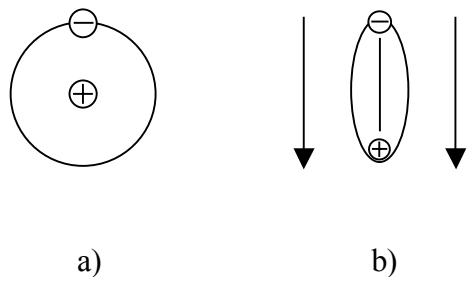

Figure 2.1. Typical atom in (a) the absence of an applied field and (b) under an applied field (after Balanis, 1989)

2.3.2 Polarization Concept

Electric dipoles are formed when dielectric materials are subjected to external field. The formation of the electric dipoles is usually referred as orientational polarization. The polarization dipoles interact with the applied electromagnetic field. This interaction gives the dielectric materials the ability to store energy. The energy is stored by the shift in the positions of the bound charges. This is analogous to the potential energy stored in a stretched spring.

Electric polarization may occur in dielectric materials in one or more of three different forms (mechanisms). These three different mechanisms are Dipole or orientational polarization, ionic or molecular polarization, and electronic polarization, as shown in Figure 2.2.

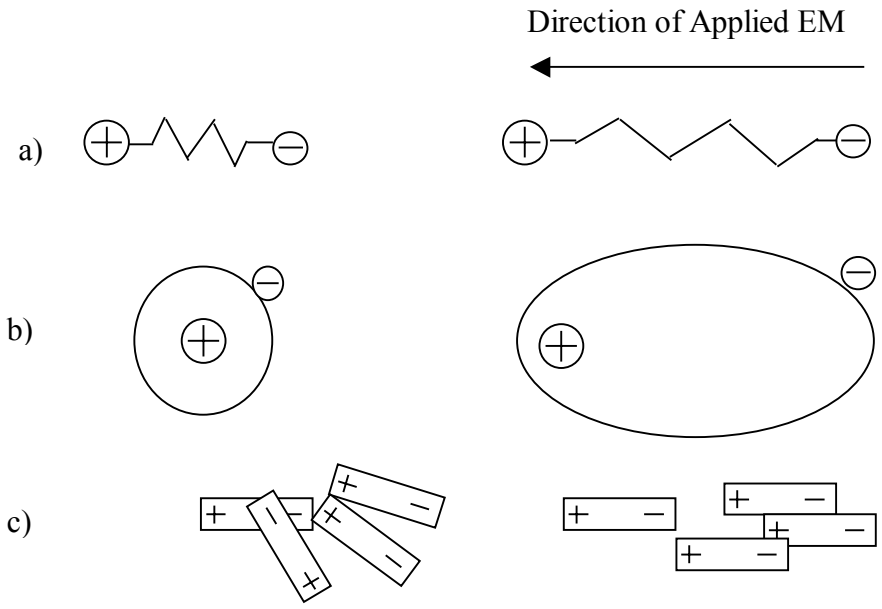

Figure 2.2. Representation of dielectric polarization: (a) dipole, (b) electronic, (c) ionic (after Jastrzebski, 1977)

Dipole polarization is evident in materials that possess permanent dipole moments that are randomly oriented. These materials are called polar materials. The dipoles will align with the applied electromagnetic field when they are subjected to it. Ionic polarization is evident in materials that possess both negative and positive ions, such as sodium chloride (NaCl). Ions will displace themselves when they are subjected to an external electromagnetic field. Electronic polarization is evident in most materials. It exists when an applied electromagnetic field shifts the orbiting electron distribution with respect to the center of the nucleus.

Polarization results in the separation between positive and negative charges or the center of their distributions. The corresponding dipole moment for each charge (center) is determined by the amount of charges and the separation distance (moment = charges * separation distance). The total of the dipole moments (p_t) per unit volume will be called P, which is considered the electric polarization vector. Materials that have $p_t = 0$ and $P = 0$ are called non-polar materials, while polar materials have $P \neq 0$ and $p_t \neq 0$, where p_t is the summation of dp_i.

When a uniform electromagnetic field (E_a) is applied to a dielectric material, one surface of the material will have a net positive surface charge density (ρ_s) and the other surface will have a net negative surface charge density. While the volume charge density (ρ_v) inside the material is zero due the balance of the positive and negative charges, the formation of the positive and

negative surface charge density in the dielectric material will result in developing an electric polarization vector (*P*) within the material itself and it will have the same direction of the electromagnetic field. Thus, an electric flux density (*D*) will be formed inside the material and it will be related to that in free space (D_0) and *P* by the following equation:

$$D = D_0 + P$$

where,

$$D_0 = \varepsilon_0 * E_a$$

where,

ε_0 is the free-space permittivity.

The following relation can also represent D:

$$D = \varepsilon_s * E_a$$

where,

ε_s is the material permittivity.

Using the above equations, ε_s material permittivity can be re-written as the following:

$$\varepsilon_s = \varepsilon_0 * (1+\chi_e)$$

where,

χ_e is called the electric susceptibility and equal to (P / D_0).

Relative permittivity (ε_{sr}) is the ratio of material permittivity to free-space permittivity and can be represented by the following relation:

$$\varepsilon_{sr} = \varepsilon_s / \varepsilon_0 = (1+\chi_e).$$

Relative permittivity of a material is better known as the dielectric constant of the material. It represents a parameter that indicates the relative (to free-space) charge (or energy) storage capabilities of a dielectric material. The dielectric constant of PCC and its relation with PCC properties and deterioration types will be our point of interest in this research (Balanis, 1989).

As a dielectric material, PCC is described by its complex permittivity. Complex permittivity includes both real and imaginary parts. The real part reflects the ability of PCC to store electric energy due to polarization, and the imaginary part reflects the loss due to conduction and

molecular friction. The imaginary part of the complex relative permittivity is greater than zero and much smaller that the real part (Al-Qadi and Riad, 1996).

2.4 Use of EM Waves Techniques to Detect PCC Deterioration

Nondestructive evaluation (NDE) techniques have been used in recent years for in-service monitoring of infrastructure (Halabe *et al.,* 1999). The degradation of civil infrastructure has caused researchers focus on effective NDE techniques to correctly assess the condition of existing PCC structures (Wooh and Azar, 1999). NDE techniques have been used for monitoring damages in PCC due to crack growth in PCC beams (Subramaniam *et al.,* 1999). Over the last fifteen years, state and federal transportation agencies have paid increasing attention to local and global deterioration of bridge structures (Bolton *et al.,* 1999). This requires a need for practical methodologies to evaluate nondestructively the structural properties of bridges. Nondestructive evaluation methods can nondestructively detect, locate, and assess damage in an existing structure while simultaneously evaluating the condition of the same structure (Stubbs *et al*., 1999). Moreover, NDE techniques have been used for quality control during the construction/fabrication stages of transportation infrastructure (Halabe *et al*, 1999).

Electromagnetic wave techniques have been used to evaluate bridge conditions (Fisk, 1998). Some researchers have studied the hydration process of cement paste and its relation with PCC electromagnetic properties (McCarter, 1996). The relationship between PCC electrical properties and deterioration types has been investigated using wide-band electromagnetic (EM) wave techniques (Diefenderfer *et al*., 1998; Haddad and Al-Qadi, 1998; Al-Qadi *et al*., 1997). Electromagnetic wave techniques have also played an important role in the way an engineer looks at the properties of the cement paste mix. Electromagnetic wave techniques have been used to determine the sand-to-cement (s/c) ratio rather than the water-to-cement (w/c) ratio (Bois *et al*., 1997). Among the NDE techniques, Ground penetrating radar (GPR), which is an electromagnetic pulse-echo system, has shown increasing potential in soils or PCC diagnostic efforts (Cattin *et al.,* 1998). It has been used to locate the reinforcement in PCC, locate delamination and measure thicknesses of PCC (Shaw and Xu, 1997; Al-Qadi *et al*., 2000(a); Al-Qadi *et al*., 2000(b)).

Al-Qadi and Riad (1996) have investigated PCC properties over a wide-band frequency range. Ground penetrating radar, which uses microwave frequencies for detecting flaws in

concrete, has been developed as a non-destructive technique to monitor concrete bridge health for nearly a decade. A GPR system has been developed by Huston *et al*. (1999) to provide a more accurate method for obtaining the location and magnitude of the delamination and deterioration of PCC. The system was able to distinguish flaws at least 360 mm deep in PCC (Huston *et al*., 1999). Since permittivity and conductivity were considered important electromagnetic parameters in PCC, GPR was used to study the effect of both variations in PCC composition and the fractional water content in these electrical properties (Shaw 1998).

Ground penetrating radar technology has been used in the evaluation of pavements, bridge decks, abutments, piers, and other constructed facilities to assess as-built conditions and evaluate damage and deterioration that develops over time (Maser, 1996). Ground penetrating radar can be used to locate voids and reinforcing in PCC. Its expedient use saves time and reduces cost, inconvenience, and adverse publicity (Mallinson, 1997). The GPR can successfully detect the thickness of hot mix asphalt (HMA) overlay and the delamination with cracks filled with plain water, saline water or air (Chen *et al*., 1997).

Several researchers have studied the dielectric properties of PCC using low frequencies such as radio frequencies (RF). Al-Qadi and Riad (1996) and Haddad and Al-Qadi (1996) have developed a parallel-plate capacitor fixture to measure concrete properties over a RF range of 0.1 to 40.1 MHz. Low radio frequencies (RF) have been used to detect PCC deterioration due to chloride contamination by evaluating PCC electrical properties, such as complex permittivity, over frequencies ranging from 0.1 to 40.1 MHz (Al-Qadi *et al.*, 1997). Gu and Beaudoin (1996) have conducted a study to investigate the dielectric properties of hardened cement paste at various water/cement ratios over the frequency range of 1 MHz to 1 GHz. Low frequencies have been used to evaluate the hydration process of the cement paste at its early stages (Starrs and McCarter, 1998). McCarter (1996) has investigated the complex impedance response of fresh concrete over the frequency range of 100 Hz to 10 MHz. Cement-paste content, cement type, and aggregate content have also been investigated using low frequency range (McCarter, 1994). Most of these studies, conducted to investigate PCC properties using their dielectric parameters, are suitable for laboratory use.

To evaluate the dielectric properties of PCC in the field, in-situ techniques are needed to identify PCC properties and deterioration. Diefenderfer *et al.*, (1998) have developed a preliminary system to be used in the field. The system, called a capacitor probe (C-Probe), uses electromagnetic waves at low radio frequencies (100 KHz to 20 MHz) to measure the

dielectric properties of PCC with a HP Network Analyzer. A description of the system is presented in the following section.

2.5 Systems Used in this Study

This section describes the systems used in this research: the C-Probe and the parallel-plate capacitor fixtures. In addition, the HP Network Analyzer and the scattering parameters matrix method are described.

2.5.1 The C-Probe

The C-Probe, developed at Virginia Tech (Diefenderfer *et al*., 1998), consists of two flexible conducting plates (75 x 75 mm) with a determined separation distance (50 mm) between the plates. The conducting plates are made of copper and attached with 250 x 125 x 0.6 mm rubber backing to ensure adequate support. These two plates are connected to the Network Analyzer by a coaxial cable. The capacitor probe configuration is shown in Figure 2.3.

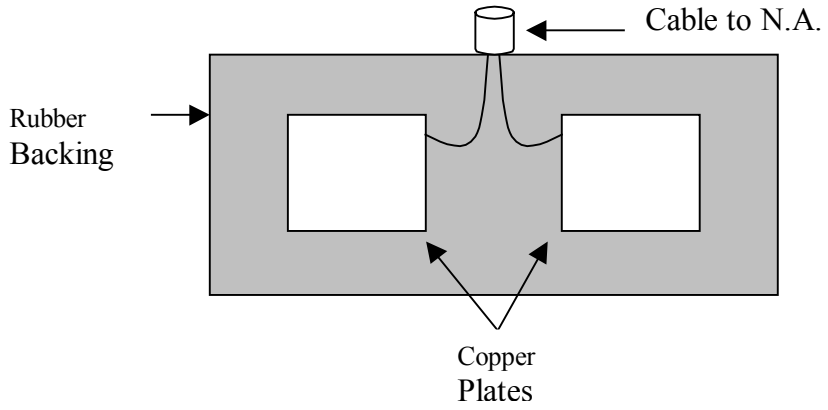

Figure 2.3. C-Probe setup

The C-Probe setup is suitable for relatively low radio frequency measurements. It induces an electromagnetic field over an adequate area of PCC specimens, as shown in Figure 2.4.

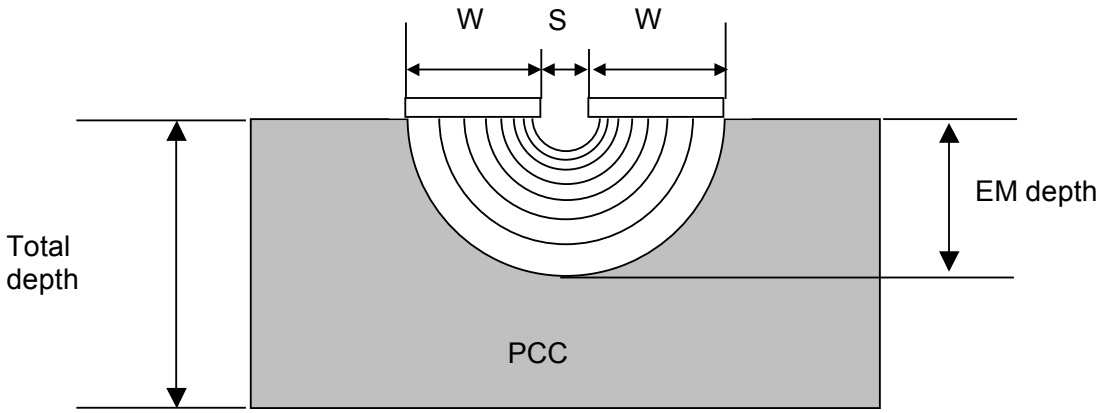

Figure 2.4. Field distribution of C-Probe setup

The C-Probe is suitable for both laboratory research and in-situ measurements. It is simple and convenient for measuring dielectric properties of different specimen sizes due to its flexibility feature. In addition, the C-Probe fixture can be used with different geometric shapes of PCC structure elements.

2.5.2 Parallel-Plate Capacitor

A parallel-plate capacitor fixture, developed at Virginia Tech (Al-Qadi *et al*., 1994), was used in this research. The fixture is made of two 460 x 460 x 13 mm parallel steel plates, which were fabricated and stress-relieved before they were cut. Four supporting piers hold the upper plate while a threaded rod, centrally located, supports the lower plate. This rod allows vertical movements of the lower plate to provide a 5- to 30-mm separation between the two plates. In addition, a vertical rod, connected to the Network Analyzer, is mounted to transfer the electrical current to the upper plate, while the lower plate acts as grounding plate. The parallel plate configuration is shown in Figure 2.5.

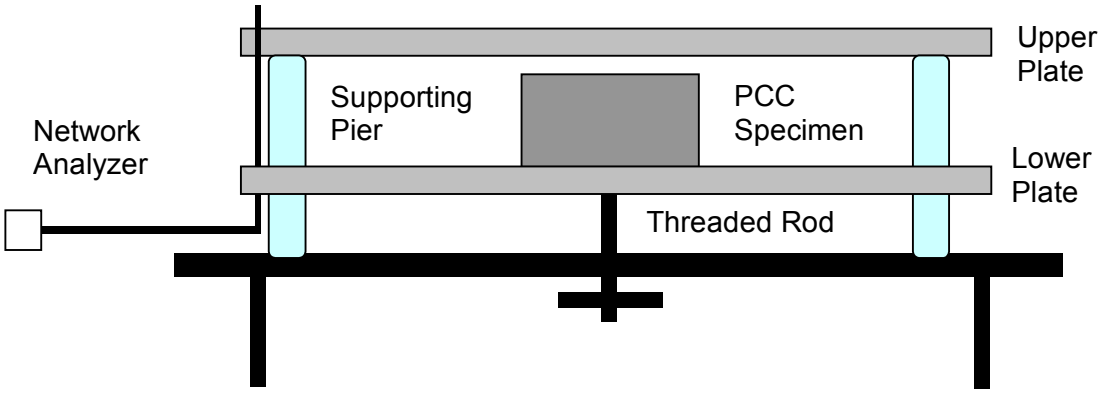

Figure 2.5. Parallel-plate capacitor setup

The parallel-plate capacitor setup is suitable for low radio frequency measurements. It induces a uniform electromagnetic field over an adequate space for PCC specimens, as shown in Figure 2.6.

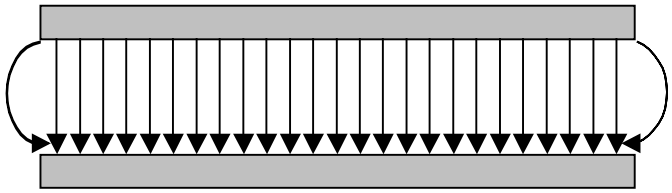

Figure 2.6. Uniform field distribution of the parallel-plate capacitor setup

To ensure a uniform field on the PCC specimen, its horizontal dimensions should not exceed one-third the plate dimension in each direction and it should be placed at the center of the lower plate as shown in Figure 2.7.

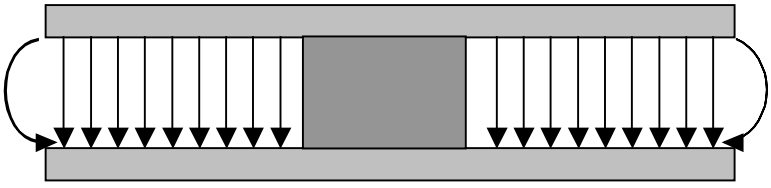

Figure 2.7. PCC specimen placement

The parallel-plate capacitor is suitable for laboratory research only. The adjustable distance between its two plates makes it a simple and convenient device for measuring the dielectric properties of different specimen sizes. Moreover, the PCC specimens used with the fixture are small and easy to handle.

2.5.3 Capacitor Meter

A capacitor meter (C-Meter) has been used in this research to verify measurements that cannot be obtained from the parallel plate capacitor (PPC). The C-Meter works with the same principle of the PPC. It computes the capacitor and the loss tangent of the material by applying an EM field through two parallel plates made from copper sheets that are attached to the opposite surfaces of the material under test (MUT). The two copper sheets were contacted with a conductor probe that is connected to the C-Meter. The C-Meter displays the capacitance value and the loss tangent for a specific frequency. A schematic draw for the C-Meter setup is shown in Figure 2.8.

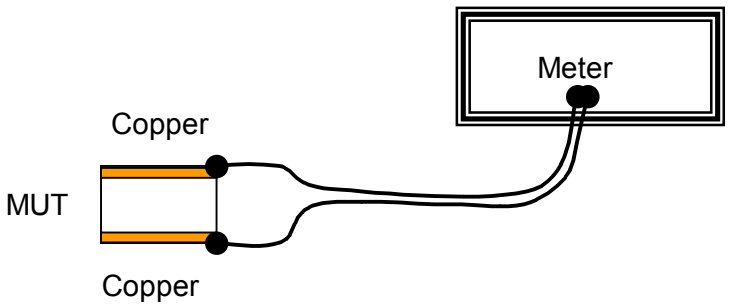

Figure 2.8. A schematic for the C-Meter setup

2.5.4 Network Analyzer (NA)

This research uses the HP4195A Network Analyzer with the two considered fixtures, the capacitor probe, and parallel-plate capacitor. It is a high-performance analyzer. It covers a frequency range from 10 Hz through 500 MHz. It also has the accuracy and resolution that are required for developing advanced equipment and convenient soft key operation and marker

functions that make deriving device parameters quick and easy. The measured results can be directly printed or plotted without an external computer connected to the Network Analyzer. However, a built-in disk drive is provided to enable users to carry out additional computational tasks as needed. This disk drive, allows the Network Analyzer user to save the instrument state, data, and user functions on external disk for future applications. The Network Analyzer uses its own calibration standards (open, short, and load) for calibrating the measured results. The user should perform this calibration procedure before measuring the dielectric properties of the material under consideration.

3 CHAPTER 3: RESEARCH PROGRAM

This chapter presents the research program applied in this study to advance the current understanding of the measuring dielectric properties of PCC, and consists of four main sections. Section 3.1 explains the procedure followed to calibrate the C-Probe measurements. Section 3.2 explains the methodology used to optimize the C-Probe design configuration. Section 3.3 reports the procedure used to validate the C-Probe fixture for field applications. Finally, Section 3.4 discusses the methodology used in evaluating the mixture behavior of PCC.

3.1 C-Probe Calibration

In the C-Probe calibration phase, the investigation has been conducted in three steps: the use of the C-Meter, measure the dielectric properties of standard materials, and establish calibration procedures used in the C-Probe measurements. These three steps are the key elements of the calibration process.

3.1.1 The Use of C-Meter

C-Meter device has been used to measure the dielectric constants of materials with known dielectric properties (Teflon and nylons) used in the C-Probe calibration. The Teflon has a dielectric constant of 2.1 and extruded nylon 3.3. In addition, the C-Meter has been used to measure the C-Probe PCC specimen (100 x 300 x 450 mm), because the parallel-plate capacitor cannot accommodate its size. A schematic setup of the C- Meter is shown in Figure 2.8.

The capacitance and the loss tangent measured by the C-Meter were used to calculate the dielectric constant of the MUT using the following relationship:

$$\varepsilon' = \frac{C\,d}{\varepsilon_0 A}\ ,$$

$$\varepsilon'' = (\tan\delta)\,\varepsilon'$$

where,

C = capacitance in Farad;

ε_0 = 8.85 x 10^{-12} in Farad/meter;

d = height of the specimen in m.;

A = surface area of the specimen in m^2;

$\tan\delta$ = loss tangent; and

ε', ε'' = real and imaginary parts of the dielectric constant of the material.

3.1.2 Dielectric Properties of the Standard Materials

The dielectric properties of the standard materials used in the C-Probe calibration were investigated using the C-Meter. Since Teflon is known as an isotropic material and fairly frequency independent, the investigation has been focused on the effect of the frequency on the dielectric properties of the nylon. In addition, the isotropy behavior of the nylon has also been investigated by measuring the nylon specimen in more than one direction. Figure 3.1 and Table 3.1 show the dimensions of the available standard materials.

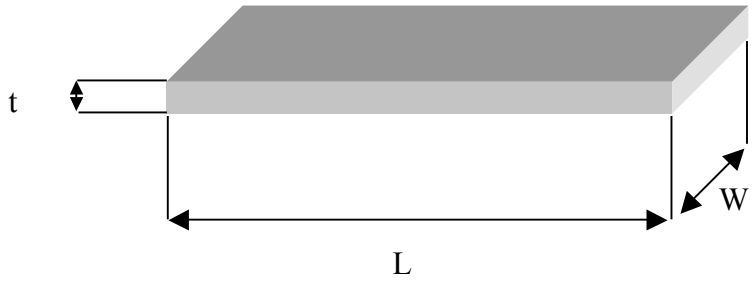

Figure 3.1. Standard materials used in the calibration

Table 3.1. Dimensions of the standard materials (mm)

Material	L	W	t
Teflon	534/610	305	57
Extruded Nylon	407	280	51

3.1.3 C-Probe Calibration Methods

Five calibration methods were developed and evaluated for measuring PCC specimen using the C-Probe. The measurements of the different calibration methods were compared with the C-Meter measurement for verification. The five calibration methods were divided into two categories: scattering-parameter form and bilinear transformation form.

A scattering parameter matrix is one of the best techniques used to represent the governing equation of a multi-port network. Both the capacitor probe setup and the parallel-plate capacitor utilize multi-port networks that have two ports. A schematic of the scattering parameter with a two-port network is shown in Figure 3.2

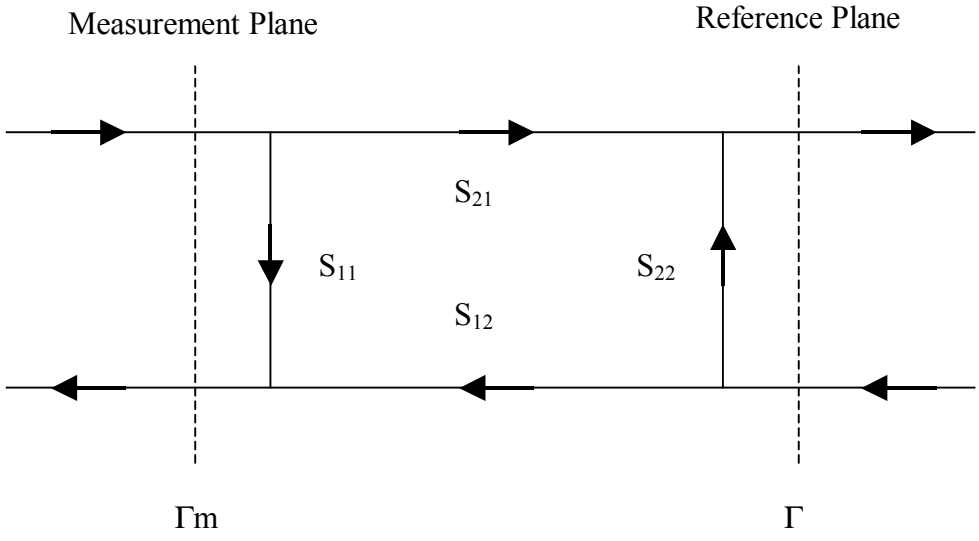

Figure 3.2. A schematic for scattering-parameter matrix of two-port network

where,

S_{11}, S_{21}, S_{12}, and S_{22} = propagation coefficients;

*a*1 = voltage wave input by Network Analyzer;

*b*1 = voltage wave reflected by the entire measurement system to the Network Analyzer;

*a*2 = voltage wave reflected by the MUT;

*b*2 = voltage wave incident to MUT;

Γ_M = reflection coefficient measured by N.A. at the reference plane; and

Γ = reflection coefficient of the MUT at the measurement plane.

The scattering-parameter matrix relates the measured reflection coefficient to the MUT reflection coefficient. The relationship is represented in the following governing equation:

$$\Gamma_m = S_{11} + \frac{S_p \Gamma}{1 - S_{22}\Gamma}$$

where,

$$S_p = (S_{12})(S_{21})$$

Given S-parameters (S_{11}, S_{22}, and S_p), Γ can be computed from Γ_M, which is calculated by the Network Analyzer. To determine the S-parameters, three known devices are needed as calibration standards. Open, short, and load (matched impedance) are usually used as calibration standards for solving the S-parameters. This technique is used for calibrating the Network Analyzer and also for calibrating the C-Probe as well as the parallel-plate capacitor. In this technique, the reflection coefficient (Γ) for the load standard is considered to be zero by using a 50 Ω resistor. The reflection coefficient (Γ) for the short standard is considered to be (-1) by assuming it as a perfect conductor. The reflection coefficient (Γ) for the open standard is a function of the mapping factor (F) as indicated in the governing equations of the scattering parameter methods in Appendix A. The mapping factor of the parallel plate capacitor equals the contacting surface area of the MUT divided by its height (the distance between the two parallel plates). However, the mapping factor of the C-Probe forms another unknown in the scattering parameter methods. To solve the governing equations in this method, an additional unknown has to be determined.

In the scattering-parameter form, two methods were developed: the first method uses open, short, and two loads (50 Ω and 151 Ω) for calibrating the C-Probe measurements, and the second method uses open, short, and one load (50 Ω). Computer simulation is used to compute the mapping factor (F) of the C-Probe configuration.

The load standards were modeled to have a resistor (R_L) and a capacitor (C_L) only, while the inductance (L_L) is neglected. The governing equation and the MatLab codes for these two methods are reported in Appendix A. The notation and the calibration standards used in these two methods are presented in Table 3.2.

Table 3.2. Calibration methods and standards used in the scattering-parameter form

Method	Standards
OSLL	Open, short, and two loads
OSLF	Open, short, and load (F is computed)

In the bilinear transformation form, three methods were developed. While the first method uses the open standard and two known materials (Teflon and nylon) for calibrating the C-Probe measurements, the second method uses the short standard and the same two known materials. The third method uses the open and short standards and Teflon material. The measured reflection coefficient (Γ_m) was related to the dielectric constant of the MUT by the following relationship:

$$\Gamma_m = \frac{a + b\varepsilon_r}{1 + c\varepsilon_r}$$

where, a, b, and c are the bilinear coefficients and ε_r is the relative dielectric constant of the MUT.

The bilinear transformation coefficients were obtained by using the three calibration standards in each method, while Γ_m was obtained from the Network Analyzer reading for the PCC under test. The dielectric constant for the open and the short standard were considered to be 1 and ∞ (infinity), respectively. In addition, the dielectric constant of the standard materials was measured using the C-Meter, as mentioned earlier. The governing equations and the MatLab codes for these three methods are reported in Appendix A. Table 3.3 shows the three developed methods of the bilinear transformation form.

Table 3.3. Calibration methods and their standards used in the bilinear transformation form

Method	Standards
OMM	Open and two standard materials (Teflon, extruded nylon)
SMM	Short and two standard materials (Teflon, extruded nylon)
OSM	Open, short, and standard material (Teflon)

Out of the five-mentioned calibration methods, the best method has been recommended based on the compliance of the C-Probe measurements using this method with the C-Meter measurements for the same PCC specimen.

3.2 C-Probe Optimization

The C-Probe design configuration was optimized to achieve the maximum interaction between the EM field and the PCC slab under test for specific slab thickness. The plates' size and the separation between them were considered the design configuration parameters in the optimization process. Three different values for each parameter were selected. The dielectric constant of PCC under test was considered as an additional parameter. Table 3.4 shows the different values considered for each parameter.

Table 3.4. Values considered for each parameter in the C-Probe optimization

W: Plate dimension (mm)			
76	102	127	
S: Distance between plates (mm)			
25	51	76	
ε: PCC dielectric constant			
5	10	15	20

In this task, a computer simulation was used to determine the effective depth of the EM field in the PCC slab under test based on the considered plates' size (W), the separation between them (S), and the dielectric constant of the PCC slab under test (Eps). A preliminary simulation has been conducted to determine the upper limit value of the PCC slab thicknesses. The upper limit value has been set to be equal the minimum slab thickness that does not cause change in the computed capacitance of the C-Probe configuration. It has been found that the computed capacitor value of the largest considered C-Probe configuration (127 x 127 mm plates' size with 76 mm separation between them) has not been changed for slab thickness of 254 mm and greater. For each considered C-Probe design configuration, 25 mm air void thickness has been placed at the bottom of the PCC slab and increased by a 12.5 mm increment. The C-Probe, PCC, and air void initial setup used in the simulation is shown in Figure 3.3.

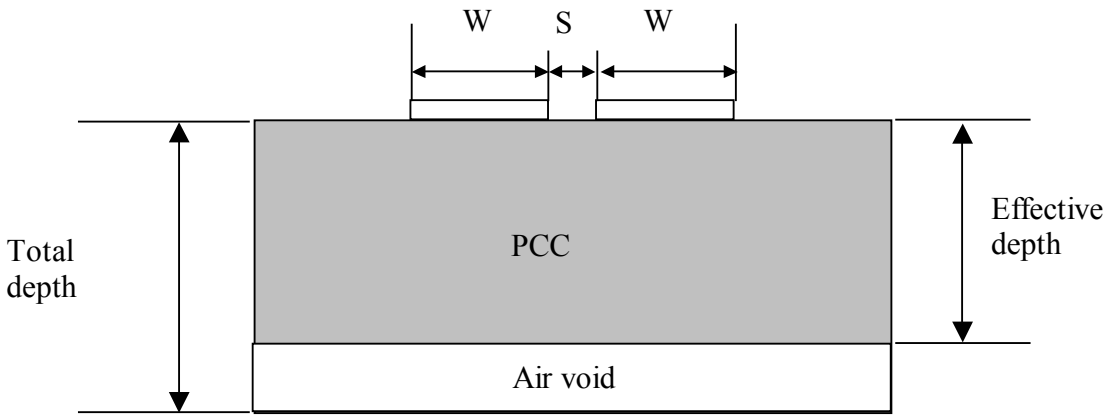

Figure 3.3. C-Probe and PCC slab initial setup used in the simulation

Percentages of change have been computed to determine the effective depth of the EM field in the PCC slab under test with the three considered values of the dielectric constant. The effective depth has been determined at a specific cutoff of change from the maximum capacitance value of the C-Probe configuration, obtained with PCC slab thickness of 254 mm. The percentage of change has been computed using the following equation:

$$P_n = \frac{C_{10} - C_n}{C_{10}}$$

where,

P_n = percentage of change,

C_{10} = capacitance value of the C-Probe configuration at slab thickness of 254 mm,

C_n = capacitance value of the C-Probe slab thickness of n.

Based on the effective depth of each C-Probe design configuration and the dielectric constant of the PCC slab under test, a predictive model has been developed using a regression analysis technique to correlate the effective depth of the EM field with the size of the plates (W), the separation between them (S), and the dielectric constant of PCC (Eps). The developed model has been used to determine the optimum design configuration for different PCC slab thicknesses. For simulation purposes, a thickness of 63 mm was used with an increment of 12.7 mm up to 127 mm. Figure 3.4 shows the effective depth of the EM field in PCC.

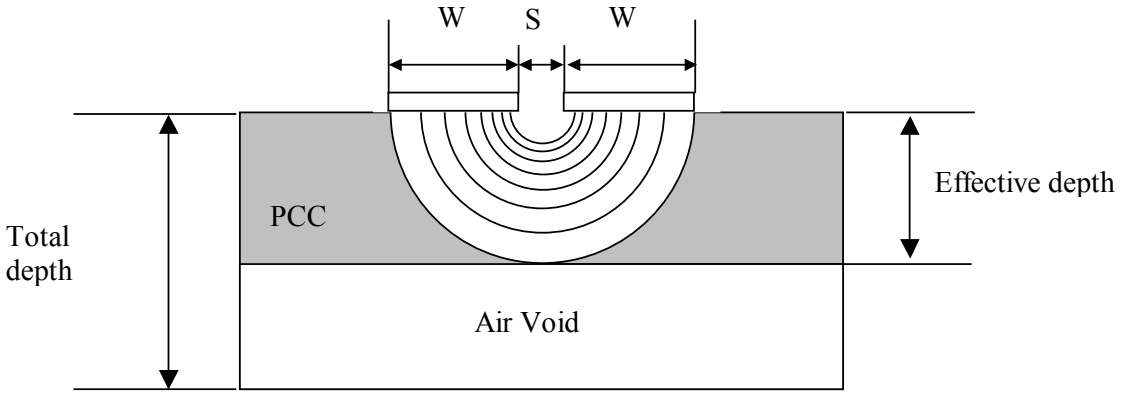

Figure 3.4. EM field shape under the C-Probe

3.3 C-Probe Field Validation

The C-Probe has been validated for use in both the laboratory and in the field for detecting different PCC properties and internal flaws. In the laboratory, the C-Probe has been used to measure the dielectric constant of PCC specimens (450 x 300 x 100 mm) prepared by Diefenderfer (1998). These specimens were cast with simulated air void thicknesses using 7.5-mm- and 15-mm-thick Styrofoam, respectively, placed at 25 mm deep from the surface. To validate the C-Probe in detecting different air void thicknesses at different depths, the specimens have been measured from both top and bottom surfaces. Mix design, quality control data, and specimen conditions for all PCC specimens are reported in Appendix C. Figure 3.5 shows a schematic for the placement of the Styrofoam in the laboratory PCC specimens

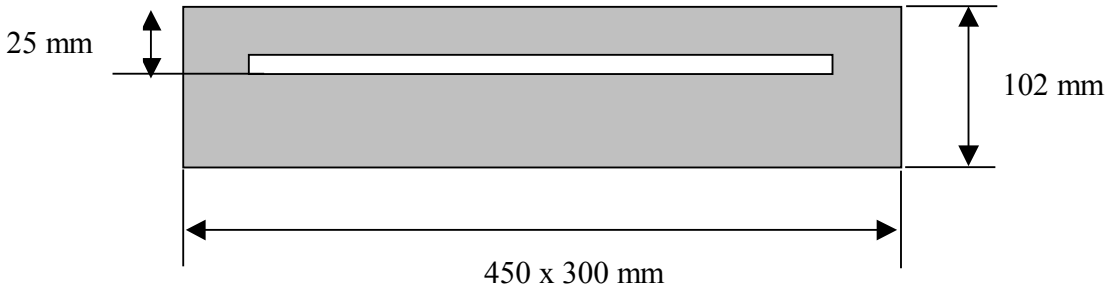

Figure 3.5. Position of the simulated air void in the laboratory PCC specimens

To validate the use of the C-Probe for field applications, it has been used to measure the dielectric constant of PCC slabs (1.5 x 1.5 m), prepared by Loulizi (1999), with three different slab thicknesses of 102, 127, and 152 mm. These slabs were cast with five different mix designs. Two slabs of each mix design were cast with 6.4 mm and 12.7 mm thick Styrofoam placed at 51 mm depth from the surface. Two slabs were cast with one-way and two-way reinforcement. Mix design, quality control data, and specimen conditions for all PCC specimens are reported in Appendix C. Figure 3.6 shows a schematic for the placement of the Styrofoam in the PCC slabs.

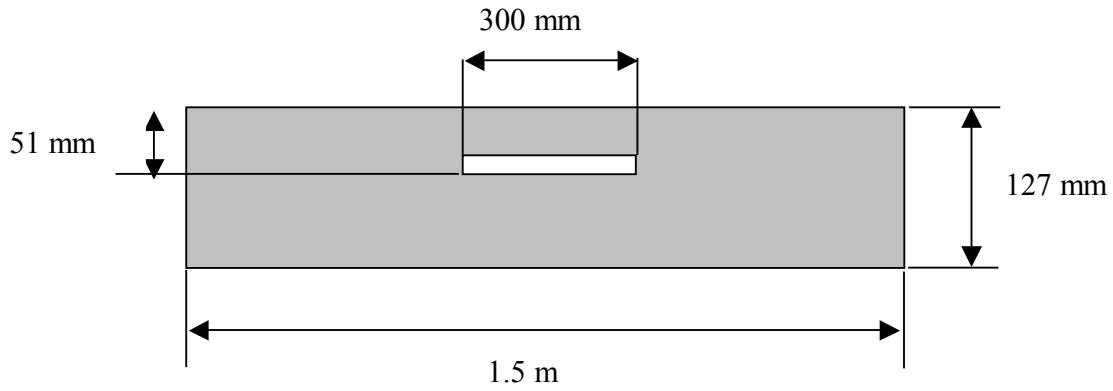

Figure 3.6. Position of the simulated air void (Styrofoam) in the PCC slabs

In this part of the study, several factors were considered for the C-Probe field validation. Three factors were considered to study the variability in the C-Probe measurements, when used in the field. These factors were: the orientation of the C-Probe fixture within the same position, the position of the C-Probe within the same sample, and the sample of the PCC slab within the same mix design. Figure 3.7 shows the orientation and the position considered in this study and Table 3.5 presents all different levels of these factors.

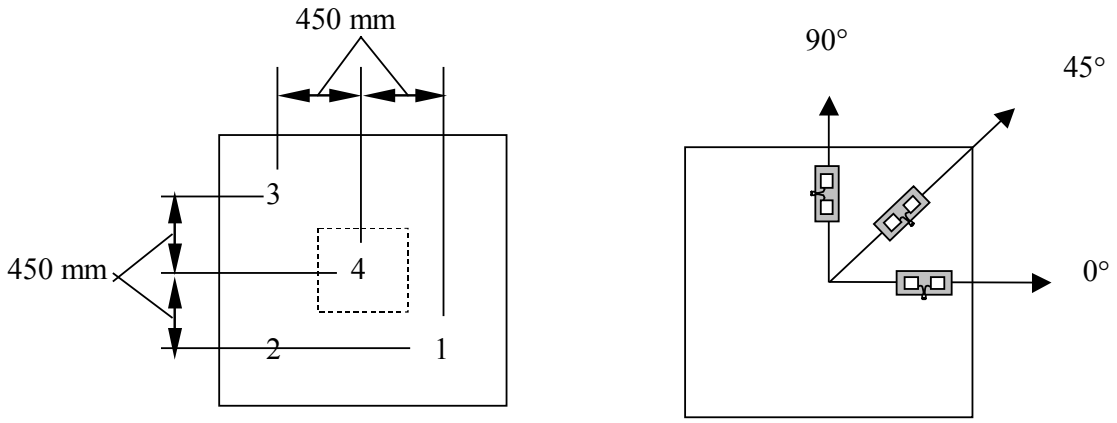

Figure 3.7. Position and orientation of the slab measurements

Table 3.5. Factors considered in the variability measurements

Orientation		
0°	45°	40°
Position		
1	2	3
Specimen		
1	2	

In addition, three other factors were considered in the field validation phase: The mix design, the presence of one or two-way steel reinforcements, and air void thickness. Table 3.6 shows the different levels of considered factors.

Table 3.6. Factors considered for different PCC properties

Mix design				
1	2	3	4	5
Steel Reinforcement				
None	One way	Two ways		
Void thickness (mm) at 51 mm from surface				
None	6.4	12.7		

All measurements were taken at the center of the slab (position 4) for studying these three factors.

3.4 Mixture Theory Evaluation

The significance of measuring the dielectric properties of PCC has been recently increased due to the new development in the utilization of EM waves in NDE measurements for PCC structures

As mentioned earlier, PCC is a heterogeneous and highly complex material. To predict the dielectric properties of a heterogeneous material, Maxwell introduced a dielectric mixture theory formula back in 1891 (Priou 1992). After Maxwell, several researchers have modified, added to, and improved this mixture theory formula. However, these formulas provide an exact solution for only a few idealized and geometrically well-defined systems. At best, they only approximate the geometries of the mixture components for many natural materials (Tinga, 1992). A summery of the major mixture formulas is presented in Table 3.7.

Table 3.7. Theoretical mixture formulas considered for comparison (after Priou, 1992)

Author	Mixture Formula
Maxwell 1891	$\varepsilon = \varepsilon_h + \frac{3V_i\,\varepsilon_h}{\left[\frac{\varepsilon_i + 2\varepsilon_h}{\varepsilon_i - \varepsilon_h}\right] - V_i}$
Bruggemann 1935	$\left[\frac{\varepsilon_i - \varepsilon}{\varepsilon_i - \varepsilon_h}\right] = (1 - V_i)\left[\frac{\varepsilon}{\varepsilon_h}\right]^{1/3}$
Bottcher 1945	$\left[\frac{\varepsilon - \varepsilon_h}{3\varepsilon}\right] = (V_i)\left[\frac{\varepsilon_i - \varepsilon_h}{\varepsilon_i + 2\varepsilon_h}\right]$
Looyenga 1965	$\varepsilon^{1/3} = V_i\varepsilon_i^{1/3} + (1 - V_i)\varepsilon_h^{1/3}$

To evaluate these theoretical formulas, a predictive model to correlate the bulk dielectric constant of PCC with its critical mix parameters (cement, aggregate, and air content) has been developed using a regression analysis technique. The ANOVA technique was used to identify the significant parameters first. Two experimental designs were developed for this purpose.

The first was designed to show the significance of the aggregate physical properties, such as volume, shape, and particle size on the bulk dielectric constant of the PCC. The second experimental design added the air content to the significant parameters obtained from the first experimental design. After identifying the critical parameters obtained from the second experimental design, it was possible to develop predictive model. All potential factors considered, as well as their levels, are presented in Table 3.8.

Table 3.8. Potential factors considered in the mixture theory study

Aggregate Shape			
Circular	Square		
Aggregate size			
1/12 of aggregate volume	1/24 of aggregate volume		
Aggregate Volume (%)			
55	60	65	
Air Content (%)			
0	2	4	6
Cement/Aggregate dielectric constant ratio			
2.5	5.0	7.5	10.0

Experimental design data were collected using a two-dimensional computer simulation with a parallel plate capacitor setup. The scattering effect was not considered in this study, because the maximum size of the inclusion (aggregate) is far below the wavelength resulting from the applied frequency. The schematic of the aggregate shapes in PCC specimen used in the simulation work is shown in Figure 3.8.

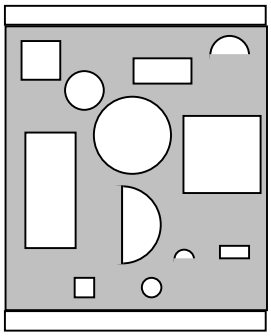

Figure 3.8. Aggregate shapes in PCC specimens used in simulation of mixture theory evaluation

At the end of this phase, the major theoretical mixture formulas have been evaluated by comparing their results with the results obtained from the developed model to determine the best mixture formula for computing the bulk dielectric constant of PCC. Moreover, the theoretical mixture formulas have been also evaluated with a change of the cement to aggregate dielectric constant ratio (DCR) from 2.5 to 10.

4 CHAPTER 4: RESULTS AND DATA ANALYSIS

This chapter presents, discusses, and analyzes the results obtained in this research. It consists of four main sections similar to those of Chapter 3. Section 4.1 discusses the results of the C-Probe calibration data. Section 4.2 reports and analyzes the results obtained in the C-Probe optimization phase. Section 4.3 discusses the C-Probe validation results obtained by measuring both the laboratory PCC specimens and the field PCC slabs. Finally, the mixture theory evaluation conducted in this research project is presented in Section 4.4.

4.1 C-Probe Calibration Data

In this phase of the study, the investigation was conducted in three main areas: the use of the C-Meter, the dielectric properties of the standard materials, and the calibration methods used in the C-Probe measurements. These three areas form the key elements of the calibration process.

4.1.1 The Use of the C-Meter

The C-Meter replaces the Parallel Plate Capacitor (PPC), previously used for measuring the dielectric constant of the standard materials, which are used in the C-Probe calibration process. The C-Meter measurements for Teflon and nylon are relatively more consistent than those obtained by the PPC. To account for the fringing effect in the C-Meter measurements, the Teflon material with a known dielectric constant, ε = 2.1, was measured using the C-Meter. It was found that the fringing effect is about five percent. This fringing effect value was used to adjust all C-Meter measurements.

In addition, the C-Meter replaces the PPC in verifying the C-Probe measurements because the PPC setup cannot accommodate large size PCC specimens (450 x 300 x 100 mm) cast for the C-Probe setup. The dielectric constant of the small PCC specimens (75 x 75 x 100 mm) cast for PPC setup was measured using both the PPC and the C-Meter to verify the measurements of the C-Meter on PCC material. The measurements are shown in Figures 4.1 and 4.2 for the real and the imaginary parts, respectively.

Due to the aforementioned two reasons, the C-Meter was used in this research to determine the dielectric constant of the standard materials (Teflon and extruded nylon) and to verify the C-Probe measurements for the large PCC specimen.

Figures 4.1 and 4.2 show that the dielectric constant of C1 is lower than that of A1 because C1 was cast with 6% air content (AC) while A1 was cast with 2% AC only. The mix design properties for A1 and C1 are presented in Appendix C.

It was found that the dielectric constant of the small specimen cast for the PPC setup is lower than that of the large specimen of the same mix design. Figures 4.3 and 4.4 show the real and the imaginary parts, respectively, of the dielectric constant measurements of both the small and the large specimens for C1 mix design using the C-Meter.

The C-Meter measurements for the dielectric constant of the large C1 PCC specimen were used in Section 4.1.3 to evaluate the developed calibration methods of the C-Probe measurements. The C-Meter measurement values of Teflon, extruded nylon, small PCC samples (A1, C1), and large PCC specimen (C1), are reported in Appendix A.

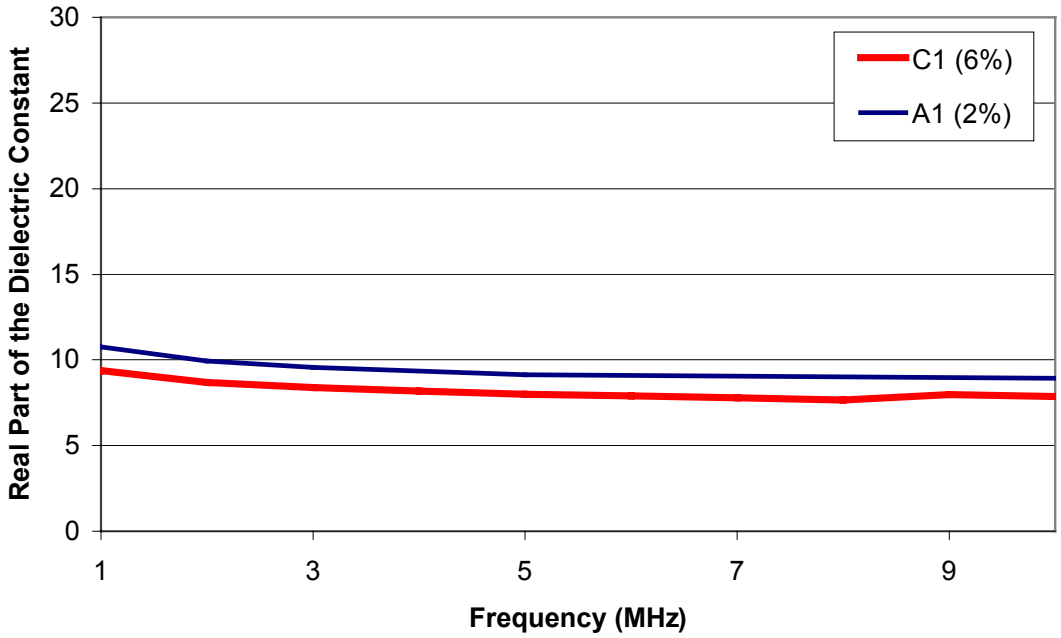

Figure 4.1. Real dielectric constant for the small PCC specimens using C-Meter

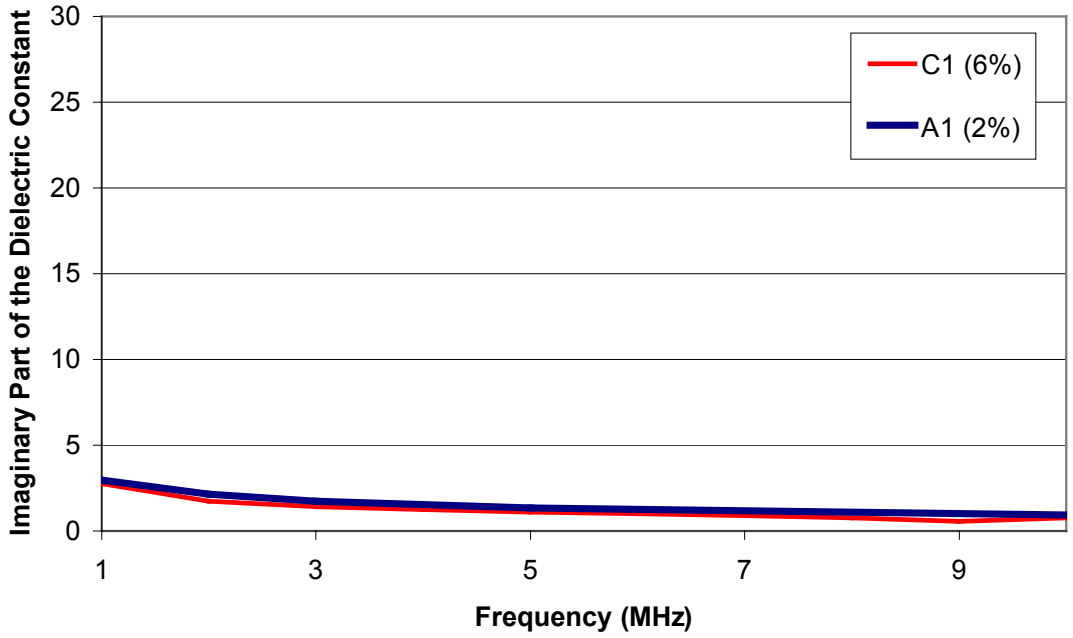

Figure 4.2. Imaginary dielectric constant for the small PCC specimens using C-Meter

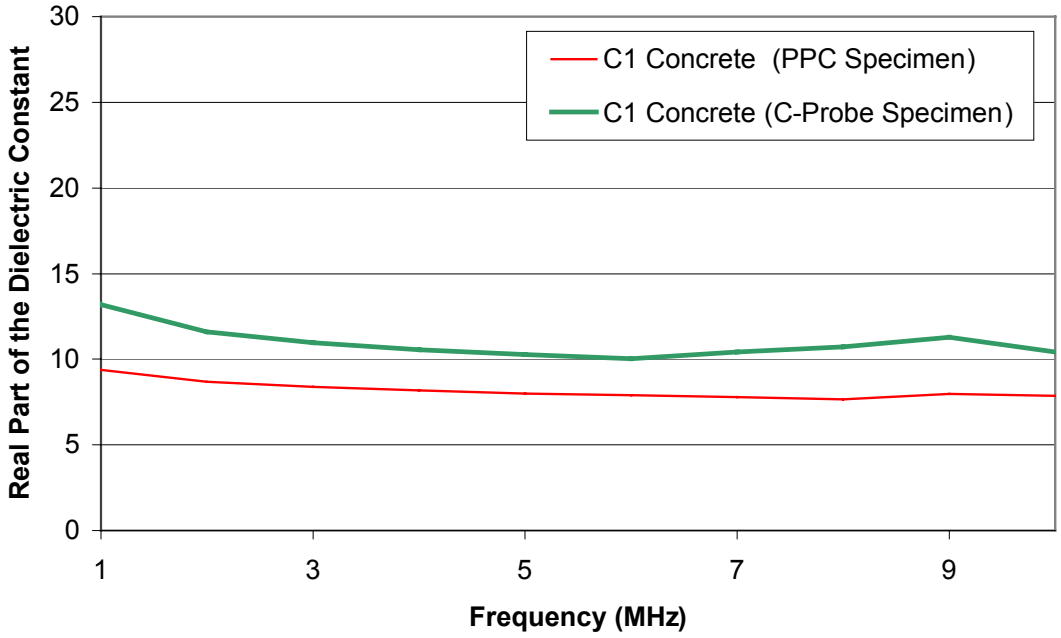

Figure 4.3. Real dielectric constant for the small and large specimens using C-Meter

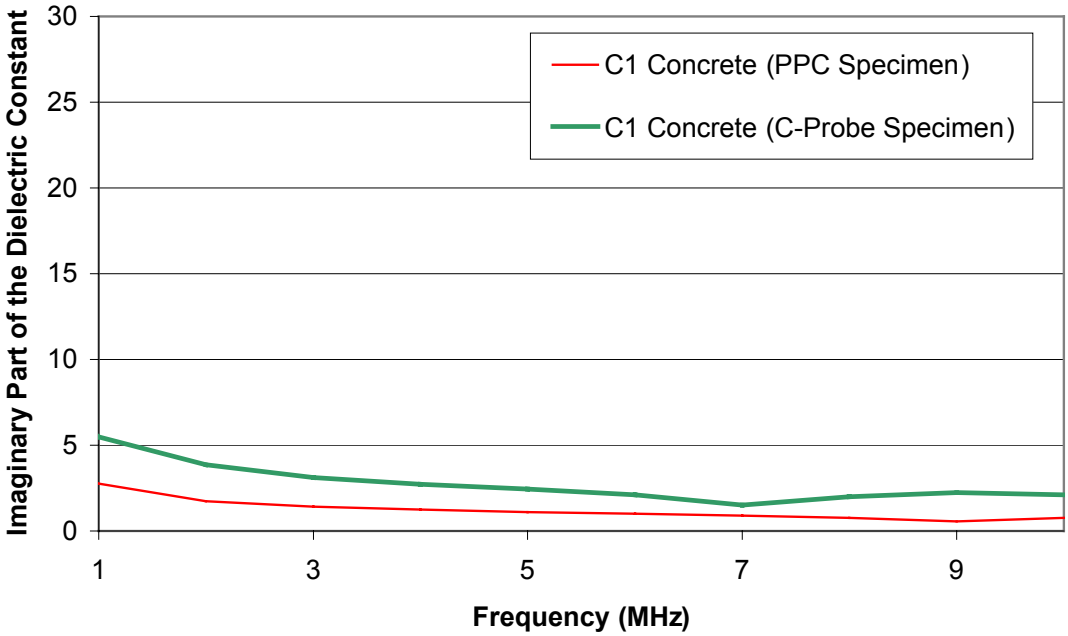

Figure 4.4. Imaginary dielectric constant for the small and large specimens using C-Meter

4.1.2 Dielectric Properties of the Standard Materials

The standard materials (Teflon and extruded nylon) have been measured at different low frequencies using the C-Meter to investigate their dielectric properties over a specific range of frequency from 0.1 MHz to 5 MHz. The dielectric constant of Teflon material was shown to be frequency-independent, while the dielectric constant of extruded nylon was shown to decrease slightly with the increase of the frequency, as shown in Figure 4.5.

The dielectric constant of the two standard materials have been measured in more than one orientation using the C-Meter in order to study the isotropy dielectric behavior of these materials. The isotropy dielectric behavior was studied because the interaction between the EM field and the material being tested occurs in one direction between the two plates of the C-Meter (or the PPC) and in more than one direction between the two plates of the C-Probe. A slightly different dielectric constant was measured for the extruded nylon when the orientation of the material changed as shown in Table A.2 (in Appendix A) and Figure 4.6. Therefore, when used in the C-Probe calibration, the anisotropy dielectric behavior of the extruded nylon should be considered. Since C-Probe provides interaction between the EM field and the material being

tested in more than one direction, the dielectric constant value for the extruded nylon has been averaged between the two values of both orientations when used in the C-Probe calibration process. The average real dielectric constant value of the extruded nylon was found to be 3.3; while Teflon, an isotropic material, was found to be 2.1. Teflon specimen has been measured in different orientations using the C-Meter to confirm this fact. Both materials have an imaginary dielectric constant of 0. Table 4.1 summarizes the dielectric properties obtained for each standard material used in this study.

Table 4.1. Dielectric properties of the standard materials used in the C-Probe calibration process

Material	Isotropy	Dielectric Constant	Loss	(ε′, ε″)
Teflon	Isotropic	Frequency independent	Low loss	(2.1, 0)
Extruded Nylon	Anisotropic	Changes slightly with frequency	Low loss	(3.3, 0)

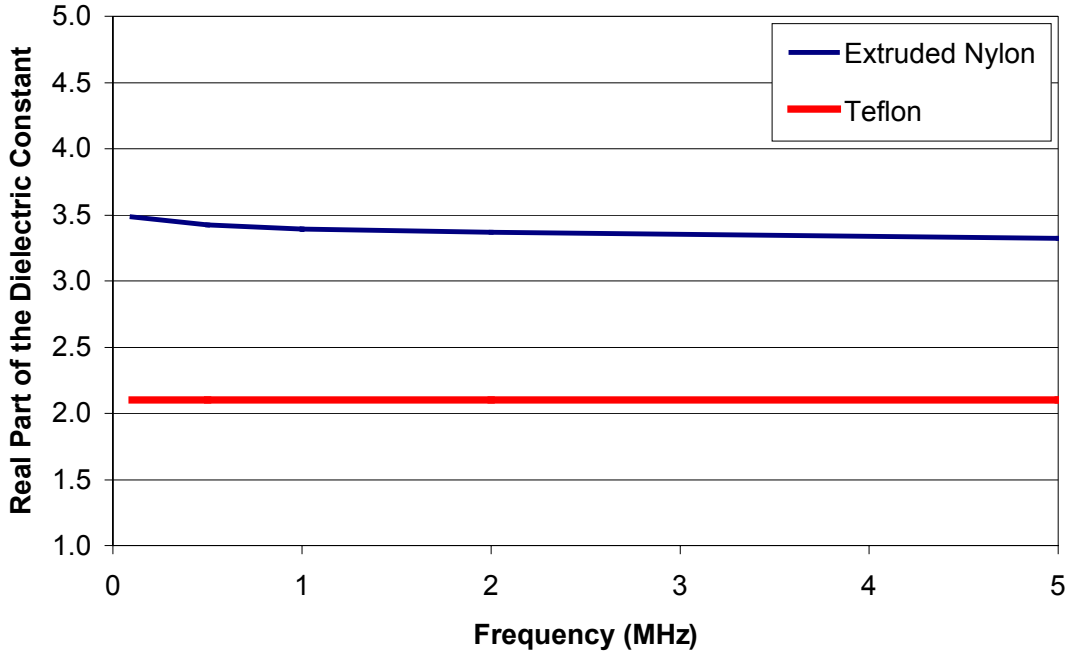

Figure 4.5. Real dielectric constant of standard materials using C-Meter

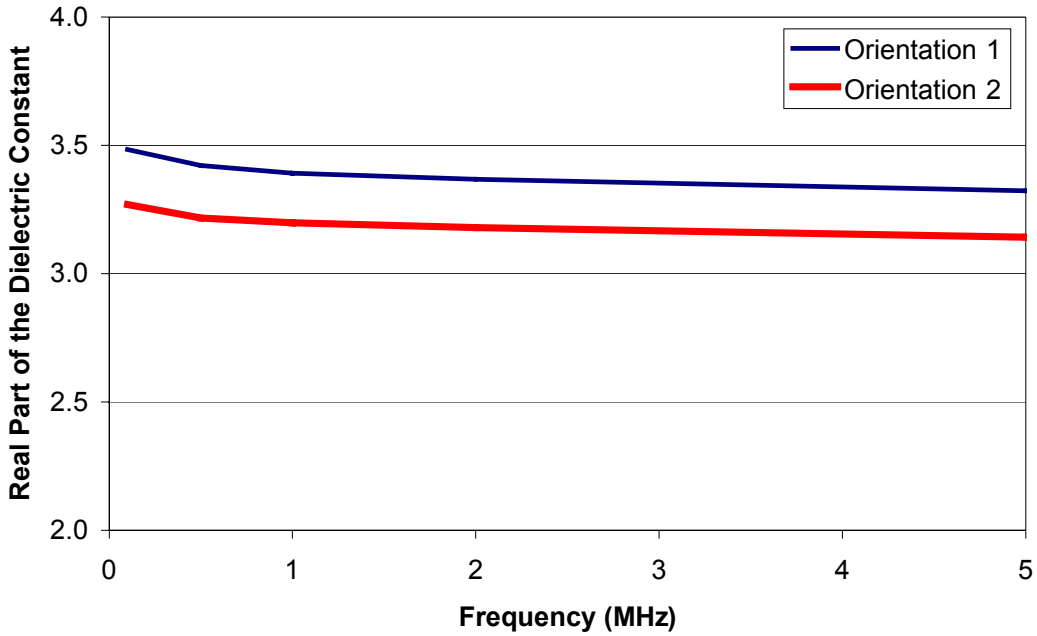

Figure 4.6. Real dielectric constant of the extruded nylon using C-Meter at different orientation

4.1.3 C-Probe Calibration Methods

Five calibration methods have been developed in this research for the C-Probe measurements. To evaluate these methods, their measurements have been compared with the C-Meter measurements for C1 PCC specimen. The dimensions are shown in Figure 3.3 and the PCC mix design for the specimen is given in Appendix C. The calibration method notation and the calibration standards are reported in Tables 3.2 and 3.3.

As stated in Section 3.1.3, the five calibration methods have been divided into two categories: the scattering-parameter form (OSLL and OSLF), and the bilinear transformation form (OMM, SMM, OSM).

In evaluating the OSLL method, the results have shown that adding one more load standard did not provide acceptable measurements. In evaluating the OSLF method, the results have shown that the estimated EM mapping factor (F) value obtained from a computer simulation was not accurate and consequently led to incorrect measurements. The measurements obtained

using the OSLF were higher in value than those obtained using the C-Meter for both the real and the imaginary parts of the dielectric constant. The measurements obtained using these methods are reported in Appendix A.

In the bilinear transformation form, the governing equations of the three methods relate the dielectric constant of the MUT to the measured reflection coefficient through only three bilinear transformation coefficients as discussed earlier in Section 3.1.3.

To obtain these coefficients (a, b, and c), three standards have been used in each method. The first method (OMM) used the open standard with ε = 1, the Teflon material with ε = 2.1, and the extruded nylon with ε = 3.3. Evaluation of the OMM method showed that this method gives incorrect measurements for the dielectric constant of PCC. The measurements obtained from this method were lower in value than those obtained using the C-Meter for both the real and the imaginary part of the dielectric constant. Moreover, the imaginary part measurements were negative, and more noise was present in the measurements; results are reported in Appendix A.

The second method (SMM) of the bilinear transformation form used the short standard with ε = ∞ instead of the open standard that was used in the first method (OMM). Evaluation of the SMM method showed that this method gives reasonable measurements. However, slightly smaller values have been obtained for both the real and the imaginary parts of the dielectric constant when compared to C-Meter measurements. The variation of the measured dielectric constant values was within an acceptable range. The measurements, using this method, are reported in Appendix A.

The third method (OSM) used the open standard, the short standard, and the Teflon materials as three calibration standards. Evaluation of the OSM method showed that this method gives the best measurements for the C1 PCC specimen using the C-Probe fixture. Both the real and imaginary parts of the dielectric constant measurements were in agreement with the reference measurements obtained using the C-Meter. Figures 4.7 and 4.8 shows, respectively, the real and the imaginary parts of the dielectric constant measurements using both the C-Probe and the C-Meter for C1 specimen.

Out of the five calibration methods studied, the OSM method was selected to be used in calibrating the C-Probe measurements for the PCC material. This method was used in Section 4.2 in validating the use of the C-Probe fixture for field application. Table 4.2 shows an evaluation summary for all considered calibration methods.

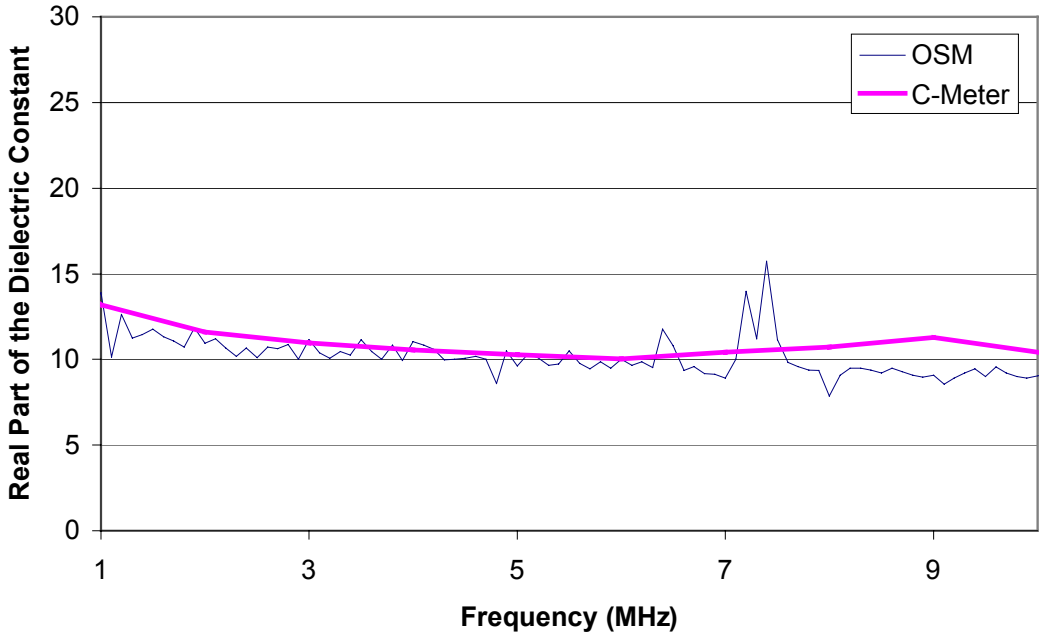

Figure 4.7. Real dielectric constant of PCC specimen using C-Probe with OSM and C-Meter

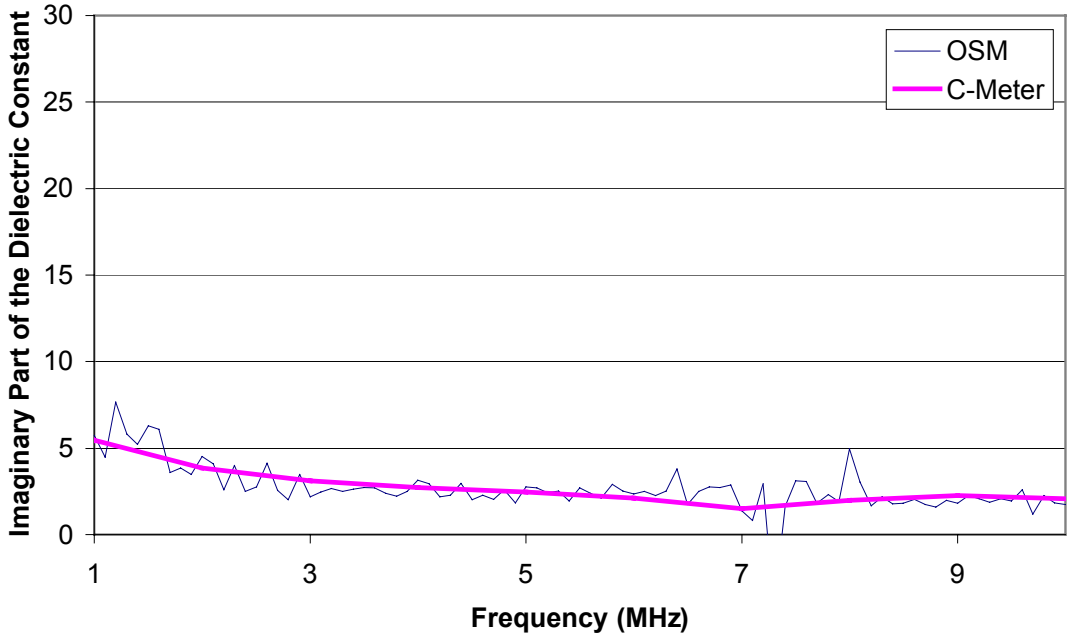

Figure 4.8. Imaginary dielectric constant of PCC specimen using C-Probe with OSM and C-Meter

Table 4.2. Comparison between the considered calibration schemes

Scheme	Comments	Conclusion
OSLF	1. requires computer simulation to calculate F 2. dose not require a standard material 3. does not yield to an acceptable accuracy	Not appropriate
OSLL	1. dose not require a standard material 2. does not yield to an acceptable accuracy	Not appropriate
OMM	1. requires two isotropic standard materials 2. dose not require use of the load standard 3. does not yield to an acceptable accuracy	Not appropriate
SMM	1. requires two isotropic standard materials 2. dose not require use of the load standard 3. yields to an acceptable accuracy	Acceptable
OSM	1. requires one isotropic standard material 2. dose not require use of the load standard 3. yields to an acceptable accuracy	Best

4.2 C-Probe Optimization

The penetration depth of the EM field in the PCC depends on the C-Probe design configuration. Therefore, it is necessary to obtain an optimum design configuration for the C-Probe to maximize the interaction of the EM field with the tested PCC. In addition, the optimum design configuration should not provide a penetration depth of the EM field that exceeds the slab thickness or the level of the reinforcing steel. This would prevent EM filed from interacting with other material beneath the slab, such as soil, or air in the case of plain PCC, or steel in the case of reinforced PCC.

An optimum design configuration has been obtained for different desired penetration depth using a computer simulation technique. As stated in Section 3.3, three variables have been considered as the critical parameters in the C-Probe design optimization: the plates' size (W), the separation between the plates (S), and the dielectric constant of the PCC slab under test (Eps). These parameters, as well as their levels, are presented in Table 3.6.

To achieve the C-Probe design optimization, the effective penetration depth of the EM field in the PCC slab has been determined first. Second, a predictive model has been developed using a regression analysis technique to correlate the effective depth with the critical parameters of

the C-Probe design configuration. Finally, an optimum design for the C-Probe configuration has been obtained for different desired thicknesses by normalizing the effective depth of each considered design to the desired thickness. The optimum design has been identified with a normalized value of one.

The first step in the optimization process has been conducted by using a computer simulation to determine the effective penetration depth of the EM field for each considered C-Probe design configuration. To achieve this, an air void thickness has been placed at 254 mm depth, which has been found to be beyond the effect of the EM field. Then, the air void layer has been increased by 25 mm increments until the computed capacitance changed significantly. The effective penetration depth has been identified at 7.5% reduction from the maximum capacitance value.

Table 4.3 shows the percentages of change in the capacitance corresponding to each air void depth for 76 mm x 76 mm plates' size with 51 mm separation between them. The summary of the remaining C-Probe design configurations are presented in Appendix B.

Table 4.3. Percentage of capacitance change due to air void depth using 76 x 76 x 51 mm C-Probe

Air Void Depth (mm)	Eps							
	20		15		10		5	
	C	Change (%)	C	Change (%)	C	Change (%)	C	Change (%)
254	149.35		112.02		74.70		37.37	
229	149.93	-0.39	112.48	-0.41	75.03	-0.44	37.58	-0.56
203	148.57	0.52	111.49	0.47	74.42	0.37	37.33	0.11
178	151.28	-1.29	113.58	-1.39	75.87	-1.57	38.15	-2.09
152	147.55	1.21	110.86	1.04	74.13	0.76	37.42	-0.13
127	139.54	6.57	104.97	6.29	70.39	5.77	35.74	4.36
102	131.18	12.17	98.87	11.74	66.54	10.92	34.12	8.70
76	119.05	20.29	90.04	19.62	61.27	17.98	31.80	14.91
51	101.29	32.18	77.10	31.17	52.51	29.71	28.40	24.00
25	69.23	53.65	53.51	52.23	37.75	49.46	21.72	41.88

The effective depth for each considered design configuration has been determined at 7.5% change from the maximum capacitance. A linear interpolation has been used where it has been deemed necessary. Table 4.4 shows the effective depth of each design configuration at the four considered values of the PCC dielectric constant.

Table 4.4. Effective depth of each considered design configuration (mm)

S (mm)	Eps											
	20			15			10			5		
	W (mm)			W (mm)			W (mm)			W (mm)		
	76	102	127	76	102	127	76	102	127	76	102	127
25	93	113	143	91	111	142	88	107	138	76	97	126
51	123	139	164	121	137	162	118	133	159	109	122	149
76	155	168	165	154	166	164	151	162	161	140	149	151

Analysis of variance (ANOVA) has been conducted to identify the critical parameters that significantly affect the EM field penetration depth. Complete output data for ANOVA are presented in Appendix B. Table 4.5 shows the p-value obtained for each considered factor.

Table 4.5. P-value for each considered parameter

Factor	P-value
W	0.000
S	0.000
Eps	0.000

The results have shown that the main effects of all considered factors were significant. In addition, a mean comparison technique has been conducted using Tukey's to identify the significant differences among the considered levels of each factor. The results have shown that there is no significant difference between the means of the dielectric constant of 10, 15, and 20, while there is a significant difference between the means of 5 and all the other values. Table 4.6 shows the p-values of the mean comparison analysis for Eps. Thus, The analysis has concluded that when the dielectric constant of PCC is greater than 10, its effect on the effective penetration depth becomes insignificant.

Table 4.6. P-values of the mean comparison analysis for Eps

Comparison	P-value
5-10	0.049
5-15	0.006
5-20	0.002
10-15	0.822
10-20	0.580
15-20	0.975

Regression analysis has been conducted to predict a model that correlates the effective depth of the EM field with the critical parameters of the C-Probe design configuration. The analysis has been conducted in two steps. First, full two-way interaction has been implemented to identify the significant effects of all considered parameters. The parameter that has insignificant effect has been removed from the model. The results of the first step have shown that there is no sufficient evidence to conclude that the quadratic effect of the plates' size (W) and the separation between them (S) significantly influenced the effective depth of the EM field of the C-Probe. The quadratic effect of W has been removed from the developed model in the second step. The predictive model is as follows:

d = - 84.0 + 3.33 Eps + 1.45 W + 2.50 S - 0.0155 W*S - 0.0922 Eps**2

where,

d = effective depth in mm;

Eps = dielectric constant of PCC slab;

W = plates' size in mm; and

S = separation between the plates in mm

The result of the regression analysis has shown that the separation (S) between the plates has a relatively higher influence than that of the plates' size on the effective depth of the EM field and consequently affects the selection of the optimum design of the C-Probe. In addition, the regression analysis has shown that the effective depth of the EM field in PCC is related quadratically to the separation distance between the plate and the dielectric constant of PCC (Eps). To obtain the optimum design of the C-Probe configuration for different slab thickness, a normalized factor has been computed for each C-Probe design configuration. This factor is the ratio of the effective depth to the desired slab thickness. The optimum design has been identified with a normalized factor that is close to but not grater than one.

The results have shown that none of the considered C-Probe design configurations are suitable for use with 63 mm or less desired penetration depth. Moreover, among the considered design configurations, C-Probe with 127 mm plates' size and 76 mm separation between them has proved to be the optimum design for slab thickness of 191 mm. Table 4.7 shows the optimum design configuration for different desired penetration depth from 76 mm to 178 mm with 12.7 mm increment.

Table 4.7. Optimum design configurations for different desired penetration depth

Desired Penetration Depth (mm)	Eps	W x S (mm)
76	5	76 x 25
	10	None
	15	None
	20	None
89	5	89 x 38
	10	76 x 25
	15	76 x 25
	20	76 x 25
102	5	102 x 25
	10	76 x 38
	15	89 x 25
	20	89 x 25
114	5	114 x 25
	10	89 x 38
	15	102 x 25
	20	102 x 25
127	5	127 x 25
	10	89 x 51
	15	102 x 38
	20	102 x 38
140	5	127 x 51
	10	89 x 63
	15	102 x 51
	20	114 x 38
152	5	114 x 76
	10	114 x 63
	15	102 x 63
	20	102 x 63
165	5	127 x 76
	10	127 x 76
	15	127 x 63
	20	114 x 76
178	5	127 x 76
	10	127 x 76
	15	127 x 63
	20	127 x 63

4.3 C-Probe Field Validation

This section presents and discusses the results obtained from the field validation of the C-Probe. The C-Probe design configuration used in this validation task was 76 mm x 76 mm plates' size and 51 mm separation between plates.

In the laboratory, the C-Probe has been used to measure the dielectric constant of a PCC specimen (450 x 300 x 100 mm) prepared by Diefenderfer (1998). The specimens include plain PCC specimen, and two PCC specimens with simulated voids at thicknesses of 7.5 mm and 15 mm. The air voids were simulated with Styrofoam. The Styrofoam has been placed at 25 mm depth from the surface. To validate the C-Probe for detecting different void thicknesses at different depths, the PCC specimens have been measured from both the top and bottom surfaces. Figures 4.9 through 4.16 show the resulting measurements for all PCC specimens measured from both surfaces.

Laboratory measurements show that the C-Probe was able to detect air void thicknesses of 7.5 mm and 15 mm at 25 mm depth from the surface, as shown in Figures 4.9 and 4.10. The presence of the air void reduced the bulk dielectric constant values of the PCC specimen under test. This reduction was more pronounced in the real part of the bulk dielectric constant than in the imaginary part. This is because the real part of the dielectric constant of air is equal to 1, which significantly different from that of PCC (10). However, the imaginary dielectric constant of PCC is 2, which would relatively be less affected by air (imaginary part = 0). It has been noticed that the bulk dielectric constant is a function of the volume of each material as will be discussed in Section 4.4.

The effect of the air void thickness at 25 mm depth from the surface was noticeable in Figure 4.9. The 15 mm air void thickness caused more reduction to the bulk dielectric constant than the 7.5 mm thicknesses did. As would be expected, this effect has been noticed on the real part of the dielectric constant but not on the imaginary part.

At 75 mm depth from the surface, the 7.5 mm air void thickness has been hardly detected because the reduction in the bulk dielectric constant is very small for the real part, and zero for the imaginary part as shown in Figures 4.11 and 4.12, respectively. However, the 15 mm air void thickness at 75 mm depth from the surface has been detected by noticeable reduction in the real part and to a less extent in the imaginary part of the measured dielectric constant.

The above analysis concludes that 7.5 mm air void thickness may lead to significant reduction at 25 mm depth from the surface and is negligible at 75 mm depth from the surface as

shown in Figures 4.13 and 4.14. The 15 mm air void thickness, however, can result in noticeable reduction of the dielectric constant at 75 mm depth from the surface and significant reduction at 25 mm depth from the surface as shown in Figure 4.15 and 4.16. The reductions in the bulk dielectric constant due to air void presence are more pronounced in the real part than the imaginary part. The difficulties in detecting the air void thickness at 75 mm deep indicate that the EM field of the C-Probe configuration used (76 mm x 76 mm plates' size with 51 mm separation between them) possesses low intensities at that depth.

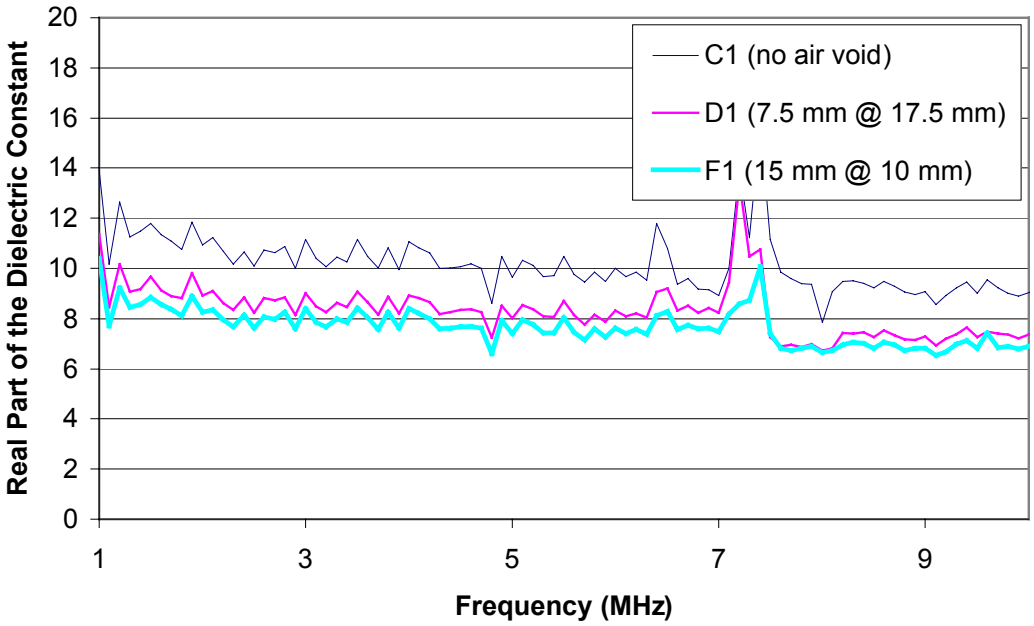

Figure 4.9. Effect of air void thickness on the real dielectric constant of PCC

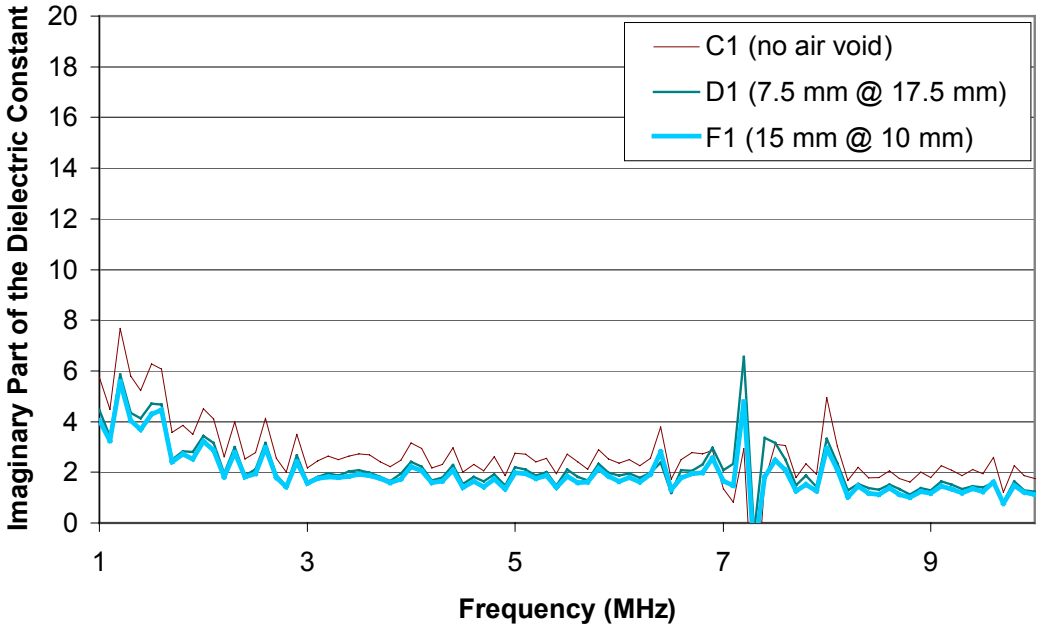

Figure 4.10. Effect of air void thickness on the imaginary dielectric constant of PCC

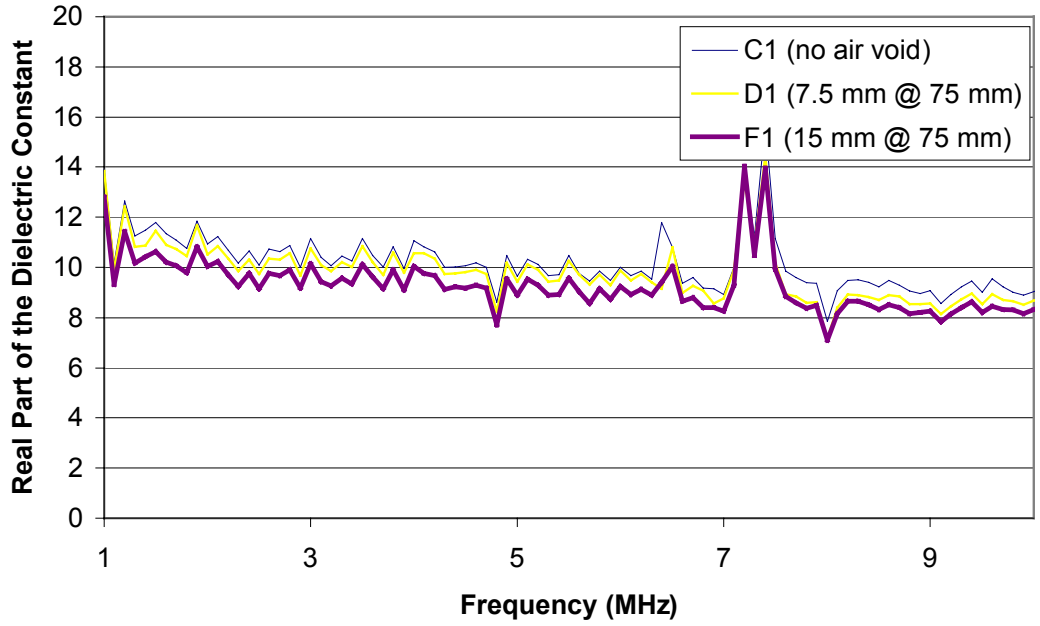

Figure 4.11. Effect of air void thickness on the real dielectric constant of PCC

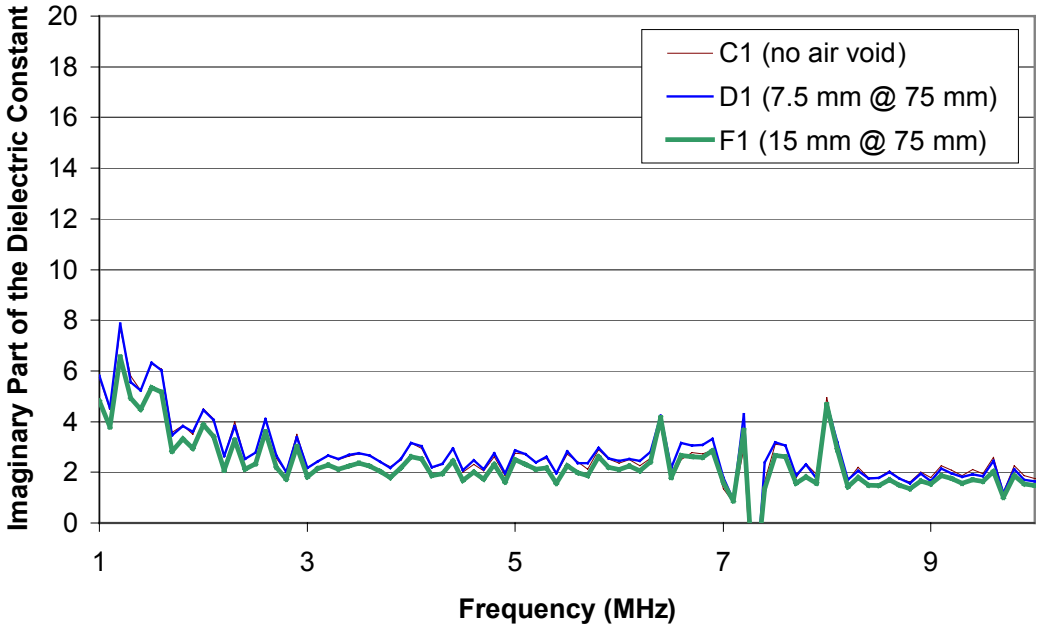

Figure 4.12. Effect of air void thickness on the imaginary dielectric constant of PCC

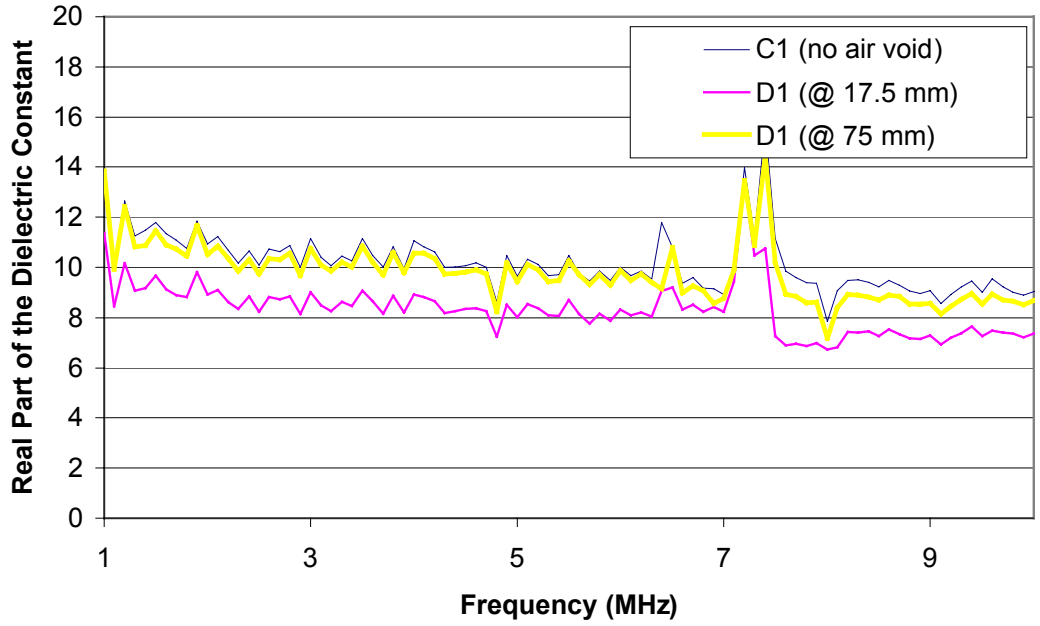

Figure 4.13. Effect of the 7.5 mm air void depth on the real part of PCC

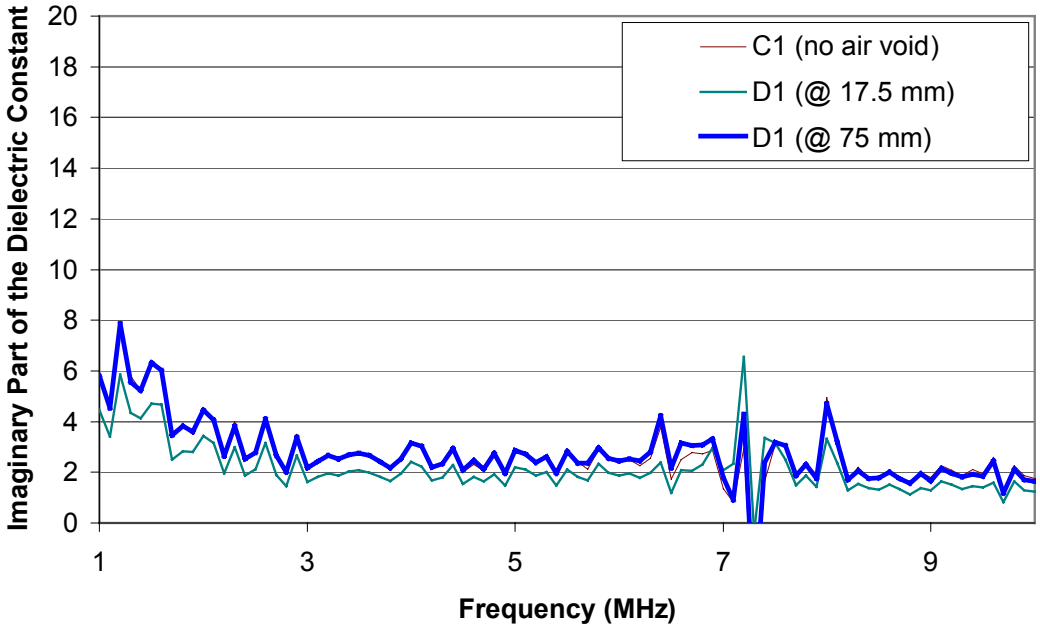

Figure 4.14. Effect of the 7.5 mm air void depth on the imaginary part of PCC

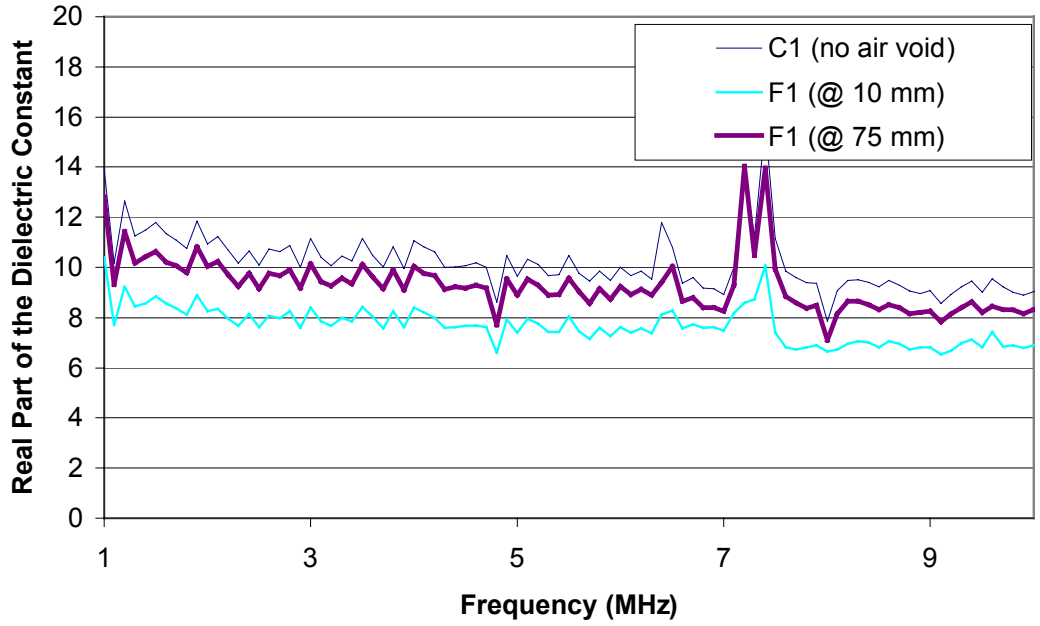

Figure 4.15. Effect of the 15 mm air void depth on the real part of PCC

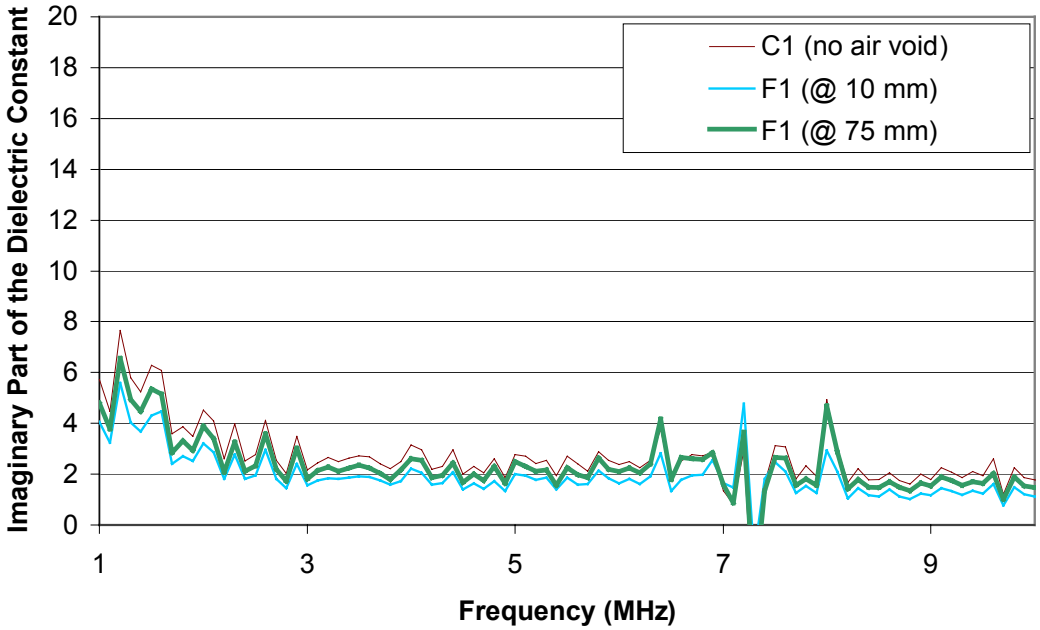

Figure 4.16. Effect of the 15 mm air void depth on the imaginary part of PCC

In validating the C-Probe for field application, the dielectric constants of 1.5 m x 1.5 m PCC slabs have been measured using the same C-Probe fixture used in the laboratory (76 mm x 76 mm plates' size with 51 mm separation between them). As stated earlier in Section 3.3, these slabs have been cast from five different mixes. The mix design properties, the notations used in this research, and the induced flaws in these slabs are reported in Appendix C. The variability of the C-Probe measurements in the field has been studied at three settings: different C-Probe orientation within the same positions, different positions within the same specimen, and different slabs of the same mix design. In addition, to study the effect of the different mix designs on the measured dielectric constant of the PCC, the study investigates the effect of reinforcement and different flaws in PCC slabs on the measured dielectric constant. This includes detecting air void of different thicknesses (6.4 and 12.7 mm) at 51 mm deep from the PCC surface. The effect of the slab thickness on the measured dielectric constant has been originally considered. However, because the configuration design of the used C-Probe fixture (76 mm x 76 mm plates' size with 51 mm separation between them) did not provide a penetration depth of more than 127 mm, this factor has not been included in this study.

Three measurements have been taken for each considered parameter. The resulting measurements are reported in Appendix C. This section includes only sample measurements for each investigated parameters.

In studying the variability of the C-Probe measurements for different orientations within the same position, three orientations have been considered (0°, 45°, 90°), as shown in Figure 3.5 . The results show that different orientations of the C-Probe do not affect the measurements of the dielectric constant. Figures 4.17 and 4.18 show respectively the real and the imaginary dielectric constant measurements for the PCC slab with different orientations within the same position.

In studying the variability of the C-Probe measurement for different positions within the same slab, the measurements have been taken at three different positions, as shown in Figure 3.5 . The results of these measurements show that the position of the C-Probe does not affect the measurements of the dielectric constant of the PCC slab. Figures 4.19 and 4.20 show the real and the imaginary dielectric constant measurements, respectively, for the PCC slab at different positions.

The variability of the C-Probe measurements for different slabs of the same mix design has been found insignificant. Figures 4.21 and 4.22 show the real and the imaginary parts of the dielectric constant, respectively, for different slabs of the same mix design.

Regarding the effect of different mix designs on the measured dielectric constant, the results have shown that the mix design affects the measured dielectric constant values for both the real and the imaginary parts of the dielectric constant as shown in Figures 4.23 and 4.24. In general, the PCC mix with silica fume has shown lower dielectric constant values. Although one would expect the dielectric constant of the PCC with limestone aggregate ($\varepsilon \approx 6$) is greater than that of PCC with sandstone ($\varepsilon \approx 4$), the presence of a higher air content ($\varepsilon \approx 1$) in the mixes with limestone than that in the mixes with sandstone results in similar bulk dielectric constant of the two mixes.

The presence of steel reinforcements has also shown no significant effect on the measured dielectric constant of the PCC slabs as shown in Figures 4.25 and 4.26. This indicated that the EM field penetration was limited and weak at the steel reinforcements level.

Finally, the C-Probe measurements were significantly affected by the existence of the simulated air void thickness of 12.7 mm at 51 mm depth from the surface. The measured real and imaginary dielectric constant values have been significantly less when simulated air void is

introduced. However, the simulated air void thickness of 6.4 mm has been detected at one measurement taken out of three measurements. Figures 4.27 and 4.28 show the real and the imaginary parts of the dielectric constant, respectively, for different slabs with different air void thickness.

The above analysis concludes that the C-Probe measurements do not possess significant variability with either the orientation, the position of the C-Probe fixture, or between different slabs of the same mix. The steel reinforcement at 63 mm deep has insignificant effect on the measured dielectric constant. However, dielectric measurements have been affected by the mix design and the presence of 12.7 mm air void thickness at 51mm. The results show that the C-Probe did not provide acceptable measurements below frequency of 1 MHz for PCC specimen under test. Tables 4.8 and 4.9 presents summary of the results obtained from the field validation study.

Table 4.8. Summary of the results of variability study of the C-Probe measurements

Variability	Significance
Different orientations	None
Different positions	None
Different slabs of same design mix	None

Table 4.9. Summary of the detection of the C-Probe of different PCC slabs

Condition	Detection
Mix design	Yes
Steel reinforcements	No
6.4 mm air void at 51 mm depth	Yes (Low)
12.7 mm air void at 51 mm depth	Yes

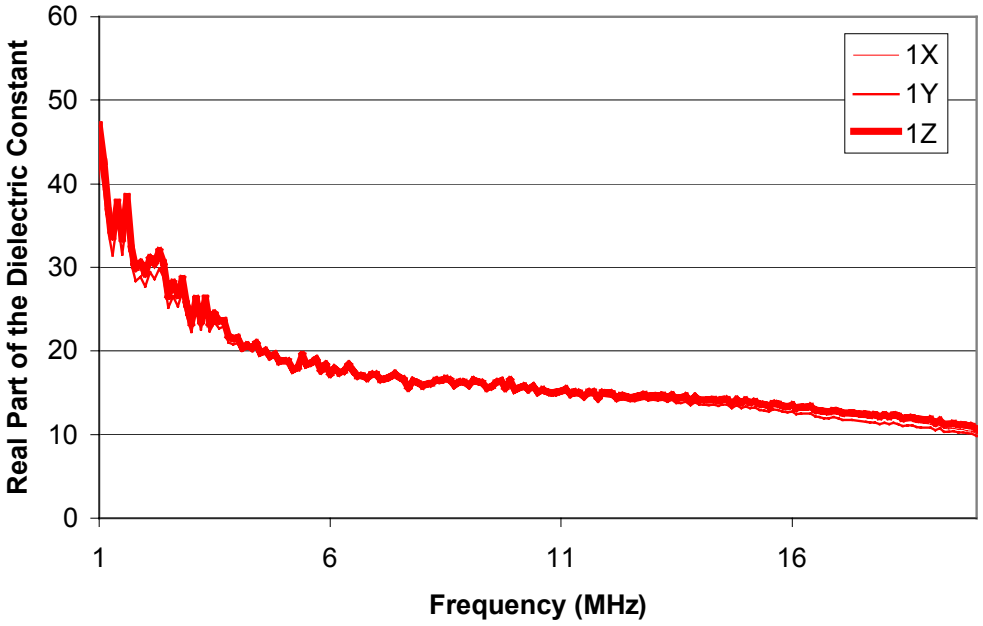

Figure 4.17. Effect of orientation on the real part of the dielectric constant

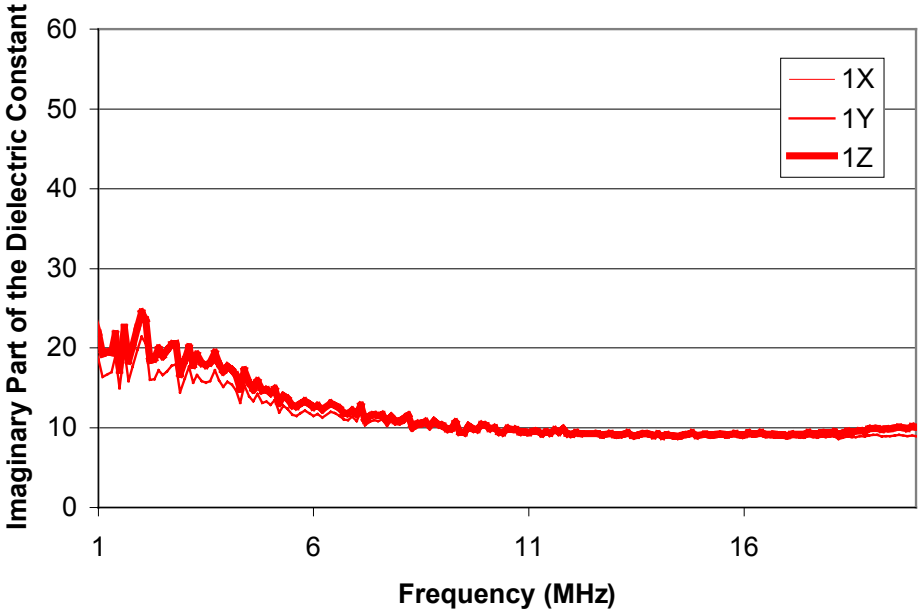

Figure 4.18. Effect of orientation on the imaginary part of the dielectric constant

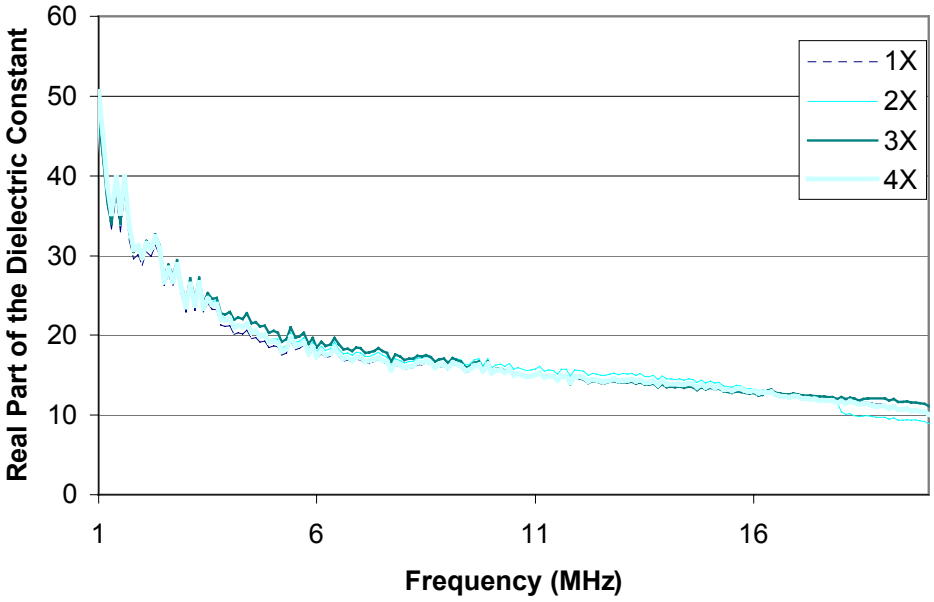

Figure 4.19. Effect of position on the real part of the dielectric constant

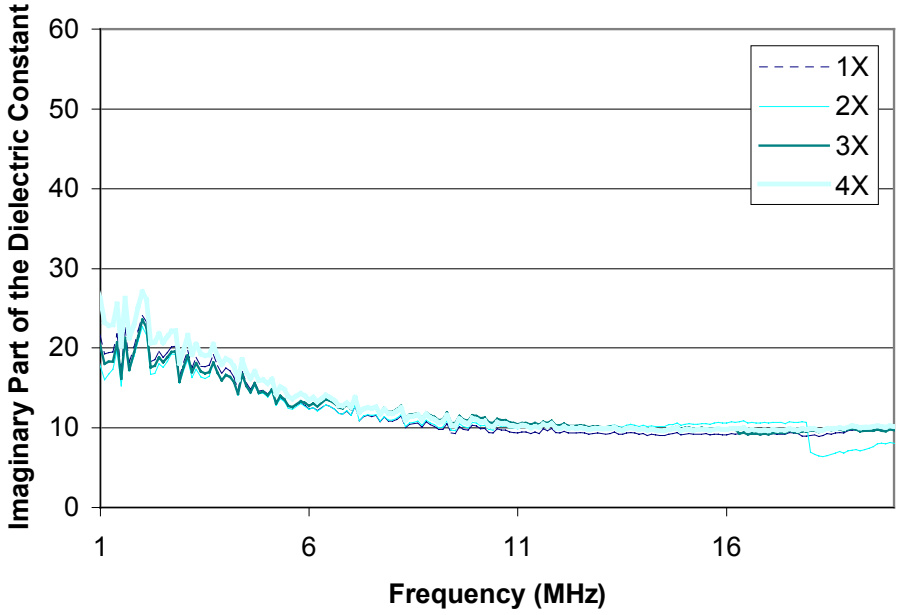

Figure 4.20. Effect of position on the imaginary part of the dielectric constant

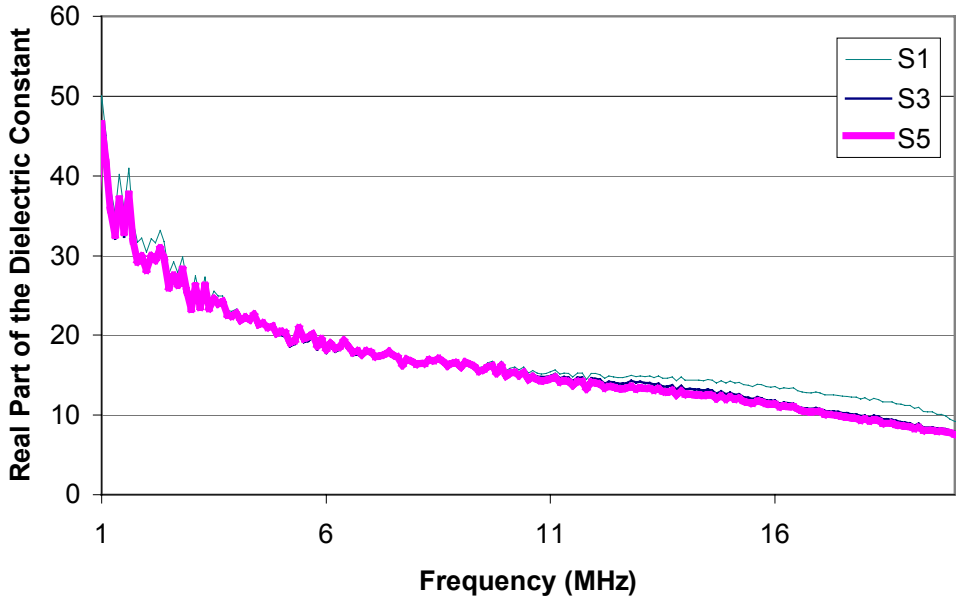

Figure 4.21. Effect of PCC mixing and casting on the real part of the dielectric constant

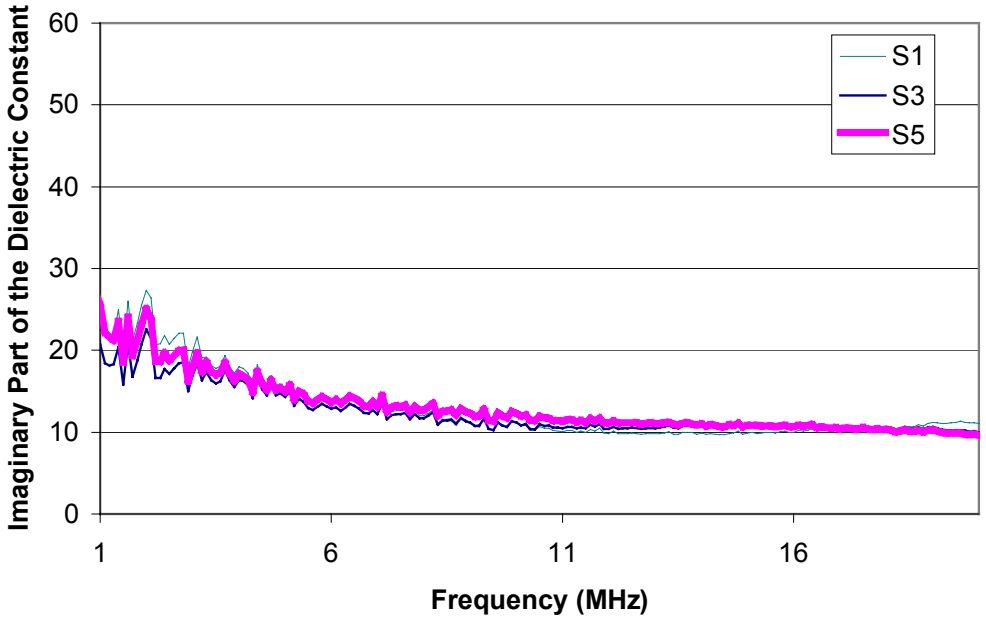

Figure 4.22. Effect of PCC mixing and casting on the imaginary part of the dielectric constant

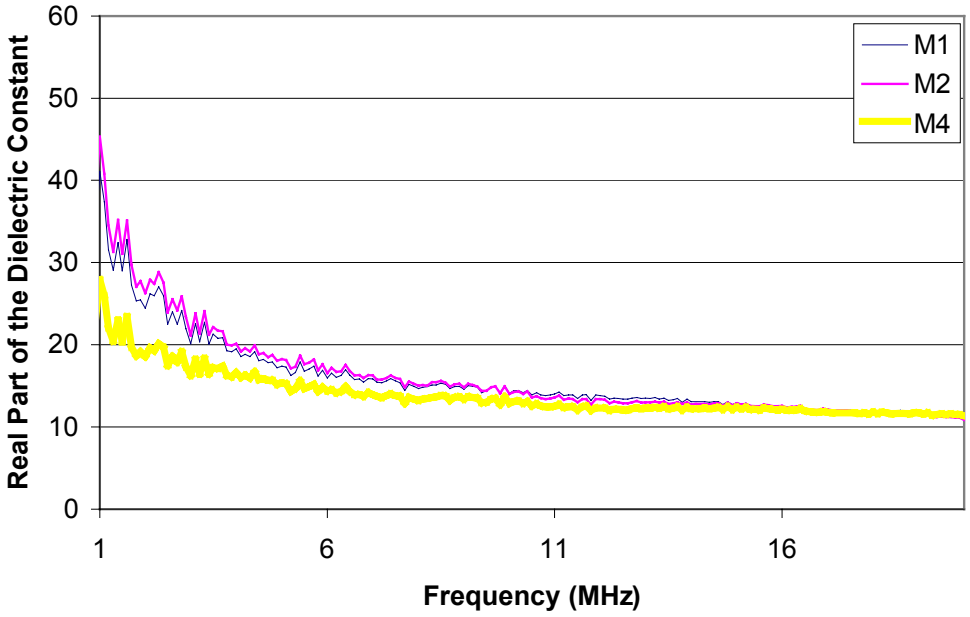

Figure 4.23. Effect of PCC mix design on the real part of the dielectric constant

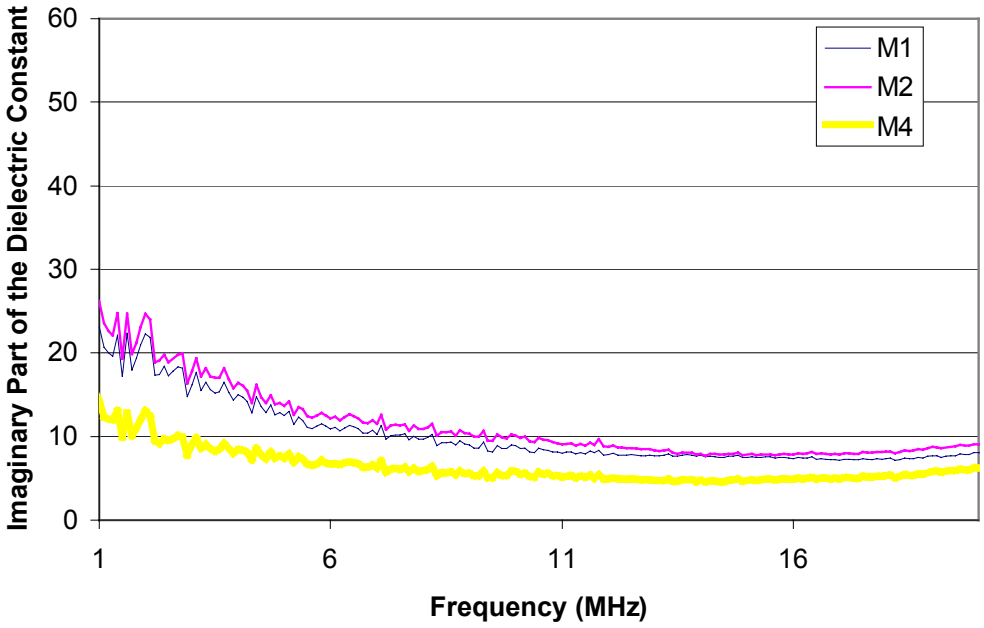

Figure 4.24. Effect of PCC mix design on the imaginary part of the dielectric constant

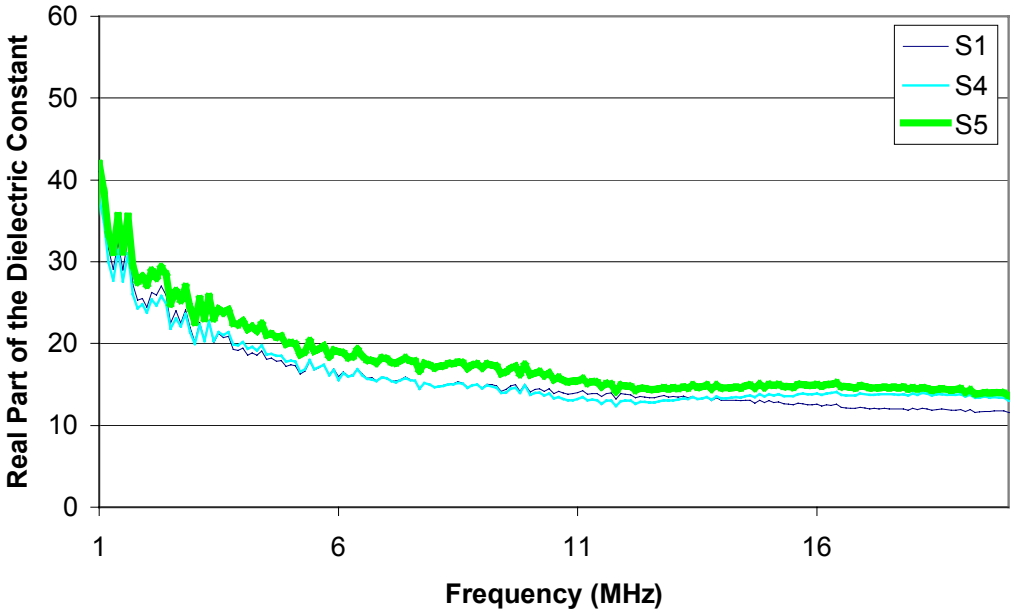

Figure 4.25. Effect of the steel reinforcement on the real part of the dielectric constant

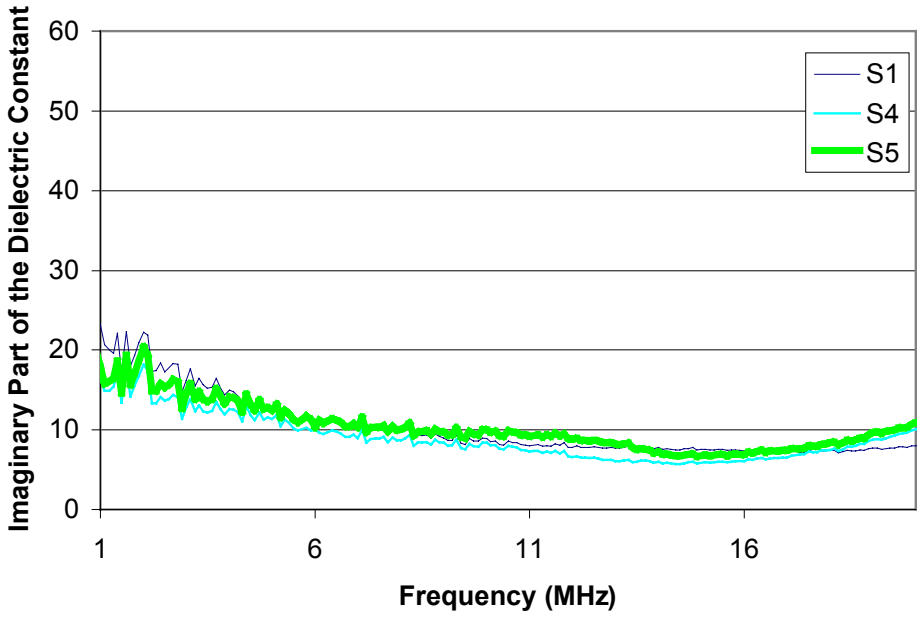

Figure 4.26. Effect of the steel reinforcement on the imaginary part of the dielectric constant

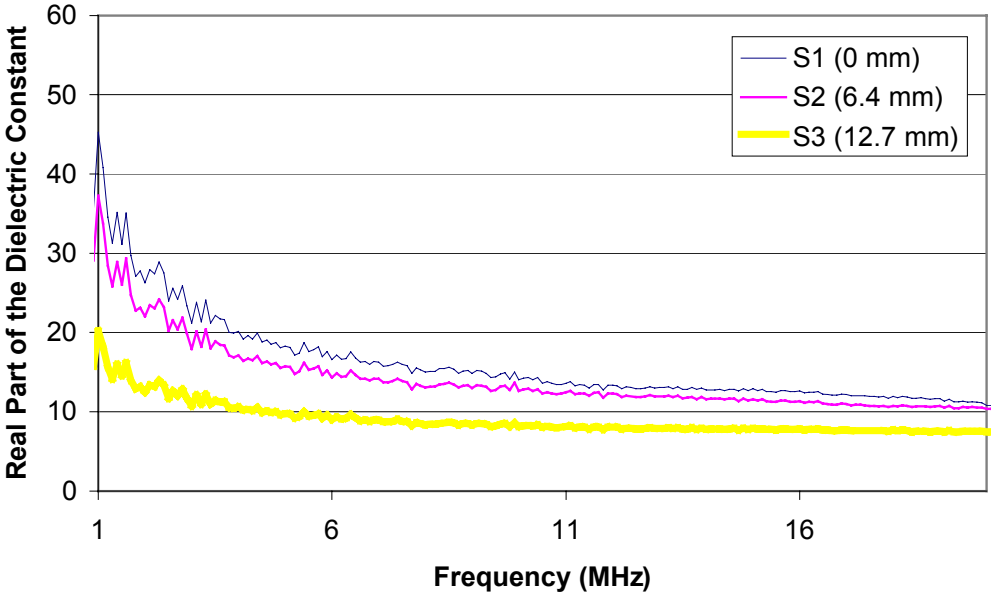

Figure 4.27. Effect of the air void thickness on the real part of the dielectric constant

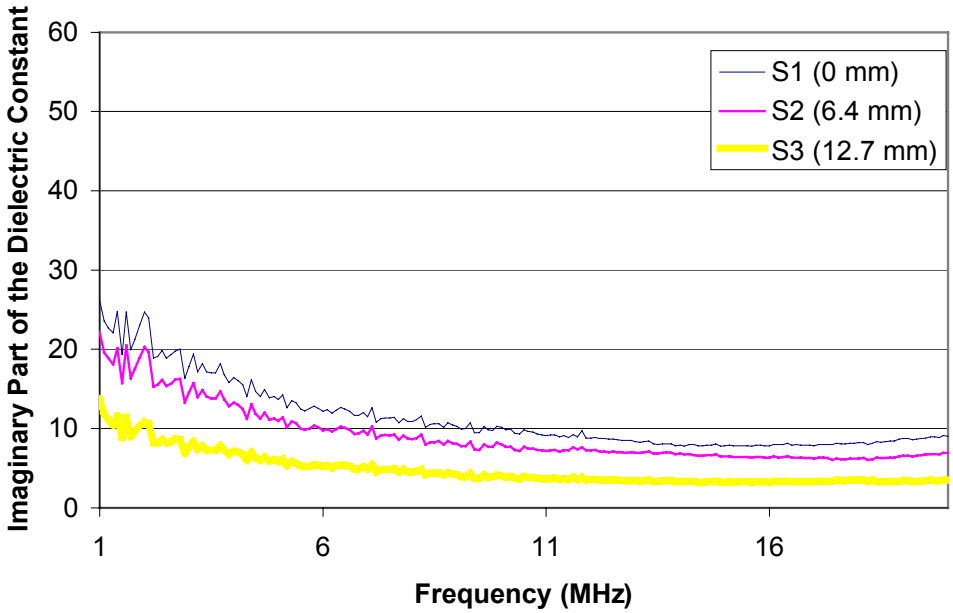

Figure 4.28. Effect of the air void thickness on the imaginary part of the dielectric constant

4.4 Mixture Theory Evaluation

Major theoretical mixture formulas to compute the bulk dielectric constant of PCC (Eps) from its constituents (cement, aggregate, and air content) have been evaluated. The evaluation task has been conducted in three phases. First, an experimental design has been developed to study the effect of the aggregate properties (aggregate volume, particle shape, and particle size) on the computed Eps. In the second phase, a predictive model has been developed to correlate the critical parameters of PCC constituents with its computed Eps. To achieve this, a second experimental design has been developed. The levels of the considered factors for both experimental designs are reported in Table 3.8. The input data (Eps) for these experimental designs have been collected using a computer simulation. Complete output data of the computer simulation for both experimental designs are presented in Appendix D. In the third phase of the evaluation, comparison has been made between several major theoretical mixture formulas and the developed model outputs for the Eps.

ANOVA technique has been conducted on the first experimental design to identify the critical parameters that affect the computed Eps. ANOVA has been conducted in two steps. In the first step, full two-way interaction has been included in the analysis. Next, the insignificant interaction parameters have been removed from the second step. The p-values of the first step are reported in Table 4.10. The results of the first step have shown that there is no sufficient evidence to conclude that the considered interactions significantly affect the response (Eps).

Table 4.10. P-values for the main and the interaction effects

Main and Interaction Effect	P-value
Volume	0.000
Shape	0.183
Gradation	0.821
Volume * Shape	0.802
Volume * Gradation	0.395
Shape * Gradation	0.429
Volume * Shape * Gradation	0.771

In the second step, only the main effects have been included in the model to insure their significance on the computed Eps in the absence of their interactions. Table 4.11 shows the p-values for the second step of ANOVA technique. The results have shown that there is no

sufficient evidence to conclude that the aggregate particle shape or size has a significant effect on the computed Eps.

Table 4.11. P-values for the main effects

Main Effect	P-value
Volume	0.000
Shape	0.162
Gradation	0.812

In the second phase of the mixture theory evaluation, the second experimental design has been analyzed using regression analysis technique. The objective of this phase is to predict a model that correlates Eps with aggregate volume (V), dielectric constant ratio of cement to aggregate (DCR), and the air content (AC). The regression analysis has been conducted in two steps. In the first step, full quadratic terms for all considered parameters have been included in the model. The p-values for all parameters of the first step are reported in Table 4.12. The results of the first step of the regression analysis have indicated that there is no sufficient evidence to conclude that the quadratic term of the AC significantly affects the response (Eps).

Table 4.12. P-values for all parameters considered in the first step

Parameter	P-value
Volume	0.000
DCR	0.000
AC	0.000
Volume*DCR	0.000
Volume*AC	0.000
DCR*AC	0.000
Volume*Volume	0.000
DCR*DCR	0.000
AC*AC	0.870

The insignificant term identified in the first step has then been removed from the model of the second step to insure the significance of the other parameters. The results of this step show that all considered parameters have significant effects to the level of confidence of 5% on the response (Eps). Finally, three predictive models have been developed from the second regression analysis to calculate Eps from the critical parameters (V, DCR, AC) for three aggregate dielectric constant values (4, 6, and 8):

Aggregate dielectric constant = 4:

Eps = 34.7 - 1.06 Volume + 2.94 DCR - 0.360 AC - 0.0310 V*DCR + 0.00530 V*AC

- 0.0295 AC*DCR + 0.00893 V**2 - 0.0102 DCR**2

Aggregate dielectric constant = 6:

Eps = 58.4 - 1.80 Volume + 4.42 DCR - 0.570 AC - 0.0466 V*DCR + 0.00823 V*AC

- 0.0442 AC*DCR + 0.0152 V**2 - 0.0156 DCR**2

Aggregate dielectric constant = 8:

Eps = 82.2 - 2.55 Volume + 5.90 DCR - 0.781 AC - 0.0621 V*DCR + 0.0112 V*AC

- 0.0588 AC*DCR + 0.0214 V**2 - 0.0210 DCR**2

Predicted bulk dielectric constant of PCC based on the three models for typical dielectric constant values of the PCC composition materials are presented in Table 4.13.

Table 4.13 Predicted bulk dielectric constant of PCC based on three typical dielectric constant value of aggregate (4, 6, and 8)

AC (%)	DCR	Dielectric Constant of Aggregate								
		4			6			8		
		Aggregate Volume (%)			Aggregate Volume (%)			Aggregate Volume (%)		
		55	60	65	55	60	65	55	60	65
0	2.5	2.5	6.34	5.77	5.65	9.52	8.62	8.49	12.70	11.48
	5	5	9.24	8.28	7.77	13.87	12.39	11.67	18.51	16.50
	7.5	7.5	12.00	10.66	9.76	18.02	15.96	14.66	24.05	21.27
	10	10	14.64	12.91	11.63	21.98	19.34	17.46	29.32	25.77
2	2.5	2.5	6.06	5.54	5.47	9.06	8.25	8.20	12.07	10.96
	5	5	8.80	7.90	7.45	13.19	11.80	11.16	17.58	15.69
	7.5	7.5	11.42	10.13	9.29	17.13	15.15	13.93	22.83	20.16
	10	10	13.92	12.24	11.01	20.86	18.30	16.50	27.81	24.37
4	2.5	2.5	5.77	5.31	5.30	8.61	7.88	7.90	11.45	10.44
	5	5	8.37	7.52	7.12	12.52	11.20	10.65	16.66	14.88
	7.5	7.5	10.84	9.61	8.82	16.23	14.33	13.19	21.61	19.06
	10	10	13.19	11.56	10.39	19.75	17.27	15.55	26.30	22.97
6	2.5	2.5	5.49	5.08	5.12	8.15	7.50	7.61	10.82	9.93
	5	5	7.94	7.14	6.79	11.84	10.61	10.14	15.74	14.07
	7.5	7.5	10.27	9.08	8.34	15.33	13.52	12.46	20.40	17.95
	10	10	12.46	10.89	9.77	18.63	16.23	14.59	24.79	21.57

Another general predictive model, which includes the dielectric constant of aggregate as an independent variable, has been developed:

$$Eps = 1.25 + 0.00990 [\varepsilon_{agg} V] + 0.00539 [\varepsilon_{cem} (100 - V - AC)] - 0.0971 [AC] + 0.000003 [\varepsilon_{agg} V] [\varepsilon_{cem} (100 - V - AC)]$$

where,

ε_{agg} = dielectric constant value of aggregate

ε_{cem} = dielectric constant value of cement

Table 4.14 provides a summary of the predicted bulk dielectric constant of PCC based on the dielectric constant values of the PCC composition materials.

Table 4.14 Summary of the predicted bulk dielectric constant of PCC based on the dielectric constant values of the PCC composition materials

AC (%)	Dielectric Constant of Cement	Dielectric Constant of Aggregate								
		4			6			8		
		Aggregate Volume (%)			Aggregate Volume (%)			Aggregate Volume (%)		
		55	60	65	55	60	65	55	60	65
0	10	6.15	6.07	5.98	7.39	7.40	7.41	8.63	8.73	8.83
	20	8.87	8.51	8.14	10.26	9.99	9.70	11.65	11.47	11.26
	30	11.60	10.96	10.30	13.13	12.58	12.00	14.66	14.20	13.70
	40	14.32	13.40	12.46	16.00	15.17	14.30	17.68	16.93	16.13
2	10	5.84	5.75	5.67	7.07	7.08	7.08	8.30	8.40	8.50
	20	8.44	8.08	7.70	9.81	9.54	9.25	11.18	11.00	10.79
	30	11.04	10.40	9.74	12.55	12.00	11.41	14.07	13.59	13.08
	40	13.64	12.72	11.77	15.30	14.45	13.58	16.95	16.19	15.38
4	10	5.52	5.44	5.35	6.74	6.75	6.76	7.97	8.07	8.16
	20	8.00	7.64	7.26	9.36	9.08	8.79	10.72	10.53	10.32
	30	10.48	9.84	9.17	11.98	11.41	10.82	13.47	12.99	12.47
	40	12.96	12.04	11.09	14.59	13.74	12.86	16.22	15.45	14.63
6	10	5.20	5.12	5.03	6.42	6.43	6.43	7.64	7.74	7.83
	20	7.56	7.20	6.82	8.91	8.63	8.33	10.26	10.06	9.85
	30	9.92	9.28	8.61	11.40	10.83	10.24	12.87	12.39	11.86
	40	12.28	11.35	10.40	13.89	13.03	12.14	15.49	14.71	13.88

In the third phase of the evaluation task, comparison has been made between major theoretical mixture formulas, listed in Table 3.7, and the results obtained from the developed model. Complete comparison results for the three considered volumes of aggregate, which has a dielectric constant of 4, are reported in Appendix D. Table 4.15 shows the comparison results for aggregate volume of 60% and dielectric constant of 4. The results of the comparison phase show that the Looyenga theoretical formula (Tinga, 1992) is the most comparable formula to the developed model. In addition, Bottcher has also shown considerable agreements with the developed model output.

Table 4.15. The comparison results for 60% aggregate volume at dielectric constant of 4

AC (%)	Method	Eps (cement) 40		30		20		10	
		Eps	Variation (%)	Eps	Variation (%)	Eps	Variation (%)	Eps	Variation (%)
0	**Predictive Model**	13.03		10.77		8.39		5.88	
	Maxwell	15.45	18.59	12.36	14.72	9.25	10.21	6.09	3.50
	Rayleigh	15.45	18.59	12.36	14.72	9.25	10.21	6.09	3.50
	Wiener	15.45	18.59	12.36	14.72	9.25	10.21	6.09	3.50
	Bruggemann	14.20	9.00	11.60	7.66	8.90	6.04	6.02	2.31
	Bottcher	12.20	-6.36	10.40	-3.47	8.40	0.08	5.95	1.12
	Looyenga	12.49	-4.13	10.58	-1.80	8.47	0.92	5.97	1.46
2	**Predictive Model**	12.35		10.25		8.01		5.65	
	Maxwell	14.31	15.83	11.51	12.32	8.70	8.56	5.83	3.14
	Bottcher	11.25	-8.94	9.80	-4.37	8.00	-0.17	5.75	1.72
	Looyenga	11.73	-5.05	9.98	-2.61	8.05	0.45	5.75	1.72
4	**Predictive Model**	11.68		9.72		7.64		5.42	
	Maxwell	13.19	12.93	10.68	9.86	8.16	6.88	5.58	2.93
	Bottcher	10.50	-10.10	9.20	-5.36	7.55	-1.11	5.52	1.82
	Looyenga	10.99	-5.91	9.41	-3.20	7.64	0.07	5.53	2.01
6	**Predictive Model**	11.01		9.19		7.26		5.19	
	Maxwell	12.09	9.85	9.87	7.34	7.63	5.15	5.33	2.70
	Bottcher	9.70	-11.87	8.60	-6.47	7.15	-1.46	5.35	3.09
	Looyenga	10.29	-6.51	8.86	-3.64	7.25	-0.08	5.31	2.32

ANOVA technique followed by mean comparison has been conducted to study the effect of the considered parameters on the variation of the mixture formulas from the developed model results. The ANOVA and the mean comparison analysis output are reported in Appendix D for aggregate dielectric constant of 4. The analysis has shown that all considered theoretical mixture formulas provide approximately same results when the DCR is equal to 2.5, which reflects the ratio of the dielectric constant between the cement and the aggregate.

5 CHAPTER 5: SUMMARY, FINDINGS, CONCLUSIONS, AND RECOMMENDATIONS

5.1 Summary

The work in this research has been focused on developing a resonable method for measuring the dielectric constant of PCC using the recently developed C-Probe. The results of this research have shown that open, short, and Teflon material (OSM) is the most appropriate calibration method for the C-Probe measurements. In addition, the developed method has been used to validate the C-Probe for field application to detect flaws in PCC. Several C-Probe design configurations have been simulated, in this research, to optimize the penetration depth of EM field in the PCC slab under test. For each desired PCC slab thickness, there is an optimum C-Probe design configuration that is related to the plates' size and the separation between them, as well as the dielectric constant of PCC slab under test. Furthermore, this research has investigated the mixture behavior of PCC and identified the critical mix parameters that affect the bulk dielectric constant of PCC. Finally, several major theoretical mixture formulas, previously developed, have been correlated to a model developed to predict the bulk dielectric constant of PCC based on its constituents.

5.2 Findings

During this research study, the following findings were obtained:

- OSM (open, short, and Teflon material) has been proven to be the most appropriate calibration method for measuring the dielectric constant of PCC using the C-Probe.
- The C-Probe has been shown to have a significant capability for detecting PCC flaws such as delamination that occurs underneath the surface.
- For each desired EM field penetration, there is an optimum design configuration that maximizes the interaction of the EM field with the PCC under test.
- Aggregate volume and air content are significant parameters that affect the bulk dielectric constant of PCC while the effects of aggregate shape and size have been shown to be insignificant.

5.3 Conclusions

Based on this research, the followings can be concluded:

- A reliable calibration method has been developed for the C-Probe measurements.
- Optimum design configurations have been obtained for different desired PCC slab thicknesses.
- A predictive model has been developed to correlate the bulk dielectric constant of PCC with its critical mix parameters.
- The predicted bulk dielectric constant correlates with that obtained by the Looyenga theoretical mixture formula (Tinga, 1992).

5.4 Recommendations

Based on the results of the research, the following recommendations are offered for further investigation:

- Since the C-Probe has shown a significant capability to detect one type of PCC deterioration such as delamination, the C-Probe ability to detect other types of PCC deterioration, such as the chloride content in PCC, may be studied.
- The development and testing of more design configurations of the C-Probe are recommended for future research.
- Development of three dimensional simulation techniques is recommended to extend the understanding of PCC constituents on its measured bulk dielectric constant.

REFERENCES

Aavik, J. and S. Chandra, “Influence of Organic Admixtures and Testing Method of Freeze Thaw Resistance of Concrete,” *ACI Materials Journal*, Vol. 92, No. 1, Jan/Feb 1995, pp.10-14.

Abou-Zeid, M. N., J. B. Wojakowski, and S. A. Cross, “High Dosage Type-C Fly Ash and Limestone in Sand Gravel Concrete,” *Transportation Research Record*, No. 1532, Sept 1996, Washington, DC, pp. 36-43.

Al-Qadi, I. L. and S. M. Riad, Characterization of Portland Cement Concrete: Electromagnetic and Ultrasonic Measurement Techniques, Report Submitted to National Science Foundation Grant No. MSS-9212318, Department of Civil Engineering, Virginia Polytechnic institute and State University, Blacksburg, VA, 1996.

Al-Qadi, I. L., S. M. Riad, B. K. Diefenderfer, and A. Loulizi, Capacitor Probe: Development of an In-Situ System to Measure Concrete Dielectric Properties and Detect Internal Flaws, Final Report to the US Air Force, The Via Department of Civil Engineering, Virginia Tech, Blacksburg, VA, Apr 1998, 93 p.

Al-Qadi, I. L., O. A. Hazim, W. Su, N. Al-Akhras, and S. M. Riad, “Variation of Dielectric Properties of Portland Cement Concrete During Curing Time over Low RF Frequencies,” Paper No. 940479, *Transportation Research Board 73rd Annual Meetin*g, Jan, 1994 Washington, DC.

Al-Qadi, I. L., R. H. Haddad, and S. M. Riad, “Detection of Chlorides in Concrete Using Low Radio Frequencies,” *Journal of Materials in Civil Engineering*, ASCE, Vol. 9, No. 1, Feb, 1997, pp. 29-34.

Al-Qadi, I. L., A. Loulizi, and S. Lahouar, "GPR Calibration at the Virginia Smart Road," GPR 2000, *Proceedings of the 8th International Conference on Ground Penetrating Radar*, D. A. Noon, G. F. Stickley, and D. Longstaff, Eds., SPIE Vol. 4084, Gold Cost, Queensland, Australia, May 23-26, 2000, pp.176-181.

Al-Qadi, I. L., A. Loulizi, and S. Lahouar, "Using Ground Penetrating Radar to Evaluate Pavement Structures," *Non-Destructive Testing in Civil Engineering 2000*, T. Uomoto, Ed., Tokyo, Japan, April 25-27, 2000, pp. 499-508.

ASCE, “1998 Report Card for America’s Infrastructure,” American Society for Civil Engineers, Washington D.C., 1998.

Balanis, C. A., *Advanced Engineering Electromagnetic.* John Wiley & Sons, New York, NY, 1989

Bois, K. J., A. Benally, P. S. Nowak, and R. Zoughi, “Microwave Nondestructive Determination of Sand to Cement Ratio in Mortar,” *Research in Nondestructive Evaluation*, Vol. 9, No. 4, 1997, pp. 227-238.

Bolton, R., N. Stubbs, S. Park, S. Choi, and C. Sikorsky, “Measuring Bridge Modal Parameters for Use in Non Destructive Damage Detection and Performance Algorithms,” *Proceedings of the International Modal Analysis Conference IMAC*, Vol. 2, SEM, Bethel, CT, USA, 1999, pp.1269-1275.

Cady, P. D. and R. E. Weyers, ”Predicting Service Life of Concrete Bridge Decks Subject to Reinforcement Corrosion,” *Symposium on Corrosion Forms and Control for Infrastructure*, ASTM Special Technical Publication, No. 1137, ASTM, Philadelphia, PA, 1992, pp. 328-338.

Cattin, V., J. J. Chaillout, and R. Blanpain, “Detection and Localization With a Step Frequency Radar,” IEEE Conference Publication, No. 458, IEEE, Stevenage, UK, 1998, pp. 86-90.

Chen, R.H. L., U. Halabe, L. Pei, and M. Allu, “Experimental Evaluation of Concrete Bridge Decks and Pavements Using Ground Penetrating Radar,” Building to Last Structures Congress Proceedings, Vol. 2, ASCE, New York, NY, 1997, pp. 1508-1512.

Diefenderfer, B. K., “Development and Testing of a Capacitor Probe to Detect Deterioration in Portland Cement Concrete,” Thesis Submitted to the Civil and Environmental Engineering Department at Virginia Polytechnic institute and State University, Blacksburg, VA Sept 1998.

Diefenderfer, B. K., I. L. Al-Qadi, J. J. Yoho.; S. M. Riad, and A. Loulizi, “Development of a Capacitor Probe to Detect Subsurface Deterioration in Concrete,” Nondestructive Characterization of Materials in Aging Systems Materials Research Society Symposium Proceedings, Vol. 503, MRS, Warrendale, PA, USA, 1998, pp. 231-236.

Fisk, P. S., “Nondestructive Assessment of Unknown Bridge Condition,” *International Water Resources Engineering Conference Proceedings*, Vol. 1, ASCE, Reston, VA, 1998, pp. 127-132.

Gillott, J. E. and J. A. Soles,“Petrography of Concrete Cores from New Brunswick, Relating to the Durability Problem,” *Cement and Concrete Composites*, Vol. 15, No. 1-2, 1993, pp. 101-114.

Gu, P. and J. J. Beaudoin, “Dielectric Behaviour of Hardened Cement Paste Systems,” *Journal of Materials Science Letters*, Vol.15, No. 2, Jan 15, 1996, pp. 182-184.

Haddad, R. H and I. L. Al-Qadi, “Measuring Dielectric Properties of Concrete over Low RF,” *Materials for the New Millennium Proceedings of the Materials Engineering Conference*, Vol. 2, ASCE, New York, NY, USA, 1996, pp.1139-1149.

Haddad, R. H. and I. L. Al-Qadi, “Characterization of Portland Cement Concrete Using Electromagnetic Waves over the Microwave Frequencies,” *Cement and Concrete Research*, Vol.28, No. 10, Oct, 1998, pp.1379-1391.

Halabe, U. B., D. R. Martinelli, and S. H. Petro, “Enhancing Quality Control in Transportation Construction through Nondestructive Testing,” Proceedings of SPIE the International Society for Optical Engineering, Vol. 3585, Mar 3-5, 1999, pp. 190-196.

Heralds, S. E., M. Henry, I. L. Al-Qadi, R. E. Weyers, M. A. Feeney, Condition Evaluation of Concrete Bridges Relative to Reinforcement Corrosion, Vol. 6, Method for Field Determination of Total Chloride Content, Final Report, Department of Civil Engineering, Virginia Polytechnic Institute and State University, Blacksburg, VA, 1992.

Hori, M. and H. Morihiro, “Micromechanical Analysis of Deterioration Due to Freezing and Thawing in Porous Brittle Materials,” *International Journal of Engineering Science*, Vol. 36, No. 4, March, 1998, pp. 511-522.

HP Test and Measurement Catalog, Santa Clara, CA, 1995, pp.339.

Hudson, W. R., R. Haas, and W. Uddin, *Infrastructure Management: Design*, *Construction, Maintenance, Rehabilitation, Renovation*, McGraw Hill, NY, NY, 1997.

Huston, D. R., J. Q. Hu, K. Maser, W. Weedon, and C. Adam, “Ground Penetrating Radar for Concrete Bridge Health Monitoring Applications,” *Proceedings of SPIE the International Society for Optical Engineering*, Vol. 3587, Mar 3-5, 1999, pp. 170-179.

Jastrzebski, Z. D., *The Nature and Properties of Engineering Materials*, Second Edition, SI Version, John Willey and Sons, New York, NY, 1977.

Johnston, C. D.,"Deicer Salt Scaling Resistance and Chloride Permeability," *Concrete International: Design and Construction*, Vol.16, No. 8, Aug, 1994, pp. 48-55.

Kurtis, K.E., Monteiro, P. J. M., J. T. Brown, and I. W. Meyer, "Expansive Reactions in Concrete Observed by Soft X-Ray Transmission Microscopy," *Applications of Synchrotron Radiation Techniques to Materials Science IV Materials Research Society Symposium Proceeding*, Vol. 524, MRS, Warrendale, PA, 1998, pp. 3-9.

Lauer, K. R., " Magnetic/ Electrical Methods," Malhotra, V.M and N.J. Carino, *CRC handbook on Nondistructive Testing of Concrete*, CRC Press, Boca Raton, FL, 1991.

Loulizi, A., " The Use of Ground Penetrating Radar to Asses Transportation Infrastructure", A proposal submitted to the Faculty of the Virginia Polytechnic Institute and State University in partial fulfillment of the requirements for the degree of Doctor of Philosophy in Civil and Environmental Engineering, March, 1999.

Mallinson, P., "Surface Penetrating Radar As An NDT tool," *Insight: Non Destructive Testing and Condition Monitoring*, Vol.39, No. 12, Dec, 1997, 874-877.

Mamlouk, M. S. and J. P. Zaniewski, *Materials of Civil and Construction Engineers*. Addison Wesley Longman, Inc, 1999.

Maser, K. R. "Condition Assessment of Transportation Infrastructure Using Ground-Penetrating Radar," *Journal of Infrastructure Systems*, ASCE, Vol. 2, No. 2, Jun, 1996, pp. 94-101.

Maso, J. C. *Proceedings of the Seventh International Congress on the Chemistry of Cements*, Vol. 1, Editions Septima, Paris, France, 1980.

McCarter, W. J., "A.C. Impedance Response of Concrete During Early Hydration," *Journal of Materials Science*, Vol. 31, No. 23, Dec. 1, 1996, pp. 6285-6292.

McCarter, W. J., "Parametric Study of the Impedance Characteristics of Cement- Aggregate Systems During Early Hydration," *Cement and Concrete Research*, ACI, Vol. 24, No. 6, 1994, pp. 1097-1110.

Mehta, P. K, and P. J. Monteiro, *Concrete Structure, Properties, and Materials.* 2nd ed. Prentice Hall, Englewood Cliff, NJ, 1993

National Science Foundation, *Civil Infrastructure Systems An integrated Research Program*. Washington, DC, 1995.

Power, T. C., "The Physical Structure and Engineering Properties of Concrete," *Bulletin 90, Portland Cement Association*, Skokie IL, 1958.

Prowell B. D., R. E. Weyers, and I. L. Al-Qadi, "Concrete Bridge Protection and Rehabilitation: Chemical and Physical Techniques: Field Validation," *Strategic Highway Research Program*, Washington, DC, Jun, 1993.

Schwartz, D., R., "D-Cracking of Concrete Pavements," *National Cooperation Highway Research Program Synth Highway Practice*, No. 134, Washington, DC, Oct, 1987.

Shaw, M. R., "Permittivity and Conductivity of Concretes at Ground Penetrating Radar Frequencies," *Advances in Cement Research*, Vol. 10, No. 4, Oct 1998, pp. 187-194.

Shaw, P., and A. Xu, “Pulse-Echo Methods in Inspection of Concrete Structures,” *Insight Non-DestructiveTesting and Condition Monitoring*, Vol. 39, No. 3, Mar 1997, pp. 180-185.

Starrs-G and W. J. McCarter, “Immittance Response of Cementitious Binders During Early Hydration,” *Advances in Cement Research*, Vol. 10, No. 4, Oct 1998, pp.179-186.

Stubbs, N., C. Sikorsky, S. Park, S. Choi, and R. Bolton, “Methodology to Nondestructively Evaluate the Structural Properties of Bridges,” *Proceedings of the International Modal Analysis Conference IMAC*, Vol. 2, SEM, Bethel, CT, 1999, pp. 1260-1268.

Subramaniam, K. V., G. Goldstein, J. S. Popovits, and S. P. Shah, “Monitoring Crack Length in Concrete Beams Using Resonance Measurements,” *Proceedings of SPIE the International Society for Optical Engineering*, Vol. 3586, 1999, pp. 129-136.

Swamy, R. N. and M. M. Al-Asali, “Engineering Properties of Concrete Affected by Alkali-Silica Reaction,” *ACI Materials Journal*, Vol. 85, No. 5, Sep 108, 1988, pp.367-374.

Thompson, N. G., D. Lankard, and M. Sprinkel, “Improved Grouts for Bonded Tendons in Post-Tensioned Bridge Structures,” Final Report Submitted to Federal Highway Administration, McLean, VA, Office of Engineering and Highway Operations Research and Development, 1992.

Tinga, W. R., “Mixture Laws and Microwave-Material Interactions,” Priou, A., *PIER 6 Progress in Electromagnetic Research*, “*Dielectric Properties of Hetrogeneous Materials*”, Elserier, New York, NY, 1992.

Van, D. T. and E. Aldrich, “Prevention of Materials-Related Distress in Concrete Pavements in Cold Regions,” *Proceedings of the International Conference on Cold Regions Engineering*, ASCE, Reston, VA, 1998, pp.489-500.

Virmani, Y. P. and G. G. Clemena, Corrosion Protection: Concrete Bridges, Final Report, Federal Highway Administration, McLean, VA.,Office of Engineering Research and Development, 1998.

Wooh, S. C. and L. Azar, “American Concrete Institute Improved Near Field Characteristics of Phased Arrays for Assessing Concrete and Cementitious Materials,” *Proceedings of SPIE the International Society for Optical Engineering*, Vol. 3586, 1999, 165-175.

Young, J. F., S. Mindess, R. J. Gray, and A. Bentur, *The Science and Technology of Civil Engineering Materials*. Prentice Hall, Upper Saddle River, NJ, 1998.

APPENDIX A: C-PROBE CALIBRATION DATA

C-Meter Measurements

Teflon

Extruded nylon

Portland cement concrete specimen

Calibration Methods

Scattering-Parameter Form

Open-Short-Load-Load (OSLL)

Open-Short-Load (OSLF)

Bilinear Transformation Form

Open and two Materials (OMM)

Short and two Materials (SMM)

Open-Short-Material (OSM)

A.1 C-Meter Measurements Data

Table A.1. C-Meter measurements data for Teflon

Freq. (MHz)	*C* (*pF*)	Eps' (*w/* Fringing)	Eps'	Fringing Effect (%)
0.10	1.43	2.21	2.1	5
0.50	1.43	2.21	2.1	5
1.00	1.44	2.23	2.1	6
2.00	1.44	2.23	2.1	6
5.00	1.43	2.21	2.1	5

Table A.2. C-Meter measurements data for extruded nylon

Fringing Orientation Freq. (MHz)	w/ Fringing 1 Real	2 Real	Fringing Effect *F* 0.05	w/o Fringing 1 Real	2 Real
0.10	3.66	3.43	0.05	3.48	3.27
0.50	3.59	3.38	0.05	3.42	3.22
1.00	3.56	3.36	0.05	3.39	3.20
2.00	3.54	3.34	0.05	3.37	3.18
5.00	3.49	3.30	0.05	3.32	3.14

*Orientation 1 and 2 are perpendicular

Table A.3. C-Meter measurements for PCC specimens without fringing effect

Sample	A1 (75x75x100 mm)		C1 (75x75x100 mm)		C1 (300x450x100 mm)	
Freq. (MHz)	Real	Imaginary	Real	Imaginary	Real	Imaginary
0.10	16.11	11.26	13.74	8.60	26.35	16.86
0.50	11.86	4.28	10.27	3.39	15.53	7.88
1.00	10.77	2.97	9.38	2.77	13.18	5.48
2.00	9.94	2.13	8.69	1.72	11.58	3.86
3.00	9.55	1.74	8.37	1.41	10.96	3.11
4.00	-	-	8.17	1.23	10.56	2.73
5.00	9.14	1.36	8.03	1.11	10.30	2.45
6.00	-	-	7.90	1.00	10.03	2.11
7.00	-	-	7.79	0.91	10.43	1.50
8.00	-	-	7.67	0.75	10.74	2.00
9.00	-	-	7.97	0.54	11.29	2.25
10.00	8.94	0.95	7.88	0.76	10.43	2.10

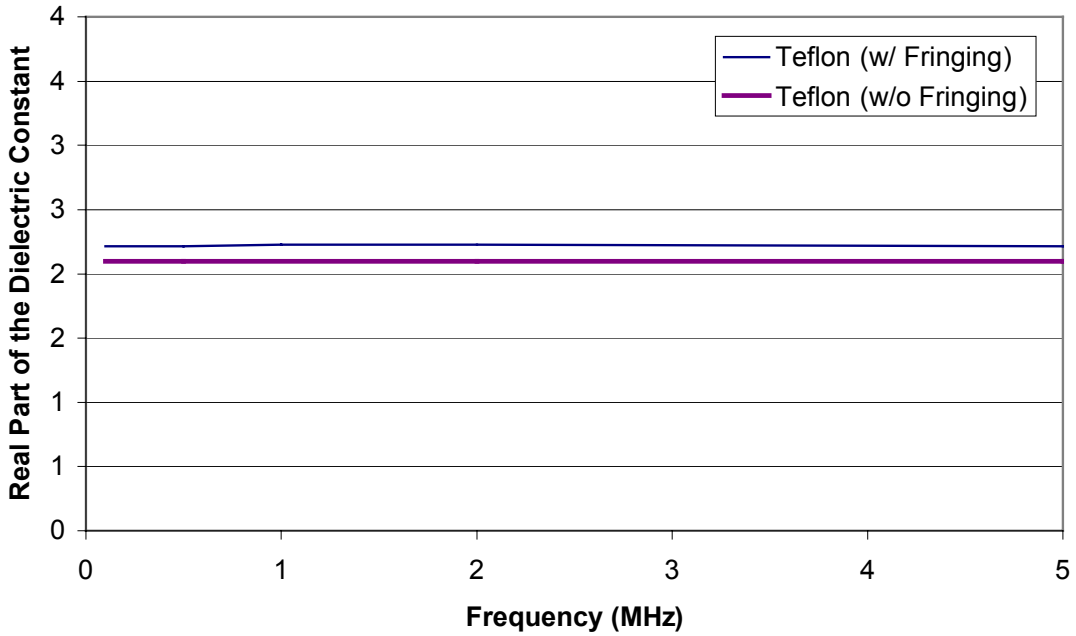

Figure A.1. Fringing effect of the C-Meter measurements for Teflon material

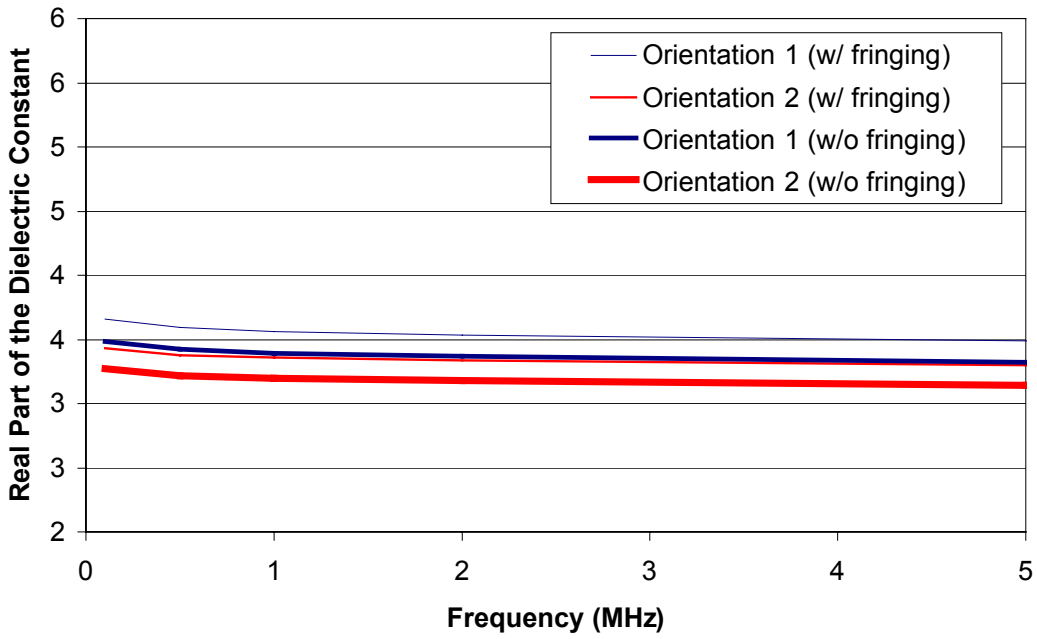

Figure A.2. C-Meter measurements for the extruded nylon with and without the fringing effect

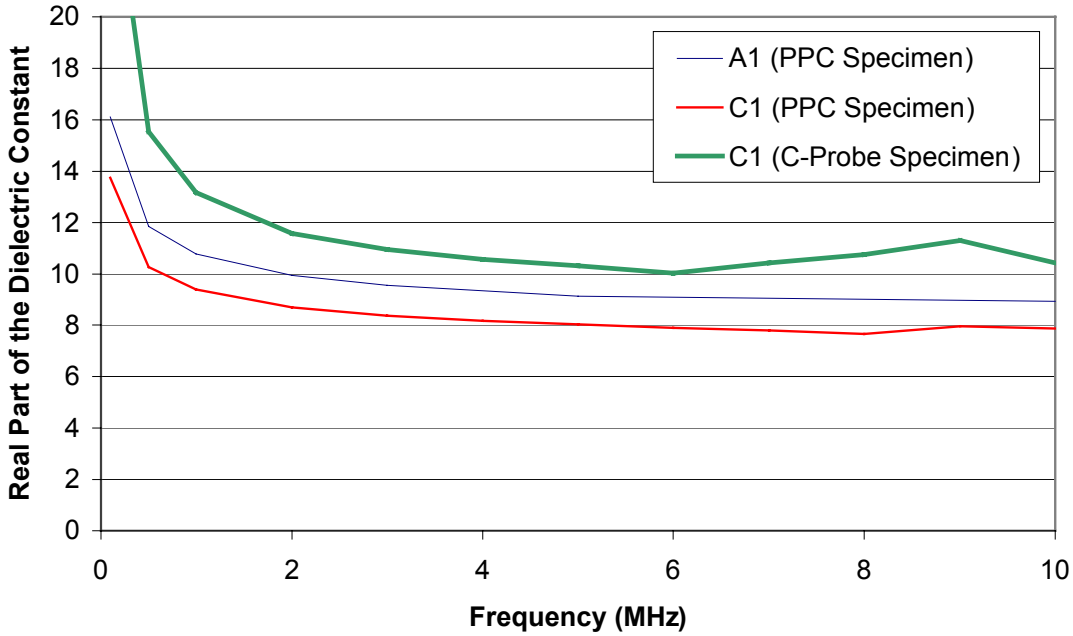

Figure A.3. C-Meter measurements for the real part of the dielectric constant of PCC specimen

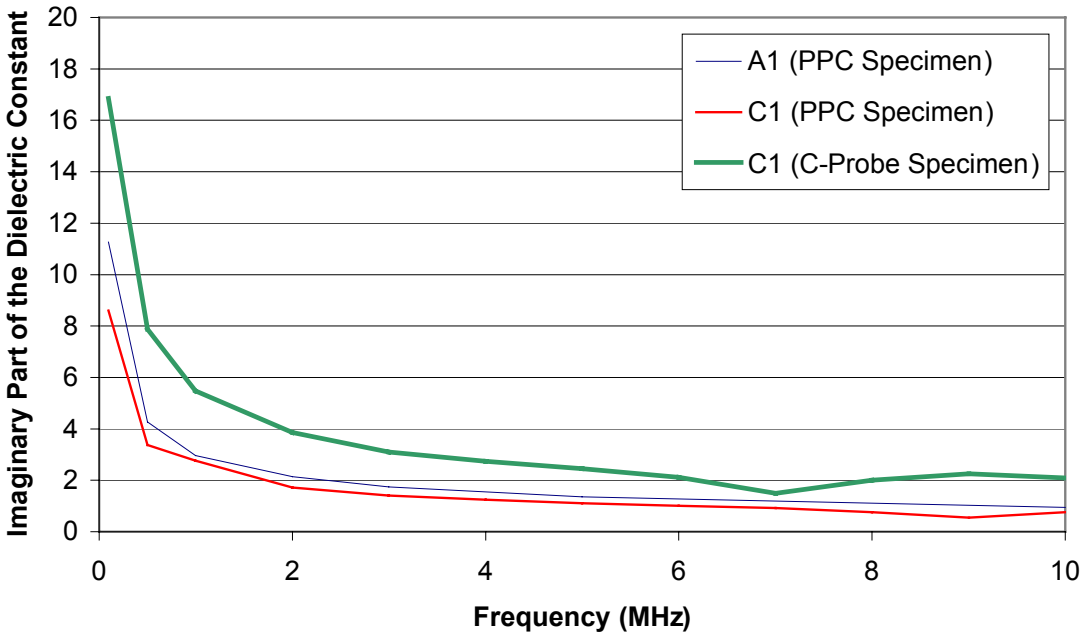

Figure A.4. C-Meter measurements for the imaginary part of the dielectric constant of PCC specimen

Open-Short-Load-Load (OSLL)

Table A.4. Governing equations of OSLL calibration scheme

Calibration	Reflection Coefficient (Γ_m)
Open	$\Gamma_{mop} = S_{11} + \frac{S_p \Gamma_{op}}{1 - S_{22}\Gamma_{op}}$
Short	$\Gamma_{ms} = S_{11} - \frac{S_p}{1 + S_{22}}$
Load	$\Gamma_{ml} = S_{11}$
Resistor	$\Gamma_{mR} = S_p + \frac{S_p \Gamma_R}{1 - S_{22}\Gamma_R}$

Table A.5. S-Parameters solutions for OSLL calibration scheme

Unknown S	Solution
S_{11}	Γ_{ml}
S_{22}	$(1- A\, \Gamma_R) / [(1 + A)\, \Gamma_R]$
S_p	$(\Gamma_{ml} - \Gamma_{ms})\, (1 + S_{22})$

where,

$S_p = S_{21}S_{12}$

$$\Gamma_R = \frac{Y_o - Y_R}{Y_o + Y_R}$$

$Y_R = Y_{R2} - Y_{err}$

$$Y_{R2} = \frac{1}{R_2} + j\,\omega C_2$$

$R_2 = 151$

C_2 = + 71 e-12

$Y_{err} = Y_L - Y_o$

Y_o = 1 / 50

$$Y_L = G_L + j\omega C_L$$

C_L = 71 *p*F (measured)

G_L= 1 / R_L

R_L = 51 Ω (measured)

$j = \sqrt{-1}$;

ω = 2π *f*

f = frequency (Hz)

$$A = \frac{\Gamma_{ml} - \Gamma_{ms}}{\Gamma_{mR} - \Gamma_{ml}}$$

The F value using the open reflection coefficient equation is determined as follows:

$$\Gamma_{op} = \frac{\Gamma_{mop} - S_{11}}{S_p + S_{22}(\Gamma_{mop} - S_{11})}$$

$$\Gamma_{op} = \frac{Y_o - Y_{op}}{Y_o + Y_{op}}$$

$$Y_{op} = Y_o \frac{1 - \Gamma_{op}}{1 + \Gamma_{op}}$$

$Y_a = Y_{op} + Y_{err}$

$$Y_a = j\omega\varepsilon_0 \mathrm{F}$$

$$F = \frac{Y_a}{j\omega\varepsilon_0}$$

The permittivity of the unknown material is determined as follows:

$$\Gamma_{um} = \frac{\Gamma_{mum} - S_{11}}{S_p - S_{11}S_{22} + S_{22}\Gamma_{mum}}$$

$$Y_{um} = Y_o \ \frac{1 - \Gamma_{um}}{1 + \Gamma_{um}}$$

$$\varepsilon_r = \frac{Y_{um} + Y_{err}}{j\omega\varepsilon_0 \mathrm{F}}$$

MatLab program code for calculating and drawing the dielectric constant measurements using OSLL calibration scheme

```
%%%%%%%%%%%%%%%%%%%%%%%%%%%%%%%%%%%%%%%%%%%%%%%%%%%%%%%%%%
% Capacitor Probe:
% OSLL Calibration Scheme
%%%%%%%%%%%%%%%%%%%%%%%%%%%%%%%%%%%%%%%%%%%%%%%%%%%%%%%%%%
clear all;
umaterial='C1ss1'; % <--------------------
%%%%%%%%%%%%%%%%%%%%%%%%%%%%%%%%%%%%%%%%%%%%%%%%%%%%%%%%%%
%network analyzer inforamation
%%%%%%%%%%%%%%%%%%%%%%%%%%%%%%%%%%%%%%%%%%%%%%%%%%%%%%%%%%
nOfMeasurments=401;%%<----------------------
freq=100e3:100e3:40.1e6;
omega=2*pi*freq;
%%%%%%%%%%%%%%%%%%%%%%%%%%%%%%%%%%%%%%%%%%%%%%%%%%%%%%%%%%
% Reading data files
%%%%%%%%%%%%%%%%%%%%%%%%%%%%%%%%%%%%%%%%%%%%%%%%%%%%%%%%%%
OpenFileName=strcat('data\open');
ShortFileName=strcat('data\short');
Load1FileName=strcat('data\load51');
Load2FileName=strcat('data\load150');
uMatFileName=strcat('data\',umaterial);
Zop=readata(OpenFileName, nOfMeasurments);
Zs=readata(ShortFileName, nOfMeasurments);
Zl1=readata(Load1FileName, nOfMeasurments);
Zl2=readata(Load2FileName, nOfMeasurments);
Zum=readata(uMatFileName, nOfMeasurments);
%%%%%%%%%%%%%%%%%%%%%%%%%%%%%%%%%%%%%%%%%%%%%%%%%%%%%%%%%%
% Constant Parameters
%%%%%%%%%%%%%%%%%%%%%%%%%%%%%%%%%%%%%%%%%%%%%%%%%%%%%%%%%%
Zo=50;
Yo=1/Zo;
%%%%%%%%%%%%%%%%%%%%%%%%%%%%%%%%%%%%%%%%%%%%%%%%%%%%%%%%%%
% Calculating Measured Reflection Coefficients
%%%%%%%%%%%%%%%%%%%%%%%%%%%%%%%%%%%%%%%%%%%%%%%%%%%%%%%%%%
```

```
Gmop=(Zop-Zo)./(Zop+Zo);
Gms=(Zs-Zo)./(Zs+Zo);
Gml1=(Zl1-Zo)./(Zl1+Zo);
Gml2=(Zl2-Zo)./(Zl2+Zo);
Gmum=(Zum-Zo)./(Zum+Zo);
%%%%%%%%%%%%%%%%%%%%%%%%%%%%%%%%%%%%%%%%%%%%%%%%%%%%%%%%%%%%%%%%
% Calculating S-Parameters
%%%%%%%%%%%%%%%%%%%%%%%%%%%%%%%%%%%%%%%%%%%%%%%%%%%%%%%%%%%%%%%%
R1=51;
L1=82e-9;
C1=71e-12; %-0.1e-12;
YL1=1./(R1+1j*omega*L1)+1j*omega*C1;
Yerr=YL1-Yo;
R2=151;
L2=82e-9;
C2=71e-12; % -0.1e-12;
YL2=1./(R2+1j*omega*L2)+1j*omega*C2;
%GL2=(Yo-YL2+Yerr)./(Yo+YL2-Yerr);
S11=Gml1;
A=(Gml1-Gms)./(Gml2-Gml1);
S22=(1-A.*Gml2)./(Gml2.*(1+A));
Sp=(Gml1-Gms).*(1+S22);
%%%%%%%%%%%%%%%%%%%%%%%%%%%%%%%%%%%%%%%%%%%%%%%%%%%%%%%%%%%%%%%%
% Calculating Eps. for the material under test (MUT) from the S-Parameters
%%%%%%%%%%%%%%%%%%%%%%%%%%%%%%%%%%%%%%%%%%%%%%%%%%%%%%%%%%%%%%%%
Epso=8.854e-12;
Gop=(Gmop-S11)./(Sp+S22.*(Gmop-S11));
Yop=Yo*(1-Gop)./(1+Gop);
Yact=Yop+Yerr;
F=Yact./(1j*omega*Epso);
Gum=(Gmum-S11)./(Sp+S22.*(Gmum-S11));
Yum=Yo*(1-Gum)./(1+Gum);
Yumact=Yum+Yerr;
Epsum=Yumact./(1j*omega.*F*Epso);
EpsRe=real(Epsum);
```

```
EspIm=-imag(Epsum);
%%%%%%%%%%%%%%%%%%%%%%%%%%%%%%%%%%%%%%%%%%%%%%%%%%%%%%%%%%%%%%%%
% Drawing the real and the imaginary part of Eps. of MUT
%%%%%%%%%%%%%%%%%%%%%%%%%%%%%%%%%%%%%%%%%%%%%%%%%%%%%%%%%%%%%%%%
figure(1);
hold on;
set(1,'Name','Imag(Epsilon)');
plot(freq*1e-6,EspIm,'r');
hold off;
figure(2);
hold on;
set(2,'Name','Real(Epsilon)');
plot(freq*1e-6,EpsRe,'r');
hold off;
%%%%%%%%%%%%%%%%%%%%%%%%%%%%%%%%%%%%%%%%%%%%%%%%%%%%%%%%%%%%%%%%
% Writing the results in an output file
%%%%%%%%%%%%%%%%%%%%%%%%%%%%%%%%%%%%%%%%%%%%%%%%%%%%%%%%%%%%%%%%
fn=strcat('data\',umaterial,'.txt');
fptr=fopen(fn,'wt');
clear length;
for k=1: length(freq)
  fprintf(fptr,'%10.5e %10.5e %10.5e\n',freq(k), EpsRe(k), EspIm(k));
end
fclose(fptr);
%%%%%%%%%%%%%%%%%%%%%%%%%%%%%%%%%%%%%%%%%%%%%%%%%%%%%%%%%%%%%%%%
% End of the program, and have a nice output...
%%%%%%%%%%%%%%%%%%%%%%%%%%%%%%%%%%%%%%%%%%%%%%%%%%%%%%%%%%%%%%%%
```

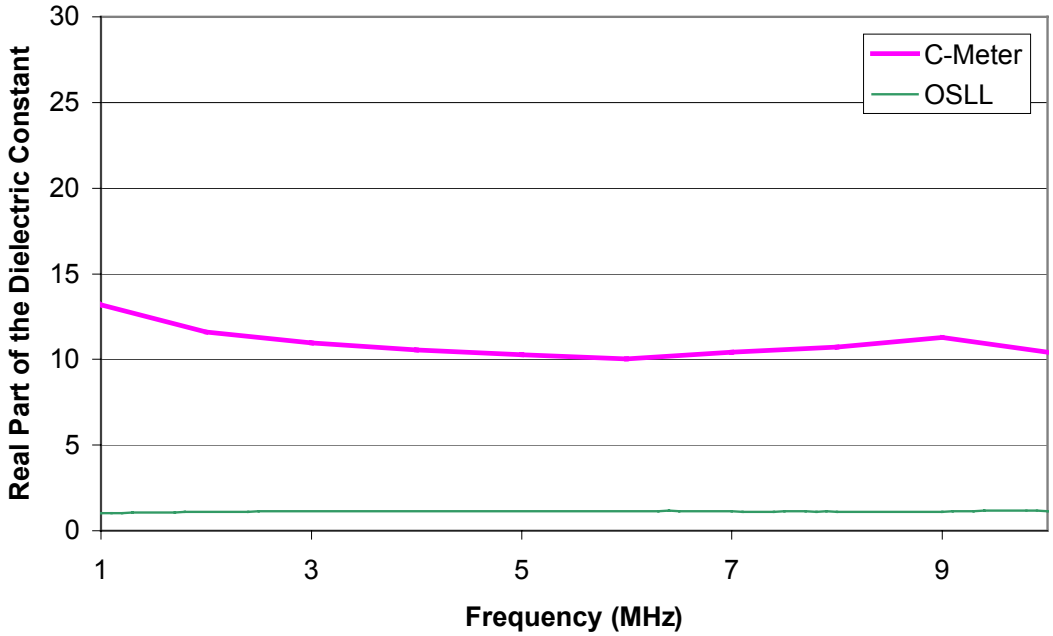

Figure A.4. OSLL vs. C-Meter measurements for the real dielectric constant of C1

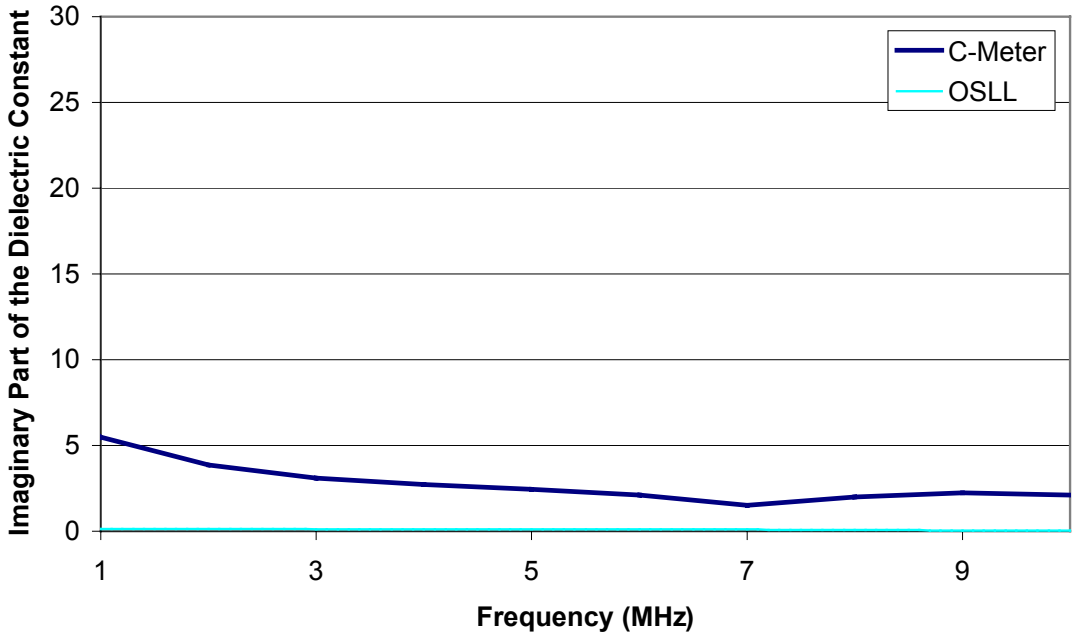

Figure A.5. OSLL vs. C-Meter measurements for the imaginary dielectric constant of C1

Open-Short-Load (OSLF)

Table A.6. Governing equations of OSLF calibration scheme

Calibration	Reflection Coefficient (Γ_m)
Open	$\Gamma_{mop} = S_{11} + \frac{S_p \Gamma_{op}}{1 - S_{22}\Gamma_{op}}$
Short	$\Gamma_{ms} = S_{11} - \frac{S_p}{1 + S_{22}}$
Load	$\Gamma_{ml} = S_{11}$

Table A.7. S-Parameters solutions for OSL calibration scheme

Unknown S	Solution
S_{11}	Γ_{ml}
S_{22}	$(A - \Gamma_{op}) / [(1 + A) \Gamma_{op}]$
S_p	$(\Gamma_{ml} - \Gamma_{ms}) (1 + S_{22})$

where,

$S_p = S_{21}S_{12}$

$$\Gamma_{op} = \frac{Y_o - Y_{op}}{Y_o + Y_{op}}$$

$Y_{op} = Y_a - Y_{err}$

$$Y_a = j\omega\varepsilon_0 F$$

F = 0.118 (measured using Zeland software)

$Y_{err} = Y_L - Y_0$

Y_o = 1 / 50

$$Y_l = G_L + j\omega C_L$$

C_L = + 71 *p*F (measured)

G_L= 1 / R_L

R_L = 51 Ω (measured)

$$A = \frac{\Gamma_{mop} - \Gamma_{ml}}{\Gamma_{ml} - \Gamma_{ms}}$$

The permittivity of the unknown material may be determined as follows:

$$\Gamma_{um} = \frac{\Gamma_{mum} - S_{11}}{S_p - S_{11}S_{22} + S_{22}\Gamma_{mum}}$$

$$Y_{um} = Y_o \frac{1 - \Gamma_{um}}{1 + \Gamma_{um}}$$

$$\varepsilon_r = \frac{Y_{um} + Y_{err}}{j\omega\varepsilon_0 \mathrm{F}}$$

MatLab program code for calculating and drawing the dielectric constant measurements using OSLF calibration scheme

```
%%%%%%%%%%%%%%%%%%%%%%%%%%%%%%%%%%%%%%%%%%%%%%%%
% Capacitor Probe:
% OSLF Calibration Scheme (F=0.118 fron Zeland)
%%%%%%%%%%%%%%%%%%%%%%%%%%%%%%%%%%%%%%%%%%%%%%%%
clear all;
umaterial='C1ss1'; % <--------------------
%%%%%%%%%%%%%%%%%%%%%%%%%%%%%%%%%%%%%%%%%%%%%%%%
%network analyzer inforamation
%%%%%%%%%%%%%%%%%%%%%%%%%%%%%%%%%%%%%%%%%%%%%%%%
nOfMeasurments=401;%%<----------------------
freq=100e3:100e3:40.1e6;
omega=2*pi*freq;
%%%%%%%%%%%%%%%%%%%%%%%%%%%%%%%%%%%%%%%%%%%%%%%%
% Reading data files
%%%%%%%%%%%%%%%%%%%%%%%%%%%%%%%%%%%%%%%%%%%%%%%%
OpenFileName=strcat('data\open');
ShortFileName=strcat('data\short');
LoadFileName=strcat('data\load51');
uMatFileName=strcat('data\',umaterial);
Zop=readata(OpenFileName, nOfMeasurments);
Zs=readata(ShortFileName, nOfMeasurments);
Zl=readata(LoadFileName, nOfMeasurments);
Zum=readata(uMatFileName, nOfMeasurments);
%%%%%%%%%%%%%%%%%%%%%%%%%%%%%%%%%%%%%%%%%%%%%%%%
% Constant Parameters
%%%%%%%%%%%%%%%%%%%%%%%%%%%%%%%%%%%%%%%%%%%%%%%%
Zo=50;
Epso=8.854e-12;
%%%%%%%%%%%%%%%%%%%%%%%%%%%%%%%%%%%%%%%%%%%%%%%%
% Calculating Measured Reflection Coefficients
%%%%%%%%%%%%%%%%%%%%%%%%%%%%%%%%%%%%%%%%%%%%%%%%
Gmop=(Zop-Zo)./(Zop+Zo);
Gms=(Zs-Zo)./(Zs+Zo);
```

```
Gml=(Zl-Zo)./(Zl+Zo);
Gmum=(Zum-Zo)./(Zum+Zo);
%%%%%%%%%%%%%%%%%%%%%%%%%%%%%%%%%%%%%%%%%%%%%%%%%%%%%%%%%%%%%%%%
% Calculating S-Parameters
%%%%%%%%%%%%%%%%%%%%%%%%%%%%%%%%%%%%%%%%%%%%%%%%%%%%%%%%%%%%%%%%
Rl=50.5;
Ll=82e-9;
Cl=0.1e-12;
Yo=1/Zo;
YL=1./(Rl+1j*omega*Ll)+1j*omega*Cl;
Yoff=YL-Yo;
Goff=(Yo+Yoff)./(Yo-Yoff);
S11=Gml;
A=(Gmop-Gml)./(Gml-Gms);
S22=(A-Goff)./(Goff.*(1+A));
Sp=(Gml-Gms).*(1+S22);
%%%%%%%%%%%%%%%%%%%%%%%%%%%%%%%%%%%%%%%%%%%%%%%%%%%%%%%%%%%%%%%%
% Calculating Eps. for the material under test (MUT) from the S-Parameters
%%%%%%%%%%%%%%%%%%%%%%%%%%%%%%%%%%%%%%%%%%%%%%%%%%%%%%%%%%%%%%%%
Epso=8.854e-12;
F=0.118;
Gum=(Gmum-S11)./(Sp+S22.*(Gmum-S11));
Yum=Yo*(1-Gum)./(1+Gum);
Yumact=Yum+Yoff;
Epsum=1+Yumact./(1j*omega.*F*Epso);
EpsRe=real(Epsum);
EspIm=-imag(Epsum);
%%%%%%%%%%%%%%%%%%%%%%%%%%%%%%%%%%%%%%%%%%%%%%%%%%%%%%%%%%%%%%%%
% Drawing the real and the imaginary part of Eps. of MUT
%%%%%%%%%%%%%%%%%%%%%%%%%%%%%%%%%%%%%%%%%%%%%%%%%%%%%%%%%%%%%%%%
figure(1);
hold on;
set(1,'Name','Imag(Epsilon)');
plot(freq*1e-6,EspIm,'b');
hold off;
```

```
figure(2);
hold on;
set(2,'Name','Real(Epsilon)');
plot(freq*1e-6,EpsRe,'b');
hold off;
%%%%%%%%%%%%%%%%%%%%%%%%%%%%%%%%%%%%%%%%%%%%%%%%%%%%%%%%%%%%%%%%
% Writing the results in an output file
%%%%%%%%%%%%%%%%%%%%%%%%%%%%%%%%%%%%%%%%%%%%%%%%%%%%%%%%%%%%%%%%
fn=strcat('data\',umaterial,'.txt');
fptr=fopen(fn,'wt');
clear length;
for k=1: length(freq)
  fprintf(fptr,'%10.5e %10.5e %10.5e\n',freq(k), EpsRe(k), EspIm(k));
end
fclose(fptr);
%%%%%%%%%%%%%%%%%%%%%%%%%%%%%%%%%%%%%%%%%%%%%%%%%%%%%%%%%%%%%%%%
% End of the program, and have a nice output...
%%%%%%%%%%%%%%%%%%%%%%%%%%%%%%%%%%%%%%%%%%%%%%%%%%%%%%%%%%%%%%%%
```

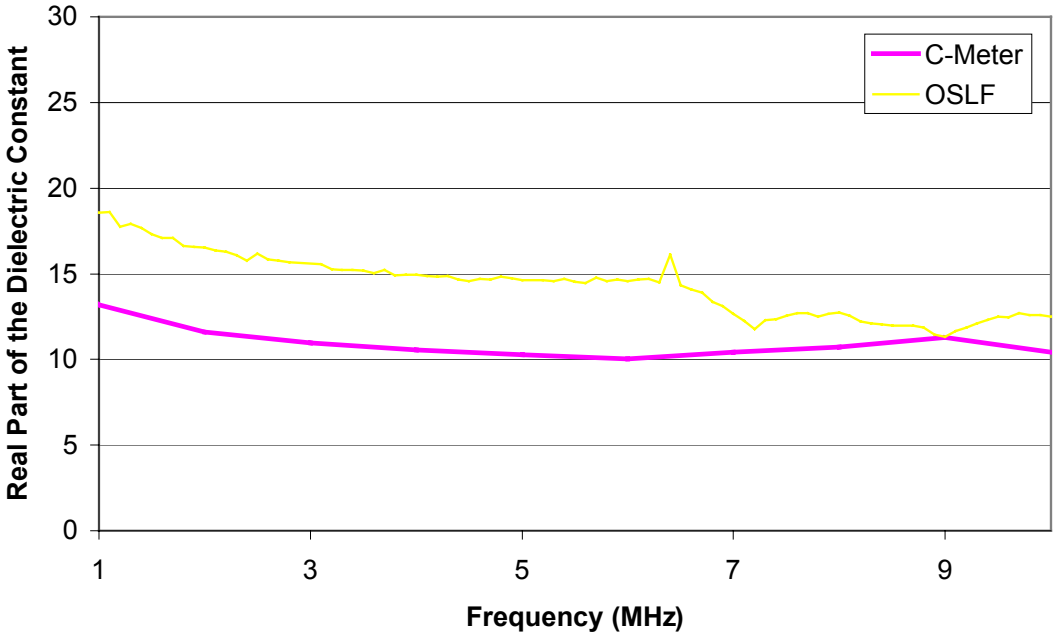

Figure A.6. OSLF vs. C-Meter measurements for the real dielectric constant of C1

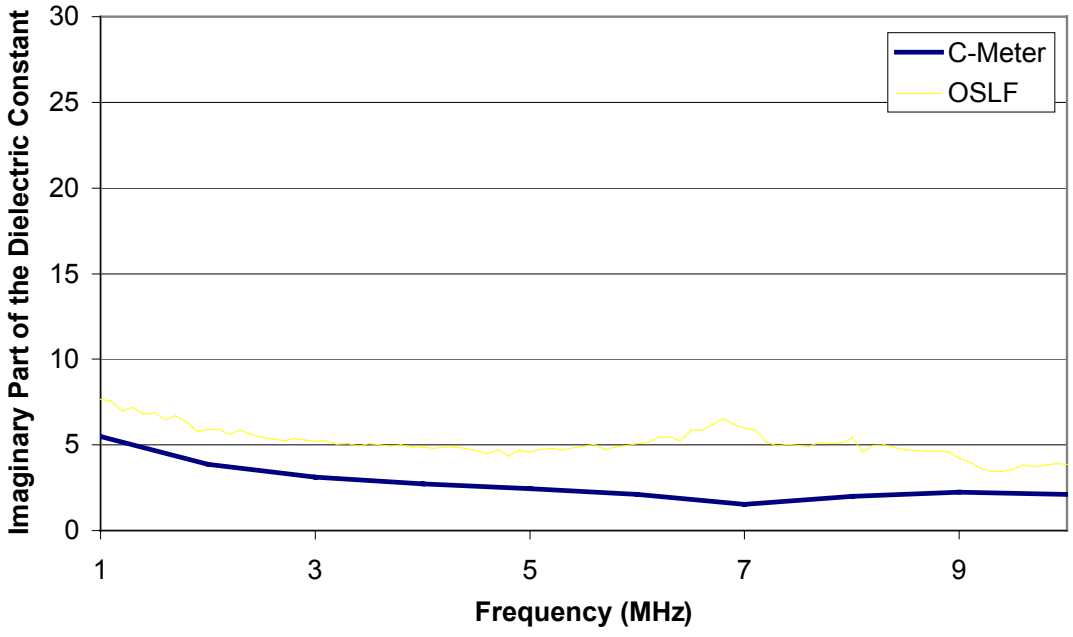

Figure A.7. OSLF vs. C-Meter measurements for the imaginary dielectric constant of C1

Open-Material-Material (OMM)

Table A.8. Governing equations of OMM calibration scheme

Calibration	Reflection Coefficient (Γ_m)
Open	$\Gamma_{mop} = \frac{a+b}{1+c}$
Material 1	$\Gamma_{mm1} = \frac{a+b\varepsilon_{r1}}{1+c\varepsilon_{r1}}$
Material 2	$\Gamma_{mm2} = \frac{a+b\varepsilon_{r2}}{1+c\varepsilon_{r2}}$

Table A.9. Coefficients solution for OMM calibration scheme

Unknowns	Solution
c	$\frac{(\Gamma_{mm2} - \Gamma_{mop})(\varepsilon_{r1}-1) - (\Gamma_{mm1} - \Gamma_{mop})(\varepsilon_{r2}-1)}{(\Gamma_{mop} - \varepsilon_{r2}\Gamma_{mm2})(\varepsilon_{r1}-1) - (\Gamma_{mop} - \varepsilon_{r1}\Gamma_{mm1})(\varepsilon_{r2}-1)}$
b	$\frac{(\Gamma_{mm1} - \Gamma_{mop}) + (\varepsilon_{r1}\Gamma_{mm1} - \Gamma_{mop})\, c}{\varepsilon_{r1}-1}$
a	$\Gamma_{mop} + c\,\Gamma_{mop} - b$

The permittivity of the unknown material is determined as follows:

$$\Gamma_{mum} = \frac{a+b\varepsilon_{rum}}{1+c\varepsilon_{rum}}$$

$$\varepsilon_{rum} = \frac{\Gamma_{mum} - a}{b - c\,\Gamma_{mum}}$$

MatLab program code for calculating and drawing the dielectric constant measurements using OMM calibration scheme

```
%%%%%%%%%%%%%%%%%%%%%%%%%%%%%%%%%%%%%%%%%%%%%%%%
% Capacitor Probe:
% OMM Calibration Scheme
%%%%%%%%%%%%%%%%%%%%%%%%%%%%%%%%%%%%%%%%%%%%%%%%
clear all;
k1material='Tefss1'; % <----known material 1
k2material='enss2'; % <----known material 2
umaterial='C1ss1'; % <--unknown material
%%%%%%%%%%%%%%%%%%%%%%%%%%%%%%%%%%%%%%%%%%%%%%%%
%network analyzer inforamation
%%%%%%%%%%%%%%%%%%%%%%%%%%%%%%%%%%%%%%%%%%%%%%%%
nOfMeasurments=401;%%<---------------------
freq=100e3:100e3:40.1e6;
omega=2*pi*freq;
%%%%%%%%%%%%%%%%%%%%%%%%%%%%%%%%%%%%%%%%%%%%%%%%
% Reading data files
%%%%%%%%%%%%%%%%%%%%%%%%%%%%%%%%%%%%%%%%%%%%%%%%
OpenFileName=strcat('data\open');
k1MatFileName=strcat('data\',k1material);
k2MatFileName=strcat('data\',k2material);
uMatFileName=strcat('data\',umaterial);
Zop=readata(OpenFileName, nOfMeasurments);
Zkm1=readata(k1MatFileName, nOfMeasurments);
Zkm2=readata(k2MatFileName, nOfMeasurments);
Zum=readata(uMatFileName, nOfMeasurments);
%%%%%%%%%%%%%%%%%%%%%%%%%%%%%%%%%%%%%%%%%%%%%%%%
% Constant Parameters
%%%%%%%%%%%%%%%%%%%%%%%%%%%%%%%%%%%%%%%%%%%%%%%%
Zo=50;
%%%%%%%%%%%%%%%%%%%%%%%%%%%%%%%%%%%%%%%%%%%%%%%%
% Calculating Measured Reflection Coefficients
%%%%%%%%%%%%%%%%%%%%%%%%%%%%%%%%%%%%%%%%%%%%%%%%
Gmop=(Zop-Zo)./(Zop+Zo);
```

```
Gmkm1=(Zkm1-Zo)./(Zkm1+Zo);
Gmkm2=(Zkm2-Zo)./(Zkm2+Zo);
Gmum=(Zum-Zo)./(Zum+Zo);
%%%%%%%%%%%%%%%%%%%%%%%%%%%%%%%%%%%%%%%%%%%%%%%%%%%%%%%%%%%%
% The dielectric constant of the known materials measured from PPC fixture
%%%%%%%%%%%%%%%%%%%%%%%%%%%%%%%%%%%%%%%%%%%%%%%%%%%%%%%%%%%%
Eps1=2.1;%<----- or an estimated value
Eps2=3.3;%<----- or an estimated value
%%%%%%%%%%%%%%%%%%%%%%%%%%%%%%%%%%%%%%%%%%%%%%%%%%%%%%%%%%%%
% Calculating Bilinear Transformation Coeffecients
%%%%%%%%%%%%%%%%%%%%%%%%%%%%%%%%%%%%%%%%%%%%%%%%%%%%%%%%%%%%
g=(Eps1-1).*(Gmop-Eps2.*Gmkm2)-(Eps2-1).*(Gmop-Eps1.*Gmkm1);
d=(Eps1-1).*(Gmkm2-Gmop)-(Eps2-1).*(Gmkm1-Gmop);
c=(d)./(g);
b=((Gmkm1-Gmop)+c.*(Eps1.*Gmkm1-Gmop))./(Eps1-1);
a=Gmop+c.*Gmop-b;
%%%%%%%%%%%%%%%%%%%%%%%%%%%%%%%%%%%%%%%%%%%%%%%%%%%%%%%%%%%%
% Calculating Eps. for the material under test (MUT) from the S-Parameters
%%%%%%%%%%%%%%%%%%%%%%%%%%%%%%%%%%%%%%%%%%%%%%%%%%%%%%%%%%%%
Epsum=(a-Gmum)./(c.*Gmum-b);
EpsRe=real(Epsum);
EspIm=-imag(Epsum);
%%%%%%%%%%%%%%%%%%%%%%%%%%%%%%%%%%%%%%%%%%%%%%%%%%%%%%%%%%%%
% Drawing the real and the imaginary part of Eps. of MUT
%%%%%%%%%%%%%%%%%%%%%%%%%%%%%%%%%%%%%%%%%%%%%%%%%%%%%%%%%%%%
figure(1);
hold on;
set(1,'Name','Imag(Epsilon)');
plot(freq*1e-6,EspIm,'k');
hold off;
figure(2);
hold on;
set(2,'Name','Real(Epsilon)');
plot(freq*1e-6,EpsRe,'k');
hold off;
```

```
%%%%%%%%%%%%%%%%%%%%%%%%%%%%%%%%%%%%%%%%%%%
% Writing the results in an output file
%%%%%%%%%%%%%%%%%%%%%%%%%%%%%%%%%%%%%%%%%%%
fn=strcat('data\',umaterial,'.txt');
fptr=fopen(fn,'wt');
clear length;
for k=1: length(freq)
  fprintf(fptr,'%10.5e %10.5e %10.5e\n',freq(k), EpsRe(k), EspIm(k));
end
fclose(fptr);
%%%%%%%%%%%%%%%%%%%%%%%%%%%%%%%%%%%%%%%%%%%
% End of the program, and have a nice output...
%%%%%%%%%%%%%%%%%%%%%%%%%%%%%%%%%%%%%%%%%%%
```

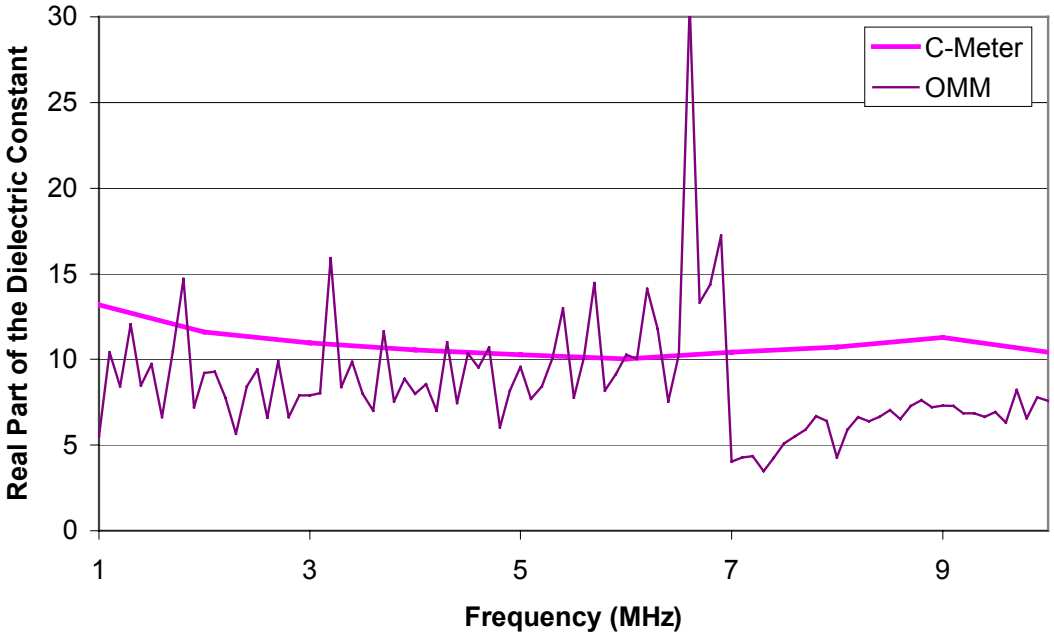

Figure A.8. OMM vs. C-Meter measurements for the real dielectric constant of C1

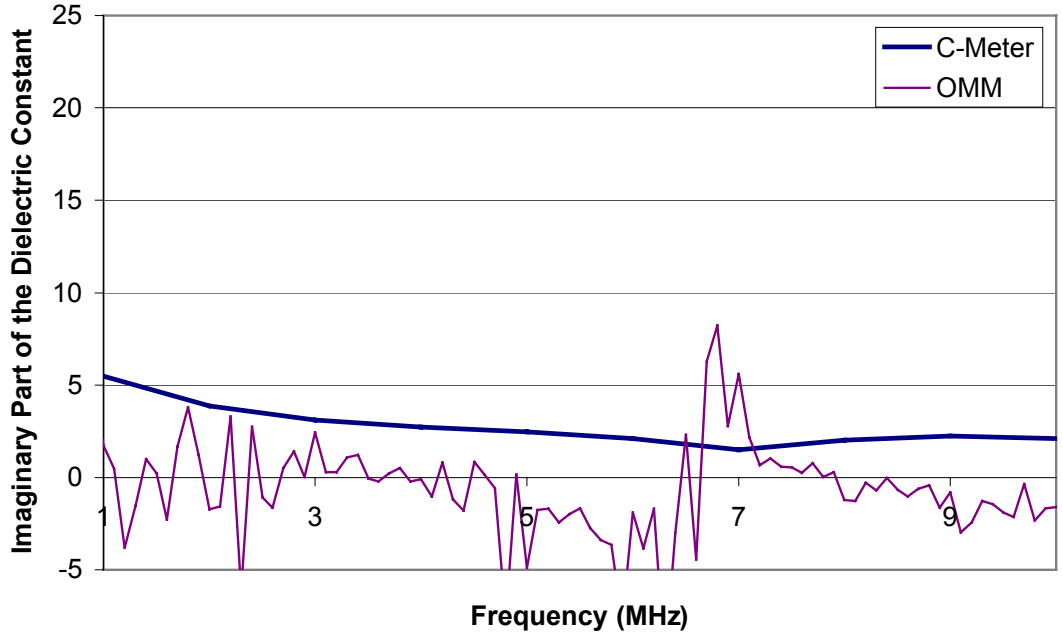

Figure A.9. OMM vs. C-Meter measurements for the imaginary dielectric constant of C1

Short-Material-Material (SMM)

Table A.10. Governing equations of SMM calibration scheme

Calibration	Reflection Coefficient (Γ_m)
Short	$\Gamma_{ms} = b / a$
Material 1	$\Gamma_{mm1} = \dfrac{a + b\varepsilon_{r1}}{1 + c\varepsilon_{r1}}$
Material 2	$\Gamma_{mm2} = \dfrac{a + b\varepsilon_{r2}}{1 + c\varepsilon_{r2}}$

Table A.11. Coefficients solution for OMM calibration scheme

Unknown	Solution
c	$\dfrac{\Gamma_{mm2} - \Gamma_{mm1}}{\varepsilon_{r1}(\Gamma_{mm1} - \Gamma_{ms}) - \varepsilon_{r2}(\Gamma_{mm2} - \Gamma_{ms})}$
b	$c.\ \Gamma_{ms}$
a	$\Gamma_{mm1} + (c\ \Gamma_{mm1} - b)\ \varepsilon_{r1}$

The permittivity of the unknown material is determined as follows:

$$\Gamma_{mum} = \frac{a + b\varepsilon_{rum}}{1 + c\varepsilon_{rum}}$$

$$\varepsilon_{rum} = \frac{\Gamma_{mum} - a}{b - c\,\Gamma_{mum}}$$

MatLab program code for calculating and drawing the dielectric constant measurements using SMM calibration scheme

```
%%%%%%%%%%%%%%%%%%%%%%%%%%%%%%%%%%%%%%%%%%%%%%%%
% Capacitor Probe:
% SMM Calibration Scheme
%%%%%%%%%%%%%%%%%%%%%%%%%%%%%%%%%%%%%%%%%%%%%%%%
clear all;
k1material='Tefss1'; % <----known material 1 from the data directory
k2material='enss1'; % <----known material 2 from the data directory
umaterial='C1ss1'; % <--unknown material from the data directory
%%%%%%%%%%%%%%%%%%%%%%%%%%%%%%%%%%%%%%%%%%%%%%%%
%network analyzer inforamation
%%%%%%%%%%%%%%%%%%%%%%%%%%%%%%%%%%%%%%%%%%%%%%%%
nOfMeasurments=401;%%<---------------------
freq=100e3:100e3:40.1e6;
omega=2*pi*freq;
%%%%%%%%%%%%%%%%%%%%%%%%%%%%%%%%%%%%%%%%%%%%%%%%
% Reading data files
%%%%%%%%%%%%%%%%%%%%%%%%%%%%%%%%%%%%%%%%%%%%%%%%
ShortFileName=strcat('data\short');
k1MatFileName=strcat('data\',k1material);
k2MatFileName=strcat('data\',k2material);
uMatFileName=strcat('data\',umaterial);
Zs=readata(ShortFileName, nOfMeasurments);
Zkm1=readata(k1MatFileName, nOfMeasurments);
Zkm2=readata(k2MatFileName, nOfMeasurments);
Zum=readata(uMatFileName, nOfMeasurments);
%%%%%%%%%%%%%%%%%%%%%%%%%%%%%%%%%%%%%%%%%%%%%%%%
% Constant Parameters
%%%%%%%%%%%%%%%%%%%%%%%%%%%%%%%%%%%%%%%%%%%%%%%%
Zo=50;
%%%%%%%%%%%%%%%%%%%%%%%%%%%%%%%%%%%%%%%%%%%%%%%%
% Calculating Measured Reflection Coefficients
%%%%%%%%%%%%%%%%%%%%%%%%%%%%%%%%%%%%%%%%%%%%%%%%
Gms=(Zs-Zo)./(Zs+Zo);
```

```
Gmkm1=(Zkm1-Zo)./(Zkm1+Zo);
Gmkm2=(Zkm2-Zo)./(Zkm2+Zo);
Gmum=(Zum-Zo)./(Zum+Zo);
%%%%%%%%%%%%%%%%%%%%%%%%%%%%%%%%%%%%%%%%%%%%%%%%%%%%%%%%%%%%
% The dielectric constant of the known materials measured from PPC fixture
%%%%%%%%%%%%%%%%%%%%%%%%%%%%%%%%%%%%%%%%%%%%%%%%%%%%%%%%%%%%
Eps1=2.10;%<----- or an estimated value
Eps2=3.3;%<----- or an estimated value
%%%%%%%%%%%%%%%%%%%%%%%%%%%%%%%%%%%%%%%%%%%%%%%%%%%%%%%%%%%%
% Calculating Bilinear Transformation Coeffecients
%%%%%%%%%%%%%%%%%%%%%%%%%%%%%%%%%%%%%%%%%%%%%%%%%%%%%%%%%%%%
c=(Gmkm2-Gmkm1)./(Eps1.*(Gmkm1-Gms)+Eps2.*(Gms-Gmkm2));
b=c.*Gms;
a=Gmkm1+Eps1.*(c.*Gmkm1-b);
%%%%%%%%%%%%%%%%%%%%%%%%%%%%%%%%%%%%%%%%%%%%%%%%%%%%%%%%%%%%
% Calculating Eps. for the material under test (MUT) from the S-Parameters
%%%%%%%%%%%%%%%%%%%%%%%%%%%%%%%%%%%%%%%%%%%%%%%%%%%%%%%%%%%%
Epsum=(a-Gmum)./(c.*Gmum-b);
EpsRe=real(Epsum);
EspIm=-imag(Epsum);
%%%%%%%%%%%%%%%%%%%%%%%%%%%%%%%%%%%%%%%%%%%%%%%%%%%%%%%%%%%%
% Drawing the real and the imaginary part of Eps. of MUT
%%%%%%%%%%%%%%%%%%%%%%%%%%%%%%%%%%%%%%%%%%%%%%%%%%%%%%%%%%%%
figure(1);
hold on;
set(1,'Name','Imag(Epsilon)');
plot(freq*1e-6,EspIm,'y');
hold off;
figure(2);
hold on;
set(2,'Name','Real(Epsilon)');
plot(freq*1e-6,EpsRe,'y');
hold off;
%%%%%%%%%%%%%%%%%%%%%%%%%%%%%%%%%%%%%%%%%%%%%%%%%%%%%%%%%%%%
% Writing the results in an output file
```

```
%%%%%%%%%%%%%%%%%%%%%%%%%%%%%%%%%%%%%%%%%%%%%%%%
fn=strcat('data\',umaterial,'.txt');
fptr=fopen(fn,'wt');
clear length;
for k=1: length(freq)
   fprintf(fptr,'%10.5e %10.5e %10.5e\n',freq(k), EpsRe(k), EspIm(k));
end
fclose(fptr);
%%%%%%%%%%%%%%%%%%%%%%%%%%%%%%%%%%%%%%%%%%%%%%%%
% End of the program, and have a nice output...
%%%%%%%%%%%%%%%%%%%%%%%%%%%%%%%%%%%%%%%%%%%%%%%%
```

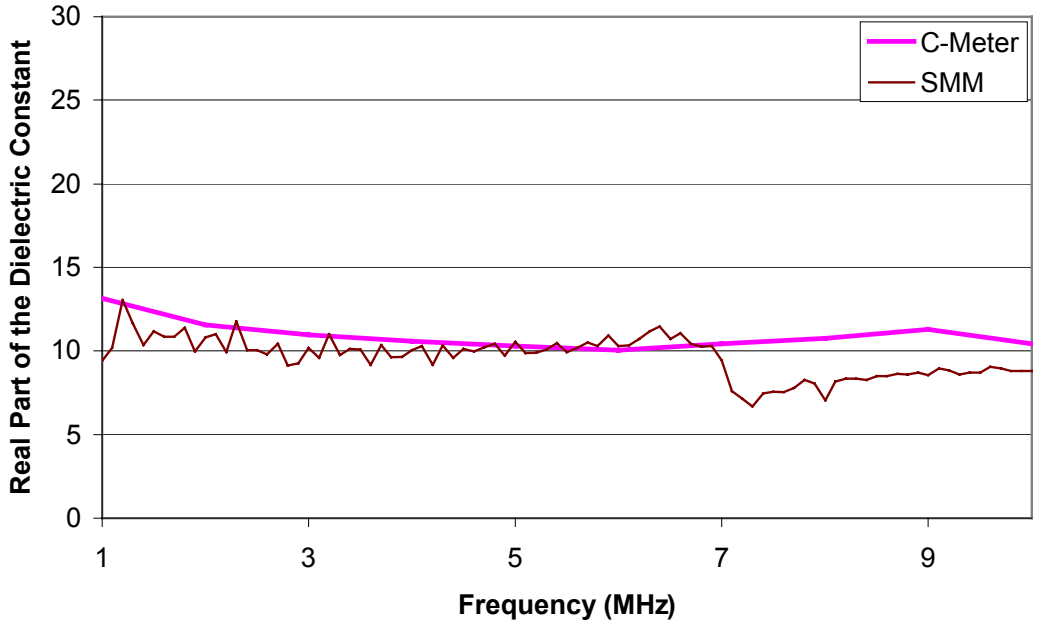

Figure A.10. SMM vs. C-Meter measurements for the real dielectric constant of C1

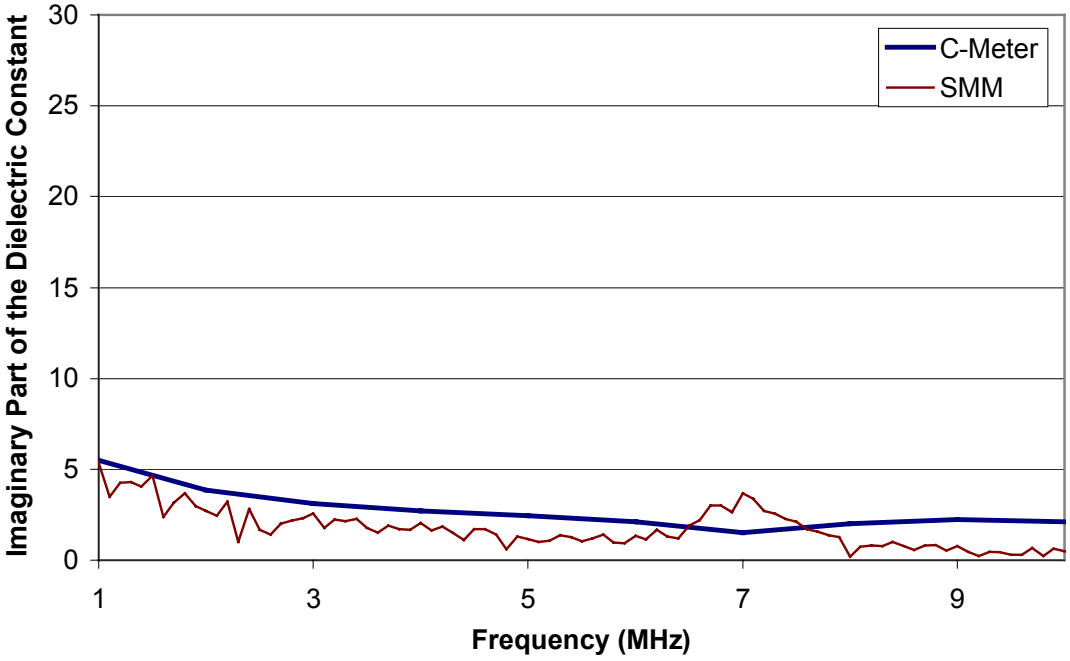

Figure A.11. SMM vs. C-Meter measurements for the imaginary dielectric constant of C1

Open-Short-Material (OSM)

Table A.12. Governing equations of OSM calibration scheme

Calibration	Reflection Coefficient (Γ_m)
Open	$\Gamma_{mop} = \frac{a+b}{1+c}$
Short	$\Gamma_{ms} = b/c$
Material	$\Gamma_{mkm} = \frac{a+b\varepsilon_{rkm}}{1+c\varepsilon_{rkm}}$

Table A.13. Coefficients solution for OSM calibration scheme

Unknown	Solution
c	$\frac{\Gamma_{mkm} - \Gamma_{mop}}{\Gamma_{mop} + (\varepsilon_{rkm} - 1)\Gamma_{ms} - \varepsilon_{rkm}\Gamma_{mkm}}$
b	$c\,\Gamma_{ms}$
a	$\Gamma_{mop} + (\Gamma_{mop} - \Gamma_{ms})\,c$

The permittivity of the unknown material is determined as follows:

$$\Gamma_{mum} = \frac{a+b\varepsilon_{rum}}{1+c\varepsilon_{rum}}$$

$$\varepsilon_{rum} = \frac{\Gamma_{mum} - a}{b - c\,\Gamma_{mum}}$$

MatLab program code for calculating and drawing the dielectric constant measurements using OSM calibration scheme

```
%%%%%%%%%%%%%%%%%%%%%%%%%%%%%%%%%%%%%%%%%%%%%%%%%
% Capacitor Probe:
% OSM Calibration Scheme
%%%%%%%%%%%%%%%%%%%%%%%%%%%%%%%%%%%%%%%%%%%%%%%%%
clear all;
kmaterial='Tefss1'; % <----known material
umaterial='f1ss1b'; % <--unknown material
%%%%%%%%%%%%%%%%%%%%%%%%%%%%%%%%%%%%%%%%%%%%%%%%%
%network analyzer inforamation
%%%%%%%%%%%%%%%%%%%%%%%%%%%%%%%%%%%%%%%%%%%%%%%%%
nOfMeasurments=401;%%<----------------------
freq=100e3:100e3:40.1e6;
omega=2*pi*freq;
%%%%%%%%%%%%%%%%%%%%%%%%%%%%%%%%%%%%%%%%%%%%%%%%%
% The dielectric constant of the known material measured from PPC fixture
%%%%%%%%%%%%%%%%%%%%%%%%%%%%%%%%%%%%%%%%%%%%%%%%%
Epskm=2.1;%<-----

%%%%%%%%%%%%%%%%%%%%%%%%%%%%%%%%%%%%%%%%%%%%%%%%%
% Reading data files
%%%%%%%%%%%%%%%%%%%%%%%%%%%%%%%%%%%%%%%%%%%%%%%%%
OpenFileName=strcat('data\open');
ShortFileName=strcat('data\short');
kMatFileName=strcat('data\',kmaterial);
uMatFileName=strcat('data\',umaterial);
Zop=readata(OpenFileName, nOfMeasurments);
Zs=readata(ShortFileName, nOfMeasurments);
Zkm=readata(kMatFileName, nOfMeasurments);
Zum=readata(uMatFileName, nOfMeasurments);
%%%%%%%%%%%%%%%%%%%%%%%%%%%%%%%%%%%%%%%%%%%%%%%%%
% Constant Parameters
%%%%%%%%%%%%%%%%%%%%%%%%%%%%%%%%%%%%%%%%%%%%%%%%%
Zo=50;
```

```
%%%%%%%%%%%%%%%%%%%%%%%%%%%%%%%%%%%%%%%%%%%%%%%%
% Calculating Measured Reflection Coefficients
%%%%%%%%%%%%%%%%%%%%%%%%%%%%%%%%%%%%%%%%%%%%%%%%
Gmop=(Zop-Zo)./(Zop+Zo);
Gms=(Zs-Zo)./(Zs+Zo);
Gmkm=(Zkm-Zo)./(Zkm+Zo);
Gmum=(Zum-Zo)./(Zum+Zo);
%%%%%%%%%%%%%%%%%%%%%%%%%%%%%%%%%%%%%%%%%%%%%%%%
% Calculating Bilinear Transformation Coeffecients
%%%%%%%%%%%%%%%%%%%%%%%%%%%%%%%%%%%%%%%%%%%%%%%%
c=(Gmkm-Gmop)./(Gmop+(Epskm-1).*Gms-Epskm.*Gmkm);
b=c.*Gms;
a=Gmop+c.*(Gmop-Gms);
%%%%%%%%%%%%%%%%%%%%%%%%%%%%%%%%%%%%%%%%%%%%%%%%
% Calculating Eps. for the material under test (MUT) from the S-Parameters
%%%%%%%%%%%%%%%%%%%%%%%%%%%%%%%%%%%%%%%%%%%%%%%%
Epsum=(a-Gmum)./(c.*Gmum-b);
EpsRe=real(Epsum);
EspIm=-imag(Epsum);
%%%%%%%%%%%%%%%%%%%%%%%%%%%%%%%%%%%%%%%%%%%%%%%%
% Drawing the real and the imaginary part of Eps. of MUT
%%%%%%%%%%%%%%%%%%%%%%%%%%%%%%%%%%%%%%%%%%%%%%%%
figure(1);
hold on;
set(1,'Name','Imag(Epsilon)');
plot(freq*1e-6,EspIm,'r');
%la(freq*1e-6,EspIm,1,'Imag(Epsilon)');
hold off;
figure(2);
hold on;
set(2,'Name','Real(Epsilon)');
plot(freq*1e-6,EpsRe,'r');
%la(freq*1e-6,EpsRe,2,'Real(Epsilon)');
hold off;
%%%%%%%%%%%%%%%%%%%%%%%%%%%%%%%%%%%%%%%%%%%%%%%%
```

```
% Writing the results in an output file
%%%%%%%%%%%%%%%%%%%%%%%%%%%%%%%%%%%%%%%%%%%%%%%%%%%%%%%%%%%%%%%%
fn=strcat('data\',umaterial,'.txt');
fptr=fopen(fn,'wt');
clear length;
for k=1: length(freq)
   fprintf(fptr,'%10.5e %10.5e %10.5e\n',freq(k), EpsRe(k), EspIm(k));
end
fclose(fptr);
%%%%%%%%%%%%%%%%%%%%%%%%%%%%%%%%%%%%%%%%%%%%%%%%%%%%%%%%%%%%%%%%
% End of the program, and have a nice output...
%%%%%%%%%%%%%%%%%%%%%%%%%%%%%%%%%%%%%%%%%%%%%%%%%%%%%%%%%%%%%%%%
```

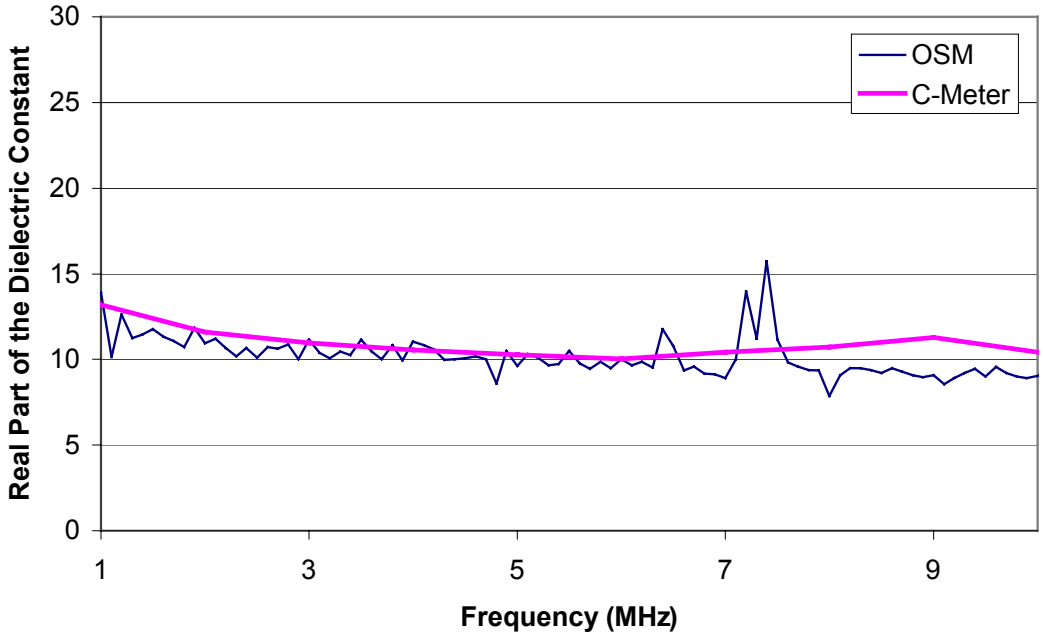

Figure A.12. OSM vs. C-Meter measurements for the real dielectric constant of C1

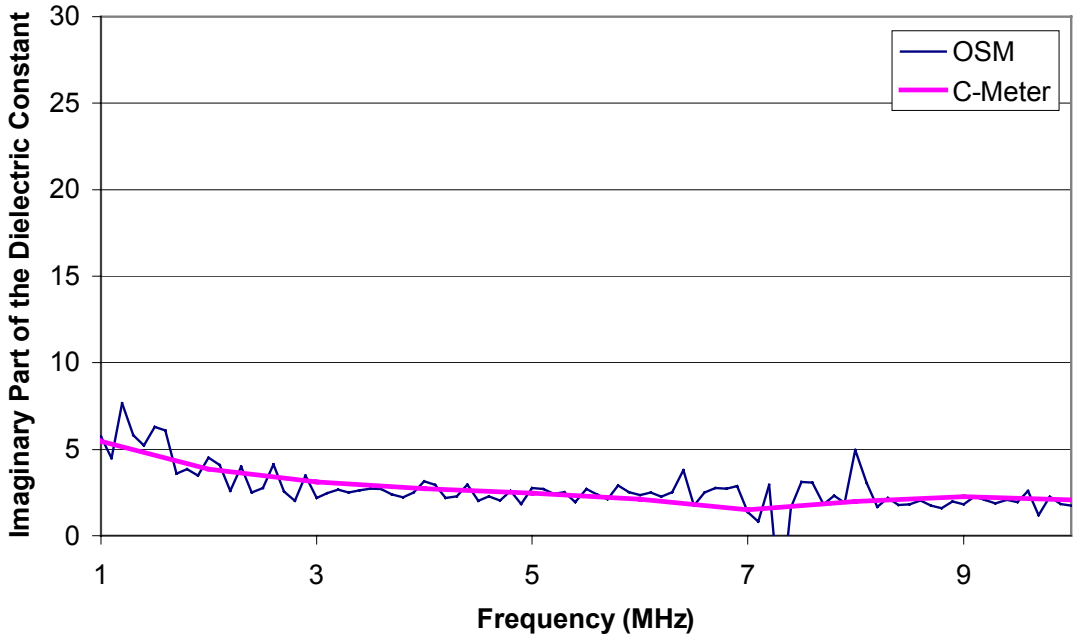

Figure A.13. OSM vs. C-Meter measurements for the imaginary dielectric constant of C1

APPENDIX B: C-PROBE OPTIMIZATION DATA

Percentage of change due to air void depth for each considered design configuration

Effective depth in mm

Effective depth normalized to different slab thicknesses

Optimum design for different slab thicknesses

Regression Analysis

- Data
- Results

Table B.1. Percentage of change due to air void depth using 76 mm x 25 mm

Air Void Depth (mm)	Eps							
	20		15		10		5	
	C	Change (%)	C	Change (%)	C	Change (%)	C	Change (%)
254	183.04		137.29		91.54		45.79	
229	182.96	0.04	137.25	0.03	91.53	0.01	45.82	-0.07
203	182.00	0.57	136.55	0.54	91.10	0.48	45.65	0.31
178	185.83	-1.52	139.47	-1.59	93.11	-1.72	46.73	-2.05
152	182.68	0.20	137.18	0.08	91.68	-0.16	46.12	-0.72
127	179.84	1.75	135.15	1.56	90.45	1.19	45.70	0.20
102	173.06	5.45	130.24	5.14	87.39	4.53	44.45	2.93
76	161.89	11.55	122.12	11.05	82.32	10.07	42.36	7.49
51	142.58	22.10	108.05	21.30	73.47	19.74	38.64	15.61
25	103.32	43.55	79.16	42.34	54.92	40.01	30.41	33.59

Table B.02. Percentage of change due to air void depth using 76 mm x 51 mm

Air Void Depth (mm)	Eps							
	20		15		10		5	
	C	Change (%)	C	Change (%)	C	Change (%)	C	Change (%)
254	149.35		112.02		74.70		37.37	
229	149.93	-0.39	112.48	-0.41	75.03	-0.44	37.58	-0.56
203	148.57	0.52	111.49	0.47	74.42	0.37	37.33	0.11
178	151.28	-1.29	113.58	-1.39	75.87	-1.57	38.15	-2.09
152	147.55	1.21	110.86	1.04	74.13	0.76	37.42	-0.13
127	139.54	6.57	104.97	6.29	70.39	5.77	35.74	4.36
102	131.18	12.17	98.87	11.74	66.54	10.92	34.12	8.70
76	119.05	20.29	90.04	19.62	61.27	17.98	31.80	14.91
51	101.29	32.18	77.10	31.17	52.51	29.71	28.40	24.00
25	69.23	53.65	53.51	52.23	37.75	49.46	21.72	41.88

Table B.3. Percentage of change due to air void depth using 76 mm x 76 mm

Air Void Depth (mm)	Eps							
	20		15		10		5	
	C	Change (%)	C	Change (%)	C	Change (%)	C	Change (%)
254	133.77		100.34		66.92		33.49	
229	131.16	1.95	98.41	1.92	65.65	1.90	32.90	1.76
203	129.08	3.51	96.89	3.44	64.69	3.33	32.48	3.02
178	127.41	4.75	95.69	4.63	63.97	4.41	32.23	3.76
152	123.25	7.86	92.65	7.66	62.05	7.28	31.41	6.21
127	118.24	11.61	89.02	11.28	59.79	10.65	30.50	8.93
102	109.05	18.48	82.31	17.97	55.54	17.01	28.68	14.36
76	97.54	27.08	73.93	26.32	50.29	24.85	26.50	20.87
51	79.90	40.27	61.03	39.18	42.18	36.97	23.04	31.20
25	52.58	60.69	40.92	59.22	29.14	56.46	17.33	48.25

Table B.4. Percentage of change due to air void depth using 102 mm x 25 mm

Air Void Depth (mm)	Eps 20		15		10		5	
	C	Change (%)	C	Change (%)	C	Change (%)	C	Change (%)
254	194.31		145.75		97.19		48.62	
229	194.65	-0.17	146.03	-0.19	97.39	-0.21	48.78	-0.33
203	191.22	1.59	143.50	1.54	95.77	1.46	48.03	1.21
178	194.95	-0.33	146.35	-0.41	97.75	-0.58	49.13	-1.05
152	190.49	1.97	143.10	1.82	95.70	1.53	48.26	0.74
127	184.37	5.12	138.64	4.88	92.90	4.41	47.09	3.15
102	175.89	9.48	132.47	9.11	89.03	8.40	45.50	6.42
76	162.19	16.53	122.48	15.97	82.73	14.88	42.83	11.91
51	138.25	28.85	104.90	28.03	71.44	26.49	37.90	22.05
25	103.30	46.84	79.20	45.66	55.05	43.36	30.67	36.92

Table B.5. Percentage of change due to air void depth using 102 mm x 51 mm

Air Void Depth (mm)	Eps 20		15		10		5	
	C	Change (%)	C	Change (%)	C	Change (%)	C	Change (%)
254	158.65		119.00		79.36		39.71	
229	157.82	0.52	118.41	0.50	79.01	0.44	39.59	0.30
203	155.88	1.75	117.00	1.68	78.12	1.56	39.23	1.21
178	152.86	3.65	114.80	3.53	76.74	3.30	38.65	2.67
152	150.07	5.41	112.81	5.20	75.54	4.81	38.23	3.73
127	143.88	9.31	108.31	8.98	72.71	8.38	37.06	6.67
102	134.66	15.12	101.59	14.63	68.49	13.70	35.29	11.13
76	121.26	23.57	91.80	22.86	61.76	22.18	32.68	17.70
51	101.50	36.02	77.33	35.02	53.11	33.08	28.73	27.65
25	68.97	56.53	63.36	46.76	37.70	52.50	21.87	44.93

Table B.6. Percentage of change due to air void depth using 102 mm x 76 mm

Air Void Depth (mm)	Eps 20		15		10		5	
	C	Change (%)	C	Change (%)	C	Change (%)	C	Change (%)
254	141.27		105.97		70.67		35.37	
229	137.01	3.02	102.81	2.98	68.60	2.93	34.40	2.74
203	135.13	4.35	101.45	4.27	67.76	4.12	34.06	3.70
178	131.92	6.62	99.11	6.47	66.29	6.20	33.45	5.43
152	128.54	9.01	96.68	8.77	64.81	8.29	32.90	6.98
127	121.78	13.80	91.75	13.42	61.70	12.69	31.59	10.69
102	111.42	21.13	84.17	20.57	56.90	19.48	29.53	16.51
76	99.41	29.63	75.42	28.83	51.39	27.28	27.24	22.99
51	80.43	43.07	61.50	41.96	42.52	39.83	23.39	33.87
25	52.81	62.62	41.14	61.18	29.23	58.64	17.57	50.33

Table B.7. Percentage of change due to air void depth using 127 mm x 25 mm

Air Void Depth (mm)	Eps							
	20		15		10		5	
	C	Change (%)	C	Change (%)	C	Change (%)	C	Change (%)
254	209.37		157.05		104.73		52.40	
229	202.71	3.18	152.09	3.16	101.46	3.12	50.83	3.00
203	200.37	4.30	150.40	4.23	100.40	4.13	50.38	3.85
178	201.74	3.64	151.49	3.54	101.22	3.35	50.94	2.79
152	196.12	6.33	147.38	6.16	98.62	5.83	49.83	4.90
127	189.16	9.65	142.31	9.39	95.44	8.87	48.50	7.44
102	174.24	16.78	131.32	16.38	88.37	15.62	45.32	13.51
76	164.51	21.43	124.30	20.85	84.05	19.75	43.66	16.68
51	138.75	33.73	105.32	32.94	71.85	31.40	38.22	27.06
25	103.37	50.63	79.29	49.51	55.15	47.34	30.85	41.13

Table B.8. Percentage of change due to air void depth using 127 mm x 51 mm

Air Void Depth (mm)	Eps							
	20		15		10		5	
	C	Change (%)	C	Change (%)	C	Change (%)	C	Change (%)
254	169.13		126.87		84.61		42.34	
229	164.09	2.98	123.12	2.96	82.11	2.95	41.18	2.74
203	163.11	3.56	122.44	3.49	81.77	3.36	41.09	2.95
178	159.36	5.78	119.71	5.64	80.06	5.38	40.37	4.65
152	154.14	8.86	115.91	8.64	77.66	8.21	39.38	6.99
127	146.36	13.46	110.22	13.12	74.07	12.46	37.86	10.58
102	146.36	13.46	110.22	13.12	74.07	12.46	37.85	10.60
76	121.14	28.37	91.77	27.67	62.33	26.33	32.84	22.44
51	100.92	40.33	76.93	39.36	52.93	37.44	28.73	32.14
25	69.53	58.89	53.81	57.59	38.04	55.04	22.14	47.71

Table B.9. Percentage of change due to air void depth using 127 mm x 76 mm

Air Void Depth (mm)	Eps							
	20		15		10		5	
	C	Change (%)	C	Change (%)	C	Change (%)	C	Change (%)
254	145.36		109.04		72.72		36.41	
229	143.00	1.62	107.30	1.60	71.61	1.53	35.92	1.35
203	140.08	3.63	105.18	3.54	70.27	3.37	35.35	2.91
178	137.54	5.38	103.36	5.21	69.16	4.90	34.95	4.01
152	131.47	9.56	98.92	9.28	66.35	8.76	33.74	7.33
127	122.93	15.43	92.67	15.01	62.38	14.22	32.03	12.03
102	112.60	22.54	85.11	21.95	57.60	20.79	30.00	17.61
76	98.79	32.04	75.00	31.22	51.20	29.59	27.23	25.21
51	80.51	44.61	61.58	43.53	42.61	41.41	23.53	35.37
25	52.53	63.86	40.94	62.45	29.32	59.68	17.58	51.72

Table B.10. Effective depth of each considered design configuration (mm)

S (mm)	Eps = 20			Eps = 15			Eps = 10			Eps = 5		
	W (mm)			W (mm)			W (mm)			W (mm)		
	76	102	127	76	102	127	76	102	127	76	102	127
25	93	113	143	91	111	142	88	107	138	76	97	126
51	123	139	164	121	137	162	118	133	159	109	122	149
76	155	168	165	154	166	164	151	162	161	140	149	151

Table B.10. ANOVA and regression analysis input data (mm)

Eps	W	S	d	Eps*W	Eps*S	W*S	Eps**2	W**2	S**2
5	76	25	76	381	127	1935	25	5806	645
5	76	51	109	381	254	3871	25	5806	2581
5	76	76	140	381	381	5806	25	5806	5806
5	102	25	97	508	127	2581	25	10323	645
5	102	51	122	508	254	5161	25	10323	2581
5	102	76	149	508	381	7742	25	10323	5806
5	127	25	126	635	127	3226	25	16129	645
5	127	51	149	635	254	6452	25	16129	2581
5	127	76	151	635	381	9677	25	16129	5806
10	76	25	88	762	254	1935	100	5806	645
10	76	51	118	762	508	3871	100	5806	2581
10	76	76	151	762	762	5806	100	5806	5806
10	102	25	107	1016	254	2581	100	10323	645
10	102	51	133	1016	508	5161	100	10323	2581
10	102	76	162	1016	762	7742	100	10323	5806
10	127	25	138	1270	254	3226	100	16129	645
10	127	51	159	1270	508	6452	100	16129	2581
10	127	76	161	1270	762	9677	100	16129	5806
15	76	25	91	1143	381	1935	225	5806	645
15	76	51	121	1143	762	3871	225	5806	2581
15	76	76	154	1143	1143	5806	225	5806	5806
15	102	25	111	1524	381	2581	225	10323	645
15	102	51	137	1524	762	5161	225	10323	2581
15	102	76	166	1524	1143	7742	225	10323	5806
15	127	25	142	1905	381	3226	225	16129	645
15	127	51	162	1905	762	6452	225	16129	2581
15	127	76	164	1905	1143	9677	225	16129	5806
20	76	25	93	1524	508	1935	400	5806	645
20	76	51	123	1524	1016	3871	400	5806	2581
20	76	76	155	1524	1524	5806	400	5806	5806
20	102	25	113	2032	508	2581	400	10323	645
20	102	51	139	2032	1016	5161	400	10323	2581
20	102	76	168	2032	1524	7742	400	10323	5806
20	127	25	143	2540	508	3226	400	16129	645
20	127	51	164	2540	1016	6452	400	16129	2581
20	127	76	165	2540	1524	9677	400	16129	5806

General Linear Model

```
Factor     Type Levels Values
Eps       fixed      4  5 10 15 20
W         fixed      3  76.2 101.6 127.0
S         fixed      3 25.4 50.8 76.2

Analysis of Variance for d, using Adjusted SS for Tests

Source     DF     Seq SS     Adj SS     Adj MS       F      P
Eps         3     1396.8     1396.7      465.6    6.54  0.002
W           2     6851.4     6851.4     3425.7   48.13  0.000
S           2    13165.1    13165.1     6582.5   92.47  0.000
Error      28     1993.1     1993.1       71.2
Total      35    23406.3

Tukey Simultaneous Tests
Response Variable d
All Pairwise Comparisons among Levels of Eps

Eps = 5 subtracted from:

Level   Difference       SE of             Adjusted
Eps       of Means  Difference   T-Value    P-Value
10           10.89       3.977     2.738     0.0492
15           14.33       3.977     3.604     0.0062
20           16.00       3.977     4.023     0.0021

Eps = 10 subtracted from:

Level   Difference       SE of             Adjusted
Eps       of Means  Difference   T-Value    P-Value
15           3.444       3.977    0.8660     0.8222
20           5.111       3.977    1.2851     0.5797

Eps = 15 subtracted from:

Level   Difference       SE of             Adjusted
Eps       of Means  Difference   T-Value    P-Value
20           1.667       3.977    0.4191     0.9748

Tukey Simultaneous Tests
Response Variable d
All Pairwise Comparisons among Levels of W

W = 76.2 subtracted from:

Level     Difference       SE of             Adjusted
W           of Means  Difference   T-Value    P-Value
101.6          15.42       3.444     4.476     0.0003
127.0          33.75       3.444     9.799     0.0000

W = 101.6 subtracted from:

Level     Difference       SE of             Adjusted
```

```
W           of Means  Difference   T-Value    P-Value
127.0          18.33       3.444     5.323     0.0000

Tukey Simultaneous Tests
Response Variable d
All Pairwise Comparisons among Levels of S

S = 25.4 subtracted from:

Level    Difference       SE of             Adjusted
S          of Means  Difference   T-Value    P-Value
50.8          25.92       3.444     7.524     0.0000
76.2          46.75       3.444    13.573     0.0000

S = 50.8 subtracted from:

Level    Difference       SE of             Adjusted
S          of Means  Difference   T-Value    P-Value
76.2          20.83       3.444     6.048     0.0000
```

Regression Analysis

```
The regression equation is
d = - 84.0 + 3.33 Eps + 1.45 W + 2.50 S - 0.0155 W*S - 0.0922 Eps**2

Predictor        Coef       StDev          T        P
Constant      -84.000       9.508      -8.83    0.000
Eps            3.3344      0.6746       4.94    0.000
W             1.45177     0.08472      17.14    0.000
S              2.4951      0.1601      15.58    0.000
W*S         -0.015500    0.001544     -10.04    0.000
Eps**2       -0.09222     0.02656      -3.47    0.002

S = 3.984       R-Sq = 98.0%     R-Sq(adj) = 97.6%

Analysis of Variance

Source            DF          SS          MS         F        P
Regression         5     22930.0      4586.0    288.88    0.000
Residual Error    30       476.3        15.9
Total             35     23406.3

Source       DF      Seq SS
Eps           1      1190.9
W             1      6834.4
S             1     13113.4
W*S           1      1600.0
Eps**2        1       191.4

Unusual Observations
Obs        Eps          d         Fit   StDev Fit    Residual    St Resid
  8        5.0    149.000     141.492       1.529       7.508        2.04R
 17       10.0    159.000     151.247       1.277       7.753        2.05R

R denotes an observation with a large standardized residual
```

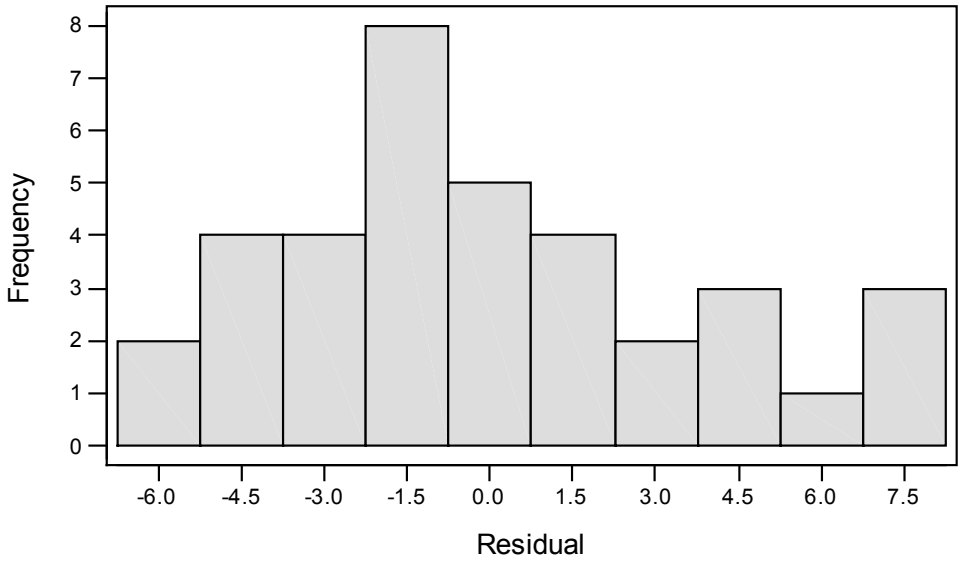

Figure B.1. Histogram of the Residuals (response is d)

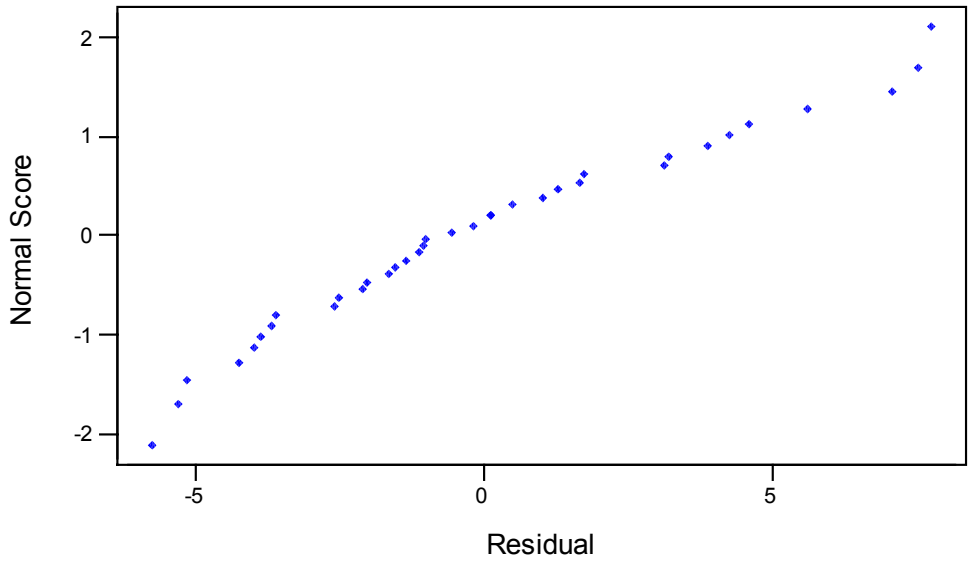

Figure B.2. Normal Probability Plot of the Residuals (response is d)

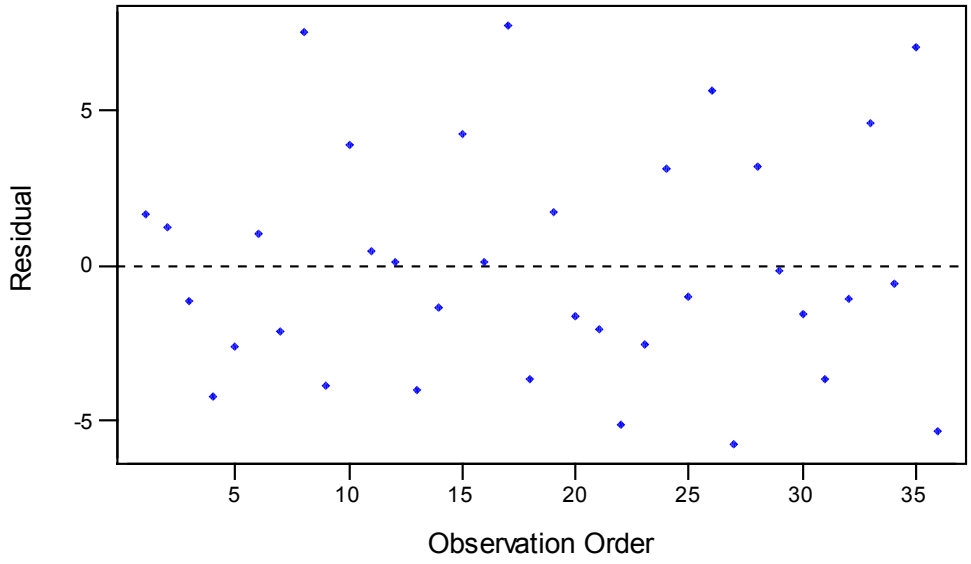

Figure B.3. Residuals versus the order of the data (response is d)

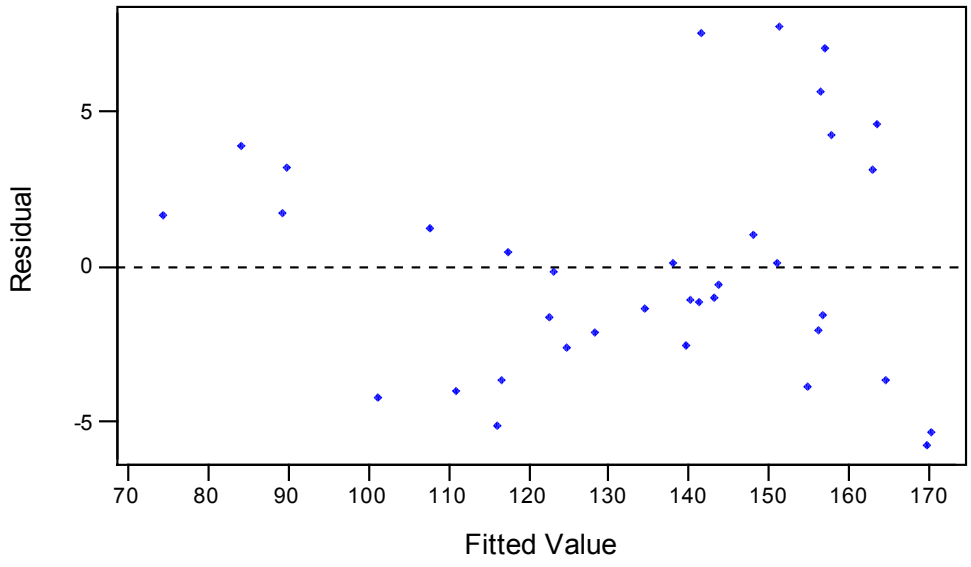

Figure B.4 Residuals versus the fitted values (response is d)

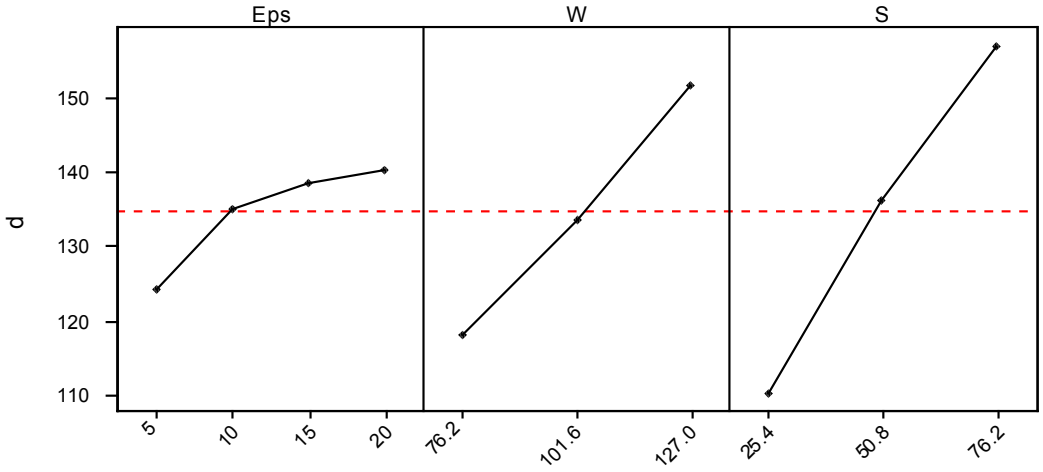

Figure B.5. Main effects plot – data means for d

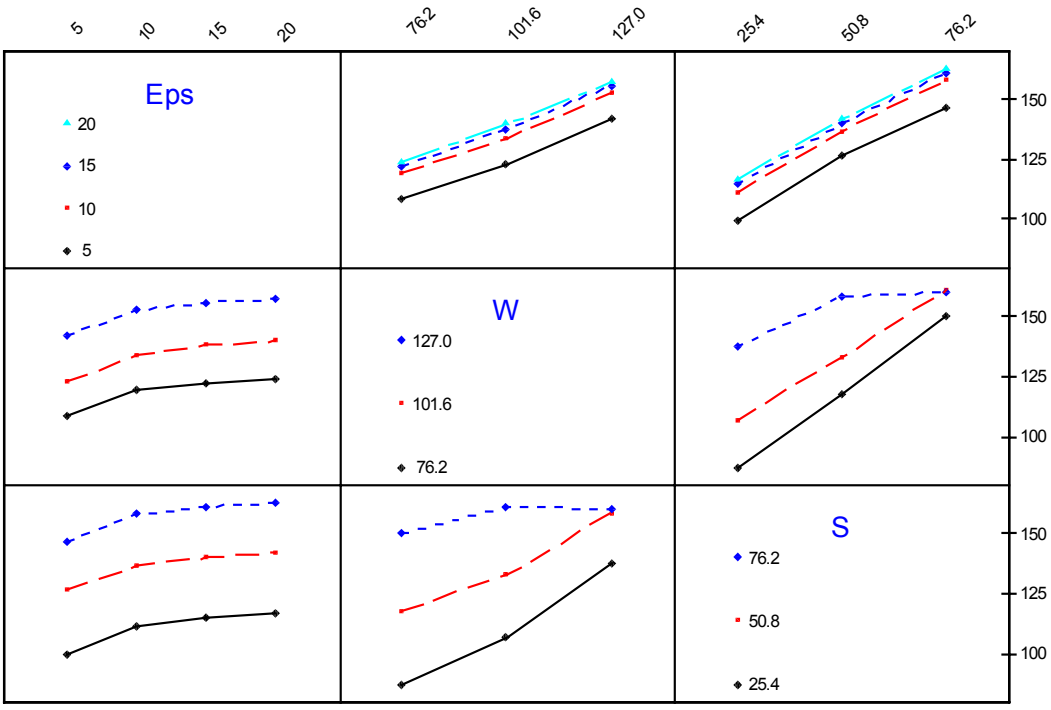

Figure B.6. Interaction plot- data means for d

Table B.12. Effective depth normalized to 64 mm slab thickness

Eps	S (mm)	W (mm)				
		76	89	102	114	127
5	25	1.17	1.38	1.59	1.80	2.02
	38	1.43	1.61	1.78	1.95	2.12
	51	1.70	1.83	1.96	2.10	2.23
	63	1.96	2.06	2.15	2.24	2.33
	76	2.23	2.28	2.33	2.39	2.44
10	25	1.32	1.54	1.75	1.96	2.17
	38	1.59	1.76	1.93	2.10	2.28
	51	1.85	1.98	2.12	2.25	2.38
	63	2.12	2.21	2.30	2.39	2.49
	76	2.38	2.43	2.49	2.54	2.59
15	25	1.40	1.62	1.83	2.04	2.25
	38	1.67	1.84	2.01	2.18	2.36
	51	1.93	2.06	2.20	2.33	2.46
	63	2.20	2.29	2.38	2.48	2.57
	76	2.46	2.51	2.57	2.62	2.67
20	25	1.41	1.62	1.84	2.05	2.26
	38	1.68	1.85	2.02	2.19	2.36
	51	1.94	2.07	2.21	2.34	2.47
	63	2.20	2.30	2.39	2.48	2.58
	76	2.47	2.52	2.58	2.63	2.68

Table B.13. Effective depth normalized to 76 mm slab thickness

Eps	S (mm)	W (mm)				
		76	89	102	114	127
5	25	0.98	1.15	1.33	1.50	1.68
	38	1.20	1.34	1.48	1.63	1.77
	51	1.42	1.53	1.64	1.75	1.86
	63	1.63	1.71	1.79	1.87	1.95
	76	1.85	1.90	1.94	1.99	2.03
10	25	1.10	1.28	1.46	1.63	1.81
	38	1.32	1.47	1.61	1.75	1.90
	51	1.54	1.65	1.76	1.87	1.98
	63	1.76	1.84	1.92	2.00	2.07
	76	1.98	2.03	2.07	2.12	2.16
15	25	1.17	1.35	1.52	1.70	1.87
	38	1.39	1.53	1.68	1.82	1.96
	51	1.61	1.72	1.83	1.94	2.05
	63	1.83	1.91	1.99	2.06	2.14
	76	2.05	2.09	2.14	2.18	2.23
20	25	1.18	1.35	1.53	1.71	1.88
	38	1.40	1.54	1.68	1.83	1.97
	51	1.62	1.73	1.84	1.95	2.06
	63	1.84	1.91	1.99	2.07	2.15
	76	2.06	2.10	2.15	2.19	2.24

Table B.14. Effective depth normalized to 89 mm slab thickness

Eps	S (mm)	W (mm)				
		76	89	102	114	127
5	25	0.84	0.99	1.14	1.29	1.44
	38	1.02	1.15	1.27	1.39	1.52
	51	1.21	1.31	1.40	1.50	1.59
	63	1.40	1.47	1.53	1.60	1.67
	76	1.59	1.63	1.67	1.71	1.74
10	25	0.95	1.10	1.25	1.40	1.55
	38	1.13	1.26	1.38	1.50	1.63
	51	1.32	1.42	1.51	1.61	1.70
	63	1.51	1.58	1.64	1.71	1.78
	76	1.70	1.74	1.78	1.81	1.85
15	25	1.00	1.15	1.31	1.46	1.61
	38	1.19	1.31	1.44	1.56	1.68
	51	1.38	1.47	1.57	1.66	1.76
	63	1.57	1.64	1.70	1.77	1.83
	76	1.76	1.80	1.83	1.87	1.91
20	25	1.01	1.16	1.31	1.46	1.61
	38	1.20	1.32	1.44	1.57	1.69
	51	1.39	1.48	1.58	1.67	1.76
	63	1.57	1.64	1.71	1.77	1.84
	76	1.76	1.80	1.84	1.88	1.92

Table B.15. Effective depth normalized to 102 mm slab thickness

Eps	S (mm)	W (mm)				
		76	89	102	114	127
5	25	0.73	0.86	1.00	1.13	1.26
	38	0.90	1.00	1.11	1.22	1.33
	51	1.06	1.14	1.23	1.31	1.39
	63	1.23	1.28	1.34	1.40	1.46
	76	1.39	1.42	1.46	1.49	1.53
10	25	0.83	0.96	1.09	1.22	1.36
	38	0.99	1.10	1.21	1.31	1.42
	51	1.16	1.24	1.32	1.41	1.49
	63	1.32	1.38	1.44	1.50	1.55
	76	1.49	1.52	1.55	1.59	1.62
15	25	0.88	1.01	1.14	1.27	1.41
	38	1.04	1.15	1.26	1.37	1.47
	51	1.21	1.29	1.37	1.46	1.54
	63	1.37	1.43	1.49	1.55	1.61
	76	1.54	1.57	1.60	1.64	1.67
20	25	0.88	1.02	1.15	1.28	1.41
	38	1.05	1.16	1.26	1.37	1.48
	51	1.21	1.30	1.38	1.46	1.54
	63	1.38	1.44	1.49	1.55	1.61
	76	1.54	1.58	1.61	1.64	1.68

Table B.16. Effective depth normalized to 114 mm slab thickness

Eps	S (mm)	W (mm)				
		76	89	102	114	127
5	25	0.65	0.77	0.89	1.00	1.12
	38	0.80	0.89	0.99	1.08	1.18
	51	0.94	1.02	1.09	1.16	1.24
	63	1.09	1.14	1.19	1.25	1.30
	76	1.24	1.27	1.30	1.33	1.36
10	25	0.74	0.85	0.97	1.09	1.20
	38	0.88	0.98	1.07	1.17	1.26
	51	1.03	1.10	1.18	1.25	1.32
	63	1.18	1.23	1.28	1.33	1.38
	76	1.32	1.35	1.38	1.41	1.44
15	25	0.78	0.90	1.02	1.13	1.25
	38	0.93	1.02	1.12	1.21	1.31
	51	1.07	1.15	1.22	1.29	1.37
	63	1.22	1.27	1.32	1.38	1.43
	76	1.37	1.40	1.43	1.46	1.49
20	25	0.78	0.90	1.02	1.14	1.25
	38	0.93	1.03	1.12	1.22	1.31
	51	1.08	1.15	1.23	1.30	1.37
	63	1.22	1.28	1.33	1.38	1.43
	76	1.37	1.40	1.43	1.46	1.49

Table B.17. Effective depth normalized to 127 mm slab thickness

Eps	S (mm)	W (mm)				
		76	89	102	114	127
5	25	0.59	0.69	0.80	0.90	1.01
	38	0.72	0.80	0.89	0.98	1.06
	51	0.85	0.92	0.98	1.05	1.11
	63	0.98	1.03	1.07	1.12	1.17
	76	1.11	1.14	1.17	1.19	1.22
10	25	0.66	0.77	0.87	0.98	1.08
	38	0.79	0.88	0.97	1.05	1.14
	51	0.93	0.99	1.06	1.12	1.19
	63	1.06	1.10	1.15	1.20	1.24
	76	1.19	1.22	1.24	1.27	1.30
15	25	0.70	0.81	0.91	1.02	1.12
	38	0.83	0.92	1.01	1.09	1.18
	51	0.97	1.03	1.10	1.16	1.23
	63	1.10	1.14	1.19	1.24	1.28
	76	1.23	1.26	1.28	1.31	1.34
20	25	0.71	0.81	0.92	1.02	1.13
	38	0.84	0.92	1.01	1.10	1.18
	51	0.97	1.04	1.10	1.17	1.24
	63	1.10	1.15	1.20	1.24	1.29
	76	1.23	1.26	1.29	1.31	1.34

Table B.18. Effective depth normalized to 140 mm slab thickness

Eps	S (mm)	W (mm)				
		76	89	102	114	127
5	25	0.53	0.63	0.72	0.82	0.92
	38	0.65	0.73	0.81	0.89	0.96
	51	0.77	0.83	0.89	0.95	1.01
	63	0.89	0.93	0.98	1.02	1.06
	76	1.01	1.04	1.06	1.09	1.11
10	25	0.60	0.70	0.79	0.89	0.99
	38	0.72	0.80	0.88	0.96	1.03
	51	0.84	0.90	0.96	1.02	1.08
	63	0.96	1.00	1.05	1.09	1.13
	76	1.08	1.11	1.13	1.15	1.18
15	25	0.64	0.73	0.83	0.93	1.02
	38	0.76	0.84	0.91	0.99	1.07
	51	0.88	0.94	1.00	1.06	1.12
	63	1.00	1.04	1.08	1.13	1.17
	76	1.12	1.14	1.17	1.19	1.22
20	25	0.64	0.74	0.83	0.93	1.03
	38	0.76	0.84	0.92	1.00	1.07
	51	0.88	0.94	1.00	1.06	1.12
	63	1.00	1.04	1.09	1.13	1.17
	76	1.12	1.15	1.17	1.20	1.22

Table B.19. Effective depth normalized to 152 mm slab thickness

Eps	S (mm)	W (mm)				
		76	89	102	114	127
5	25	0.49	0.58	0.66	0.75	0.84
	38	0.60	0.67	0.74	0.81	0.88
	51	0.71	0.76	0.82	0.87	0.93
	63	0.82	0.86	0.90	0.93	0.97
	76	0.93	0.95	0.97	0.99	1.02
10	25	0.55	0.64	0.73	0.82	0.90
	38	0.66	0.73	0.80	0.88	0.95
	51	0.77	0.83	0.88	0.94	0.99
	63	0.88	0.92	0.96	1.00	1.04
	76	0.99	1.01	1.04	1.06	1.08
15	25	0.59	0.67	0.76	0.85	0.94
	38	0.70	0.77	0.84	0.91	0.98
	51	0.81	0.86	0.92	0.97	1.03
	63	0.91	0.95	0.99	1.03	1.07
	76	1.02	1.05	1.07	1.09	1.11
20	25	0.59	0.68	0.76	0.85	0.94
	38	0.70	0.77	0.84	0.91	0.99
	51	0.81	0.86	0.92	0.97	1.03
	63	0.92	0.96	1.00	1.03	1.07
	76	1.03	1.05	1.07	1.10	1.12

Table B.20. Effective depth normalized to 165 mm slab thickness

Eps	S (mm)	W (mm)				
		76	89	102	114	127
5	25	0.45	0.53	0.61	0.69	0.78
	38	0.55	0.62	0.68	0.75	0.82
	51	0.65	0.70	0.76	0.81	0.86
	63	0.75	0.79	0.83	0.86	0.90
	76	0.86	0.88	0.90	0.92	0.94
10	25	0.51	0.59	0.67	0.75	0.83
	38	0.61	0.68	0.74	0.81	0.88
	51	0.71	0.76	0.81	0.87	0.92
	63	0.81	0.85	0.89	0.92	0.96
	76	0.92	0.94	0.96	0.98	1.00
15	25	0.54	0.62	0.70	0.78	0.87
	38	0.64	0.71	0.77	0.84	0.91
	51	0.74	0.79	0.85	0.90	0.95
	63	0.84	0.88	0.92	0.95	0.99
	76	0.95	0.97	0.99	1.01	1.03
20	25	0.54	0.62	0.71	0.79	0.87
	38	0.64	0.71	0.78	0.84	0.91
	51	0.75	0.80	0.85	0.90	0.95
	63	0.85	0.88	0.92	0.96	0.99
	76	0.95	0.97	0.99	1.01	1.03

Table B.21. Effective depth normalized to 178 mm slab thickness

Eps	S (mm)	W (mm)				
		76	89	102	114	127
5	25	0.45	0.53	0.61	0.69	0.78
	38	0.55	0.62	0.68	0.75	0.82
	51	0.65	0.70	0.76	0.81	0.86
	63	0.75	0.79	0.83	0.86	0.90
	76	0.86	0.88	0.90	0.92	0.94
10	25	0.51	0.59	0.67	0.75	0.83
	38	0.61	0.68	0.74	0.81	0.88
	51	0.71	0.76	0.81	0.87	0.92
	63	0.81	0.85	0.89	0.92	0.96
	76	0.92	0.94	0.96	0.98	1.00
15	25	0.54	0.62	0.70	0.78	0.87
	38	0.64	0.71	0.77	0.84	0.91
	51	0.74	0.79	0.85	0.90	0.95
	63	0.84	0.88	0.92	0.95	0.99
	76	0.95	0.97	0.99	1.01	1.03
20	25	0.54	0.62	0.71	0.79	0.87
	38	0.64	0.71	0.78	0.84	0.91
	51	0.75	0.80	0.85	0.90	0.95
	63	0.85	0.88	0.92	0.96	0.99
	76	0.95	0.97	0.99	1.01	1.03

Table B.22. Optimum design configurations for different desired penetration depth

Desired penetration depth (mm)	Eps	W x S (mm)
76	5	76 x 25
	10	None
	15	None
	20	None
89	5	89 x 38
	10	76 x 25
	15	76 x 25
	20	76 x 25
102	5	102 x 25 89 x 38
	10	76 x 38
	15	89 x 25
	20	89 x 25
114	5	114 x 25
	10	89 x 38
	15	102 x 25 89 x 38
	20	102 x 25
127	5	127 x 25
	10	89 x 51
	15	102 x 38
	20	102 x 38
140	5	127 x 51
	10	89 x 63
	15	102 x 51
	20	114 x 38 102 x 51 76 x 63
152	5	114 x 76
	10	114 x 63
	15	102 x 63
	20	102 x 63
165	5	127 x 76
	10	127 x 76
	15	127 x 63
	20	114 x 76
178	5	127 x 76
	10	127 x 76
	15	127 x 63
	20	127 x 63

APPENDIX C: C-PROBE VALIDATION DATA

Table C.1. Proportions for different PCC mixes (after Diefenderfer, 1998)

Mix	Water (kg)	Cement (kg)	CA* (kg)	FA**(kg)
A	13.76	30.58	69.25	54.91
C	13.76	30.58	69.25	47.69
D	13.76	30.58	69.25	47.69
F	13.76	30.58	69.25	47.69

*CA: Coarse Aggregate

**FA: Fine Aggregate

Table C.2. Results of quality control testing (after Diefenderfer, 1998)

Mix	Unit Weight (kg/ m^3)	Slump (mm)	Air Content (%)	Compressive Strength		
				3 days (MPa)	7 days (Mpa)	28 days (MPa)
A	2950.60	64	1.6	31.41	35.80	45.13
C	2841.88	83	5.8	20.30	24.97	32.24
D	2809.91	102	7.2	19.75	21.95	30.59
F	2797.12	108	7.4	19.89	20.58	31.14

Table C.3. Mix design and specimen characteristics (after Diefenderfer, 1998)

Specimen Name	W/c ratio	Aggregate type	Air void content	Void (depth)	Void Thickness
A	0.45	Limestone	2%	None	-
C	0.45	Limestone	6%	None	-
D	0.45	Limestone	6%	25 mm	7.5 mm
F	0.45	Limestone	6%	25 mm	15 mm

Table C.4. Mix Design per m^3 of PCC (after Loulizi, 1999)

		M1	M2	M3	M4	M5
Coarse Aggregate	**Limestone (kg)**	1042.2	1064.1	-	1064.1	-
	Quartzite (kg)	-	-	1028.0	-	1026.8
Fine Aggregate	**Limestone (kg)**	733.5	-	-	-	-
	Sandstone (kg)	-	676.1	609.1	676.1	688.5
Cementiteous Materials	**Cement I (kg)**	418.5	418.5	339.5	389.2	300.4
	Fly Ash (kg)	-	-	80.0	-	64.6
	Silica Fume (kg)	-	-	-	29.3	-
Water	**(kg)**	171.3	171.3	171.8	171.3	160.0
Admixtures	**AE* (liters)**	0.98	0.98	0.98	0.98	0.98
	WRR (liters)**	1.27	1.27	1.27	1.27	1.27

* Air Entrainment

** Water Reducer Retarder

Table C.5. Quality control measurements for different mixes (after Loulizi 1999)

Mix	Unit Weight (kg/ m^3)	Slump (mm)	Air Content (%)	Compressive Strength		
				3 days (MPa)	7 days (Mpa)	28 days (MPa)
M1	2337.0	114.3	7.5	25.3	29.8	33.9
M2	2368	95.3	5.0	30.2	38.4	40.8
M3	2265.0	89.0	7.0	22.0	27.1	34.4
M4	2362.7	101.6	5.5	40.3	48.7	62.3
M5	2394.8	100.0	-	22.3	29.6	42.4

Table C.6. Portland cement concrete slab notations and slab characteristics for mixes 1, 2, & 4

Slab	Mix design			Slab characteristics
	1	2	4	
1	M1S1	M2S1	M4S1	Plain
2	M1S2	M2S2	M4S2	6.4 mm void thickness
3	M1S3	M2S3	M4S3	12.7 mm void thickness
4	M1S4	M2S4	M4S4	One way reinforcement
5	M1S5	M2S5	M4S5	Two ways reinforcement

Table C.7. Portland cement concrete slab notations and slab characteristics for mix 3

Slab	Mix design 3	Slab characteristics
1	M3S1	Plain PCC, 102-mm thick slab
2	M3S2	Plain PCC, 127-mm thick slab
3	M3S3	Plain PCC, 152-mm thick slab
4	M3S4	6.4 mm void thickness, 127-mm thick slab
5	M3S5	12.7 mm void thickness, 127-mm thick slab
6	M3S6	One way reinforcement, 127-mm thick slab
7	M3S7	Two ways reinforcement, 127-mm thick slab

Table C.8. Portland cement concrete slab notations and slab characteristics for mix 5

Slab	Mix design 5	Slab characteristics
1	M5S1	Plain
2	M5S2	Plain
3	M5S3	Plain
4	M5S4	Void
5	M5S5	Two way reinforcement
6	M5S6	Two way reinforcement + void

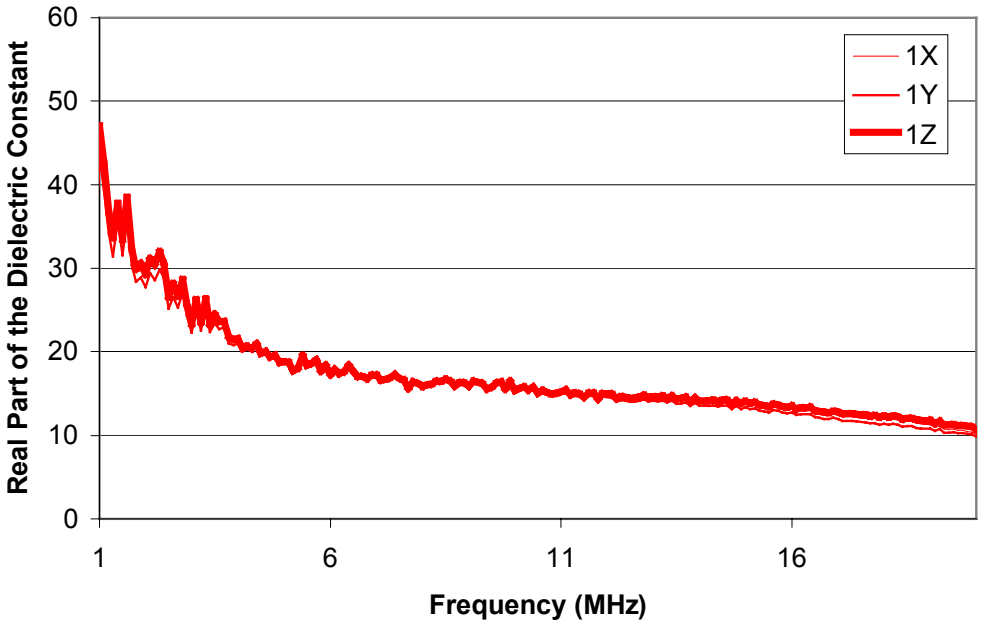

Figure C.1. Real part of the dielectric constant for different orientation at position 1

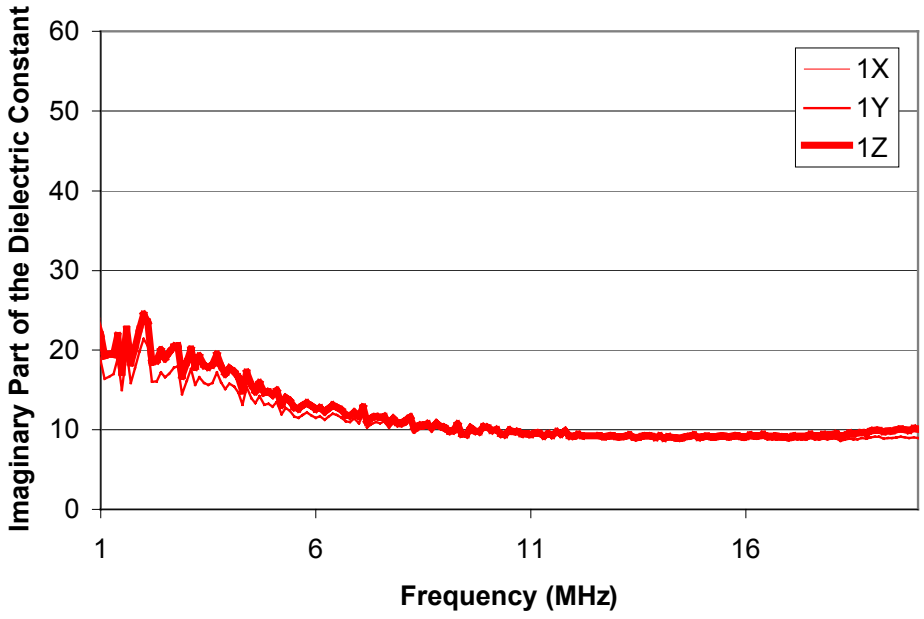

Figure C.2. Imaginary part of the dielectric constant for different orientation at position 1

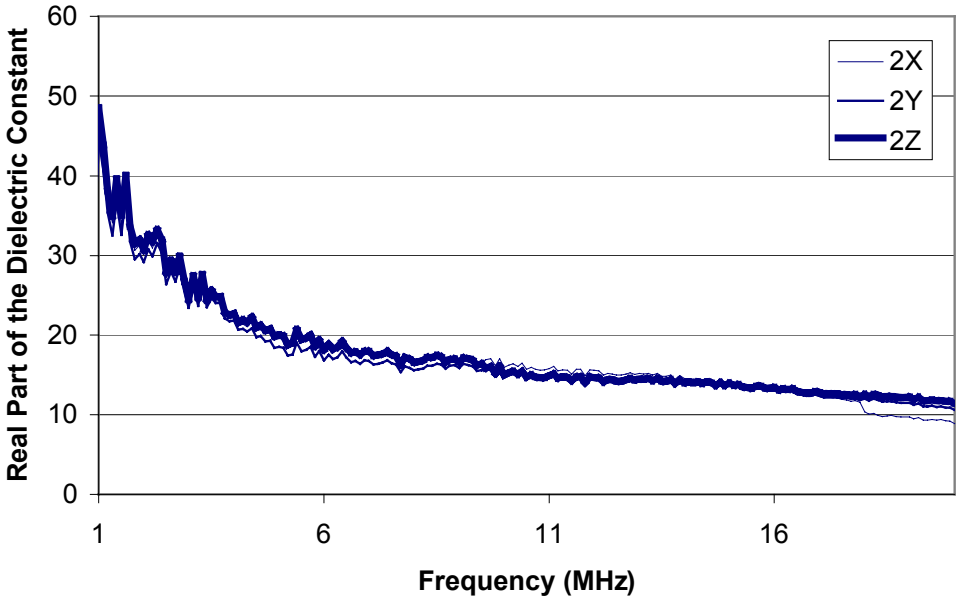

Figure C.3. Real part of the dielectric constant for different orientation at position 2

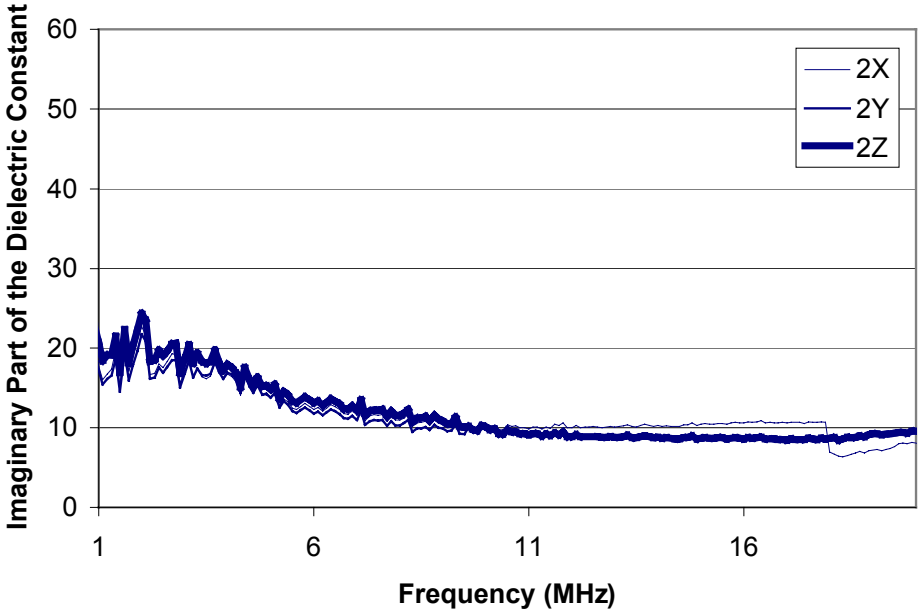

Figure C.4. Imaginary part of the dielectric constant for different orientation at position 2

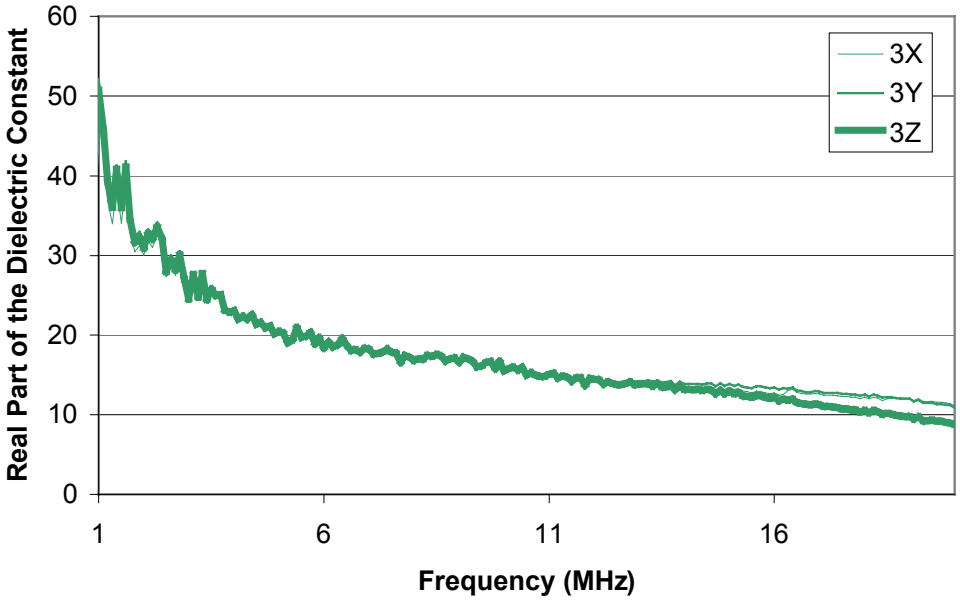

Figure C.5. Real part of the dielectric constant for different orientation at position 3

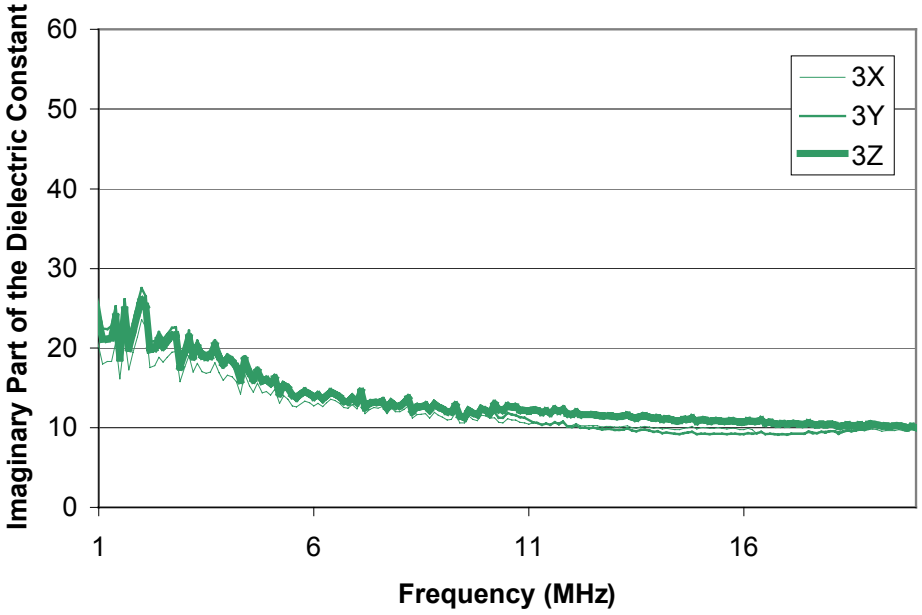

Figure C.6. Imaginary part of the dielectric constant for different orientation at position 3

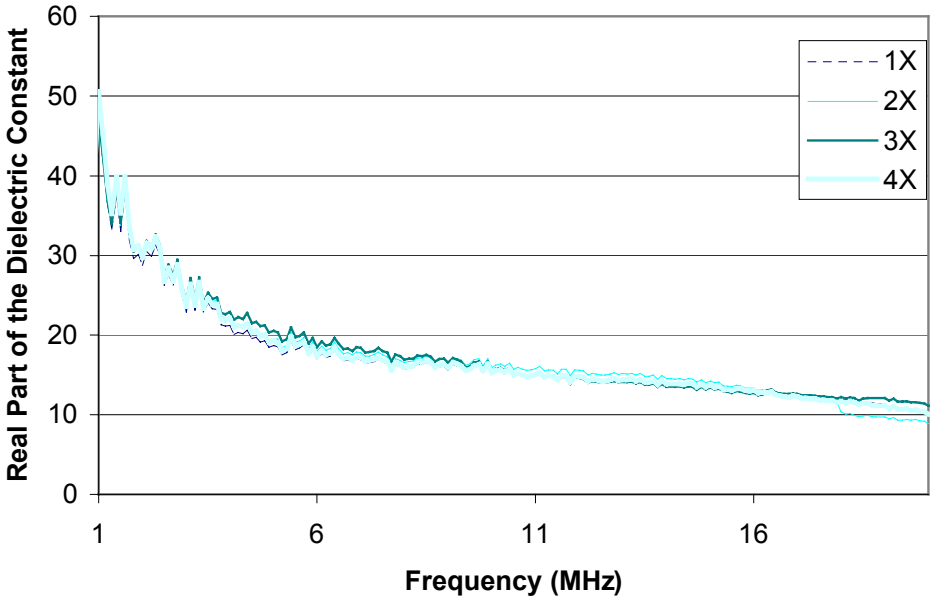

Figure C.7. Real part of the dielectric constant for different position at orientation X

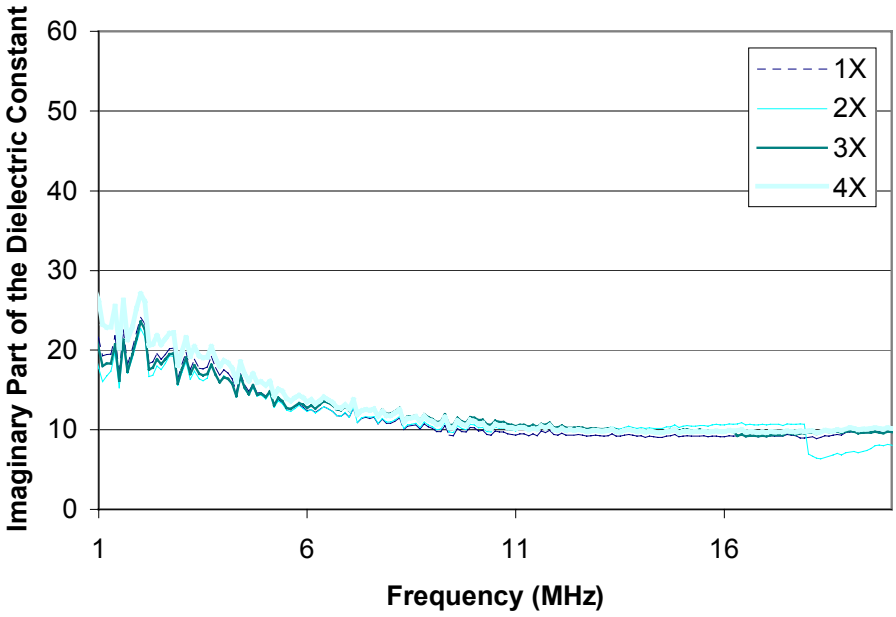

Figure C.8. Imaginary part of the dielectric constant for different position at orientation X

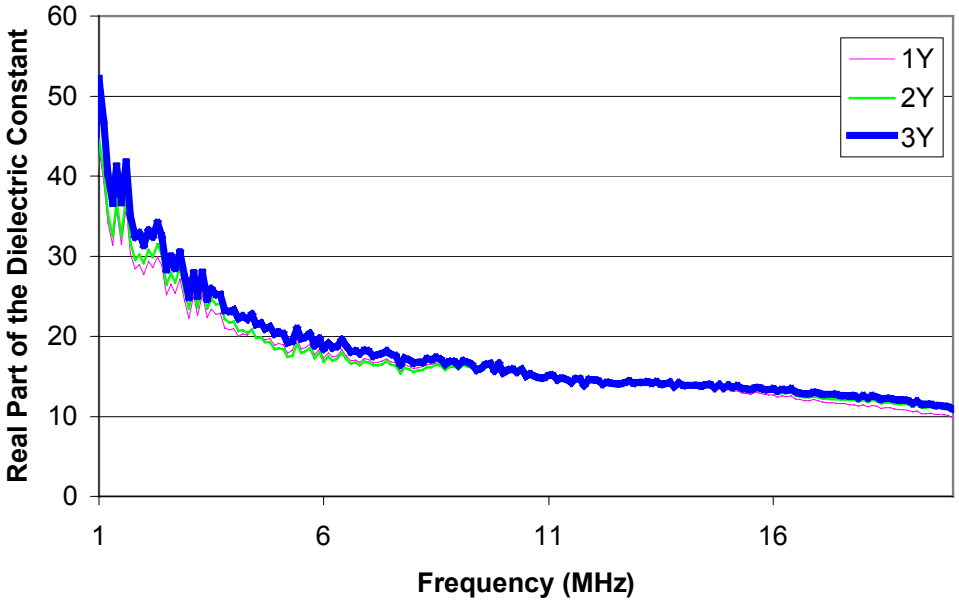

Figure C.9. Real part of the dielectric constant for different position at orientation Y

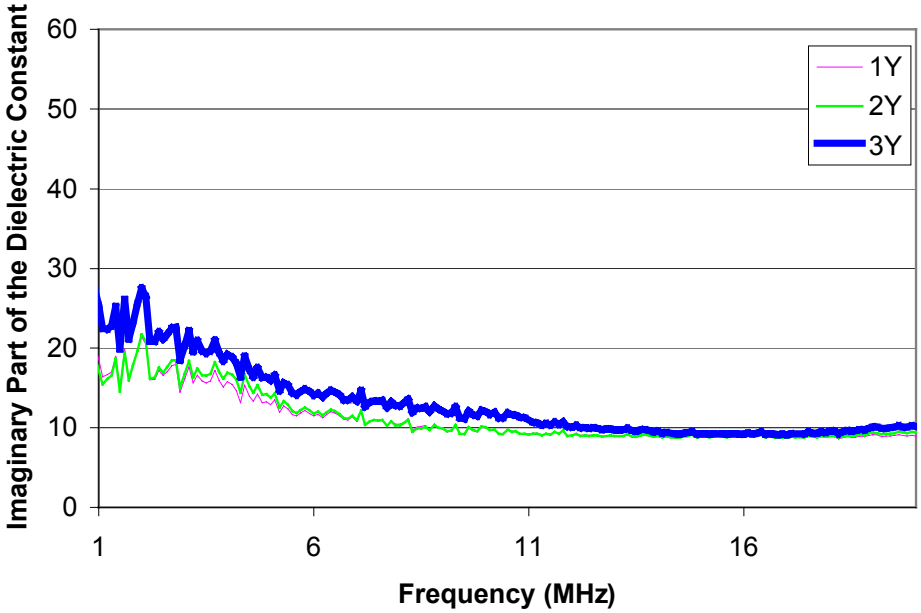

Figure C.10. Imaginary part of the dielectric constant for different position at orientation Y

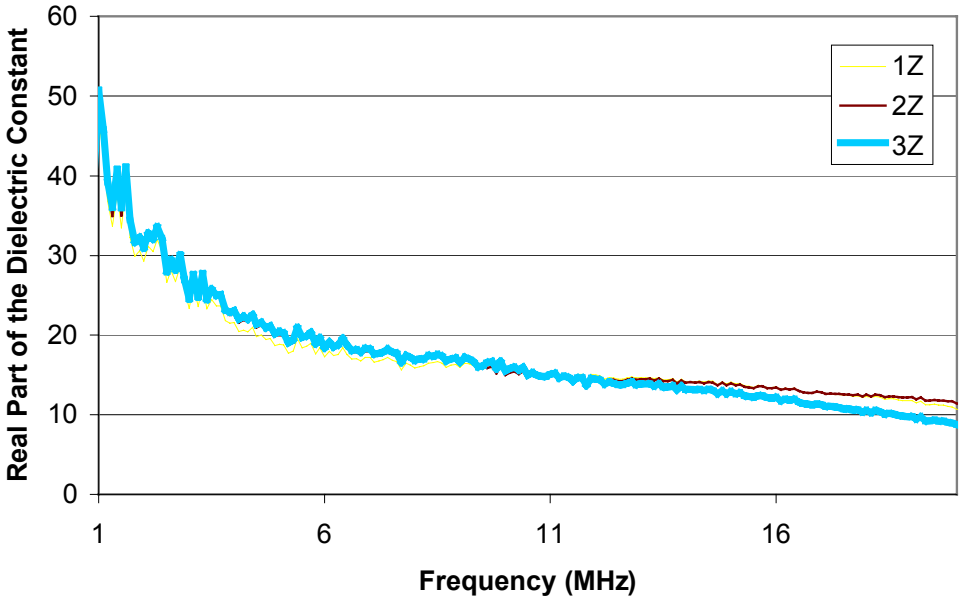

Figure C.11. Real part of the dielectric constant for different position at orientation Z

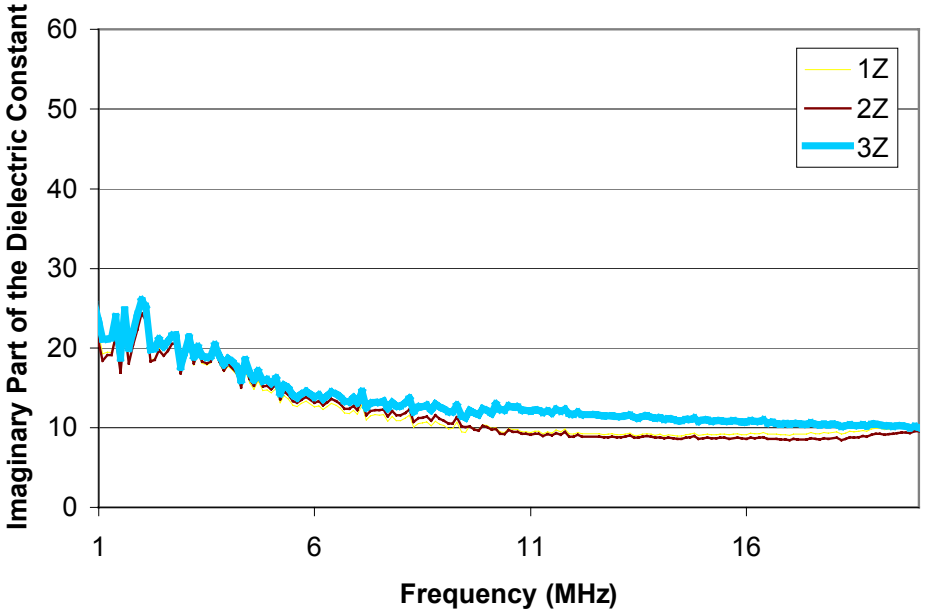

Figure C.12. Imaginary part of the dielectric constant for different position at orientation Z

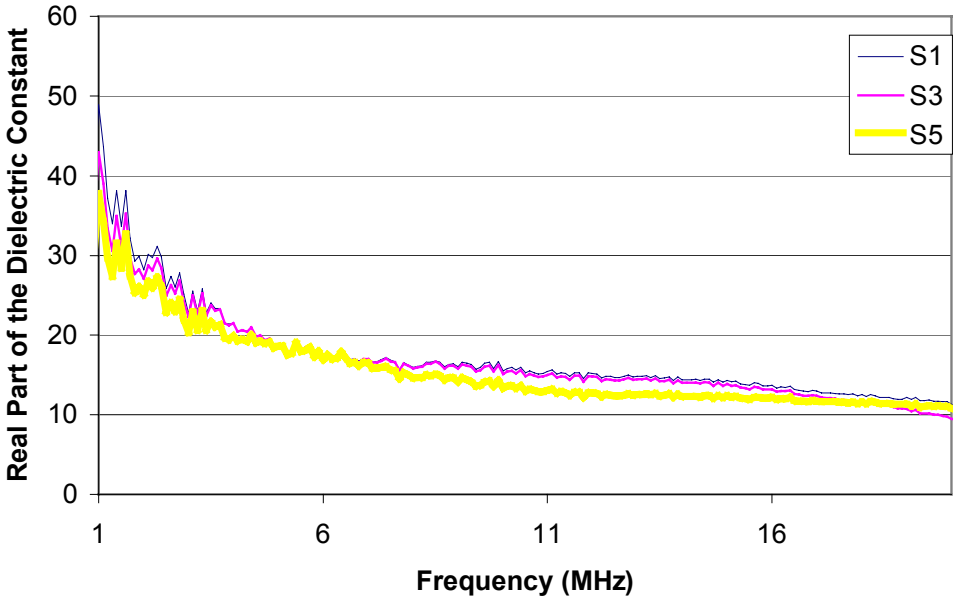

Figure C.13. Real part of the dielectric constant for different slabs at position 1X

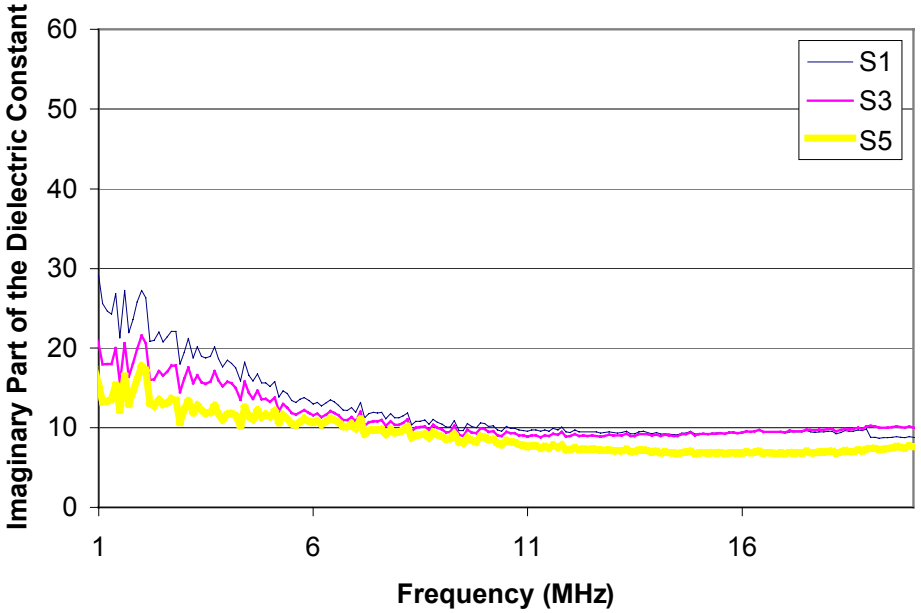

Figure C.14. Imaginary part of the dielectric constant for different slabs at position 1X

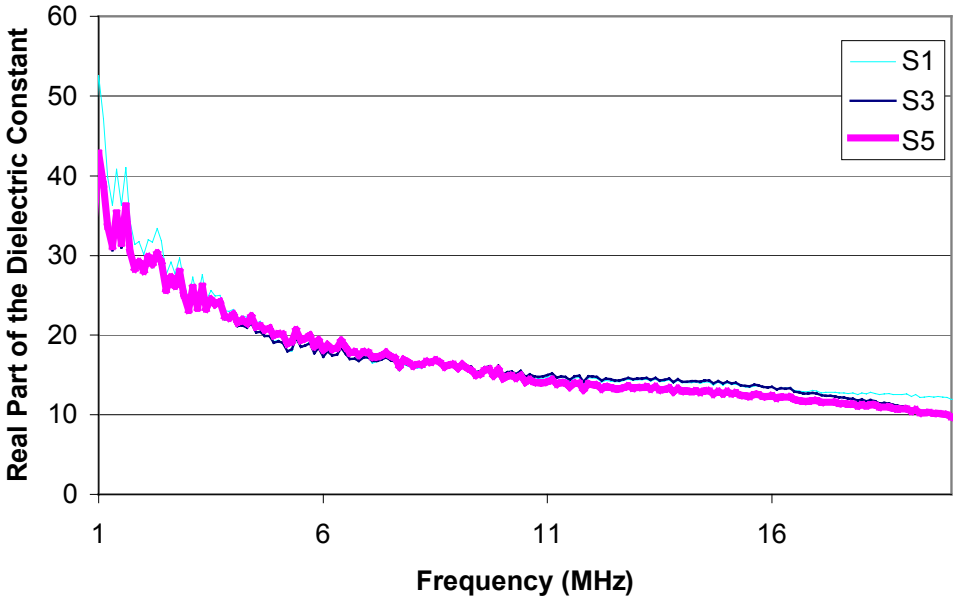

Figure C.15. Real part of the dielectric constant for different slabs at position 2X

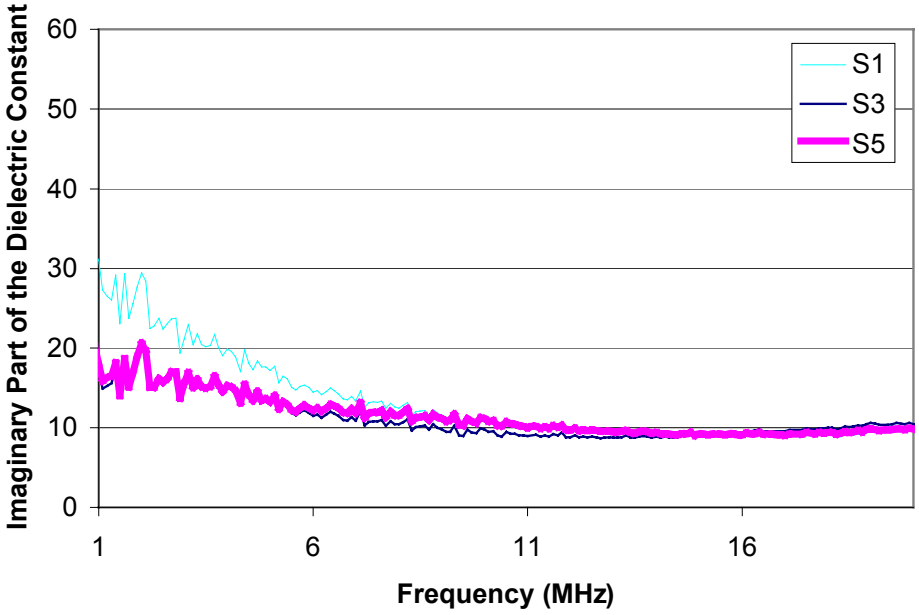

Figure C.16. Imaginary part of the dielectric constant for different slabs at position 2X

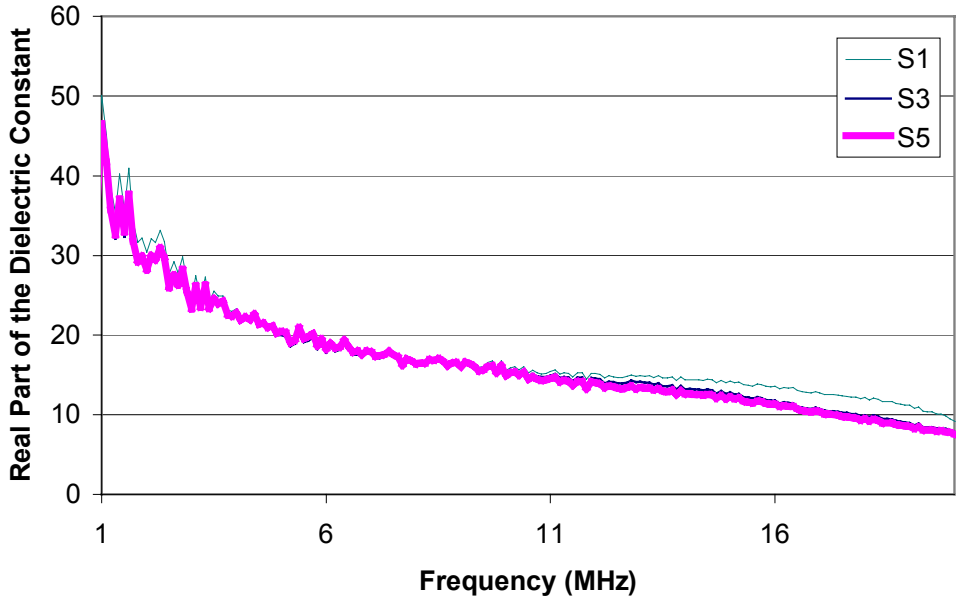

Figure C.17. Real part of the dielectric constant for different slabs at position 3X

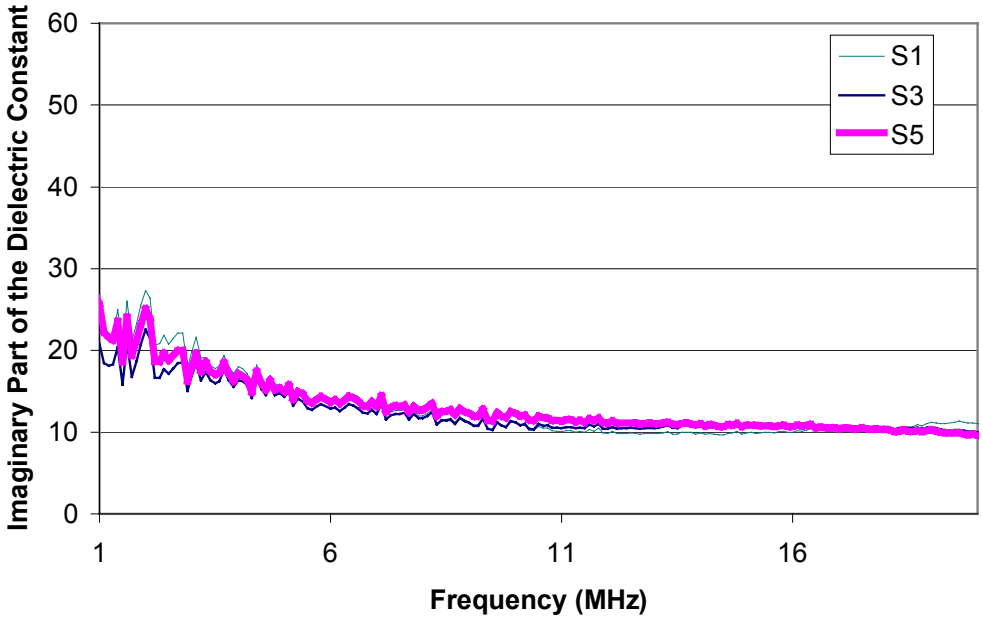

Figure C.18. Imaginary part of the dielectric constant for different slabs at position 3X

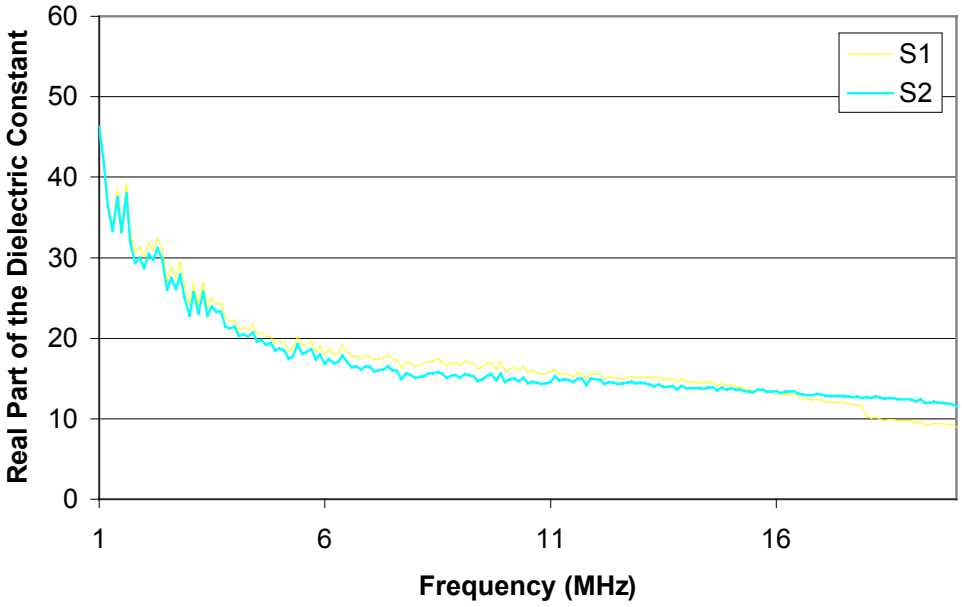

Figure C.19. Real part of the dielectric constant for different slabs at position 2X

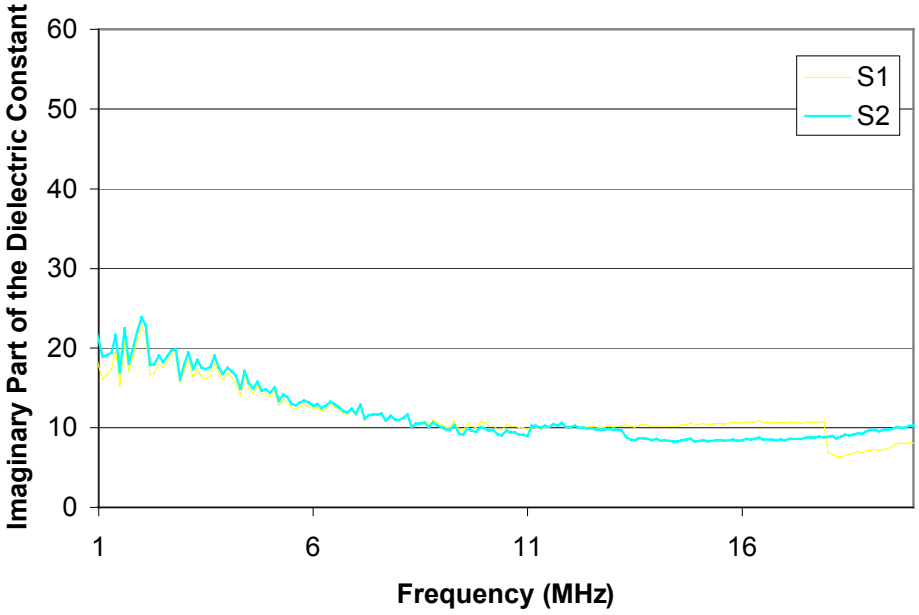

Figure C.20. Imaginary part of the dielectric constant for different slabs at position 2X

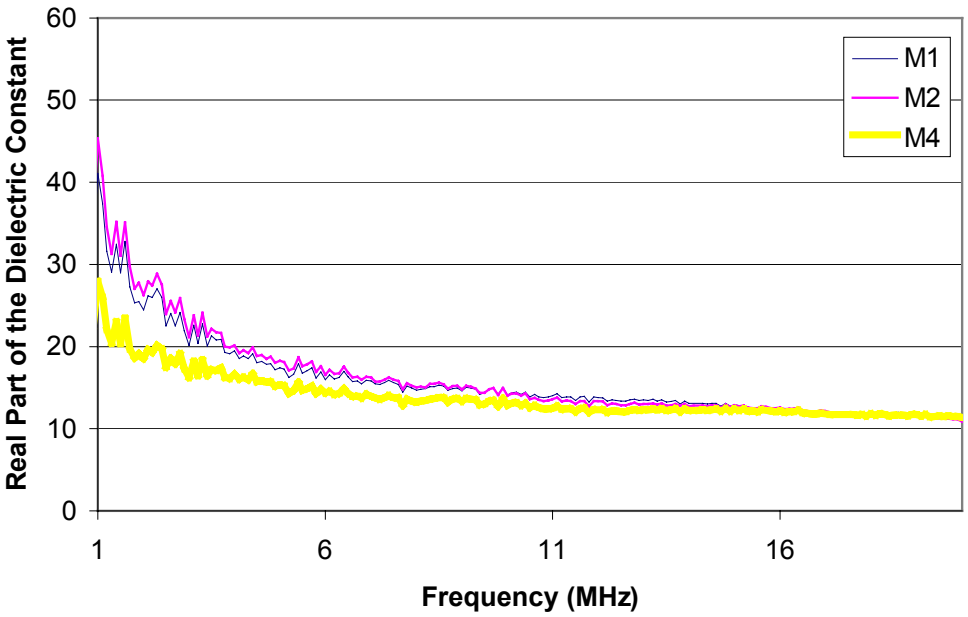

Figure C.21. Real part of the dielectric constant for S1 of different mix designs

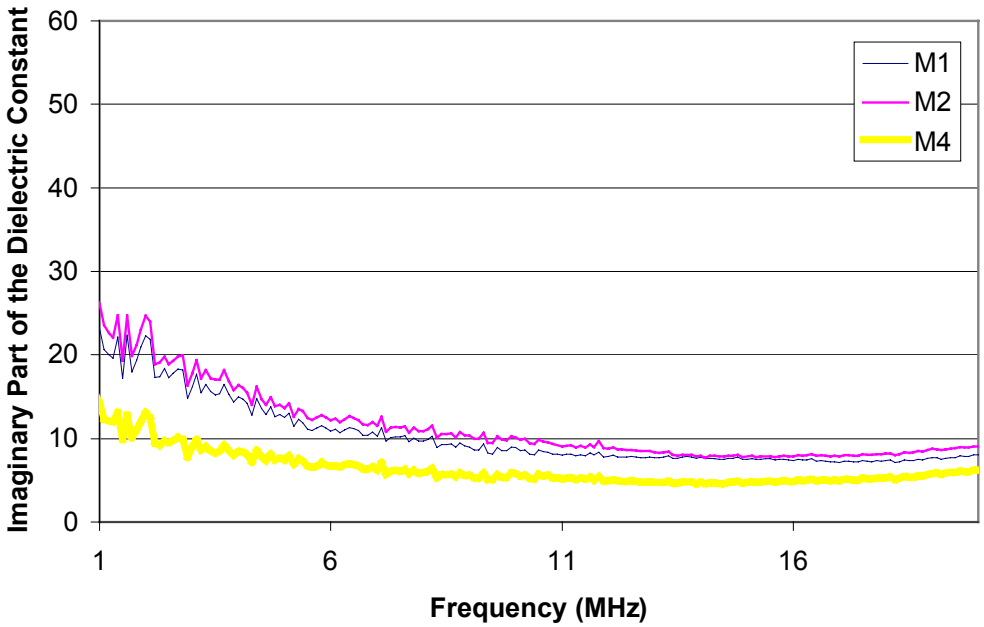

Figure C.22. Imaginary part of the dielectric constant for S1 of different mix designs

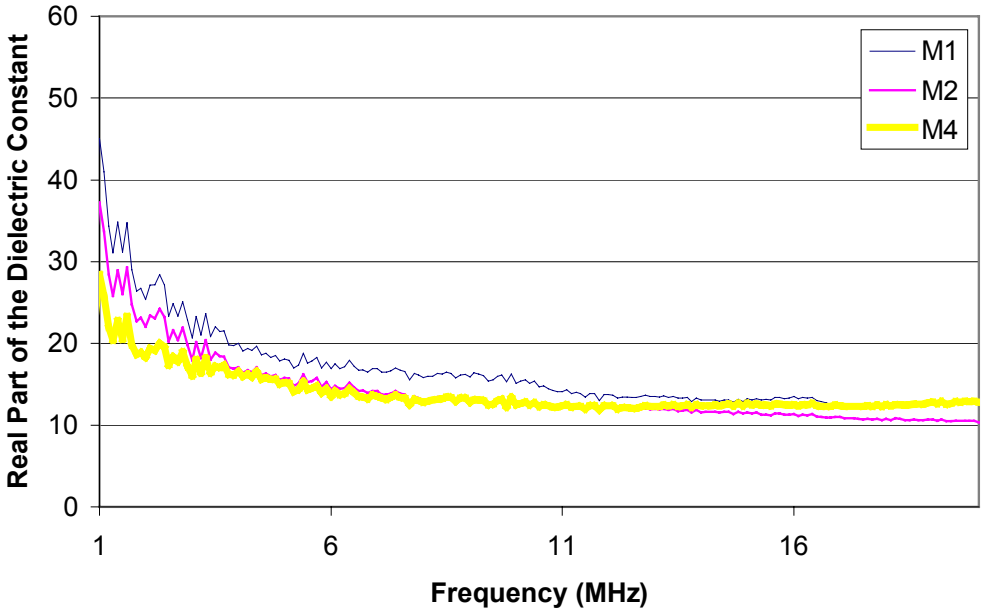

Figure C.23. Real part of the dielectric constant for S2 of different mix designs

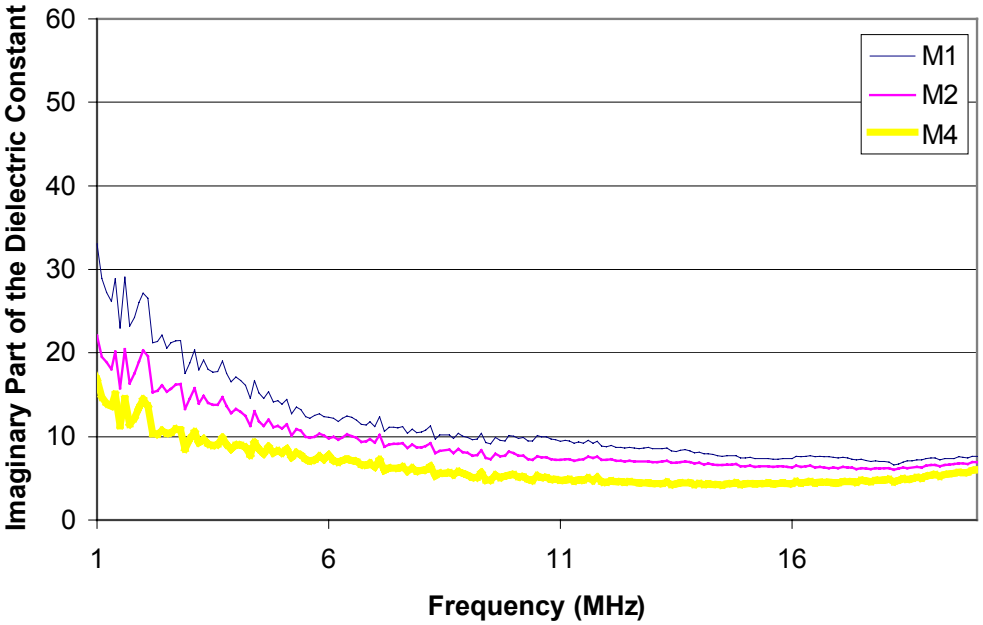

Figure C.24. Imaginary part of the dielectric constant for S2 of different mix designs

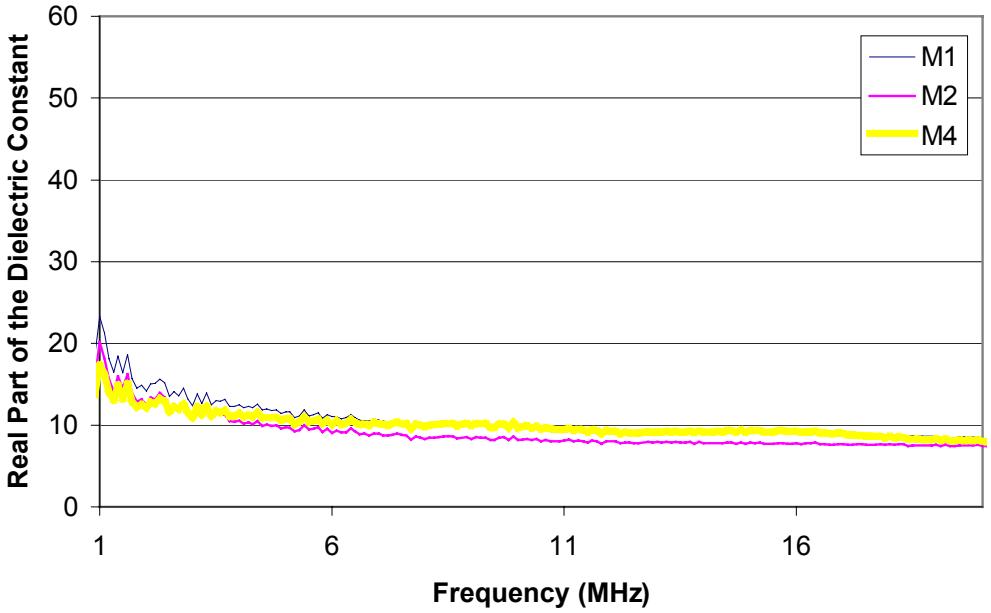

Figure C.25. Real part of the dielectric constant for S3 of different mix designs

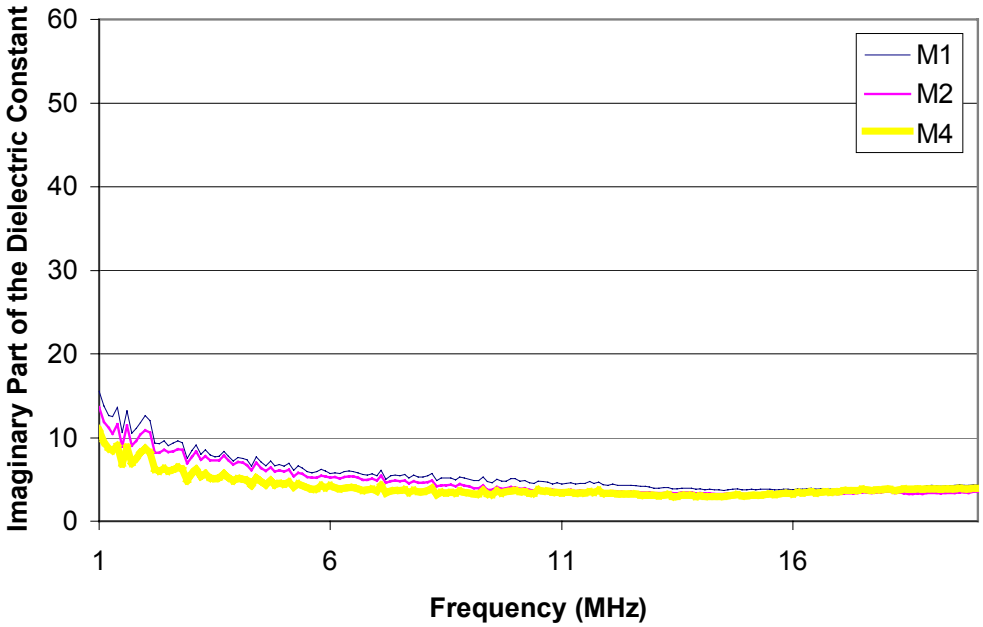

Figure C.26. Imaginary part of the dielectric constant for S3 of different mix designs

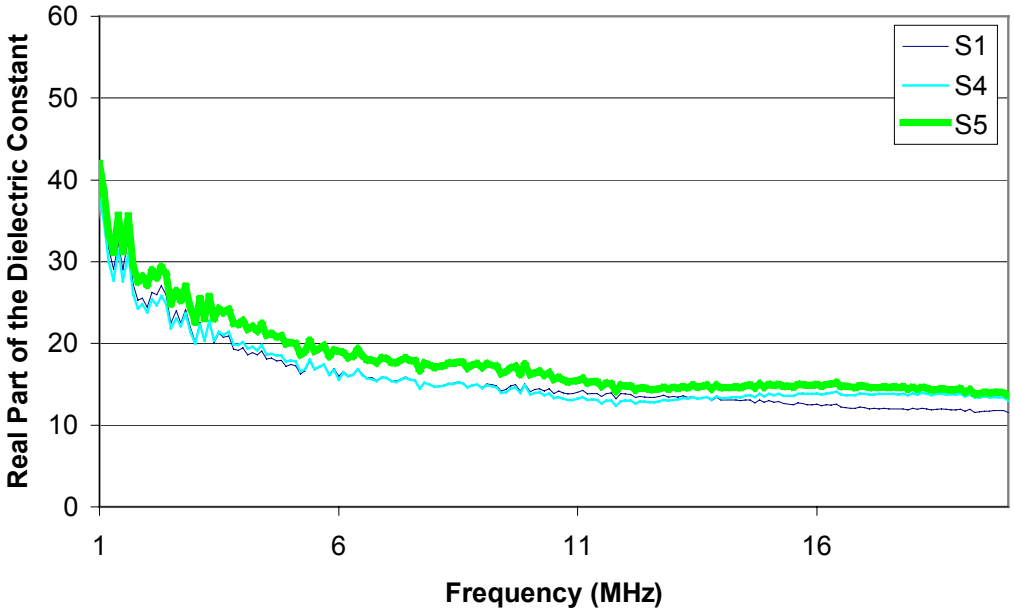

Figure C.27. Real part of the dielectric constant for M1 with different reinforcement conditions

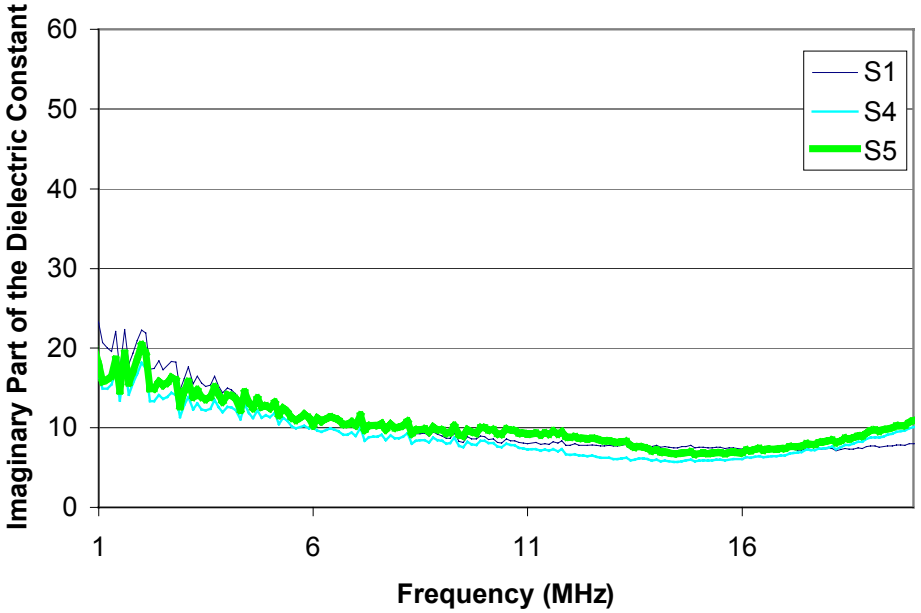

Figure C.28. Imaginary part of the dielectric constant for M1 with different reinforcement conditions

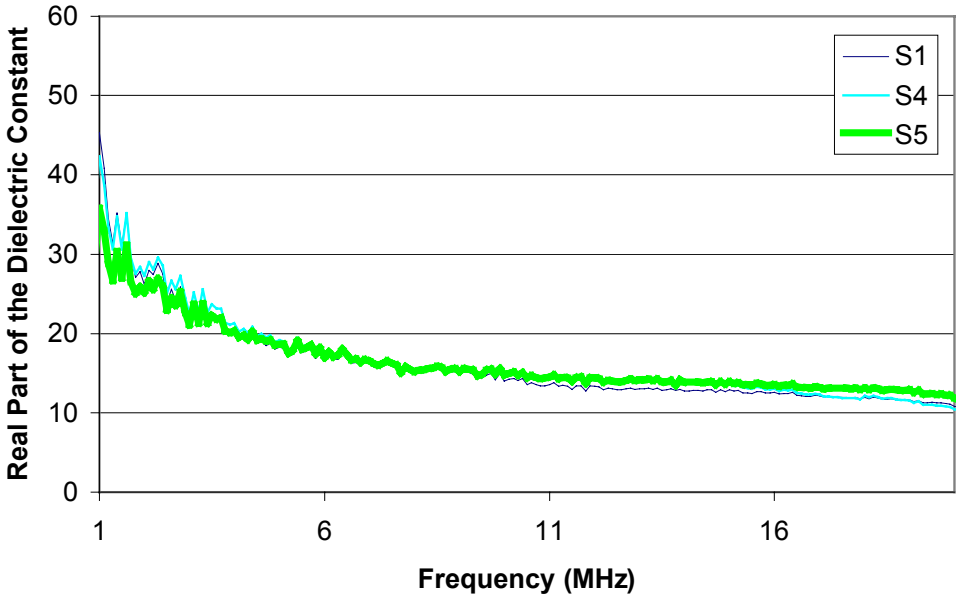

Figure C.29. Real part of the dielectric constant for M2 with different reinforcement conditions

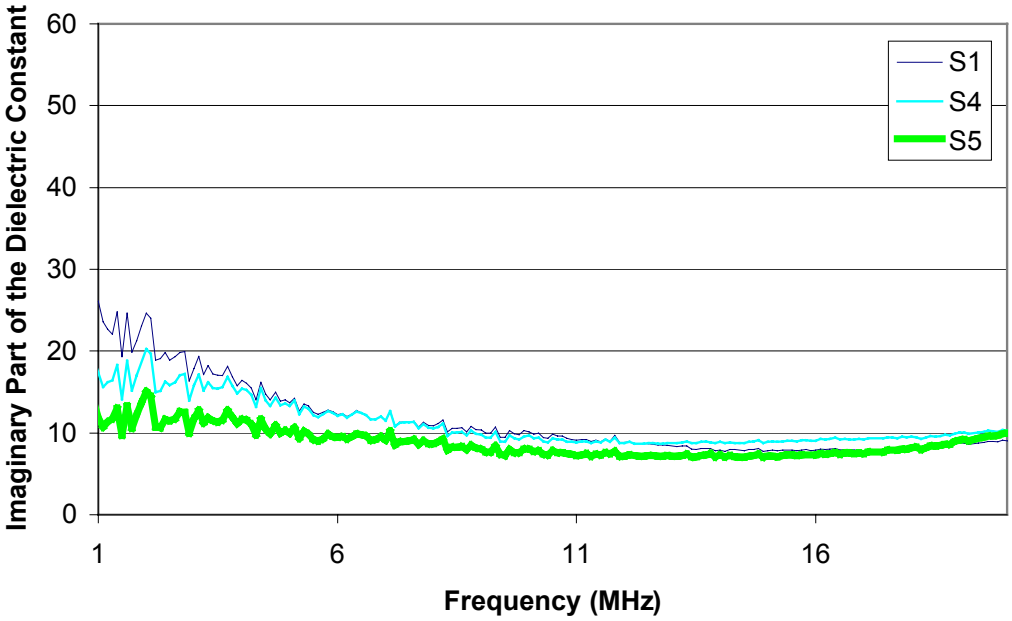

Figure C.30. Imaginary part of the dielectric constant for M2 with different reinforcement conditions

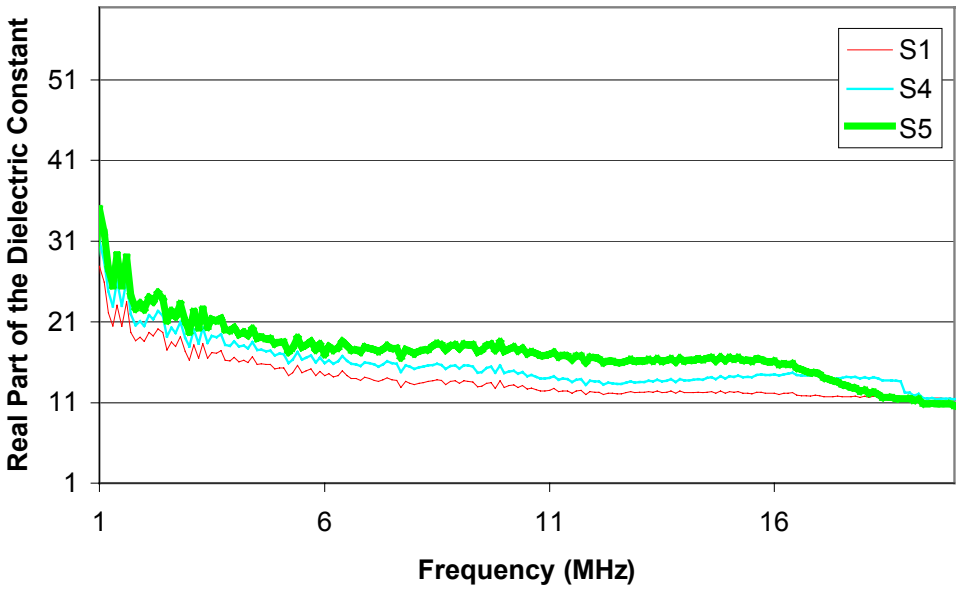

Figure C.31. Real part of the dielectric constant for M4 with different reinforcement conditions

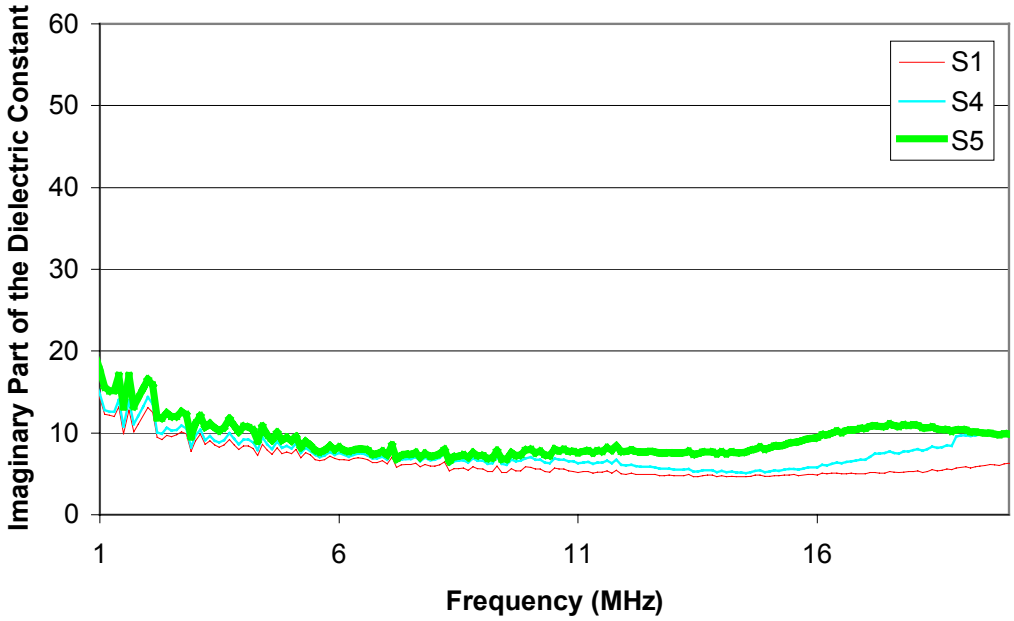

Figure C.32. Imaginary part of the dielectric constant for M4 with different reinforcement conditions

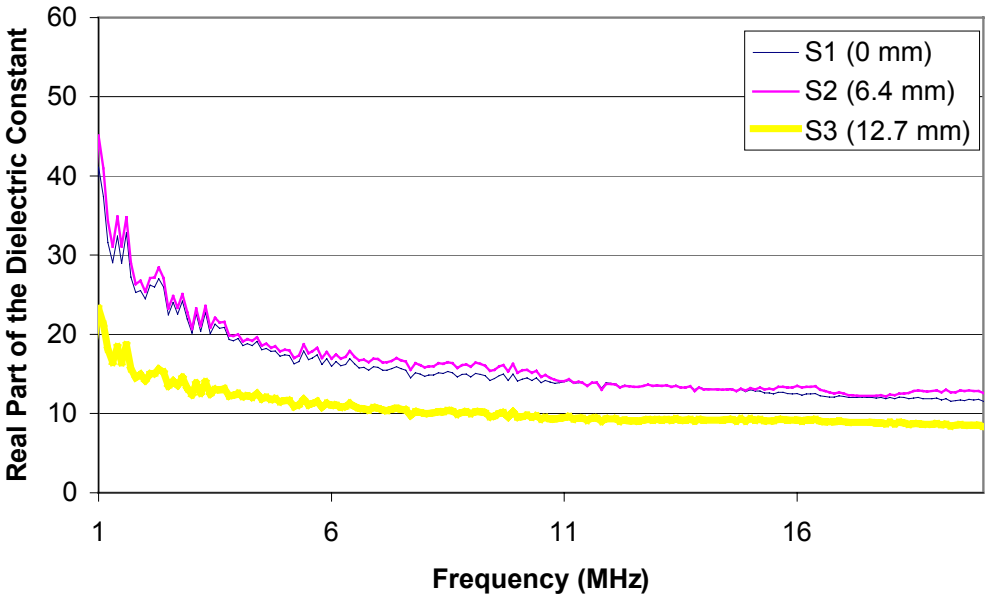

Figure C.33. Real part of the dielectric constant for M1 with different air void thicknesses

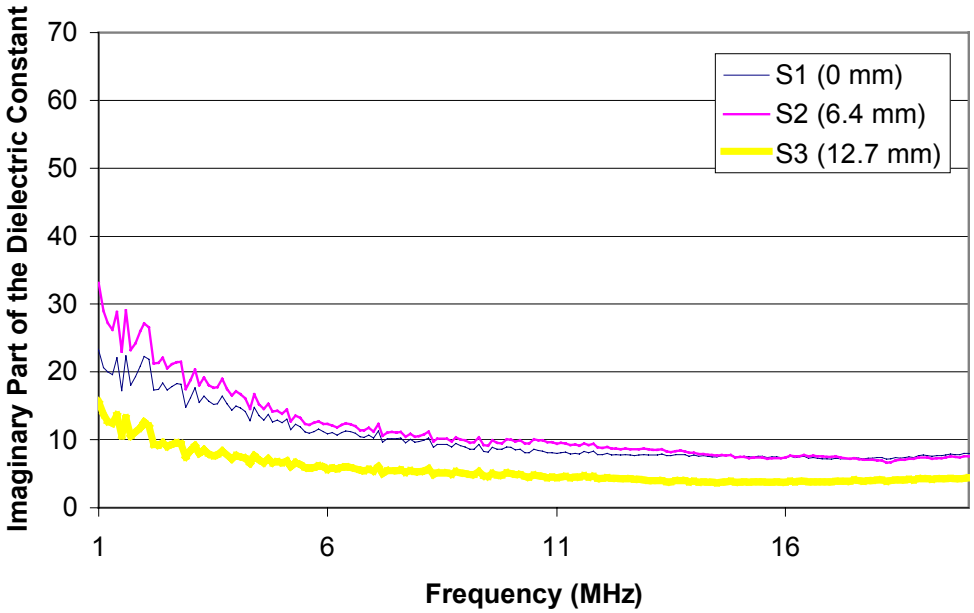

Figure C.34. Imaginary part of the dielectric constant for M1 with different air void thicknesses

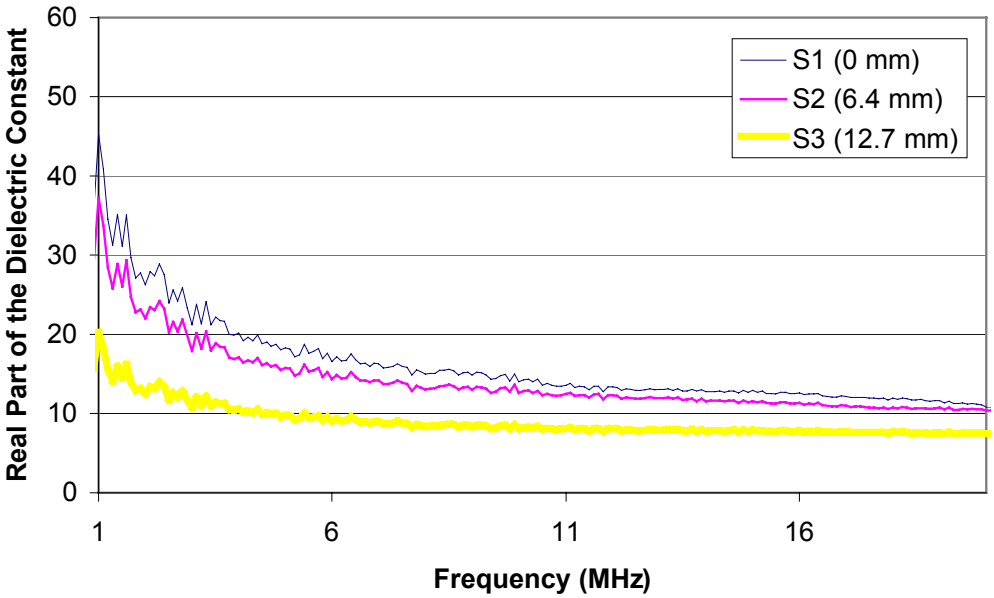

Figure C.35. Real part of the dielectric constant for M2 with different air void thicknesses

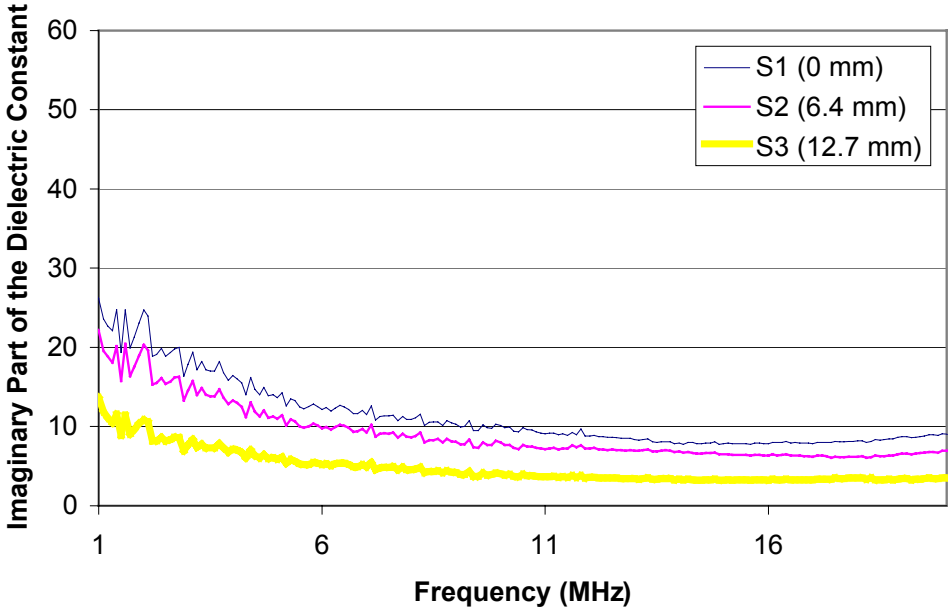

Figure C.36. Imaginary part of the dielectric constant for M1 with different air void thicknesses

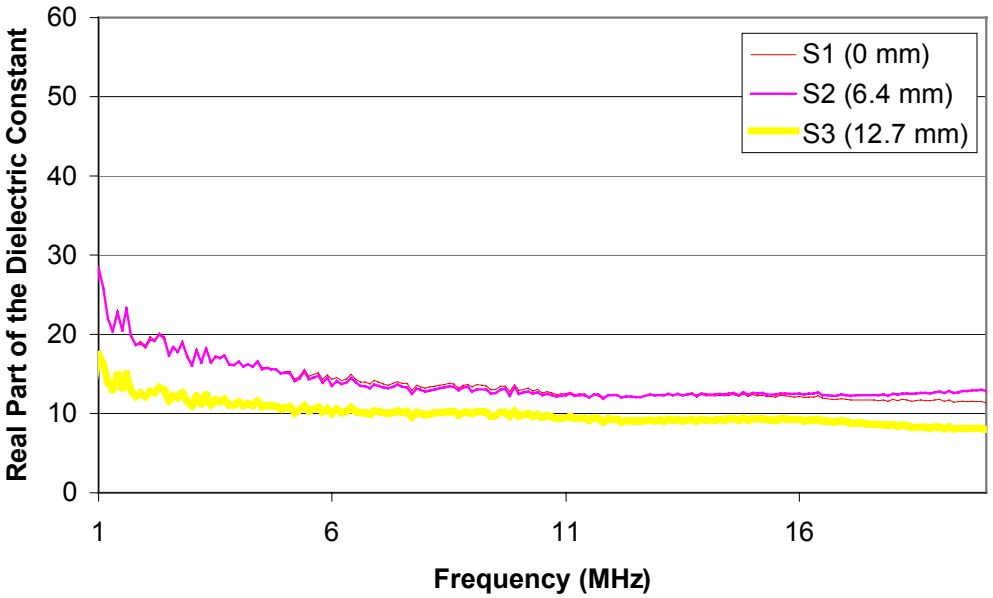

Figure C.37. Real part of the dielectric constant for M4 with different air void thicknesses

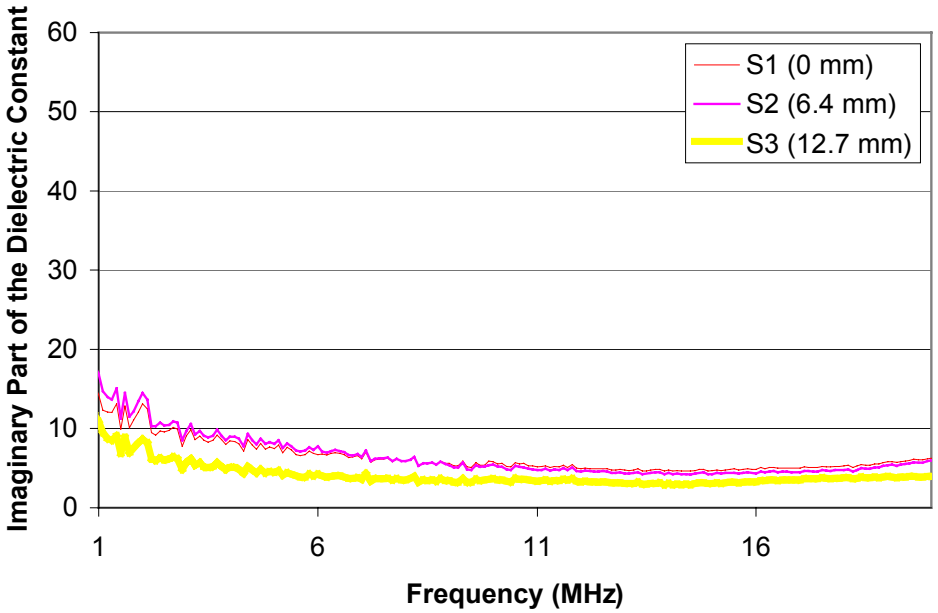

Figure C.38. Imaginary part of the dielectric constant for M4 with different air void thicknesses

APPENDIX D: MIXTURE THEORY EVALUATION DATA

First experimental design

Data

ANOVA results

Second experimental design

Data

Regression analysis results

Distribution effect

Theoretical mixture formulas evaluation

D.1 First Experimental Design

Data

Table D.1. Dielectric constant for 55% aggregate volume

DCR	Aggregate Size (of aggregate volume)	Aggregate Shape	
		Circle	Square
2.5	1/12	6.286	6.246
	1/24	6.268	6.331
5	1/12	9.554	9.460
	1/24	9.528	9.819
7.5	1/12	12.671	12.311
	1/24	12.654	13.225
10	1/12	15.733	15.255
	1/24	15.737	16.609

Table D.2. Dielectric constant for 60% aggregate volume

DCR	Aggregate Size (of aggregate volume)	Aggregate Shape	
		Circle	Square
2.5	1/12	5.926	5.931
	1/24	5.874	5.931
5	1/12	8.558	8.645
	1/24	8.322	8.571
7.5	1/12	11.052	11.252
	1/24	10.579	11.052
10	1/12	15.733	15.255
	1/24	15.737	16.609

Table D.3. Dielectric constant for 65% aggregate volume

DCR	Aggregate Size (of aggregate volume)	Aggregate Shape	
		Circle	Square
2.5	1/12	5.634	5.659
	1/24	5.598	5.661
5	1/12	7.728	7.958
	1/24	7.589	7.872
7.5	1/12	9.637	10.161
	1/24	9.374	9.924
10	1/12	11.476	12.339
	1/24	11.083	11.920

Table D.4. ANOVA input data for the first experimental design

Volume (%)	DCR	Shape	Gradation	Eps
55	2.5	Circular	12	6.29
55	2.5	Circular	24	6.27
55	2.5	Square	12	6.25
55	2.5	Square	24	6.33
55	5	Circular	12	9.55
55	5	Circular	24	9.53
55	5	Square	12	9.46
55	5	Square	24	9.82
55	7.5	Circular	12	12.67
55	7.5	Circular	24	12.65
55	7.5	Square	12	12.31
55	7.5	Square	24	13.23
55	10	Circular	12	15.73
55	10	Circular	24	15.74
55	10	Square	12	15.26
55	10	Square	24	16.61
60	2.5	Circular	12	5.93
60	2.5	Circular	24	5.87
60	2.5	Square	12	5.93
60	2.5	Square	24	5.93
60	5	Circular	12	8.56
60	5	Circular	24	8.32
60	5	Square	12	8.65
60	5	Square	24	8.57
60	7.5	Circular	12	11.05
60	7.5	Circular	24	10.58
60	7.5	Square	12	11.25
60	7.5	Square	24	11.05
60	10	Circular	12	13.5
60	10	Circular	24	12.77
60	10	Square	12	13.83
60	10	Square	24	13.48

Volume (%)	DCR	Shape	Gradation	Eps
65	2.5	Circular	12	5.63
65	2.5	Circular	24	5.6
65	2.5	Square	12	5.66
65	2.5	Square	24	5.66
65	5	Circular	12	7.73
65	5	Circular	24	7.59
65	5	Square	12	7.96
65	5	Square	24	7.87
65	7.5	Circular	12	9.64
65	7.5	Circular	24	9.37
65	7.5	Square	12	10.16
65	7.5	Square	24	9.92
65	10	Circular	12	11.48
65	10	Circular	24	11.08
65	10	Square	12	12.34
65	10	Square	24	11.92

General Linear Model

```
Factor     Type Levels Values
Volume    fixed      3 55 60 65
DCR       fixed      4  2.5  5.0  7.5 10.0
Shape     fixed      2 Circular Square
Gradatio  fixed      2 12 24

Analysis of Variance for Eps, using Adjusted SS for Tests

Source     DF     Seq SS     Adj SS     Adj MS       F      P
Volume      2     45.816     45.816     22.908   55.80  0.000
DCR         3    393.961    393.961    131.320  319.86  0.000
Shape       1      0.832      0.832      0.832    2.03  0.162
Gradatio    1      0.023      0.023      0.023    0.06  0.812
Error      40     16.422     16.422      0.411
Total      47    457.055

Unusual Observations for Eps

Obs       Eps       Fit   StDev Fit  Residual   St Resid
 16   16.6100   15.0154      0.2616    1.5946      2.73R
 46   11.0800   12.3715      0.2616   -1.2915     -2.21R

R denotes an observation with a large standardized residual.

Tukey Simultaneous Tests
Response Variable Eps
All Pairwise Comparisons among Levels of Volume

Volume = 55 subtracted from:

Level      Difference       SE of             Adjusted
Volume       of Means  Difference   T-Value    P-Value
60             -1.402      0.2265     -6.19     0.0000
65             -2.381      0.2265    -10.51     0.0000

Volume = 60 subtracted from:

Level      Difference       SE of             Adjusted
Volume       of Means  Difference   T-Value    P-Value
65            -0.9788      0.2265    -4.320     0.0003

Tukey Simultaneous Tests
Response Variable Eps
All Pairwise Comparisons among Levels of Shape

Shape = Circular subtracted from:

Level        Difference       SE of             Adjusted
Shape          of Means  Difference   T-Value    P-Value
Square           0.2633      0.1850     1.424     0.1623

Tukey Simultaneous Tests
Response Variable Eps
```

All Pairwise Comparisons among Levels of Gradatio

Gradatio = 12 subtracted from:

Level Gradatio	Difference of Means	SE of Difference	T-Value	Adjusted P-Value
24	-0.04417	0.1850	-0.2388	0.8125

D.2 Second Experimental Design

Table D.5. Dielectric constant at different aggregate volume for dielectric constant of 4

Aggregate Volume (%)		C/A=10/4 Air Content				C/A=20/4 Air Content			
		0	2	4	6	0	2	4	6
55	Eps (4/3)	6.24	6.03	5.81	5.58	9.30	8.93	8.50	8.07
	Eps (3/4)	6.17	5.98	5.78	5.57	9.05	8.71	8.36	7.96
	Average	6.21	6.01	5.80	5.58	9.17	8.82	8.43	8.01
		C/A= 30/4 Air Content				C/A= 40/4 Air Content			
		0	2	4	6	0	2	4	6
	Eps (4/3)	12.18	11.64	11.01	10.38	14.98	14.29	13.47	12.62
	Eps (3/4)	11.69	11.22	10.73	10.14	14.26	13.65	13.01	12.24
	Average	11.93	11.43	10.87	10.26	14.62	13.97	13.24	12.43
60		C/A=10/4 Air Content				C/A=20/4 Air Content			
		0	2	4	6	0	2	4	6
	Eps (4/3)	5.96	5.50	5.28	5.08	8.60	7.96	7.55	7.15
	Eps (3/4)	5.89	5.48	5.27	5.02	8.31	7.82	7.46	7.03
	Average	5.93	5.49	5.28	5.05	8.45	7.89	7.51	7.09
		C/A= 30/4 Air Content				C/A= 40/4 Air Content			
		0	2	4	6	0	2	4	6
	Eps (4/3)	11.05	10.26	9.66	9.05	13.43	12.50	11.71	10.89
	Eps (3/4)	10.52	9.94	9.46	8.86	12.65	11.98	11.37	10.62
	Average	10.78	10.10	9.56	8.96	13.04	12.24	11.54	10.76
65		C/A=10/4 Air Content				C/A=20/4 Air Content			
		0	2	4	6	0	2	4	6
	Eps (4/3)	5.69	5.49	5.30	5.08	7.91	7.55	7.24	6.82
	Eps (3/4)	5.62	5.45	5.26	5.11	7.62	7.36	7.05	6.84
	Average	5.66	5.47	5.28	5.09	7.77	7.45	7.14	6.83
		C/A= 30/4 Air Content				C/A= 40/4 Air Content			
		0	2	4	6	0	2	4	6
	Eps (4/3)	9.95	9.43	9.02	8.41	11.92	11.24	10.75	9.94
	Eps (3/4)	9.40	9.07	8.65	8.40	11.11	10.69	10.18	9.88
	Average	9.68	9.25	8.83	8.40	11.51	10.97	10.46	9.91

Table D.6. Regression analysis input data for the second experimental design

Aggregate Volume (%)	DCR	AC	Eps	V*DCR	V*AC	AC*DCR	V**2	DCR**2	AC**2
55	2.5	0	6.21	137.5	0	0	3025	6.25	0
55	2.5	2	6.01	137.5	110	5	3025	6.25	4
55	2.5	4	5.8	137.5	220	10	3025	6.25	16
55	2.5	6	5.58	137.5	330	15	3025	6.25	36
55	5	0	9.17	275	0	0	3025	25	0
55	5	2	8.82	275	110	10	3025	25	4
55	5	4	8.43	275	220	20	3025	25	16
55	5	6	8.01	275	330	30	3025	25	36
55	7.5	0	11.93	412.5	0	0	3025	56.25	0
55	7.5	2	11.43	412.5	110	15	3025	56.25	4
55	7.5	4	10.87	412.5	220	30	3025	56.25	16
55	7.5	6	10.26	412.5	330	45	3025	56.25	36
55	10	0	14.62	550	0	0	3025	100	0
55	10	2	13.97	550	110	20	3025	100	4
55	10	4	13.24	550	220	40	3025	100	16
55	10	6	12.43	550	330	60	3025	100	36
60	2.5	0	5.93	150	0	0	3600	6.25	0
60	2.5	2	5.49	150	120	5	3600	6.25	4
60	2.5	4	5.28	150	240	10	3600	6.25	16
60	2.5	6	5.05	150	360	15	3600	6.25	36
60	5	0	8.45	300	0	0	3600	25	0
60	5	2	7.89	300	120	10	3600	25	4
60	5	4	7.51	300	240	20	3600	25	16
60	5	6	7.09	300	360	30	3600	25	36
60	7.5	0	10.78	450	0	0	3600	56.25	0
60	7.5	2	10.1	450	120	15	3600	56.25	4
60	7.5	4	9.56	450	240	30	3600	56.25	16
60	7.5	6	8.96	450	360	45	3600	56.25	36
60	10	0	13.04	600	0	0	3600	100	0
60	10	2	12.24	600	120	20	3600	100	4
60	10	4	11.54	600	240	40	3600	100	16
60	10	6	10.76	600	360	60	3600	100	36

Table D.6. Regression analysis input data for the second experimental design (Cont.)

Aggregate Volume (%)	DCR	AC	Eps	V*DCR	V*AC	AC*DCR	V**2	DCR**2	AC**2
65	2.5	0	5.66	162.5	0	0	4225	6.25	0
65	2.5	2	5.47	162.5	130	5	4225	6.25	4
65	2.5	4	5.28	162.5	260	10	4225	6.25	16
65	2.5	6	5.09	162.5	390	15	4225	6.25	36
65	5	0	7.77	325	0	0	4225	25	0
65	5	2	7.45	325	130	10	4225	25	4
65	5	4	7.14	325	260	20	4225	25	16
65	5	6	6.83	325	390	30	4225	25	36
65	7.5	0	9.68	487.5	0	0	4225	56.25	0
65	7.5	2	9.25	487.5	130	15	4225	56.25	4
65	7.5	4	8.83	487.5	260	30	4225	56.25	16
65	7.5	6	8.4	487.5	390	45	4225	56.25	36
65	10	0	11.51	650	0	0	4225	100	0
65	10	2	10.97	650	130	20	4225	100	4
65	10	4	10.46	650	260	40	4225	100	16
65	10	6	9.91	650	390	60	4225	100	36

Regression Analysis

The regression equation for aggregate dielectric constant of 4 is
Eps = 34.7 - 1.06 Volume + 2.94 DCR - 0.360 AC - 0.0310 V*DCR + 0.00530 V*AC
- 0.0295 AC*DCR + 0.00893 V**2 - 0.0102 DCR**2

Predictor	Coef	StDev	T	P
Constant	34.745	3.461	10.04	0.000
Volume	-1.0623	0.1151	-9.23	0.000
DCR	2.94102	0.06381	46.09	0.000
AC	-0.35975	0.07515	-4.79	0.000
V*DCR	-0.0310200	0.0009884	-31.38	0.000
V*AC	0.005300	0.001236	4.29	0.000
AC*DCR	-0.029513	0.001805	-16.35	0.000
V**2	0.0089250	0.0009570	9.33	0.000
DCR**2	-0.010233	0.001805	-5.67	0.000

S = 0.07814 R-Sq = 99.9% R-Sq(adj) = 99.9%

Analysis of Variance

Source	DF	SS	MS	F	P
Regression	8	323.210	40.401	6616.64	0.000
Residual Error	39	0.238	0.006		
Total	47	323.448			

Source	DF	Seq SS
Volume	1	22.916
DCR	1	279.526
AC	1	12.281
V*DCR	1	6.014
V*AC	1	0.112
AC*DCR	1	1.633
V**2	1	0.531
DCR**2	1	0.196

Unusual Observations

Obs	Volume	Eps	Fit	StDev Fit	Residual	St Resid
1	55.0	6.2100	6.3416	0.0455	-0.1316	-2.07R
17	60.0	5.9300	5.7744	0.0371	0.1556	2.26R
21	60.0	8.4500	8.2821	0.0284	0.1679	2.31R
48	65.0	9.9100	9.7671	0.0455	0.1429	2.25R

R denotes an observation with a large standardized residual

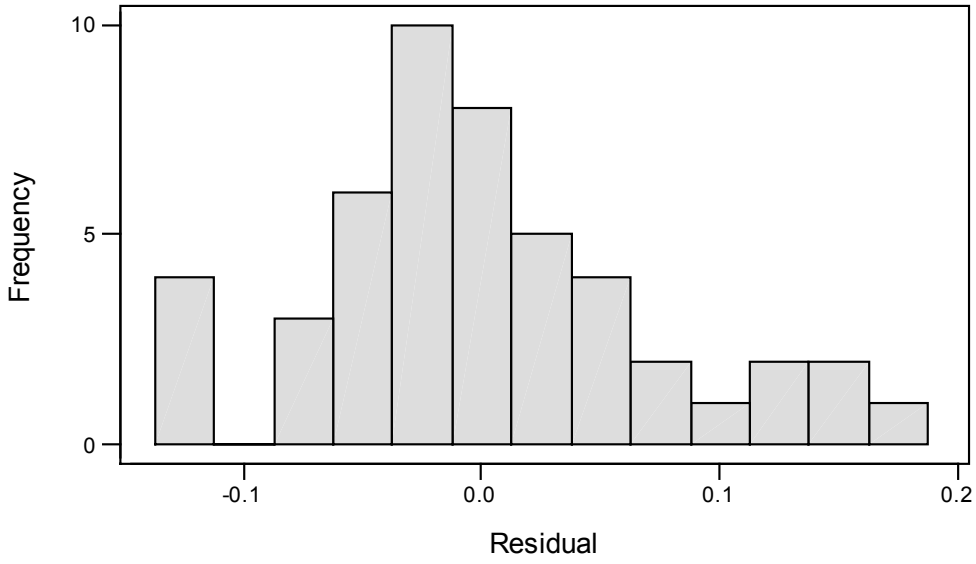

Figure D. 1. Histogram of the residuals (response is Eps)

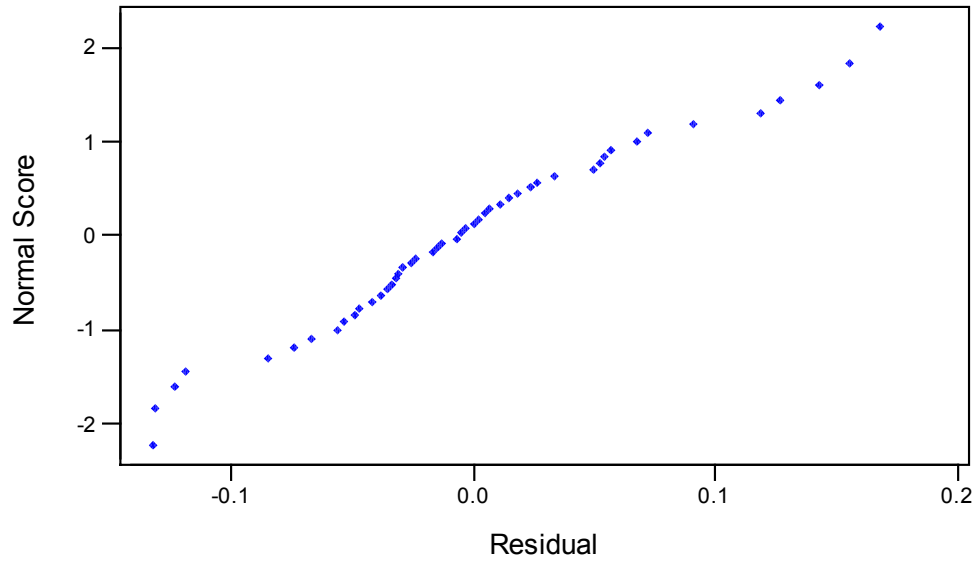

Figure D.2. Normal probability plot of the residuals (response is Eps)

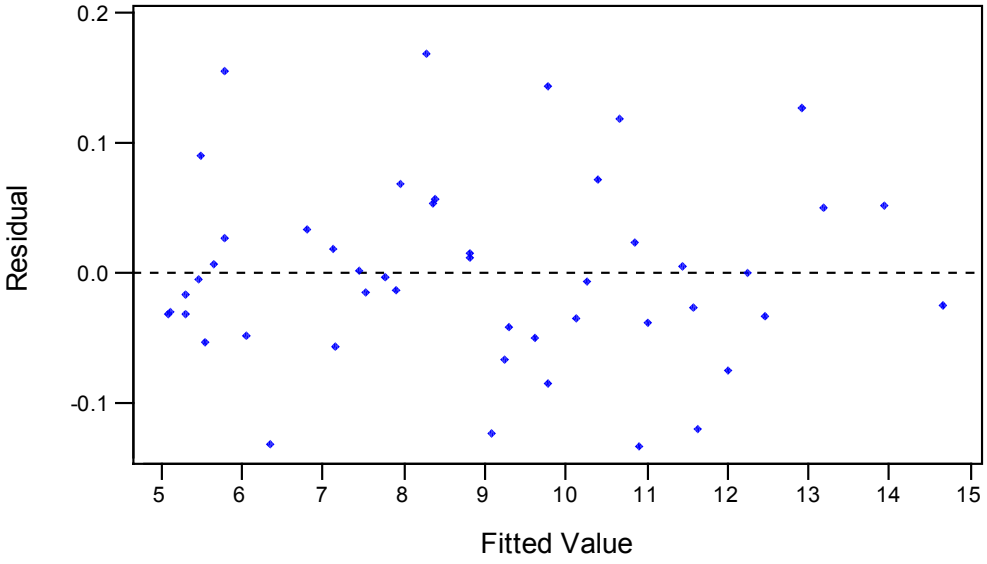

Figure D.3. Residuals versus the fitted values (response is Eps)

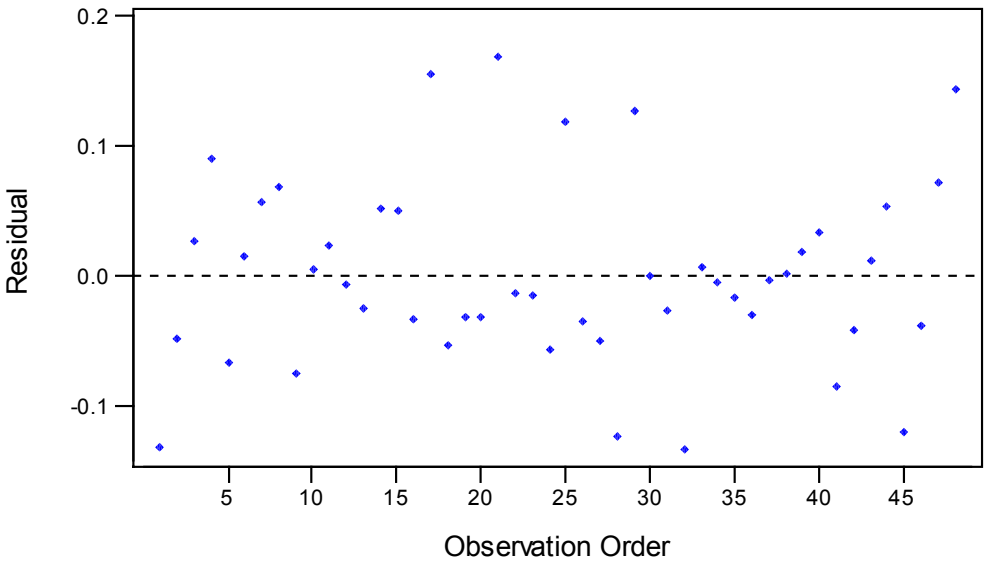

Figure D. 4 Residuals versus the order of the data (response is Eps)

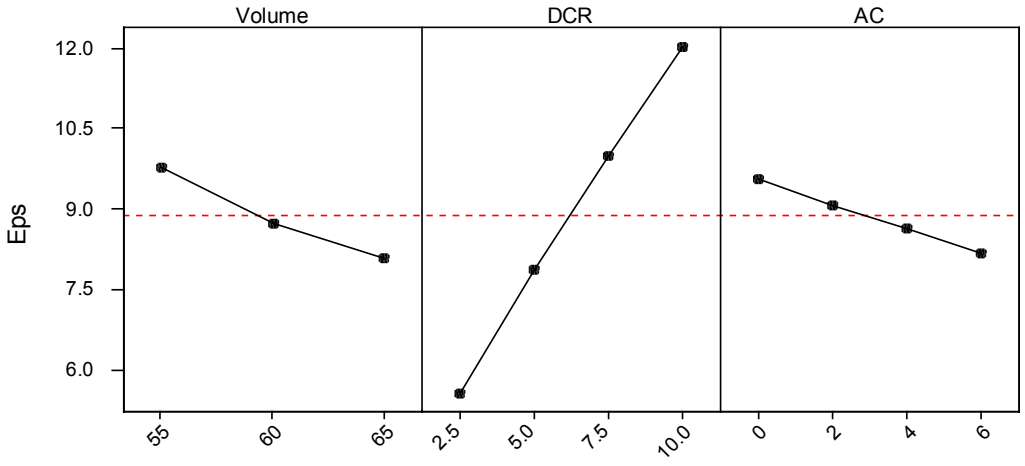

Figure D.5. Main effects plot- data means for Eps

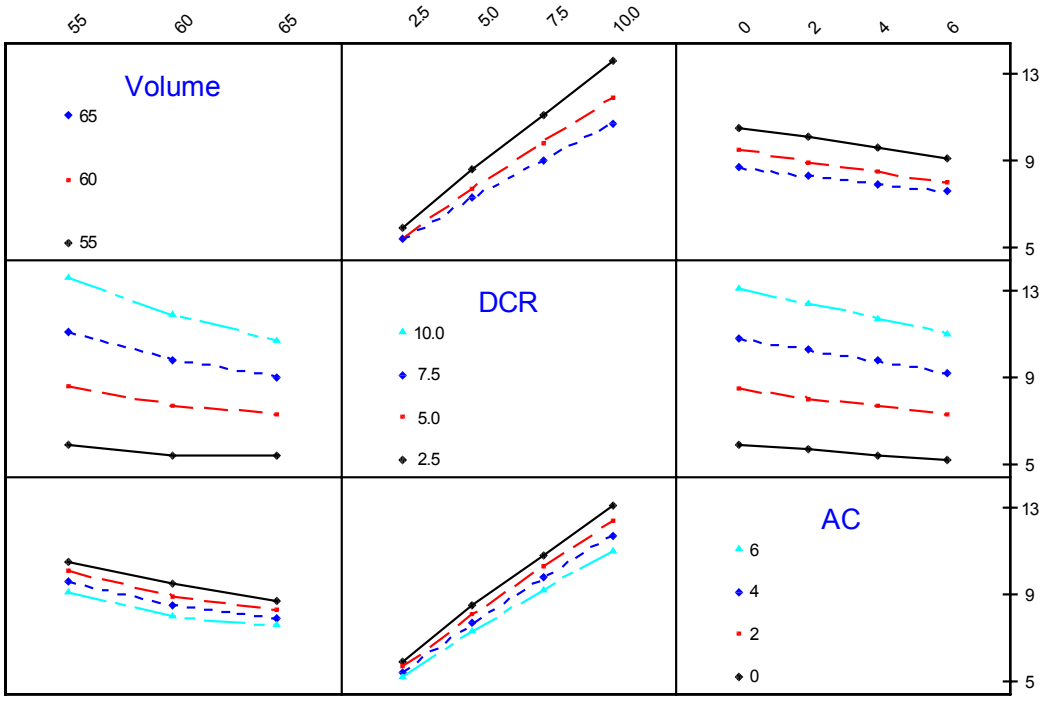

Figure D.6. Interaction plot- data means for Eps

Table D.7. Dielectric constant at different aggregate volume for dielectric constant of 6

Aggregate Volume (%)		C/A=15/6 Air Content				C/A=30/6 Air Content			
		0	2	4	6	0	2	4	6
55	Eps (4/3)	9.35	9.02	8.67	8.30	13.95	13.37	12.71	12.04
	Eps (3/4)	9.26	8.96	8.64	8.29	13.57	13.05	12.51	11.88
	Average	9.31	8.99	8.65	8.30	13.76	13.21	12.61	11.96
		C/A= 45/6 Air Content				C/A= 60/6 Air Content			
		0	2	4	6	0	2	4	6
	Eps (4/3)	18.26	17.44	16.48	15.50	22.47	21.42	20.16	18.87
	Eps (3/4)	17.54	16.81	16.06	15.15	21.38	20.46	19.49	18.30
	Average	17.90	17.13	16.27	15.32	21.93	20.94	19.83	18.59
60		C/A=15/6 Air Content				C/A=30/6 Air Content			
		0	2	4	6	0	2	4	6
	Eps (4/3)	8.94	8.17	7.83	7.50	12.89	11.87	11.23	10.61
	Eps (3/4)	8.84	8.14	7.80	7.39	12.47	11.67	11.11	10.42
	Average	8.89	8.16	7.81	7.45	12.68	11.77	11.17	10.51
		C/A= 45/6 Air Content				C/A= 60/6 Air Content			
		0	2	4	6	0	2	4	6
	Eps (4/3)	16.57	15.33	14.39	13.46	20.15	18.69	17.47	16.21
	Eps (3/4)	15.78	14.86	14.11	13.17	18.97	17.93	16.99	15.82
	Average	16.18	15.09	14.25	13.31	19.56	18.31	17.23	16.01
65		C/A=15/6 Air Content				C/A=30/6 Air Content			
		0	2	4	6	0	2	4	6
	Eps (4/3)	8.54	8.22	7.91	7.56	11.87	11.30	10.83	10.18
	Eps (3/4)	8.43	8.16	7.85	7.60	11.43	11.03	10.54	10.22
	Average	8.49	8.19	7.88	7.58	11.65	11.17	10.68	10.20
		C/A= 45/6 Air Content				C/A= 60/6 Air Content			
		0	2	4	6	0	2	4	6
	Eps (4/3)	14.93	14.12	13.50	12.56	17.88	16.84	16.09	14.86
	Eps (3/4)	14.11	13.59	12.94	12.56	16.66	16.03	15.24	14.79
	Average	14.52	13.85	13.22	12.56	17.27	16.44	15.66	14.82

Table D.8. Regression analysis input data for the second experimental design

Aggregate Volume (%)	DCR	AC	Eps	V*DCR	V*AC	AC*DCR	V**2	DCR**2	AC**2
55	2.5	0	9.31	137.5	0	0	3025	6.25	0
55	2.5	2	8.99	137.5	110	5	3025	6.25	4
55	2.5	4	8.65	137.5	220	10	3025	6.25	16
55	2.5	6	8.30	137.5	330	15	3025	6.25	36
55	5	0	13.76	275	0	0	3025	25	0
55	5	2	13.21	275	110	10	3025	25	4
55	5	4	12.61	275	220	20	3025	25	16
55	5	6	11.96	275	330	30	3025	25	36
55	7.5	0	17.90	412.5	0	0	3025	56.25	0
55	7.5	2	17.13	412.5	110	15	3025	56.25	4
55	7.5	4	16.27	412.5	220	30	3025	56.25	16
55	7.5	6	15.32	412.5	330	45	3025	56.25	36
55	10	0	21.93	550	0	0	3025	100	0
55	10	2	20.94	550	110	20	3025	100	4
55	10	4	19.83	550	220	40	3025	100	16
55	10	6	18.59	550	330	60	3025	100	36
60	2.5	0	8.89	150	0	0	3600	6.25	0
60	2.5	2	8.16	150	120	5	3600	6.25	4
60	2.5	4	7.81	150	240	10	3600	6.25	16
60	2.5	6	7.45	150	360	15	3600	6.25	36
60	5	0	12.68	300	0	0	3600	25	0
60	5	2	11.77	300	120	10	3600	25	4
60	5	4	11.17	300	240	20	3600	25	16
60	5	6	10.51	300	360	30	3600	25	36
60	7.5	0	16.18	450	0	0	3600	56.25	0
60	7.5	2	15.09	450	120	15	3600	56.25	4
60	7.5	4	14.25	450	240	30	3600	56.25	16
60	7.5	6	13.31	450	360	45	3600	56.25	36
60	10	0	19.56	600	0	0	3600	100	0
60	10	2	18.31	600	120	20	3600	100	4
60	10	4	17.23	600	240	40	3600	100	16
60	10	6	16.01	600	360	60	3600	100	36

Table D.8. Regression analysis input data for the second experimental design (Cont.)

Aggregate Volume (%)	DCR	AC	Eps	V*DCR	V*AC	AC*DCR	V**2	DCR**2	AC**2
65	2.5	0	8.49	162.5	0	0	4225	6.25	0
65	2.5	2	8.19	162.5	130	5	4225	6.25	4
65	2.5	4	7.88	162.5	260	10	4225	6.25	16
65	2.5	6	7.58	162.5	390	15	4225	6.25	36
65	5	0	11.65	325	0	0	4225	25	0
65	5	2	11.17	325	130	10	4225	25	4
65	5	4	10.68	325	260	20	4225	25	16
65	5	6	10.20	325	390	30	4225	25	36
65	7.5	0	14.52	487.5	0	0	4225	56.25	0
65	7.5	2	13.85	487.5	130	15	4225	56.25	4
65	7.5	4	13.22	487.5	260	30	4225	56.25	16
65	7.5	6	12.56	487.5	390	45	4225	56.25	36
65	10	0	17.27	650	0	0	4225	100	0
65	10	2	16.44	650	130	20	4225	100	4
65	10	4	15.66	650	260	40	4225	100	16
65	10	6	14.82	650	390	60	4225	100	36

Regression Analysis

The regression equation for aggregate dielectric constant of 6 is
Eps = 58.4 - 1.80 Volume + 4.42 DCR - 0.570 AC - 0.0466 V*DCR + 0.00823 V*AC
- 0.0442 AC*DCR + 0.0152 V**2 - 0.0156 DCR**2

Predictor	Coef	StDev	T	P
Constant	58.403	5.800	10.07	0.000
Volume	-1.8047	0.1929	-9.36	0.000
DCR	4.4200	0.1069	41.34	0.000
AC	-0.5695	0.1259	-4.52	0.000
V*DCR	-0.046600	0.001656	-28.14	0.000
V*AC	0.008225	0.002070	3.97	0.000
AC*DCR	-0.044227	0.003024	-14.63	0.000
V**2	0.015150	0.001604	9.45	0.000
DCR**2	-0.015600	0.003024	-5.16	0.000

S = 0.1309 R-Sq = 99.9% R-Sq(adj) = 99.9%

Analysis of Variance

Source	DF	SS	MS	F	P
Regression	8	730.793	91.349	5328.21	0.000
Residual Error	39	0.669	0.017		
Total	47	731.461			

Source	DF	Seq SS
Volume	1	51.308
DCR	1	630.180
AC	1	29.807
V*DCR	1	13.572
V*AC	1	0.271
AC*DCR	1	3.667
V**2	1	1.530
DCR**2	1	0.456

Unusual Observations

Obs	Volume	Eps	Fit	StDev Fit	Residual	St Resid
17	60.0	8.8900	8.6247	0.0622	0.2653	2.30R
21	60.0	12.6800	12.3922	0.0477	0.2878	2.36R
48	65.0	14.8200	14.5948	0.0762	0.2252	2.11R

R denotes an observation with a large standardized residual

Table D.9. Dielectric constant at different aggregate volume for dielectric constant of 8

Aggregate Volume (%)		C/A=20/8 Air Content				C/A=40/8 Air Content			
		0	2	4	6	0	2	4	6
55	Eps (4/3)	12.47	12.02	11.52	11.02	18.60	17.82	16.92	16.00
	Eps (3/4)	12.35	11.93	11.49	11.01	18.09	17.39	16.65	15.79
	Average	12.41	11.97	11.51	11.02	18.35	17.60	16.79	15.90
		C/A= 60/8 Air Content				C/A= 80/8 Air Content			
		0	2	4	6	0	2	4	6
	Eps (4/3)	24.35	23.25	21.95	20.62	29.96	28.55	26.85	25.12
	Eps (3/4)	23.38	22.41	21.39	20.16	28.51	27.27	25.96	24.37
	Average	23.87	22.83	21.67	20.39	29.24	27.91	26.41	24.74
60		C/A=20/8 Air Content				C/A=40/8 Air Content			
		0	2	4	6	0	2	4	6
	Eps (4/3)	11.92	10.84	10.37	9.92	17.19	15.78	14.91	14.06
	Eps (3/4)	11.78	10.81	10.32	9.74	16.63	15.52	14.75	13.79
	Average	11.85	10.83	10.34	9.83	16.91	15.65	14.83	13.93
		C/A= 60/8 Air Content				C/A= 80/8 Air Content			
		0	2	4	6	0	2	4	6
	Eps (4/3)	22.09	20.39	19.13	17.86	26.87	24.87	23.23	21.53
	Eps (3/4)	21.04	19.78	18.75	17.47	25.29	23.87	22.60	21.00
	Average	21.57	20.08	18.94	17.66	26.08	24.37	22.91	21.27
65		C/A=20/8 Air Content				C/A=40/8 Air Content			
		0	2	4	6	0	2	4	6
	Eps (4/3)	11.39	10.94	10.51	10.04	15.83	15.06	14.41	13.53
	Eps (3/4)	11.24	10.87	10.44	10.10	15.24	14.70	14.03	13.60
	Average	11.32	10.91	10.48	10.07	15.53	14.88	14.22	13.56
		C/A= 60/8 Air Content				C/A= 80/8 Air Content			
		0	2	4	6	0	2	4	6
	Eps (4/3)	19.90	18.82	17.98	16.71	23.84	22.44	21.43	19.78
	Eps (3/4)	18.81	18.11	17.24	16.72	22.22	21.36	20.30	19.69
	Average	19.35	18.46	17.61	16.71	23.03	21.90	20.86	19.73

Table D.10. Regression analysis input data for the second experimental design

Aggregate Volume (%)	DCR	AC	Eps	V*DCR	V*AC	AC*DCR	V**2	DCR**2	AC**2
55	2.5	0	12.41	137.5	0	0	3025	6.25	0
55	2.5	2	11.97	137.5	110	5	3025	6.25	4
55	2.5	4	11.51	137.5	220	10	3025	6.25	16
55	2.5	6	11.02	137.5	330	15	3025	6.25	36
55	5	0	18.35	275	0	0	3025	25	0
55	5	2	17.60	275	110	10	3025	25	4
55	5	4	16.79	275	220	20	3025	25	16
55	5	6	15.90	275	330	30	3025	25	36
55	7.5	0	23.87	412.5	0	0	3025	56.25	0
55	7.5	2	22.83	412.5	110	15	3025	56.25	4
55	7.5	4	21.67	412.5	220	30	3025	56.25	16
55	7.5	6	20.39	412.5	330	45	3025	56.25	36
55	10	0	29.24	550	0	0	3025	100	0
55	10	2	27.91	550	110	20	3025	100	4
55	10	4	26.41	550	220	40	3025	100	16
55	10	6	24.74	550	330	60	3025	100	36
60	2.5	0	11.85	150	0	0	3600	6.25	0
60	2.5	2	10.83	150	120	5	3600	6.25	4
60	2.5	4	10.34	150	240	10	3600	6.25	16
60	2.5	6	9.83	150	360	15	3600	6.25	36
60	5	0	16.91	300	0	0	3600	25	0
60	5	2	15.65	300	120	10	3600	25	4
60	5	4	14.83	300	240	20	3600	25	16
60	5	6	13.93	300	360	30	3600	25	36
60	7.5	0	21.57	450	0	0	3600	56.25	0
60	7.5	2	20.08	450	120	15	3600	56.25	4
60	7.5	4	18.94	450	240	30	3600	56.25	16
60	7.5	6	17.66	450	360	45	3600	56.25	36
60	10	0	26.08	600	0	0	3600	100	0
60	10	2	24.37	600	120	20	3600	100	4
60	10	4	22.91	600	240	40	3600	100	16
60	10	6	21.27	600	360	60	3600	100	36

Table D.10. Regression analysis input data for the second experimental design (Cont.)

Aggregate Volume (%)	DCR	AC	Eps	V*DCR	V*AC	AC*DCR	V**2	DCR**2	AC**2
65	2.5	0	11.32	162.5	0	0	4225	6.25	0
65	2.5	2	10.91	162.5	130	5	4225	6.25	4
65	2.5	4	10.48	162.5	260	10	4225	6.25	16
65	2.5	6	10.07	162.5	390	15	4225	6.25	36
65	5	0	15.53	325	0	0	4225	25	0
65	5	2	14.88	325	130	10	4225	25	4
65	5	4	14.22	325	260	20	4225	25	16
65	5	6	13.56	325	390	30	4225	25	36
65	7.5	0	19.35	487.5	0	0	4225	56.25	0
65	7.5	2	18.46	487.5	130	15	4225	56.25	4
65	7.5	4	17.61	487.5	260	30	4225	56.25	16
65	7.5	6	16.71	487.5	390	45	4225	56.25	36
65	10	0	23.03	650	0	0	4225	100	0
65	10	2	21.90	650	130	20	4225	100	4
65	10	4	20.86	650	260	40	4225	100	16
65	10	6	19.73	650	390	60	4225	100	36

Regression Analysis

The regression equation for aggregate dielectric constant of 8 is
Eps = 82.2 - 2.55 Volume + 5.90 DCR - 0.781 AC - 0.0621 V*DCR + 0.0112 V*AC
- 0.0588 AC*DCR + 0.0214 V**2 - 0.0210 DCR**2

Predictor	Coef	StDev	T	P
Constant	82.229	8.111	10.14	0.000
Volume	-2.5521	0.2697	-9.46	0.000
DCR	5.8957	0.1495	39.43	0.000
AC	-0.7813	0.1761	-4.44	0.000
V*DCR	-0.062130	0.002316	-26.82	0.000
V*AC	0.011162	0.002895	3.86	0.000
AC*DCR	-0.058773	0.004229	-13.90	0.000
V**2	0.021413	0.002243	9.55	0.000
DCR**2	-0.021000	0.004229	-4.97	0.000

S = 0.1831 R-Sq = 99.9% R-Sq(adj) = 99.9%

Analysis of Variance

Source	DF	SS	MS	F	P
Regression	8	1302.23	162.78	4854.60	0.000
Residual Error	39	1.31	0.03		
Total	47	1303.54			

Source	DF	Seq SS
Volume	1	91.09
DCR	1	1121.13
AC	1	55.03
V*DCR	1	24.13
V*AC	1	0.50
AC*DCR	1	6.48
V**2	1	3.06
DCR**2	1	0.83

Unusual Observations

Obs	Volume	Eps	Fit	StDev Fit	Residual	St Resid
17	60.0	11.8500	11.4757	0.0870	0.3743	2.32R
21	60.0	16.9100	16.5016	0.0667	0.4084	2.39R
48	65.0	19.7300	19.4213	0.1065	0.3087	2.07R

R denotes an observation with a large standardized residual

Table D.11. Dielectric constant at different aggregate volume for dielectric constant of 6

Aggregate Volume (%)		C/A=10/6 Air Content				C/A=20/6 Air Content			
		0	2	4	6	0	2	4	6
55	Eps (4/3)	7.62	7.38	7.13	6.88	10.95	10.53	10.07	9.60
	Eps (3/4)	7.60	7.37	7.14	6.89	10.77	10.39	9.99	9.55
	Average	7.61	7.38	7.13	6.88	10.86	10.46	10.03	9.58
		C/A= 30/6 Air Content				C/A= 40/6 Air Content			
		0	2	4	6	0	2	4	6
	Eps (4/3)	13.95	13.37	12.71	12.04	16.84	16.10	15.24	14.36
	Eps (3/4)	13.57	13.05	12.51	11.88	16.23	15.58	14.89	14.07
	Average	13.76	13.21	12.61	11.96	16.54	15.84	15.06	14.22
60		C/A=10/6 Air Content				C/A=20/6 Air Content			
		0	2	4	6	0	2	4	6
	Eps (4/3)	7.43	6.77	6.53	6.31	10.32	9.46	9.01	8.59
	Eps (3/4)	7.41	6.76	6.50	6.20	10.12	9.39	8.97	8.46
	Average	7.42	6.76	6.52	6.25	10.22	9.42	8.99	8.52
		C/A= 30/6 Air Content				C/A= 40/6 Air Content			
		0	2	4	6	0	2	4	6
	Eps (4/3)	12.89	11.87	11.23	10.61	15.36	14.19	13.35	12.52
	Eps (3/4)	12.47	11.67	11.11	10.42	14.69	13.82	13.12	12.27
	Average	12.68	11.77	11.17	10.51	15.03	14.00	13.24	12.39
65		C/A=10/6 Air Content				C/A=20/6 Air Content			
		0	2	4	6	0	2	4	6
	Eps (4/3)	7.25	7.01	6.77	6.54	9.71	9.30	8.93	8.48
	Eps (3/4)	7.22	7.01	6.77	6.55	9.50	9.18	8.81	8.53
	Average	7.23	7.01	6.77	6.54	9.60	9.24	8.87	8.51
		C/A= 30/6 Air Content				C/A= 40/6 Air Content			
		0	2	4	6	0	2	4	6
	Eps (4/3)	11.87	11.30	10.83	10.18	13.92	13.20	12.62	11.78
	Eps (3/4)	11.43	11.03	10.54	10.22	13.23	12.75	12.16	11.79
	Average	11.65	11.17	10.68	10.20	13.58	12.97	12.39	11.79

Table D.12. Dielectric constant at different aggregate volume for dielectric constant of 8

Aggregate Volume (%)		C/A=10/8 Air Content				C/A=20/8 Air Content			
		0	2	4	6	0	2	4	6
55	Eps (4/3)	8.87	8.60	8.32	8.04	12.47	12.02	11.52	11.02
	Eps (3/4)	8.86	8.60	8.33	8.05	12.35	11.93	11.49	11.01
	Average	8.86	8.60	8.33	8.05	12.41	11.97	11.51	11.02
		C/A= 30/8 Air Content				C/A= 40/8 Air Content			
		0	2	4	6	0	2	4	6
	Eps (4/3)	15.57	15.00	14.30	13.59	18.60	17.82	16.92	16.00
	Eps (3/4)	15.32	14.75	14.16	13.49	18.09	17.39	16.65	15.79
	Average	15.44	14.88	14.23	13.54	18.35	17.60	16.79	15.90
60		C/A=10/8 Air Content				C/A=20/8 Air Content			
		0	2	4	6	0	2	4	6
	Eps (4/3)	8.77	7.93	7.67	7.41	11.92	10.84	10.37	9.92
	Eps (3/4)	8.76	7.88	7.57	7.23	11.78	10.81	10.32	9.74
	Average	8.77	7.90	7.62	7.32	11.85	10.83	10.34	9.83
		C/A= 30/8 Air Content				C/A= 40/8 Air Content			
		0	2	4	6	0	2	4	6
	Eps (4/3)	14.63	13.38	12.71	12.06	17.19	15.78	14.91	14.06
	Eps (3/4)	14.30	13.26	12.62	11.85	16.63	15.52	14.75	13.79
	Average	14.47	13.32	12.67	11.95	16.91	15.65	14.83	13.93
65		C/A=10/8 Air Content				C/A=20/8 Air Content			
		0	2	4	6	0	2	4	6
	Eps (4/3)	8.67	8.41	8.12	7.88	11.39	10.94	10.51	10.04
	Eps (3/4)	8.67	8.41	8.13	7.85	11.24	10.87	10.44	10.10
	Average	8.67	8.41	8.13	7.86	11.32	10.91	10.48	10.07
		C/A= 30/8 Air Content				C/A= 40/8 Air Content			
		0	2	4	6	0	2	4	6
	Eps (4/3)	13.69	13.08	12.53	11.85	15.83	15.06	14.41	13.53
	Eps (3/4)	13.33	12.87	12.32	11.93	15.24	14.70	14.03	13.60
	Average	13.51	12.97	12.43	11.89	15.53	14.88	14.22	13.56

Regression Analysis

The regression equation for general predictive model is
Eps(Blk) = 1.25 + 0.00990 AGG + 0.00539 CEM - 0.0971 AC +0.000003 AGG*CEM

Predictor	Coef	StDev	T	P
Constant	1.2540	0.3084	4.07	0.000
AGG	0.0099002	0.0008105	12.21	0.000
CEM	0.0053876	0.0002972	18.13	0.000
AC	-0.09708	0.01568	-6.19	0.000
AGG*CEM	0.00000301	0.00000081	3.74	0.000

S = 0.4172 R-Sq = 98.2% R-Sq(adj) = 98.2%

Analysis of Variance

Source	DF	SS	MS	F	P
Regression	4	1333.79	333.45	1915.84	0.000
Residual Error	139	24.19	0.17		
Total	143	1357.98			

Source	DF	Seq SS
AGG	1	180.73
CEM	1	1143.90
AC	1	6.73
AGG*CEM	1	2.43

Unusual Observations

Obs	AGG	Eps(Blk)	Fit	StDev Fit	Residual	St Resid
13	220	14.6200	14.3229	0.1363	0.2971	0.75 X
109	260	11.5100	12.4674	0.0823	-0.9574	-2.34R

R denotes an observation with a large standardized residual
X denotes an observation whose X value gives it large influence.

Table D.13. Variations of mixture theory models with respect to predictive model at 55% aggregate volume and Eps aggregate of 4.0.

AC (%)	Method	Eps (cement)							
		40		30		20		10	
		Eps	Variation (%)	Eps	Variation (%)	Eps	Variation (%)	Eps	Variation (%)
0	Predictive Model	14.74		12.10		9.33		6.44	
	Maxwell	17.11	16.05	13.56	12.05	10.00	7.14	6.37	-1.04
	Rayleigh	17.11	16.05	13.56	12.05	10.00	7.14	6.37	-1.04
	Wiener	17.11	16.05	13.56	12.05	10.00	7.14	6.37	-1.04
	Bruggemann	15.90	7.85	12.80	5.77	9.65	3.39	6.32	-1.82
	Bottcher	14.00	-5.04	11.70	-3.32	9.20	-1.43	6.25	-2.91
	Looyenga	14.03	-4.84	11.72	-3.16	9.19	-1.53	6.26	-2.75
2	Predictive Model	14.02		11.52		8.90		6.15	
	Maxwell	15.97	13.94	12.72	10.39	9.45	6.16	6.12	-0.53
	Bottcher	13.00	-7.25	11.00	-4.53	8.70	-2.26	6.05	-1.67
	Looyenga	13.21	-5.75	11.08	-3.84	8.75	-1.70	6.02	-2.15
4	Predictive Model	13.29		10.94		8.47		5.87	
	Maxwell	14.84	11.67	11.88	8.56	8.91	5.20	5.87	0.03
	Bottcher	12.30	-7.44	10.30	-5.88	8.30	-2.00	5.82	-0.82
	Looyenga	12.41	-6.62	10.46	-4.41	8.32	-1.76	5.80	-1.16
6	Predictive Model	12.56		10.36		8.04		5.58	
	Maxwell	13.74	9.38	11.07	6.82	8.38	4.26	5.62	0.65
	Bottcher	11.35	-9.65	9.80	-5.44	7.90	-1.71	5.60	0.30
	Looyenga	11.65	-7.26	9.87	-4.76	7.90	-1.71	5.58	-0.06

Table D.14. Variations of mixture theory models with respect to predictive model at 60% aggregate volume and Eps aggregate of 4.0.

AC (%)	Method	Eps (cement)							
		40		30		20		10	
		Eps	Variation (%)	Eps	Variation (%)	Eps	Variation (%)	Eps	Variation (%)
0	Predictive Model	13.03		10.77		8.39		5.88	
	Maxwell	15.45	18.59	12.36	14.72	9.25	10.21	6.09	3.50
	Rayleigh	15.45	18.59	12.36	14.72	9.25	10.21	6.09	3.50
	Wiener	15.45	18.59	12.36	14.72	9.25	10.21	6.09	3.50
	Bruggemann	14.20	9.00	11.60	7.66	8.90	6.04	6.02	2.31
	Bottcher	12.20	-6.36	10.40	-3.47	8.40	0.08	5.95	1.12
	Looyenga	12.49	-4.13	10.58	-1.80	8.47	0.92	5.97	1.46
2	Predictive Model	12.35		10.25		8.01		5.65	
	Maxwell	14.31	15.83	11.51	12.32	8.70	8.56	5.83	3.14
	Bottcher	11.25	-8.94	9.80	-4.37	8.00	-0.17	5.75	1.72
	Looyenga	11.73	-5.05	9.98	-2.61	8.05	0.45	5.75	1.72
4	Predictive Model	11.68		9.72		7.64		5.42	
	Maxwell	13.19	12.93	10.68	9.86	8.16	6.88	5.58	2.93
	Bottcher	10.50	-10.10	9.20	-5.36	7.55	-1.11	5.52	1.82
	Looyenga	10.99	-5.91	9.41	-3.20	7.64	0.07	5.53	2.01
6	Predictive Model	11.01		9.19		7.26		5.19	
	Maxwell	12.09	9.85	9.87	7.34	7.63	5.15	5.33	2.70
	Bottcher	9.70	-11.87	8.60	-6.47	7.15	-1.46	5.35	3.09
	Looyenga	10.29	-6.51	8.86	-3.64	7.25	-0.08	5.31	2.32

Table D.15. Variations of mixture theory models with respect to predictive model at 65% aggregate volume and Eps aggregate of 4.0.

AC (%)	Method	Eps (cement)							
		40		30		20		10	
		Eps	Variation (%)	Eps	Variation (%)	Eps	Variation (%)	Eps	Variation (%)
0	Predictive Model	11.76		9.89		7.90		5.78	
	Maxwell	13.85	17.78	11.20	13.21	8.53	7.98	5.81	0.55
	Rayleigh	13.85	17.78	11.20	13.21	8.53	7.98	5.81	0.55
	Wiener	13.85	17.78	11.20	13.21	8.53	7.98	5.81	0.55
	Bruggemann	12.50	6.30	10.50	6.14	8.17	3.43	5.75	-0.48
	Bottcher	10.50	-10.71	9.00	-9.03	7.65	-3.16	5.67	-1.87
	Looyenga	11.07	-5.86	9.52	-3.77	7.78	-1.51	5.70	-1.35
2	Predictive Model	11.14		9.42		7.57		5.60	
	Maxwell	12.71	14.11	10.35	9.88	7.98	5.37	5.55	-0.88
	Bottcher	9.80	-12.01	8.60	-8.70	7.25	-4.27	5.46	-2.49
	Looyenga	10.37	-6.90	8.96	-4.88	7.39	-2.42	5.48	-2.13
4	Predictive Model	10.52		8.95		7.25		5.42	
	Maxwell	11.59	10.20	9.52	6.42	7.44	2.66	5.30	-2.23
	Bottcher	9.10	-13.48	8.00	-10.57	6.90	-4.79	5.28	-2.60
	Looyenga	9.69	-7.87	8.43	-5.77	7.00	-3.41	5.27	-2.79
6	Predictive Model	9.90		8.47		6.92		5.24	
	Maxwell	10.49	6.00	8.70	2.69	6.91	-0.16	5.05	-3.67
	Bottcher	8.40	-15.12	7.50	-11.48	6.50	-6.09	5.05	-3.67
	Looyenga	9.05	-8.55	7.82	-7.70	6.63	-4.21	5.06	-3.48

Table D.16. ANOVA input data for the theoretical mixture formulas evaluation at aggregate volume =55%

Volume (%)	AC (%)	DCR	Method	Variation (%)
55	0	10	Maxwell	17.04
55	0	10	Bottcher	4.23
55	0	10	Looyenga	4.03
55	0	7.5	Maxwell	13.64
55	0	7.5	Bottcher	1.95
55	0	7.5	Looyenga	1.78
55	0	5	Maxwell	9.01
55	0	5	Bottcher	0.29
55	0	5	Looyenga	0.18
55	0	2.5	Maxwell	2.66
55	0	2.5	Bottcher	0.72
55	0	2.5	Looyenga	0.89
55	2	10	Maxwell	14.33
55	2	10	Bottcher	6.93
55	2	10	Looyenga	5.42
55	2	7.5	Maxwell	11.3
55	2	7.5	Bottcher	3.75
55	2	7.5	Looyenga	3.05
55	2	5	Maxwell	7.17
55	2	5	Bottcher	1.34
55	2	5	Looyenga	0.77
55	2	2.5	Maxwell	1.89
55	2	2.5	Bottcher	0.73
55	2	2.5	Looyenga	0.23

Volume (%)	AC (%)	DCR	Method	Variation (%)
55	4	10	Maxwell	12.08
55	4	10	Bottcher	7.1
55	4	10	Looyenga	6.27
55	4	7.5	Maxwell	9.29
55	4	7.5	Bottcher	5.25
55	4	7.5	Looyenga	3.78
55	4	5	Maxwell	5.69
55	4	5	Bottcher	1.54
55	4	5	Looyenga	1.3
55	4	2.5	Maxwell	1.29
55	4	2.5	Bottcher	0.43
55	4	2.5	Looyenga	0.09
55	6	10	Maxwell	10.52
55	6	10	Bottcher	8.7
55	6	10	Looyenga	6.29
55	6	7.5	Maxwell	7.93
55	6	7.5	Bottcher	4.45
55	6	7.5	Looyenga	3.77
55	6	5	Maxwell	4.6
55	6	5	Bottcher	1.4
55	6	5	Looyenga	1.4
55	6	2.5	Maxwell	0.8
55	6	2.5	Bottcher	0.44
55	6	2.5	Looyenga	0.08

Table D.17. ANOVA Input data for the theoretical mixture formulas evaluation at aggregate volume =60%

Volume (%)	AC (%)	DCR	Method	Variation (%)	Volume (%)	AC (%)	DCR	Method	Variation (%)
60	0	10	Maxwell	18.48	**60**	4	10	Maxwell	14.28
60	0	10	Bottcher	6.44	**60**	4	10	Bottcher	9.03
60	0	10	Looyenga	4.22	**60**	4	10	Looyenga	4.78
60	0	7.5	Maxwell	14.62	**60**	4	7.5	Maxwell	11.74
60	0	7.5	Bottcher	3.56	**60**	4	7.5	Bottcher	3.74
60	0	7.5	Looyenga	1.89	**60**	4	7.5	Looyenga	1.55
60	0	5	Maxwell	9.41	**60**	4	5	Maxwell	8.7
60	0	5	Bottcher	0.65	**60**	4	5	Bottcher	0.57
60	0	5	Looyenga	0.18	**60**	4	5	Looyenga	1.77
60	0	2.5	Maxwell	2.77	**60**	4	2.5	Maxwell	5.75
60	0	2.5	Bottcher	0.41	**60**	4	2.5	Bottcher	4.62
60	0	2.5	Looyenga	0.75	**60**	4	2.5	Looyenga	4.81
60	2	10	Maxwell	16.88	**60**	6	10	Maxwell	12.39
60	2	10	Bottcher	8.12	**60**	6	10	Bottcher	9.83
60	2	10	Looyenga	4.2	**60**	6	10	Looyenga	4.35
60	2	7.5	Maxwell	13.93	**60**	6	7.5	Maxwell	10.18
60	2	7.5	Bottcher	2.99	**60**	6	7.5	Bottcher	4
60	2	7.5	Looyenga	1.21	**60**	6	7.5	Looyenga	1.1
60	2	5	Maxwell	10.26	**60**	6	5	Maxwell	7.56
60	2	5	Bottcher	1.39	**60**	6	5	Bottcher	0.8
60	2	5	Looyenga	2.02	**60**	6	5	Looyenga	2.21
60	2	2.5	Maxwell	6.22	**60**	6	2.5	Maxwell	5.46
60	2	2.5	Bottcher	4.77	**60**	6	2.5	Bottcher	5.86
60	2	2.5	Looyenga	4.77	**60**	6	2.5	Looyenga	5.06

Table D.18. ANOVA Input data for the theoretical mixture formulas evaluation at aggregate volume =65%

Volume (%)	AC (%)	DCR	Method	Variation (%)	Volume (%)	AC (%)	DCR	Method	Variation (%)
65	0	10	Maxwell	20.33	**65**	4	10	Maxwell	10.8
65	0	10	Bottcher	8.77	**65**	4	10	Bottcher	13
65	0	10	Looyenga	3.82	**65**	4	10	Looyenga	7.36
65	0	7.5	Maxwell	15.73	**65**	4	7.5	Maxwell	7.81
65	0	7.5	Bottcher	7	**65**	4	7.5	Bottcher	9.4
65	0	7.5	Looyenga	1.63	**65**	4	7.5	Looyenga	4.53
65	0	5	Maxwell	9.83	**65**	4	5	Maxwell	4.2
65	0	5	Bottcher	1.5	**65**	4	5	Bottcher	3.36
65	0	5	Looyenga	0.17	**65**	4	5	Looyenga	1.96
65	0	2.5	Maxwell	2.69	**65**	4	2.5	Maxwell	0.38
65	0	2.5	Bottcher	0.22	**65**	4	2.5	Bottcher	0
65	0	2.5	Looyenga	0.75	**65**	4	2.5	Looyenga	0.19
65	2	10	Maxwell	15.86	**65**	6	10	Maxwell	5.85
65	2	10	Bottcher	10.67	**65**	6	10	Bottcher	15.24
65	2	10	Looyenga	5.47	**65**	6	10	Looyenga	8.68
65	2	7.5	Maxwell	11.89	**65**	6	7.5	Maxwell	3.57
65	2	7.5	Bottcher	7.03	**65**	6	7.5	Bottcher	10.71
65	2	7.5	Looyenga	3.14	**65**	6	7.5	Looyenga	6.9
65	2	5	Maxwell	7.11	**65**	6	5	Maxwell	1.17
65	2	5	Bottcher	2.68	**65**	6	5	Bottcher	4.83
65	2	5	Looyenga	0.81	**65**	6	5	Looyenga	2.93
65	2	2.5	Maxwell	1.46	**65**	6	2.5	Maxwell	0.79
65	2	2.5	Bottcher	0.18	**65**	6	2.5	Bottcher	0.79
65	2	2.5	Looyenga	0.18	**65**	6	2.5	Looyenga	0.59

General Linear Model

```
Factor     Type Levels Values
Volume    fixed      3 55 60 65
DCR       fixed      4  2.5  5.0  7.5 10.0
Method    fixed      3 Bottcher Looyenga Maxwell

Analysis of Variance for Variatio, using Adjusted SS for Tests

Source     DF     Seq SS     Adj SS     Adj MS       F      P
Volume      2      43.73      43.73      21.86    3.04  0.051
DCR         3    1219.00    1219.00     406.33   56.57  0.000
Method      2     897.08     897.08     448.54   62.44  0.000
Error     136     976.90     976.90       7.18
Total     143    3136.70

Unusual Observations for Variatio

Obs  Variatio       Fit   StDev Fit  Residual   St Resid
 97   20.3300   13.1038      0.6317    7.2262      2.77R
100   15.7300    9.9926      0.6317    5.7374      2.20R
133    5.8500   13.1038      0.6317   -7.2538     -2.78R
134   15.2400    8.8135      0.6317    6.4265      2.47R
136    3.5700    9.9926      0.6317   -6.4226     -2.47R
139    1.1700    6.9640      0.6317   -5.7940     -2.22R

R denotes an observation with a large standardized residual.

Tukey Simultaneous Tests
Response Variable Variatio
All Pairwise Comparisons among Levels of Method

Method = Bottcher subtracted from:

Level        Difference       SE of             Adjusted
Method         of Means  Difference   T-Value    P-Value
Looyenga         -1.627      0.5471    -2.974     0.0097
Maxwell           4.290      0.5471     7.842     0.0000

Method = Looyenga subtracted from:

Level        Difference       SE of             Adjusted
Method         of Means  Difference   T-Value    P-Value
Maxwell           5.917      0.5471     10.82     0.0000

Tukey Simultaneous Tests
Response Variable Variatio
All Pairwise Comparisons among Levels of Volume

Volume = 55 subtracted from:

Level      Difference       SE of             Adjusted
Volume       of Means  Difference   T-Value    P-Value
60             1.3013      0.5471     2.379     0.0489
65             0.9612      0.5471     1.757     0.1881
```

Volume = 60 subtracted from:

Level Volume	Difference of Means	SE of Difference	T-Value	Adjusted P-Value
65	-0.3400	0.5471	-0.6215	0.8086

Tukey Simultaneous Tests
Response Variable Variatio
All Pairwise Comparisons among Levels of DCR

DCR = 2.5 subtracted from:

Level DCR	Difference of Means	SE of Difference	T-Value	Adjusted P-Value
5.0	1.418	0.6317	2.244	0.1167
7.5	4.446	0.6317	7.039	0.0000
10.0	7.558	0.6317	11.964	0.0000

DCR = 5.0 subtracted from:

Level DCR	Difference of Means	SE of Difference	T-Value	Adjusted P-Value
7.5	3.029	0.6317	4.794	0.0000
10.0	6.140	0.6317	9.719	0.0000

DCR = 7.5 subtracted from:

Level DCR	Difference of Means	SE of Difference	T-Value	Adjusted P-Value
10.0	3.111	0.6317	4.925	0.0000

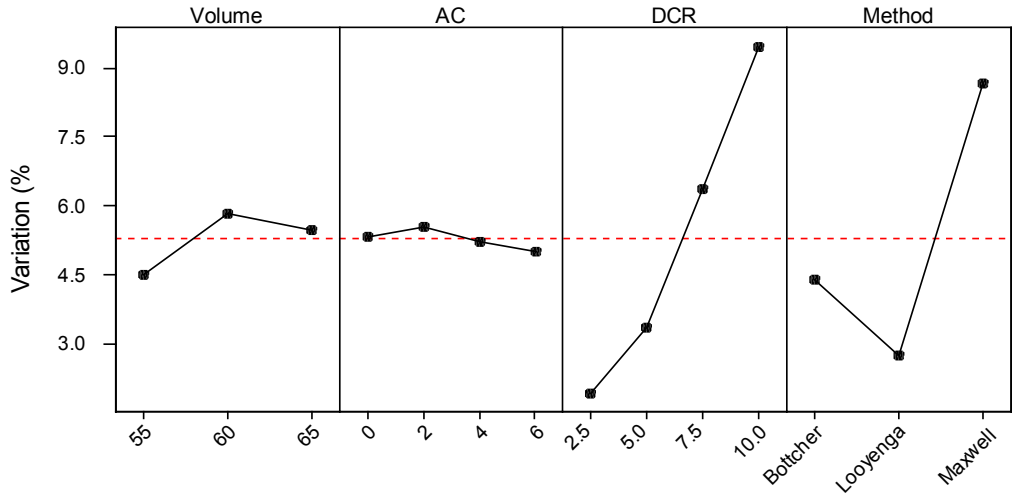

Figure D.7. Main effects plot-data means for variation (%)

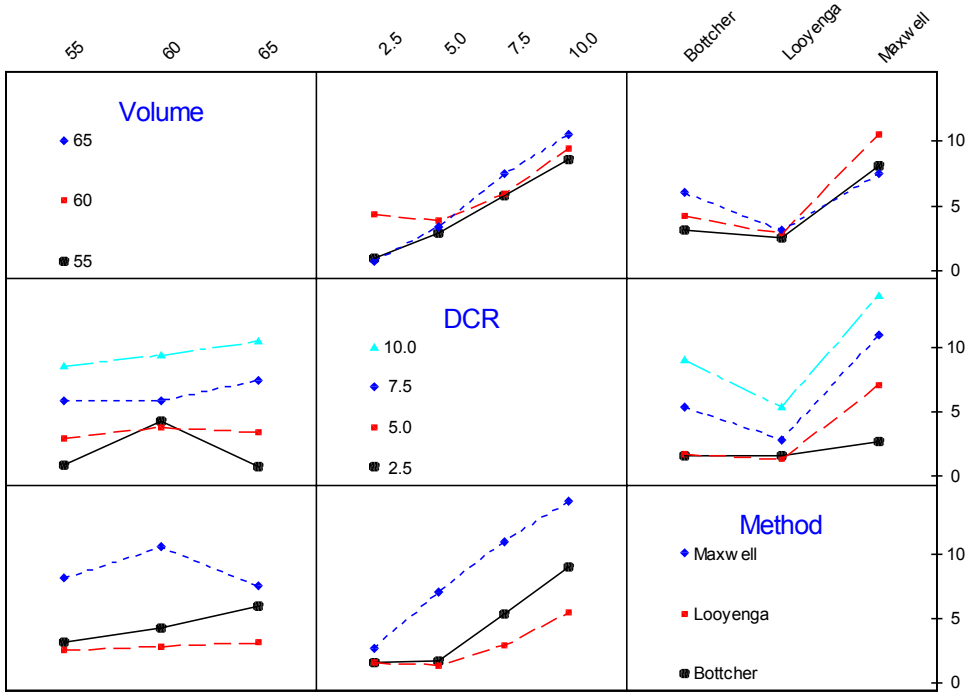

Figure D.18. Interaction plot-data means for variation (%)

Vita

Aref J. Alderbas Alzaabi was born in Kuwait City, on March 20, 1964. In 1987, he received his B.S. degree in Civil Engineering from Kuwait University. From 1987 to 1989, he worked as an engineer at Kuwait Municipality. In 1989, he has been awarded a scholarship by the government of Kuwait to peruse his graduate studies in Civil Engineering. In 1990, he received his M.S. degree from the Civil and Environmental Engineering Department at Utah State University, Logan, UT. In 2000, he completed all the requirements for the Doctor of Philosophy in Civil Engineering from Virginia Polytechnic Institute and State University, Blacksburg, VA. Within the year 2000, he enrolled in a professional training course in Asphalt technology offered by the National Center for Asphalt Technology at Auburn, AL.